



Provided by the author(s) and University of Galway in accordance with publisher policies. Please cite the published version when available.

Title	Volcanic activity, magma-sediment-water interaction, hydrothermal alteration and vein mineralisation in south County Waterford
Author(s)	Breheny, Catherine
Publication Date	2010-11-05
Item record	http://hdl.handle.net/10379/2243

Downloaded 2024-05-24T17:18:24Z

Some rights reserved. For more information, please see the item record link above.



National University of Ireland, Galway

School of Natural Sciences

**VOLCANIC ACTIVITY, MAGMA-SEDIMENT-WATER
INTERACTION, HYDROTHERMAL ALTERATION AND
VEIN MINERALISATION IN SOUTH COUNTY
WATERFORD**



Catherine Breheny

Supervisors: Dr. Kathryn Moore

Prof. Martin Feely

A thesis submitted for the degree of Doctor of Philosophy.
Earth and Ocean Sciences, School of Natural Sciences, National
University of Ireland, Galway

Table of Contents

Preliminary pages	Page no.
Contents	i
List of figures	v
List of tables	ix
Abstract	x
Acknowledgements	xi
Chapter One: Introduction	
1.1 Aims and objectives of this study	1
1.2 Rock types associated with magma-sediment-water interaction	3
1.3 Processes of magma-sediment-water interaction	7
1.4 Fluid circulation and mineralisation in seafloor settings	11
1.5 Case study of magma-sediment-water interaction and mineralisation	12
1.6 Collaborative aspects of the research	15
Chapter Two: Field relationships of the South Waterford volcanic rocks	
2.1 Introduction	16
2.2 Previous Research	18
2.2.1 The Bunmahon Formation	18
2.2.2 The Dunabrattin Formation	18
2.2.3 The Campile Formation	19
2.2.4 Volcano Reconstructions	22
2.3 Volcanological features of the Bunmahon Formation at Trawnamoe	25
2.3.1 Extrusive	25
2.3.2 Early intrusive	30
2.3.3 Late intrusive	30
2.3.4 Sedimentary rocks	31
2.4 Volcanological features of the Bunmahon and Dunabrattin Formations at Stradbally Cove	36
2.4.1 Siltstone	39

2.4.2	Mudstone	39
2.4.3	Tuffs	39
2.4.4	Intrusive rocks	42
2.4.5	Peperite lithologies	42
2.5	Additional coastal and cored localities in the Bunmahon Formation	46
2.6	Coastal and core localities in the Campile Formation	50
2.7	Mineralisation	52
2.8	Peperite rock textures	56
2.8.1	Fluidal peperite	56
2.8.2	Honeycomb peperite	57
2.8.3	Mixed morphology peperite	57
2.9	Discussion	62
2.9.1	Temporal volcano and volcano-sedimentary associations	62
2.9.2	Fragmentation processes	66
2.9.3	Effects of magma and sediment properties on juvenile clast morphology	70
2.9.4	Mineralisation	72
2.10	Conclusions	73

Chapter Three: Petrography of the major volcanic and sedimentary lithologies in south County Waterford

3.1	Introduction	75
3.2	Petrography of major rock types in Trawnamoe	
3.2.1	Tuff units	75
3.2.2	Mafic-intermediate intrusive rocks	76
3.2.3	Lava flows	80
3.2.4	Felsic intrusive rocks	80
3.3	Petrography of major rock types in Stradbally Cove	83
3.3.1	Sedimentary rocks	83
3.3.2	Mafic-intermediate intrusive rocks	86
3.4	Discussion	88
3.5	Conclusions	89

Chapter Four: Bulk rock and Mineral geochemistry

4.1	Introduction	90
4.2	Sampling and analytical techniques	91
4.3	Results	95
4.3.1	Whole rock analysis	95
4.3.2	Trace element geochemistry	104
4.3.3	Rare Earth Element geochemistry	108
4.3.4	Volcanic discrimination diagrams	111
4.3.5	Mineral chemistry	119
4.3.6	Element mapping	133
4.4	Discussion	138
4.4.1	Tectonic setting, magmatic source and provenance	138
4.4.2	Fractionation	139
4.4.3	Alteration	140
4.4.4	Secondary mineral composition	141
4.5	Conclusions	145

Chapter Five: Fluid Inclusion studies of Vein Mineralisation

5.1	Introduction	147
5.2	Sampling for fluid inclusion studies	147
5.3	Fluid inclusions – an introduction	150
5.4	Analytical techniques used in fluid inclusion studies	150
5.4.1	Fluid inclusion petrography	150
5.4.2	Microthermometry	153
5.5	Results	156
5.5.1	Trawnamoe	158
5.5.2	Stradbally Cove	158
5.6	P-T-X trapping conditions	162
5.7	Discussion	165
5.8	Conclusions	169

Chapter Six: Summary and Conclusions

6.1	Introduction	171
6.2	Summary of results	171
6.3	The evolution of the Bunmahon Volcano and its environs	172

6.4	Conclusions	181
6.5	Suggestions for future work	182
References		183
Appendix A1: Some global occurrences of peperite and details of their formation		207
Appendix A2: Core section logs and descriptions from the Bunmahon and Campile Formations		200
Appendix A3: Data sheets of lithological and geochemical characteristics of analysed rocks		213
Appendix A4: Techniques and error calculations used in image analysis of rock textures		200
Appendix A5: Methods, standards and error calculations used for geochemical whole rock analysis and table of bulk rock geochemical results		236
Appendix A6: Microthermometric results		246
Appendix A7: Dissemination of results		255

List of figures:	Page no.
1.1: Range of possible peperite textures	6
1.2: Fragmentation processes associated with magma-water interaction	7
1.3: Depth and pressure constraints of fragmentation	10
1.4: Detail of magma fragmentation	11
1.5: Geological map of southeast Ireland, with location of study area	14
2.1: Geological map of south county Waterford	17
2.2: Stratigraphic column for east and west Tramore	21
2.3: Schematic Ordovician basin evolution	24
2.4: Geological map and cliff section geology of Trawnamoe	27
2.5: Field photographs of pillow lava and lapilli tuff	28
2.6: Field photographs of bomb in lapilli tuff and sheet flows	29
2.7: Field photographs of fluidal peperite	32
2.8: Photographs of small scale features in peperite	33
2.9: Field photographs of felsic intrusive rocks	34
2.10: Field photograph of Old Red Sandstone	35
2.11a: Geological map of Stradbally Cove	37
2.11b: Cliff section geology of Stradbally Cove	38
2.12: Field photographs of deformed siltstone	40
2.13: Field photographs of lithic tuff and pyrite-rich tuff	41
2.14: Field photographs of irregular intrusive contacts	43
2.15: Field photographs of intrusive rocks	44
2.16: Field photographs of blocky and mixed morphology peperite	45
2.17: Geological map and field photograph of Kilmurrin Cove	48
2.18: Field photographs of Ballydowane Bay	49
2.19: Field photographs of Kilfarrasy Strand and Garrarus Strand	51
2.20: Field photographs of vein mineralisation at Trawnamoe	54
2.21: Field photographs of vein mineralisation at Stradbally Cove and Trawnamoe	55
2.22: Sketches of the main features in peperite	59
2.23: Field photographs and corresponding binary images of peperite	60
2.24: Frequency distribution diagram and rose diagram of peperite	61
2.25: Summary of events at the Bunmahon Volcano	64

2.26:	Cross-section of arc volcano showing location of Trawnamoe and Stradbally Cove	65
2.27:	Evolution of extrusive products with increasing rate of eruption	69
2.28:	Processes involved in the formation of peperite	71
2.29:	Summary of factors controlling the type of intrusive contact	74
3.1:	Photomicrographs of typical tuff	78
3.2:	Photomicrographs of mafic-intermediate intrusive rocks	79
3.3:	Photomicrographs of sheet flow and hyaloclastite	81
3.4:	Photomicrographs of quartz-feldspar porphyry	82
3.5:	Photomicrographs of fine-grained sedimentary rocks	84
3.6:	Photomicrographs of lithic tuff	
3.7:	Photomicrographs of mafic-intermediate rocks from Stradbally Cove	87
4.1:	Total alkalis versus silica classification diagram	97
4.2:	Igneous classification diagrams after Winchester and Floyd: SiO ₂ vs. Zr/TiO ₂ , Zr/TiO ₂ vs. Nb/Y	98
4.3:	Harker diagrams	100
4.4:	Alteration box plot after Large <i>et al.</i> , 2001	103
4.5:	Multielement profiles of lavas, intrusive rocks and tuffs from the Bunmahon Formation normalised to MORB after Pearce (1983)	105
4.6:	Multielement profiles of volcanic rocks from the Campile Formation and sedimentary rocks from the Dunabrattin Formation, normalised using values of Pearce (1983)	106
4.7:	Multielement profile of sedimentary rocks normalised to upper crust values of Rudnick and Gao (2003)	107
4.8:	Rare Earth Element profiles of lavas, intrusive rocks and tuffs from the Bunmahon Formation, normalised to MORB after Sun and McDonough (1989)	109
4.9:	Rare Earth Element profiles of volcanic rocks from the Campile Formation and sedimentary rocks from the Dunabrattin Formation, normalised MORB after Sun and McDonough (1989)	110
4.10:	Bivariate discrimination between alkaline and tholeiitic after Winchester and Floyd (1976)	112

4.11:	Bivariate plot of Zr vs. Ti after Pearce (1983)	113
4.12:	Bivariate diagram of Ta/Yb vs. Th/Yb after Pearce (1982)	114
4.13:	Ternary plot of MnO-TiO ₂ -P ₂ O ₅ after Mullen (1983)	114
4.14:	Sediment classification diagrams after Herron (1988) and Roser and Korsch (1986)	117
4.15:	Tectonic discrimination diagrams of sedimentary rocks after Bhatia (1983)	118
4.16:	Backscatter electron images of magma-sediment contact and alteration within peperite clast	123
4.17:	Graph of Si vs. Fe in chlorite and a plot of chlorite composition on a Hey (1954) classification diagram	124
4.18:	Temperature variations determined by chlorite geothermometry	127
4.19:	Backscatter electron image of epidote and pumpellyite crystals	130
4.20:	Backscatter electron image of iron-oxides in basaltic andesite	131
4.21:	Backscatter electron images of secondary sphene and pyrite	132
4.22:	Element maps across the magma-sediment contact in peperite (sample BT15)	134
4.23:	Element maps across the magma-sediment contact in peperite (sample BS32)	136
4.24:	Element maps across the magma-sediment contact in peperite (sample BS31)	137
4.25:	Cartoon depicting the variety of syn-volcanic alteration zones	146
4.26:	Cartoon depicting the circulation of Fe-rich hydrothermal fluid and Mg-rich seawater in peperite	146
5.1:	Geological map of Trawnamoe and Stradbally Cove with locations of vein samples	149
5.2:	Development of Primary and secondary fluid inclusions	151
5.3:	Sketch of fluid inclusion classification based on paragenesis and phases present	152
5.4:	Steps involved in microthermometric study of two phase (L+V) fluid inclusions	154
5.5:	Graphical representation of the relationship between T _H , T _i and trapping pressure	155
5.6:	Photomicrographs of inclusion types in vein mineralisation	157

5.7:	Frequency distribution histograms of T_H	159
5.8:	Frequency distribution histograms of salinity	160
5.9:	Bivariate diagrams of salinity vs. T_H	161
5.10:	Schematic P-T diagram for aqueous fluid	162
5.11:	Pressure determination from observed mineral assemblage	163
5.12:	Minimum, mean and maximum isochores plotted for sulphide-bearing and barren veins	164
5.13:	Typical trends in T_H -salinity space	165
5.14:	Range of salinity and T_H of fluid inclusions in vein mineralisation compared to other known deposits	168
5.15:	Fluid mixing trend compared to Carboniferous Irish-type mineralisation	168
5.16:	Summary of possible hydrothermal fluid flow and mineralisation	170
6.1:	Model tracking the evolution of the Bunmahon Volcano and its environs	175
6.2	Schematic representation of hydrothermal fluid circulation	177
6.3:	Comparison between temperature of alteration and mineralisation	179

List of tables:	Page no.
3.1: Comparison of mineral assemblage in sill and peperite clasts	34
4.1: List of samples and corresponding reference materials analysed for whole rock geochemistry	93
4.2: List of samples analysed with SEM and EPMA	94
4.3: Measure of Eu anomaly, ratio of LREE to HREE, LREE fractionation and HREE fractionation	108
4.4: Correlation between various discrimination diagrams used	111
4.5: Representative major element composition of feldspar	120
4.6: Representative major element composition of chlorite	121
4.7: Variations in Fe number in chlorite	122
4.8: Temperature of chlorite formation calculated from three different chlorite geothermometers	126
4.9: Representative major element composition of epidote and pumpellyite	129
4.10: Representative major element composition of apatite and sphene	129
5.1: Location, composition and host lithology data for vein samples	148
5.2: Various salt systems and their corresponding eutectic temperatures	154
5.3: Description and characteristics of fluid inclusions in vein mineralisation recorded from Trawnamoe and Stradbally Cove	156
6.1: Temperature variations between vein mineralisation and alteration of the host volcanic rocks	178
6.2: Comparisons between local and regional scale fluid temperatures, compositions and occurrences	180

Abstract

The Ordovician volcanic sequence of the south Waterford coast is used to investigate magma-sediment-water interaction and its role in hydrothermal systems.

Field investigations and rock textures analysis have shown that relatively constant composition intrusions were emplaced in rapidly consolidating host sediments. Early intrusions into water-laden sediments generated peperite clasts, with morphology determined primarily by magma:sediment ratio. Hydrothermal alteration (chlorite + epidote + sericite \pm pumpellyite) of the volcanic rocks is more pronounced within the more permeable and glassy sequences, such as peperite, hyaloclastite and pillow rims. The chemistry of chlorite ($\text{Fe\#} = 0.35\text{--}0.63$), its distribution, and its association with epidote, pumpellyite, pyrite and Fe-oxides have been used to determine that an iron-rich hydrothermal fluid interacted with magnesium-rich seawater in varying ratios and that fluid convection was promoted in the permeable sequence. Later intrusions show no evidence of interaction with unconsolidated sediment and/or water and as a result the dominant alteration assemblage is representative of later diagenesis.

Chlorite geothermometry shows that alteration occurred between 300°C and 400°C and, adjacent to peperitic intrusions, Na, K, Si and some REE are locally mobile within fluidised sediment. Sulphide-bearing veins were formed at lower temperatures (200°C to 350°C) as a result of mixing between a high temperature, low salinity fluid and a lower temperature, high salinity (possibly meteoric) fluid. The overall drop in temperature of the hydrothermal fluid may have contributed to the precipitation of base metals. Extensive volcanic activity within the seafloor generated an elevated geothermal gradient that drove a hydrothermal convection system and formed veins with base metals sourced from early volcanic and volcano-sedimentary products.

Authour's Declaration

I certify that this thesis is my own work and I have not obtained a degree in this university or elsewhere on the basis of this PhD thesis.

The work in this thesis is original except where indicated by special reference in the text.

SIGNED: _____

Catherine Breheny

DATE:

Acknowledgements

This project would not have been possible without the funding support of a National University of Ireland, Galway (NUIG) science faculty postgraduate fellowship, with additional funding for travel and laboratory expenses received from the Irish Geological Association (IGA), the Mineralogical Society (MinSoc), the Volcanic and Magmatic Studies Group (VMSG) and the International Mineralogical Association (IMA). This study was supervised by Dr. Kathryn Moore, whom I would like to thank for her never ending enthusiasm in all things geological. Dr. Martin Feely also provided invaluable support, in the form of geological expertise and his constant drive for perfection. Thanks also to all the technical and support staff both in the Earth and Ocean Sciences department of NUIG, and in Universitat de Barcelona and Camborne School of Mines who provided SEM and EMPA assistance. Thank you also to Dr. David Brown for pointing me in the direction of Mull, Professor Chris Stillman for sending his unpublished data and Aurum Exploration for sampling assistance.

A special thank you must go to Alex, who throughout the years has provided accommodation, laboratory assistance and training, and above all good advice. I am indebted to Bill for the extended loan of his computer, Aoife for the numerous discussions on all aspects of this project (particularly geochemistry) and Zara for help with the final printing. Thank you also to Breandán, and Aisling, who proof-read and provided constructive criticism. On that note thank you to all the postgraduate students in the EOS department for making the experience more enjoyable.

I am grateful to my family, especially my parents who provided constant support throughout the years, and Patricia for providing accommodation during the several trips to Waterford. Last but not least, thank you to Milo for providing every encouragement throughout this whole process.

Chapter One:

Introduction

1.1 Aims and objectives of this study

Magma-sediment-water interaction and its contribution to the development of Cu-bearing sulphide mineralisation was investigated using the Ordovician volcanic rocks of the southeastern belt in County Waterford as a case study. A range of analytical techniques were used to examine lithologies in order to investigate the effects of magma-sediment-water interaction on both the rock types formed as a result of this interaction and the surrounding host rocks. The main aims were to:

- 1) locate, describe and map in detail the evidence for magma-sediment and magma-water interaction and resolve the relationship between the various rock types that resulted from these interactions
- 2) determine the nature of magma-sediment-water interaction and to determine if the prevailing conditions at the time of these interactions were conducive to the generation of a hydrothermal system
- 3) study the geochemistry of the volcanic and volcano-sedimentary rocks in order to determine the extent of alteration and to resolve whether this alteration is attributed to magma-sediment-water interaction and/or subsequent metamorphism
- 4) establish the temperature of alteration and the temperature of vein mineralisation to identify whether they are related

Initial field mapping and reconnaissance was used to identify suitable areas for detailed study. Field investigations were undertaken along the stretch of coastline from Tramore towards Dungarvan and inland towards Dunhill using the Ordnance Survey published six inch maps (sheets WD024, 025 and 032; 1:10,560 scale). Trawnamoe and Stradbally Cove were investigated in greater detail (1:2,500 scale) because they display features (i.e. magmatic and sedimentary rocks, peperite and veins) suitable for investigation of the relationship between magma-sediment-water-interaction and vein mineralisation.

In order to classify peperite types, and to determine the mechanisms of peperite formation, variations in peperite were recorded and analysed through a combination of field relationships and image analysis of rock textures. Bulk rock

Introduction

geochemical analysis was used to investigate tectonic setting, magmatic affinity and fractionation trends. Similarly, the extent of alteration was examined, using both bulk rock geochemistry and micro-analytical geochemical techniques such as electron-probe micro analysis (EPMA) and scanning electron microscopy (SEM). The temperature range of alteration and/or subsequent metamorphism was calculated using elemental abundances and ratios. Temperature estimates of the hydrothermal fluid involved in vein mineralisation were derived from fluid inclusion studies and are compared to temperatures of chlorite alteration, in order to resolve the relationship between alteration and mineralisation.

1.2 Rock types associated with magma-sediment-water interaction

Interaction between magma and water is indicated by the cooled margin on the outer rim of pillow lavas, where the outer crust is composed of glass because of the rapid quenching of the molten lava when it is exposed to water (Moore, 1975). Pillow lavas are similar in morphology to sub-aerial pahoehoe lava flows (Walker, 1992) and comprise part of a system of inter-connected fingers or tubes that divide in the direction of flow (Vuagnat, 1975). As a result, a system containing large numbers of individual pillow lavas preserve magma flow direction. Although the shape of pillow lavas is largely controlled by the underlying pillows (Stark, 1939) the variety of shapes and sizes is also dependant on factors such as rate of supply of magma, magma composition and angle of the underlying slope. As basaltic lava forms smaller pillows than andesitic lava, and pillows erupted on a steep slope are significantly smaller than those on shallow depositional slopes (Walker, 1992), the original composition/viscosity of the melt and angle of the depositional surface can be determined. The extent of vesiculation of pillow lavas is a function of dissolved gas content and confining pressure, such that the distribution, size and abundance of vesicles can indicate depth of eruption (Wells *et al.*, 1979). Therefore pillow lavas containing small spherical vesicles sparsely distributed throughout the pillow are inferred to have erupted in deep water, while pillow lavas containing larger and more abundant vesicles are inferred to have erupted in shallow water. Lava extrusion onto the seafloor can also trap deep-sea sediment between individual pillows, which is usually metamorphosed and/or silicified to occur as cherts, cherty mudstone and limestones (Nichols, 1999), while accumulation of the glassy rinds of pillows commonly produces hyaloclastite deposits.

Hyaloclastite is composed of glassy shards of quenched magma and is formed as a result of explosive or non-explosive magma-water interaction. Explosive interaction between magma and water can occur as a result of increased volatile content or decreased confining pressure (Honnorez and Kirst, 1975), while non-explosive hyaloclastite formation is more likely at depths greater than ~100m and is probably the result of granulation of glassy fragments of pillow lavas (Zimanowski and Büttner, 2003). Hyaloclastite deposits may be associated with, and contain, primary pillow fragments (Aalto, 1986) or micro-globular components similar to pillows (Solomon, 1968). The development of hyaloclastite

Introduction

is also common in felsic composition volcanoes (e.g. Németh *et al.*, 2008); pumice-bearing hyaloclastites are a common product of explosive events while hyaloclastites containing lithic fragments and obsidian shards are generally associated with lava flows or lobes (Furnes *et al.*, 1980). Therefore, the primary components of hyaloclastite display evidence of their mechanism of formation (explosive vs. non-explosive). A jigsaw-fit texture of glassy shards indicates fragments have not been transported great distances while fragments with a preferred orientation indicate rapid movement during quenching of magma (Moore and Mueller, 2008). Therefore, the internal structure of hyaloclastites can aid in determination of lava flow behaviour.

Peperites are single lithological units comprising a magmatic and sedimentary component, formed as a result of interaction between magma and unconsolidated sediment. The first use of the term peperite was by Scrope (1858) who described a mixture of basalt and lime mud that was similar in appearance to pepper, but the origin or mechanism of formation of this mixture was not constrained. The most widely accepted definition of peperite was proposed by White *et al.* (2000) and is described as:

“a genetic term applied to a rock formed essentially in situ by disintegration of magma intruding and mingling with unconsolidated or poorly consolidated, typically wet sediments. The term also refers to similar mixtures generated by the same processes operating at the contacts of lavas and other hot volcanoclastic deposits with such sediments”.

The nature of magma-sediment interaction can influence clast shape, with juvenile clast morphology within peperite usually described as being fluidal or blocky (Busby-Spera and White, 1987). Fluidal forms have an irregular shape, at times with ragged edges, with the more rounded or equal aspect ratio types described as globular. Blocky clasts are more angular with clearly defined, planar contacts. Many examples of peperite have been described as containing either blocky or fluidal clasts, but more rarely, peperite contains a mixture of clast shapes, including platy and wispy clasts (Appendix A1 and references therein). A mixture of clast morphologies in peperite suggests local variations in either the magma or

Introduction

sediment properties at the time of peperite formation. Peperite can also be described as being close-packed or dispersed, similar to the sedimentary equivalent of clast- or matrix-supported breccia or conglomerate (Figure 1.1). The formation of peperite can indicate contemporaneous magmatism and sedimentation, or at least the prolonged existence of unconsolidated sediment within a volcanically active area (Befus *et al.*, 2009). Similar to both pillow lavas and hyaloclastite, features of the primary magmatic component can indicate the environment of formation e.g. intense vesiculation of intruding magma indicates a high dissolved volatile content and low confining pressure (Orth and McPhie, 2003). Trapped vesicles within the sediment indicates migration of volatiles within the unconsolidated host (Coira and Pérez, 2002; Waichel *et al.* 2007), while sediment infilling vesicles in magmatic clasts indicates disruption of the unconsolidated host as a result of magmatic intrusion (Hunns and McPhie, 1999). However, unlike pillow lavas and hyaloclastite, both interacting components are preserved as a result of peperite formation. The sedimentary component of peperite can lead to further interpretation of the environment of formation e.g. a turbiditic sequence of host sediments indicates deposition on a basin slope (Coira and Pérez, 2002). Loss of structures within the sedimentary matrix between peperite clasts is suggestive of loss of coherence and fluidisation of sediment during peperite formation (Kokelaar, 1986). As fluidisation of sediment is greatly enhanced with increasing water content, evidence of fluidised sediment indicates that the host sediment was water saturated at the time of magmatic intrusion (Wohletz, 2002). The nature of the physical relationship between the two interacting components can help deduce the conditions of peperite formation, where sedimentary laminations curving around magmatic clasts represents entrainment of sediment particles along magmatic contacts (Kokelaar, 1986), and necking of clasts or wispy tendrils of magma indicate continued magmatic flow and preserve flow direction.

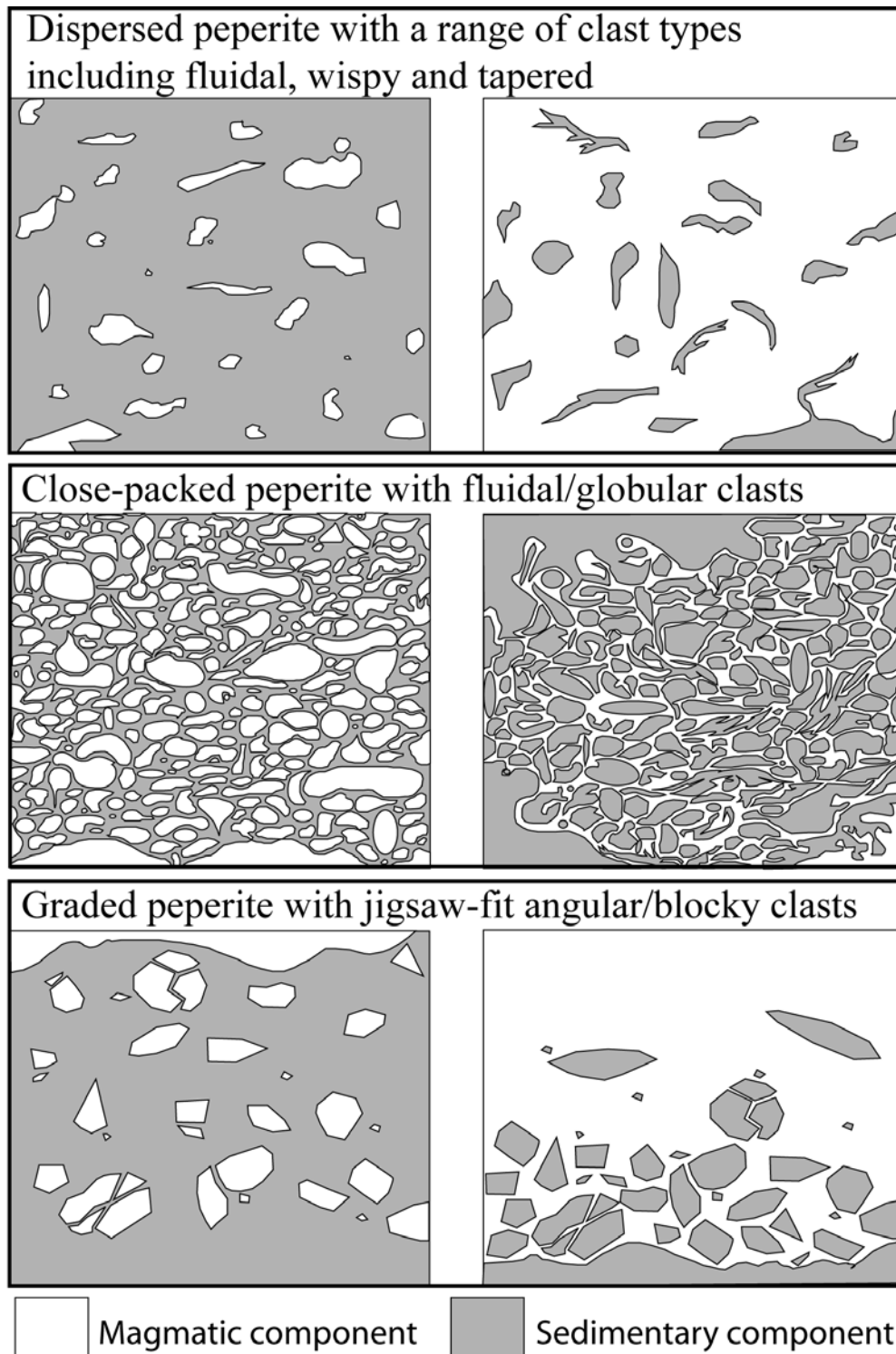


Figure 1.1: Range of possible peperite textures resulting from intrusion of magma into unconsolidated sediment. Varieties include dispersed, close-packed and graded peperite with juvenile clast morphology ranging from platy and wispy to fluidal and blocky or angular. Jigsaw fit textures are abundant in close-packed peperite clasts. Peperite types occur on a range of scales, from millimetric to decimetric.

1.3 Processes of magma-sediment-water interaction

Numerous cooling processes and fragmentation mechanisms are associated with the interaction between magma and sediment and magma and water, where commonly a combination of fragmentation mechanisms can take place within one lithology. The dominant fragmentation processes and their relationship to one another are summarised in Figure 1.2:

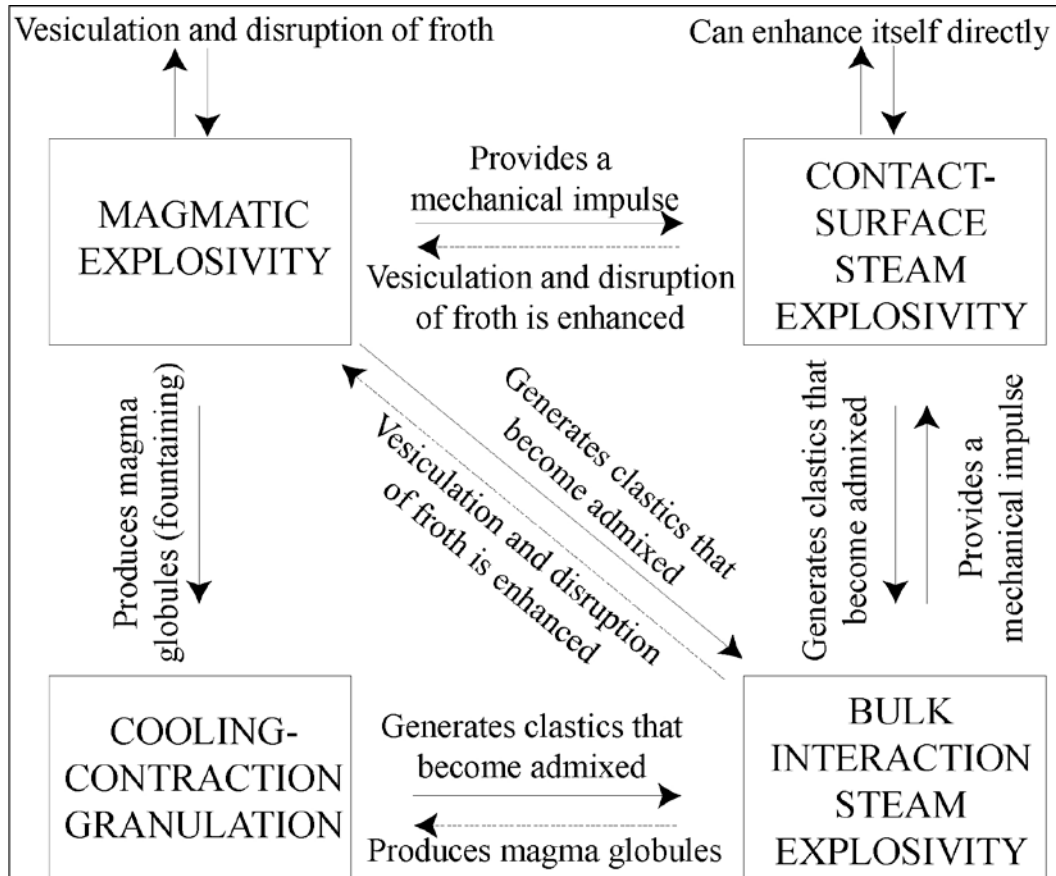


Figure 1.2: Magma fragmentation processes associated with the interaction between magma and water (modified from Kokelaar, 1986)

The growth of pillow lavas is directly related to the continuous extrusion of incandescent material into a water rich environment, where an insulating vapour film is produced between the hot body and the surrounding water at a specific critical temperature (Mills, 1984). Super heating of sediment pore water, as a result of magmatic intrusion, can also result in the development of vapour films around magmatic clasts during the formation of fluidal peperite (Kokelaar, 1982). Fluidisation of host sediment in peperite is also a result of super heating of sediment pore fluid, and is commonly associated with the development of vapour films (Kokelaar, 1982). In pillow lava formation, a fall below the critical

Introduction

temperature required for vapour film development may result in a rapid rate of evaporation and a more explosive cooling affect (Mills, 1984). Stability of vapour films in peperite decreases with decreasing pressure (Kokelaar, 1986; Waichel *et al.*, 2007), where collapse of these oscillating vapour films can cause instantaneous mingling of magma with wet sediments and result in explosive quenching and the formation of angular juvenile clasts (Wohletz, 2002).

If explosive behaviour occurs as a result of magma-water interaction, particularly at large water depths, the heat flux from the magma to the surrounding water must be significantly increased (Zimmanowski and Büttner, 2003) or an extremely large contact area between magma (fuel) and water (coolant) is required if normal heat fluxes occur (Peckover *et al.*, 1973). Therefore, a higher eruption or extrusion rate results in more explosive interaction. Smith and Batiza (1989) also suggest that rapid eruption rates, promoting clastic dominated as opposed to flow dominated eruptive behaviour, control the formation of glassy shards and the production of hyaloclastite. This accumulation of glass fragments may be due to either granulation of pillow rinds as a result of continued rapid extrusion or may be due to a more explosive interaction as a result of a much higher release of mechanical energy per unit time due to higher extrusion rates (Zimmanowski and Büttner, 2003). The rapid quenching of magma upon contact with cold sediment during the formation of peperite results in fragmentation of the magma to form blocky or angular clasts.

Magma fragmentation occurs as a result of direct contact and subsequent interaction between magma and water/wet sediment. Kokelaar (1986) suggested four primary mechanisms of magma fragmentation (Figure 1.2) to explain the formation of hyaloclastite, where these processes commonly occur together and may enhance one another:

- Contact surface steam explosivity involves the explosive expansion and collapse of steam films formed at magma-water contact surfaces.
- Bulk interaction steam explosivity occurs when the enclosure of water in magma, or entrapment of water close to magma, causes the creation and explosive expansion of steam.
- Cooling contraction granulation occurs at any depth where magma comes into contact with water and cools by conductive heat transfer at its surface, thus

Introduction

developing a temperature gradient between the centre and the surface of the fragment.

- Autobrecciation occurs where the exterior of the lava flow cools and breaks up, with some of these large clasts incorporated into the interior of the lava flow.

The same mechanical processes are at play during the formation of peperite, where sediment pore water provides the required coolant. Where vapour films are developed, the initial surface event is either self-triggering (vapour film collapse) or if the two components lie outside of the Temperature Interaction Zone an external trigger such as a pressure pulse may result in interaction (Dullforce *et al.*, 1976). The interaction consists of cyclic stages, where approximately 44% of the energy of the bubble is fed into kinetic energy for the next cycle (Buchanan and Dullforce, 1973); therefore the process is self-sustaining until the entire melt is fragmented. Conversion of water to steam in bulk interaction steam explosivity involves the enclosure of water as a result of lava flow onto a wet substrate or intrusion of magma into a wet slurry of water saturated sediment (Kokelaar, 1986). Therefore the explosive expansion will only fragment the magma in direct contact with the enclosed water or wet sediment. Cooling contraction granulation occurs in pillow lavas to produce hyaloclastite as the outer boundary becomes rigid and, when the interior cools, cracking and granulation occurs. Similarly, granulation of quenched magma occurs in the formation of peperite clasts. A summary of processes involved in magma fragmentation is given in Figure 1.3.

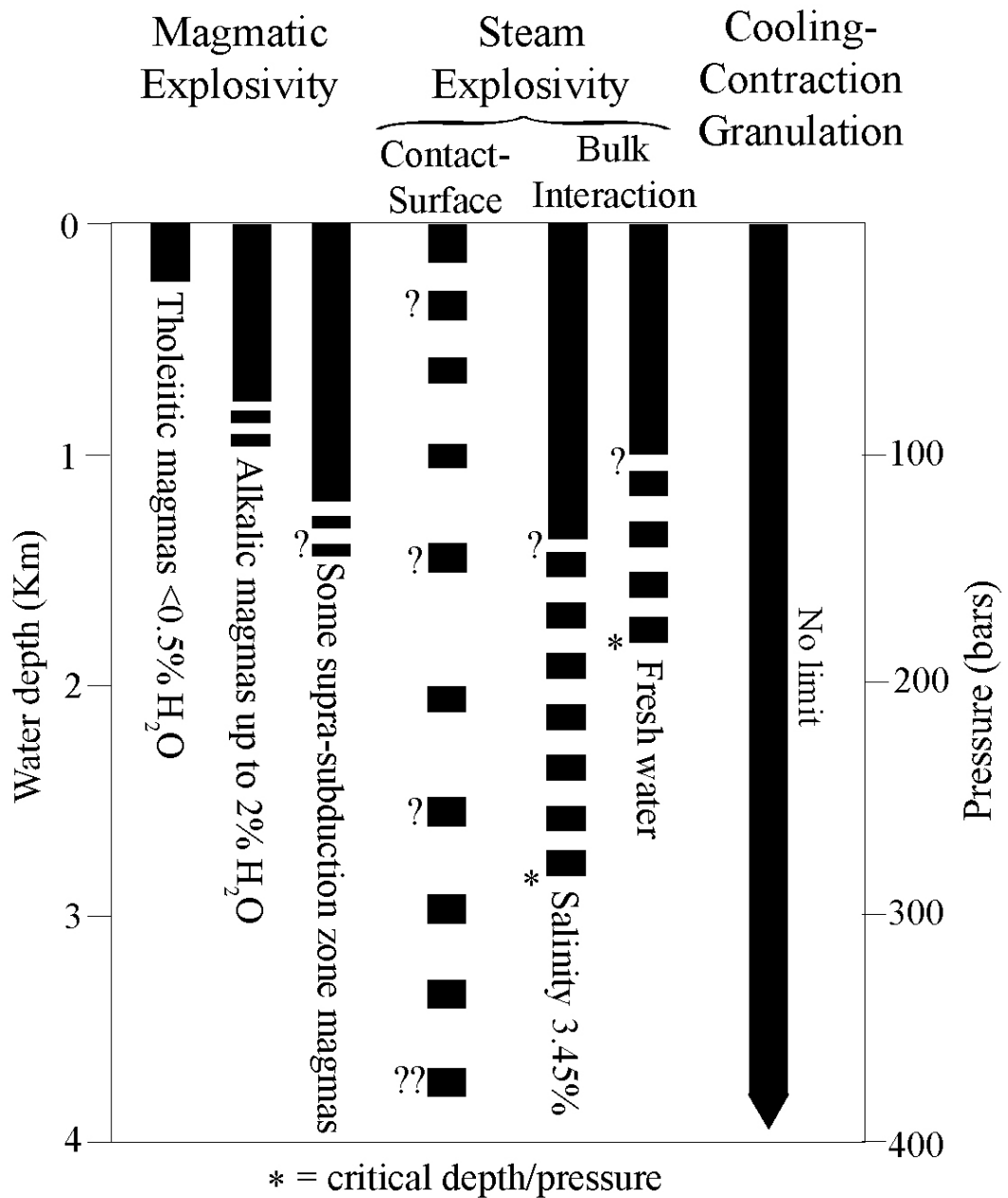


Figure 1.3: Depth and pressure constraints of the major clast forming processes that occur in both hyaloclastite and peperite formation (Drawn after Kokelaar, 1986).

SEAWATER/SEDIMENT PORE WATER

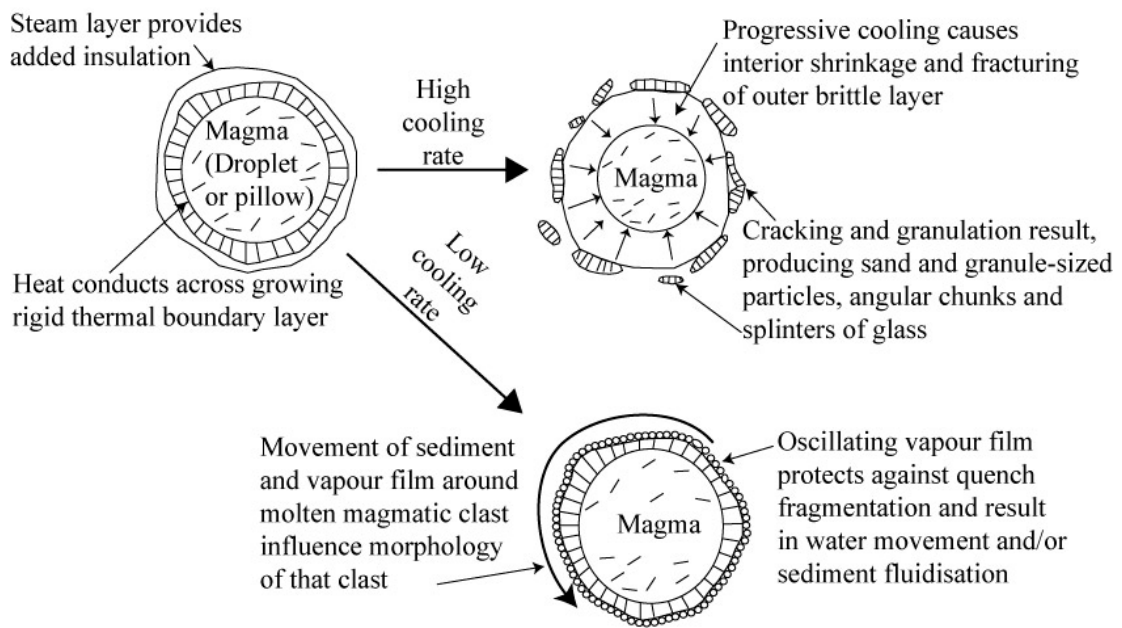


Figure 1.4: The processes involved in the fragmentation of magma to form pillow lavas, hyaloclastite and peperite. The high cooling rate results in cooling contraction granulation and the formation of glass rinds on pillows, accumulation of glass to form hyaloclastite deposits and blocky or angular clasts or glass shards in peperite. (Adapted from Head and Wilson, 2003). The low cooling rate (possibly due to continued magma recharge) results in development of an oscillating vapour film around separated magma pockets to produce pillow lavas or fluidal peperite.

1.4 Fluid circulation and mineralisation in seafloor settings

Volcanic Hosted Massive Sulphide (VHMS) deposits form on and immediately beneath the seafloor by precipitation of sulphide minerals near the discharge sites of hydrothermal fluids (Sillitoe *et al.*, 1996). Hydrothermal activity producing VHMS deposits is generated during periods of local quiescence between volcanic eruptive cycles (Gifkins *et al.*, 2005). Significant hydrothermal systems may be generated as a result of magma-sediment-water interaction, as the transfer of heat can initiate or modify fluid circulation for long periods of time (McPhie and Orth, 1999; Skilling *et al.*, 2002). The generation of these hydrothermal systems as a result of magma-sediment interactions may result in the development of VHMS deposits, such as the Iberian Pyrite Belt (Boulter *et al.*, 1999; Boulter *et al.*, 2001). Variations in ore deposits from classic VHMS to porphyry and epithermal deposits reflect the interplay of several factors in the submarine volcanic environment, such as: 1) proportions of volcanoclastic, lava, and subvolcanic

intrusive facies, 2) depth of seawater, 3) permeability and porosity of volcanic host rocks, 4) balance between magmatic components and seawater components in the ore fluid and 5) temperature and acidity of the ore fluid (Large *et al.*, 2001b). Therefore, base metal mineralisation associated with magma-sediment interaction is not dependant solely on these interactions, but rather depends on the environmental setting and surrounding rock types. The type of hydrothermal alteration associated with base metal deposits can aid in the identification of the type of deposit. Typical hydrothermal alteration associated with the formation of VHMS deposits grades from a siliceous core zone, through a carbonate zone, a chlorite zone, a sericite zone and an albite zone into unaltered volcanic rocks (Gifkins *et al.*, 2005), in host rocks varying from coherent to clastic volcanic or sedimentary facies.

1.5 Case study of magma-sediment-water interaction and mineralisation

The Bunmahon Formation, located at the southern end of the southeastern volcanic belt in Ireland (Figure 1.4), contains several localities that preserve evidence of contemporaneous magmatism and sedimentation (Scheiner, 1974; Stillman *et al.*, 1974; McConnell *et al.*, 1991; McConnell, 2000). The main mineralisation types occurring in the Bunmahon Formation are siliceous veins with disseminated pyrite and chalcopyrite, and siliceous veins with sphalerite, galena and minor pyrite and chalcopyrite (Wheatley, 1971). These siliceous veins are most abundant within the volcanic rocks. The required heat source for fluid flow may have been derived from intrusions into the volcanic sequence and for later mineralising events the volcanic sequence may have been the metal source. Boland (1983) suggests that the mineralising episode took place after the deposition and lithification of the Ordovician sequence and before the deposition of Old Red Sandstone, with the Bunmahon Formation the key target for several exploration programmes (e.g. Boland, 1982; Schaffalitzky, 1982). Two key localities within the Bunmahon Formation (Trawnamoe and Stradbally Cove) preserve evidence of magma-sediment-water interaction and associated base metal mineralisation and are examined in order to investigate the interaction between magma, water and sediment and its implications for hydrothermal mineralisation.

The NE-SW trending tract of Ordovician volcanic and sedimentary rocks, generated as a result of Iapetus Ocean closure (e.g. Wilson, 1966), is dominantly

Introduction

composed of arc-related sub-aqueous eruptions, shallow level intrusions and tuffs emplaced as a result of gravity flows of pyroclastic or epiclastic origin (Stillman and Maytham, 1973; Scheiner, 1974; Downes, 1975; Stillman and Williams, 1975; Boland, 1983; Fritz and Stillman, 1996) with rare sub-aerial eruptions (Stillman, 1971). Whereas previous investigators examined the volcanic and associated sedimentary lithologies of the Bunmahon Formation in the wider context of regional geology (Stillman *et al.*, 1974; Stillman and Williams, 1979, Boland, 1983), the relationship of these volcanic rocks to localised base metal mineralisation is now examined. The volcanic rocks at Avoca are part of a continuum of volcanic activity in the southeastern belt, reflecting supra-subduction ensialic rifting, where sulphide mineralisation was co-eval with volcanic activity (Wheatley, 1971; McConnell, 1987) representing Kuroko style mineralisation (Platt, 1977). It is deduced (Platt, 1977) that similar ore bodies to the Avoca deposits lie hidden in the volcanic rocks of the southeastern volcanic belt, such as the Bunmahon area (Figure 1.3), which was historically mined for copper and is currently (2010) being prospected by exploration companies for VHMS deposits.

Introduction

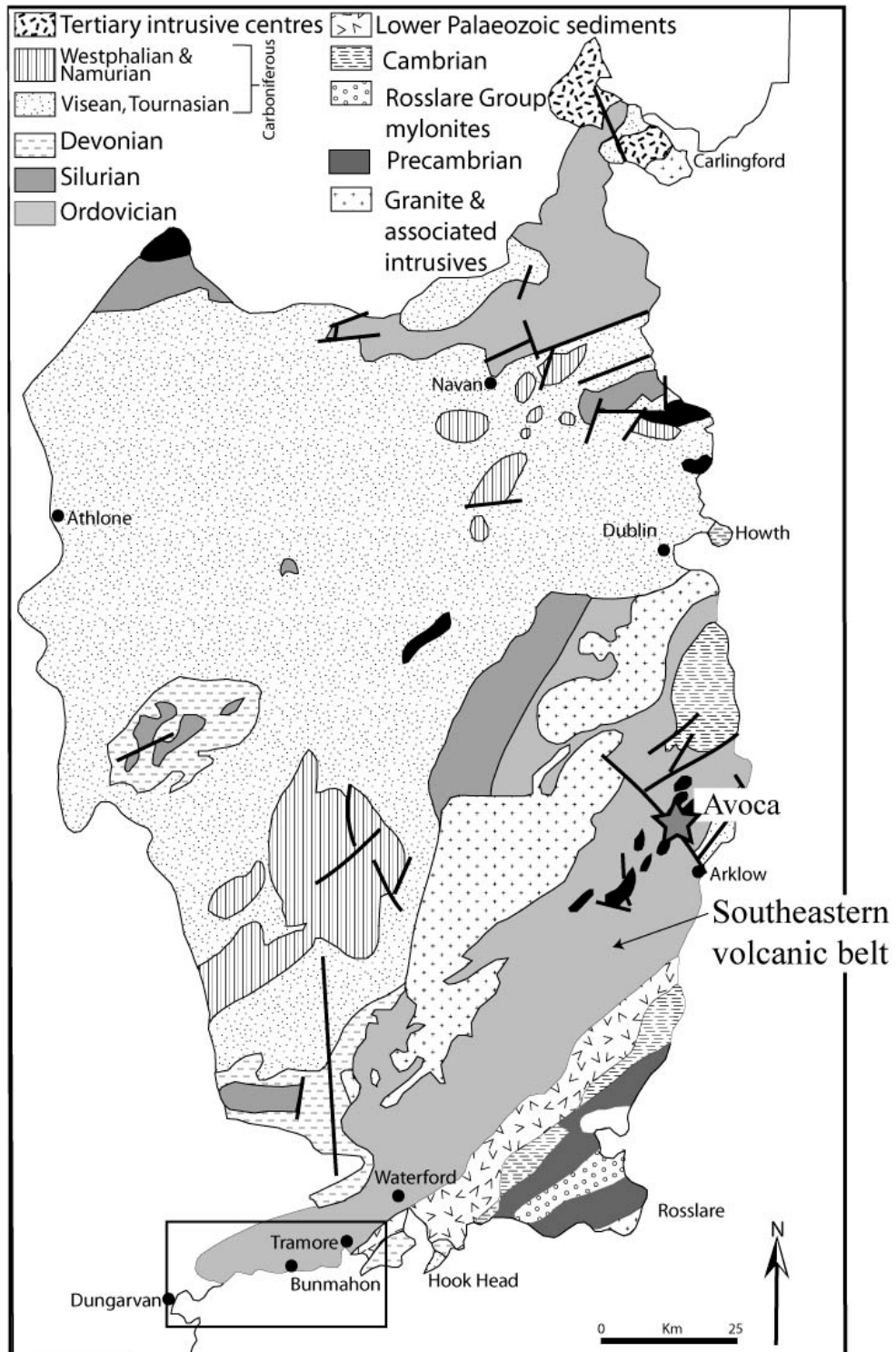


Figure 1.5: Geological map of the east and southeast coast of Ireland, showing the location and trend of the Ordovician southeastern volcanic belt and the location of Avoca and the study area (boxed area, with geology shown in more detail in Figure 2.1) within this belt. Map drawn after Stillman and Sevastopulo (2005).

1.7 Collaborative aspects of the research

Collaboration with geologists of the Copper Coast Geopark will lead to results of this study being made accessible to the general public. It is intended that research of site specific geology be made available by communication to the public through liaison with the Copper Coast Geopark. Under the guidance of the Copper Coast Geopark, special areas of interest such as Ballydowane Bay and Stradbally Cove have been selected where notice boards provide the public with information regarding the geological history and subsequent rock types preserved today. Other features provided by the Geopark include a geological garden in Bunmahon village, information pamphlets related to the history of mining in the area and pamphlets containing walking trails and maps through the landscape of the Copper Coast Geopark. Information regarding the geology of localities investigated in this study will be disseminated using a combination of geological interpretation with maps and directions, in the same format used by the Geopark for special areas of interest and information pamphlets.

Collaboration is also set up with Aurum Exploration, the holders of the exploration license in the Copper Coast Geopark, where this area is currently under investigation for the possible location of VHMS deposits (Robb, pers. Comm., 2009). Therefore, preliminary results of field and geochemical investigations from this project will be made available to Aurum Exploration in return for sampling assistance. Further collaboration includes access provided by the Geological Survey of Ireland (GSI) to drill cores and reports of exploration drilling, and unpublished bulk rock geochemical results from Prof. Chris Stillman (Trinity College Dublin).

Chapter Two:

Field relationships of the South Waterford volcanic rocks

2.1 Introduction

The Ordovician volcanic belt, exposed in a NE-SW trend along the southeast coast of Ireland (Figure 1.5), comprises the core of a major Caledonian synclorium (Shannon, 1976). The volcanic, volcanoclastic and sedimentary rocks are metamorphosed to greenschist and sub-greenschist facies assemblages with a pervasive cleavage developed throughout (Stillman and Williams, 1979). The most southern part of the volcanic belt (Figure 2.1) has been mapped on a large scale (1:10,600) by many authors (Downes, 1975; Boland, 1983; Swennan, 1984; Diskin, 1997) where the stratigraphy and naming of formations varies widely (e.g. Stillman and Williams, 1979; Carlisle, 1979; Boland, 1983; Sleeman and McConnell, 1995). Specific formation names adopted here have been the most recently suggested (GSI sheet 22, Sleeman and McConnell, 1995): the Bunmahon, Dunabrattin and Campile Formations, exposed between Tramore (east) and Dungarvan (west). The Bunmahon and Campile Formations are subjected to detailed examination because they contain lithological units that represent the growth of two submarine volcanic centres (Stillman and Sevastopulo, 2005) known as the Bunmahon Volcano and the Kilfarrasy Volcano. The Dunabrattin Formation is temporally equivalent to the Bunmahon Formation (Boland, 1983; Harper and Parkes, 2000) and represents submarine sedimentation associated with volcanic activity and tectonic instability (Stillman and Sevastopulo, 2005). Exposure is extremely poor inland due to drift cover so field relationships are described and interpreted along coastal cliff sections traversing the Bunmahon, Dunabrattin and Campile Formations (Figure 2.1).

Field relationships of the south Waterford volcanic rocks

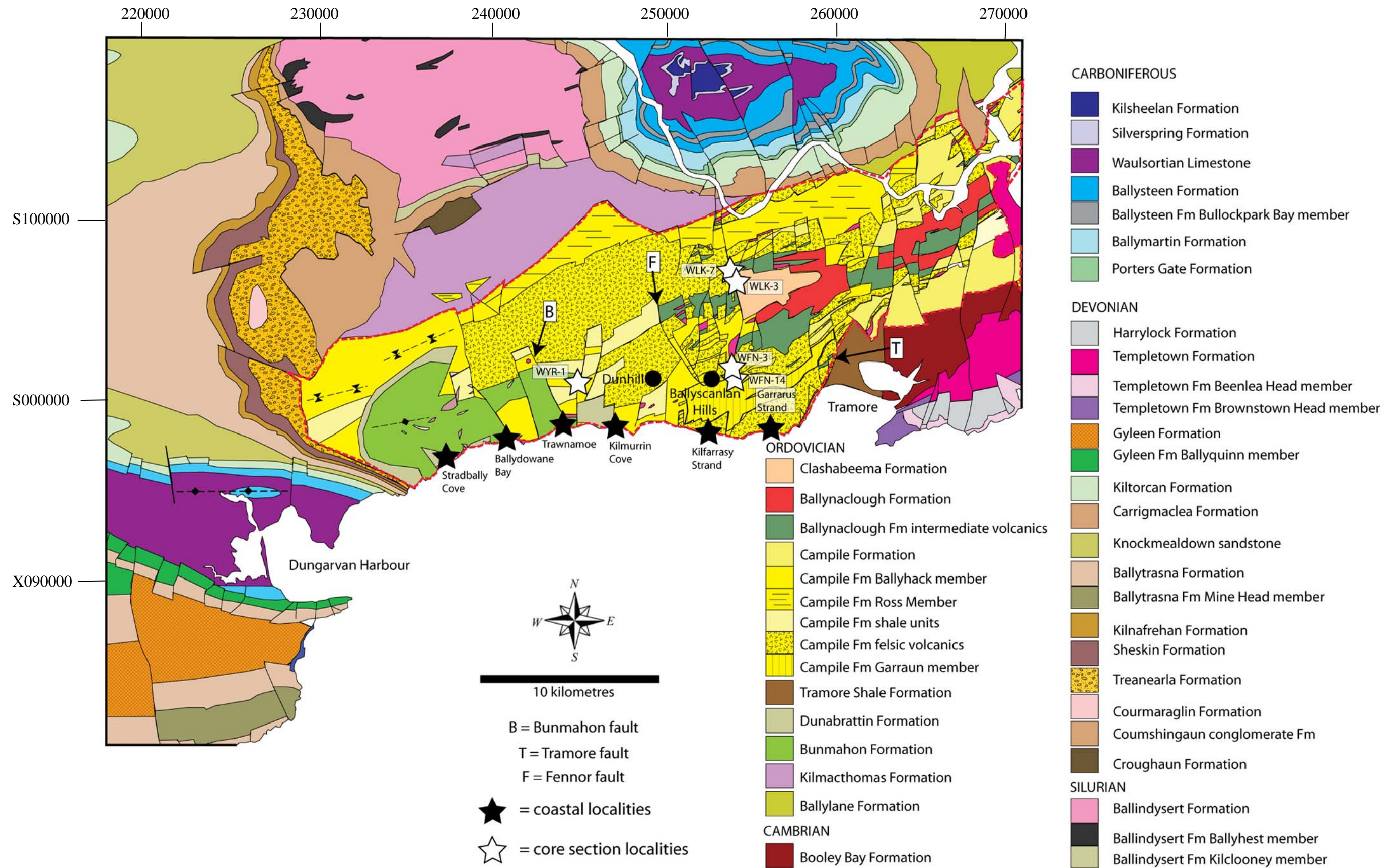


Figure 2.1: Geological map of the southeastern volcanic belt exposed in South Waterford. Modified after GSI Bedrock Geology Sheet 22 for East Cork and Waterford, and Sheet 23 for South Wexford.

2.2 Previous Research

2.2.1 The Bunmahon Formation

The 1700 metre thick Bunmahon Formation (Boland, 1983) extends from Bunmahon village in the east to Dungarvan in the west (Figure 2.1). The central vent of the former volcano is located to the southwest of the village of Bunmahon and volcanic rocks include pyroxene diorites, gabbros, and keratophyres, forming pillow lavas, unwelded tuffs and epiclastic volcanic conglomerates (Stillman *et al.*, 1974; Carlisle, 1979). The lower part of the formation is mostly fine to medium-grained lavas and hyaloclastites, or mass flows, whereas in the upper parts of the formation, there is an east-west lateral variation. Lavas, hyaloclastites and mass-flows dominate in the west while there is a greater amount of tuffaceous material in the east (Boland, 1983), and fossiliferous horizons are common in the eastern section at the top of the formation. On the basis of shelly faunas, the start of the eruptive sequences are placed at ~465Ma (Harper and Parkes, 2000), within the upper part of the Darwillian stage (Dw3 Stage Slice of Bergström *et al.*, 2009), indicating that this formation represents the oldest part of the Duncannon Group (Stillman, 2009) (Figure 2.2). Several authors have used different nomenclature to describe this formation, for example Carlisle (1979) included it in the Ballynaclogh Volcanic Formation whereas Bruck *et al.* (1979) placed it in the Lower Tramore Shale and Volcanic Group, while Boland (1983) and Sleeman and McConnell (1995) both described it as the Bunmahon Formation, also used in this project. Specific sites (Trawnamoe, Stradbally Cove and Kilmurrin Cove) within the Bunmahon Formation contain various peperite lithologies, pillow lavas, sheet flows, tuff deposits and intercalated sedimentary sequences, and are considered suitable for the investigation of magma-sediment-water interactions.

2.2.2 The Dunabrattin Formation

The Dunabrattin Formation is exposed surrounding the remnants of the Bunmahon volcanic Formation (Figure 2.1). The formation consists of a sequence of moderately pyrite-rich laminated shales, siltstones and fine sandstones with tuff bands, all intruded by contemporaneous andesite sheets (Sleeman and McConnell, 1995). Instability of the region during deposition of the sequence, resulting in slumping, intraformational breccias and convolute lamination, is attributed to tectonism associated with volcanism of the Bunmahon Formation (Boland, 1983;

Stillman and Sevastopulo, 2005). Boland (1983) and Sleeman and McConnell (1995) suggested that the Bunmahon Formation and the Dunabrattin Formations are temporally equivalent. Therefore, contemporaneous intrusive rocks in the Dunabrattin Formation are probably related to the Bunmahon Formation phase of volcanic activity and are subsequently treated in this study as part of the Bunmahon Formation.

2.2.3 The Campile Formation

The most extensive stretch of outcrop of the Campile Formation is located to the east of the Bunmahon Formation (Figure 2.1). The Campile Formation has been previously split into the Middle Tramore Volcanic Formation, the Garraun Shale and Tuff Group and the Upper Tramore Volcanic Formation (Stillman, 1978). In contrast, Carlisle (1979) separated the Campile Formation into the Carrighalia Formation, the Lower Tramore Volcanic Formation, the Garraun Shale Formation and the Upper Tramore Volcanic Formation. Boland (1983) found that none of these named units were mappable and incorporated many into the Annestown Formation, where rapid facies changes and variations were attributed as being typical of rhyolite terrains. Sleeman and McConnell (1995) renamed this as the Campile Formation, characterised by a variable internal stratigraphy, with rapid lateral and vertical facies changes resulting in an inability to correlate between outcrops. Due to the abundance of stratigraphic names and the complexity of limited exposure, Sleeman and McConnell (1995) suggested that only broad lithostratigraphic subdivisions are appropriate. Volcanic activity associated with the Campile Formation began in the Sa2 Stage Slice of the Sandbian (Owen and Parkes, 2000) (Figure 2.2), comprising quartz-feldspar porphyries, acid tuffs, flow-banded rhyolite, andesite, lapilli tuffs, ignimbrites and siliceous and dark shales. A 1500m thick succession is recorded in the east whereas only 400m is preserved in a synclinal core in the west (Boland, 1983). A volcanic centre is suggested at Ballyscanlan Hills where a rhyolitic dome has been emplaced in or near a vent (Swennan, 1984). A vent is also suggested in the vicinity of Dunhill Castle (Stillman, 1971) where potash metasomatism is taken to indicate the presence of an eruptive centre beneath exposed rhyolites (Swennan, 1984). Kilfarrasy Strand, Annestown Beach and Gararus Strand are suitable sites for the investigation of volcanic units of the Campile Formation, because each locality

Field relationships of the South Waterford volcanic rocks

contains some combination of sheet flows, tuff deposits and volcanoclastic rocks with intercalated sedimentary sequences.

Field relationships of the South Waterford volcanic rocks

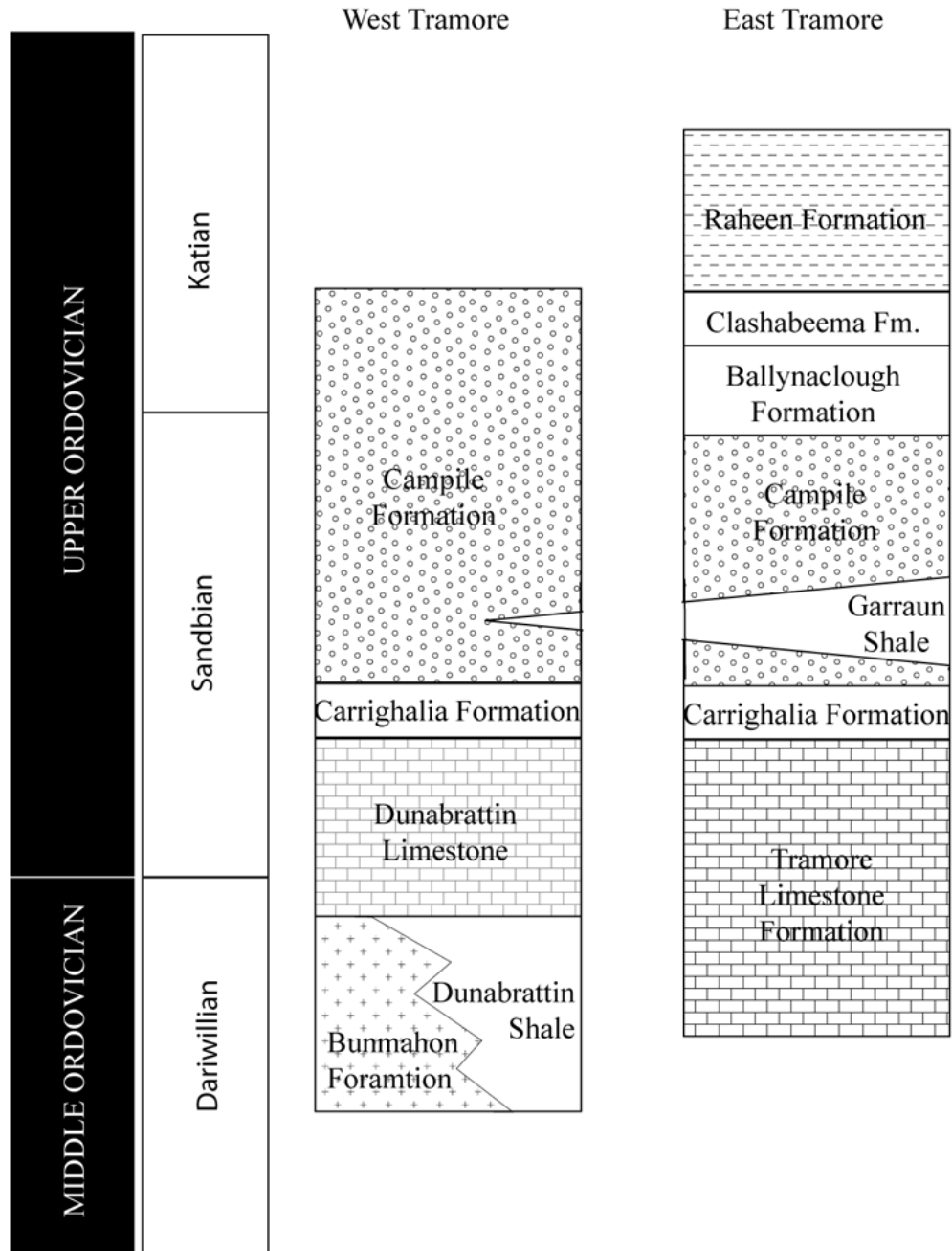


Figure 2.2: Stratigraphic column for the areas west and east of Tramore, showing the relative age relationships of volcanic activity and the variation in thickness of the Campile Formation. (Modified from Harper and Parkes (2000), to include updated Ordovician chronostratigraphic units of Bergström *et al.* (2008)).

2.2.3 Volcano Reconstructions

The Bunmahon Formation has been suggested to represent a broad cone shaped volcano (Boland, 1983) that erupted for the most part under water with magmas intruded at shallow levels into marine sediments. The succession is composed of hyaloclastites, pillow lavas, intrusive rocks, peperites and tuffs. Progressive shallowing of the sequence is recorded, where this is probably due to the build up of sea mounts and volcanic islands from successive eruptions (Stillman and Francis, 1979). Extrusive rhyolites of the Campile Formation formed domes with localised facies variations, where these domes are blanketed in places by both ash-fall and ash-flow deposits (Boland, 1983). Sub-aqueous deposition produced shales, water-lain tuffs (Boland, 1983) and rare accretionary lapilli that suggest possible sub-aerial eruptions were followed by sub-aqueous deposition (Stillman, 1971). The dominant characteristics of each volcanic centre change from 1) broadly basic to intermediate lavas and hyaloclastite dominated (Bunmahon Formation) to 2) acid volcanic rock and shale dominated (Campile Formation) (McConnell and Sleeman, 1995).

The model proposed for the region (after McConnell, 1993) includes five major events for the deposition of the Bunmahon, Campile and surrounding formations (Figure 2.3):

1. The volcanic rocks of the Bunmahon Formation were erupted, following structural weaknesses above the Bunmahon fault, and deposited in a marine basin.
2. The products of the Bunmahon Formation were covered by the Dunabrattin Formation. Slumping of these turbiditic sediments occurred as a result of volcanic or fault seismicity, or unstable depositional slopes.
3. Build up of volcanic material resulted in shallower depths of sediment deposition. East of the Bunmahon fault, calcareous beds of the Knockmahon and Tramore Limestone Formations overstep the Bunmahon and Dunabrattin Formations.
4. West of the Bunmahon fault, basin conditions resulted in deposition of the Glendalligan Formation, comprising black, graptolitic shales.

Field relationships of the South Waterford volcanic rocks

5. A secondary basin was created between the Fenor fault and the Tramore fault, while an upstanding horst was left between the Fenor fault and the Bunmahon fault. Limestone was deposited on the horst and black shales of the Carrighalia Formation were deposited on top of the Knockmahon and Tramore Limestone in the basin (McConnell, 1993).
6. Volcanic activity in the late Caradoc produced local rhyolitic lava flows and felsic ash fall deposits (Campile Formation) that blanketed the area

Field relationships of the South Waterford volcanic rocks

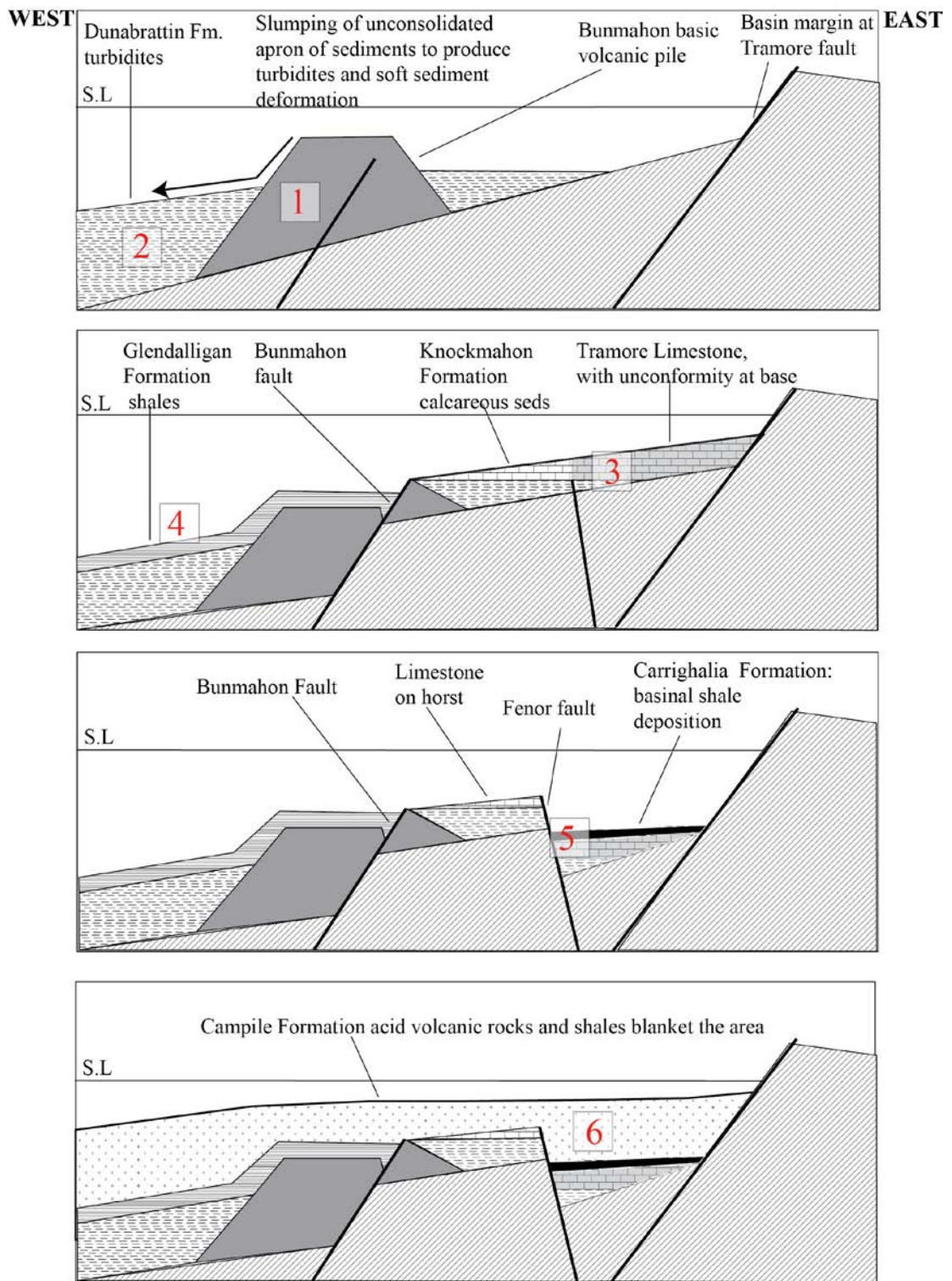


Figure 2.3: Schematic basin evolution during the mid-Ordovician in SE County Waterford after McConnell (1993). See text for description of features 1-6.

2.3 Volcanological features of the Bunmahon Formation at Trawnamoe

The type section of the Bunmahon Formation is located at Trawnamoe, a cove immediately west of Bunmahon Head, close to the village from which the Formation derives its name. The cliffs at Trawnamoe, approximately 30m high, are dominantly composed of basic-intermediate lavas and volcanoclastic rocks, with numerous adits from historic copper mining. Figure 2.4 shows the geology of the cove where a major fault separates the Ordovician volcanic and Devonian sedimentary rocks (Old Red Sandstone).

2.3.1 Extrusive rocks

Towards the western end of Trawnamoe (X 42810 98180) two separate outcrops, 20m apart each comprise both spherical or slightly elongated pillow forms, approximately 40cm across. Individual pillows comprise an outer altered glassy rim, approximately 5mm thick, and an inner vesicle-poor fine-grained basalt. Devitrification of the glassy rims has produced an iron-rich alteration assemblage, with further alteration producing clay on the upper surface of the pillows (Figure 2.5a).

A bedded tuff, composed of alternating light coloured, fine-grained layers and dark coloured, coarser grained layers drapes across the upper surface of the pillow lavas indicating younging of the sequence to the NW (Figure 2.5b). The coarse-grained layers of this tuff contain rare lithic fragments and abundant lapilli, which commonly occur in clusters and are either spherical or oval (dark-coloured) or more irregularly shaped (light-coloured). A sub-angular fine-grained clast, approximately 3cm, disturbed the underlying laminations, similar to an ejected volcanic bomb (Figure 2.6a). The lapilli tuff is overlain by hyaloclastite, with a contact varying from sharp (Figure 2.5b) to gradational.

The majority of the Trawnamoe cliff section is composed of an alternating sequence of greenish-grey coherent lava flows and a friable, fine-grained hyaloclastite (Figure 2.4). Minor faults disrupt the volcanic relationships, yet some individual sheet flows (~1m thick) can be traced for up to ten metres, in which lava grades upward into hyaloclastite, with a sharp contact preserved between the hyaloclastite and the overlying lava flow (Figure 2.6b). The geometry

Field relationships of the South Waterford volcanic rocks

of the successive lava flows and their contacts show that the younging direction of the succession is undisturbed from the east to the west end of the cliff section (younging to the ~NW). The coherent inner portions of the sheet flows are microcrystalline with unidentifiable microphenocrysts of mafic minerals comprising up to 40% volume, ranging in size from 0.5mm to 1mm. The finer grained hyaloclastite margins range in thickness from ~5cm up to 30cm, with some of the thicker sections of hyaloclastite containing separated angular blocks, up to 15cm, of the coherent sheet flow.

A parallel bedded tuff (48/19°N), exposed at the western end of the cove, comprises alternating light and dark coloured beds ranging in thickness from 0.5cm to 15cm. Rare ripple marks and load structures are preserved within some of the beds and a volcanic bomb (4cm) disturbed some of the underlying laminations. The bedded tuff is approximately 70cm thick and grades up section to a more massive tuff.

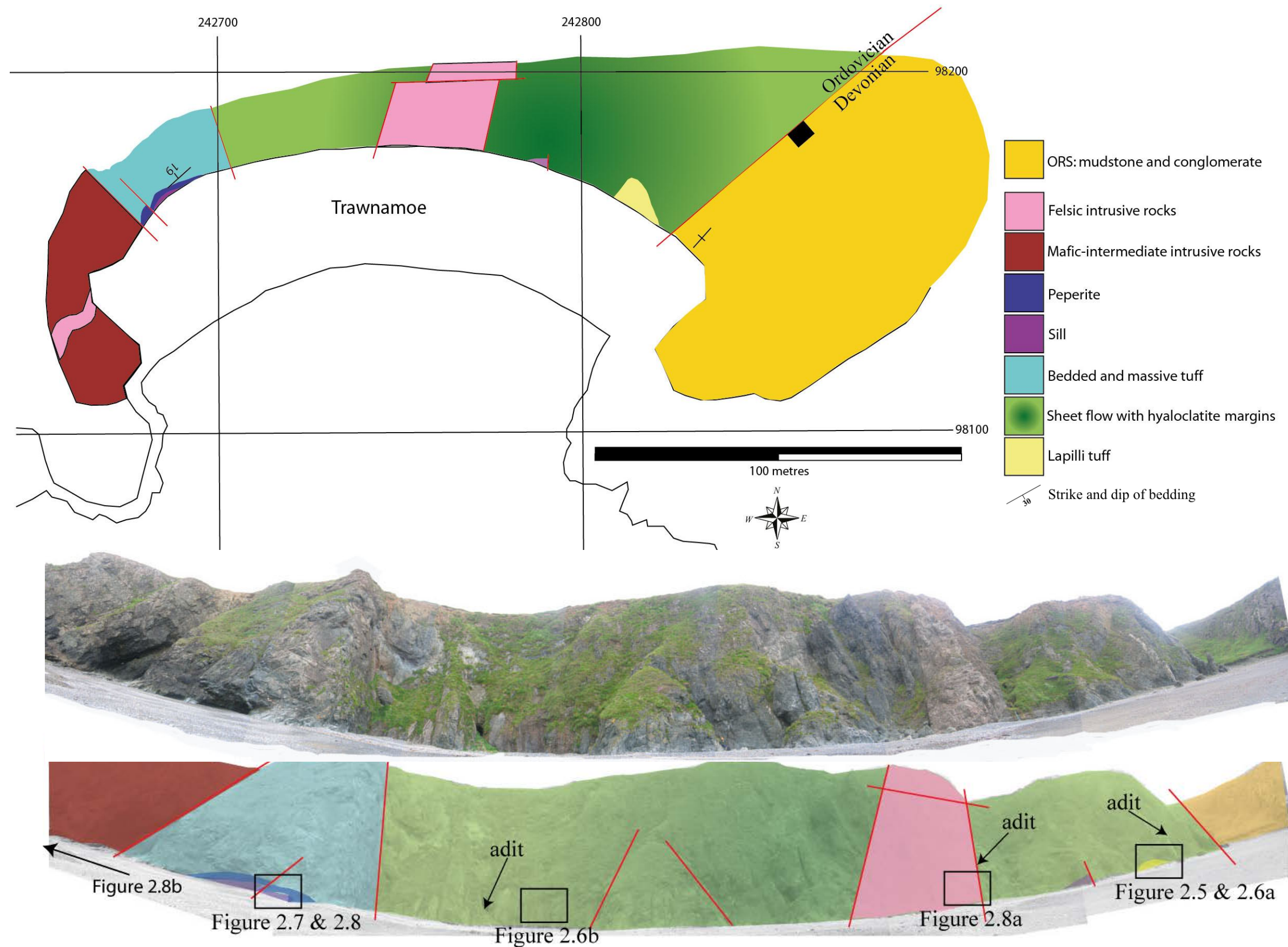


Figure 2.4: Geological map of Trawnamoe showing the location of the major lithologies and faults (a), panoramic view of the Trawnamoe cliff section (b) with the geological features overlain and location of field photographs shown (c). This shows the dominance of Ordovician volcanic rocks with Old Red Sandstone outcropping toward the east.

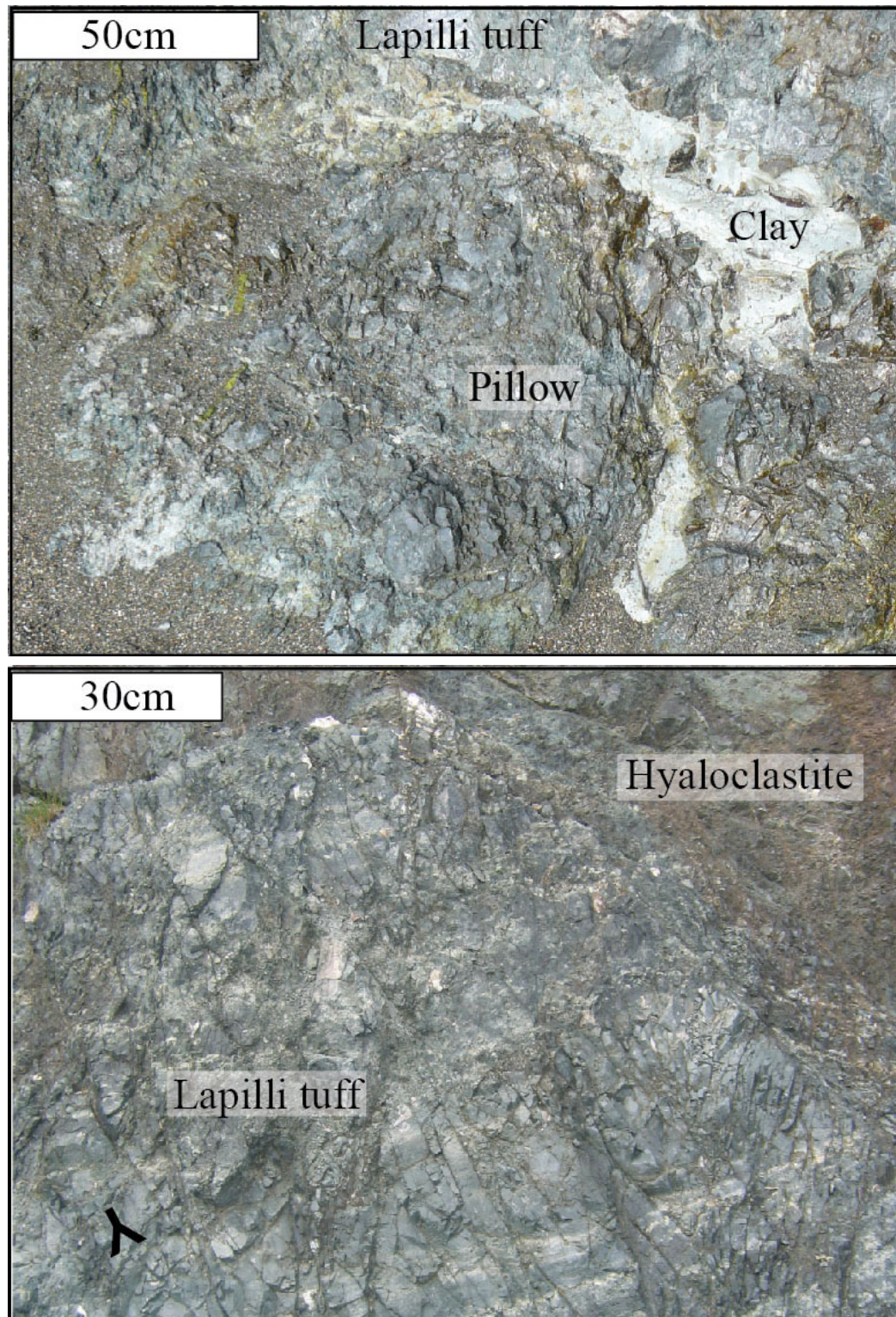


Figure 2.5: Pillow lava and lapilli tuff outcrop towards the eastern end of Trawnamoe showing (a) isolated, spherical pillow with altered glassy rim and clay developed on the pillow surface and (b) overlying lapilli tuff, consisting of alternating light and dark layers, with an overlying sheet flow with hyaloclastite margin indicating younging direction is to the NW.

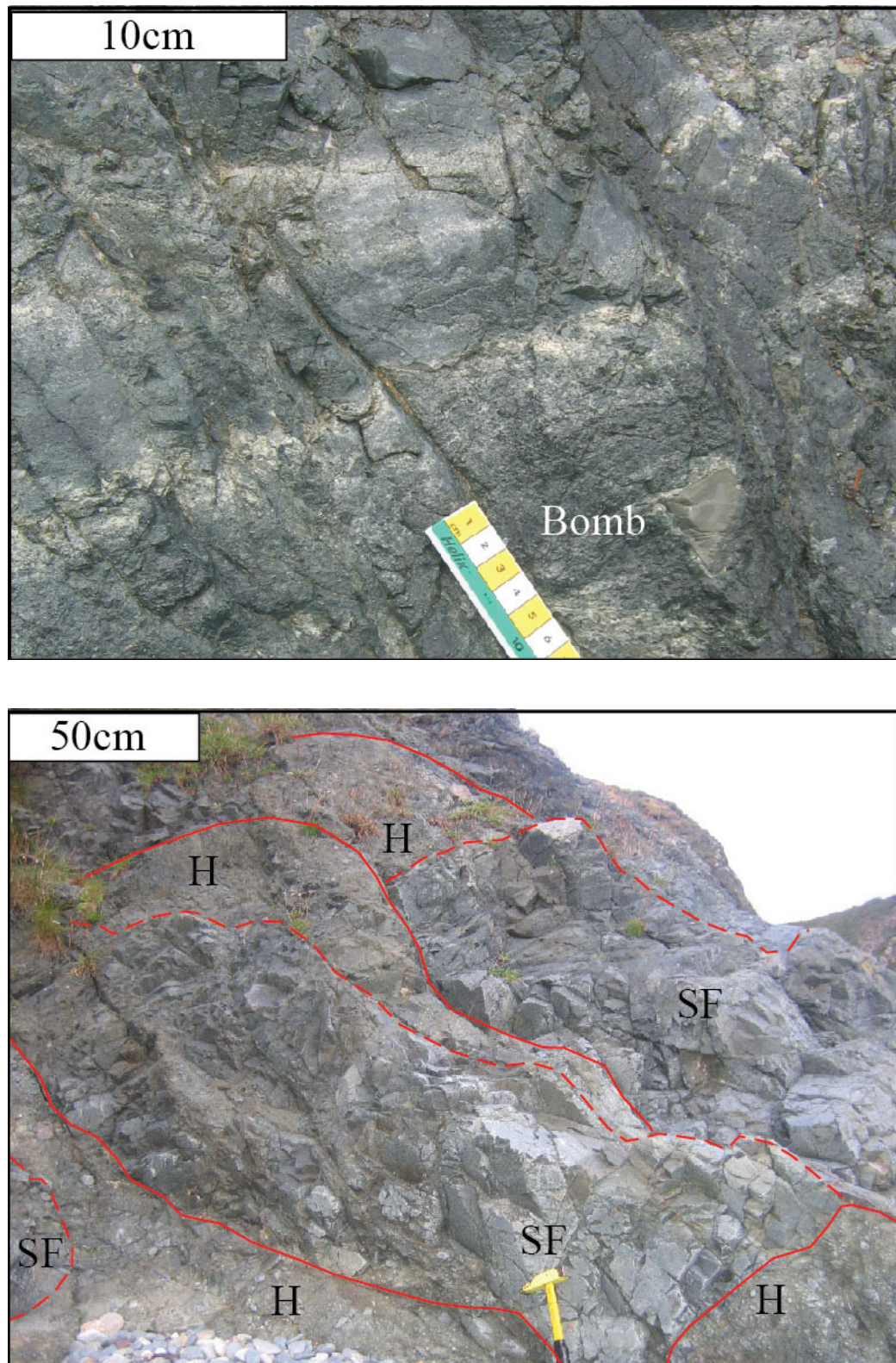


Figure 2.6: Volcanic features of extrusive rocks including (a) the lapilli tuff containing an angular volcanic bomb within one layer of ash and (b) successive sheet flows (SF) comprise coherent fine-grained andesite grading internally into hyaloclastite (H). Solid lines separate individual sheet flows and dashed lines separate the coherent portion of the sheet flow from the hyaloclastite margin.

2.3.2 Early intrusive rocks

The bedded tuff at the western end of the cove (X 42696 98170) was intruded by a pyroxene and feldspar-phyric sill, the base of which is not exposed. Peperite is developed along the upper contact of the sill, in a zone up to two metres thick, with densely packed peperite clasts at the base with more dispersed clasts toward the top (Figure 2.7a). The entire outcrop is exposed in two sections: an extremely weathered two metre high peperite exposed in a cave, cut by a reverse fault (X 42683 98152, 137/10°SW), and to the north of this, the main peperite body is exposed with a lensoid shape, 90cm-2m in height. Clasts are spherical, oval or tear-drop shaped and range in size from 1-20cm, separated by 1-2cm of sedimentary matrix. The larger, dispersed clasts at the top of the section have forced the laminations of the overlying tuff to mimic the underlying clast shape (Figure 2.7b) or have truncated laminations to produce a sharp, hummocky top surface to the peperite. The fine-grained sedimentary matrix is bleached due to silicification, with some laminations preserved between clasts (Figure 2.8a) that are microcrystalline with intense alteration along the contacts (Figure 2.8b).

The peperitic sill may be related to the large plagioclase-pyroxene-phyric sill to the west of the fault (X 42679 98133), but further analysis is required to determine these relationships.

2.3.3 Late intrusive rocks

A pink or cream coloured porphyritic intrusive rock outcrops in the centre (X 42752 98188) of the cliff section, surrounded by the sheet flow/hyaloclastite lithology. Relationships to the surrounding rocks are obscured since faults represent the contacts on all sides, with much of the rock brecciated due to fault movement, resulting in the development of cataclastite (Figure 2.9a). The cream coloured, porphyritic intrusive rock is composed of microphenocrysts (1-2mm) of quartz and feldspar in equal abundance, set in a very fine-grained groundmass (approximately 20%) of the same composition.

A fine-grained, 1.2 metres thick, meandering dyke of similar colour and grain size as the host mafic succession (Figure 2.9b) is separated from the host by a green clay, possibly representing a fault gouge with the dyke later utilising this weaker plane. A dark coloured, fine-grained sill exposed at X 42778 98179, has a faulted

relationship with the overlying hyaloclastite. The sill is porphyritic, with a fine-grained groundmass and microphenocrysts (up to 1mm) of plagioclase feldspar.

2.3.4 Sedimentary rocks

A sequence of alternating beds of mudstone and conglomerate, part of the Devonian Old Red Sandstone Group, is exposed at the eastern end of Trawnamoe, separated from the Ordovician volcanic rocks by a fault striking NE-SW. The alternating beds range in thickness from ~3cm up to one metre. The mudstone is too fine-grained to discern any individual minerals in the field but the red colour indicates a high iron (haematite) content. The intervening beds of polymict conglomerate are composed of sub-angular clasts of quartz, mudstone and volcanic fragments ranging in size from 0.5 to 3cm within a fine-grained matrix that varies between red (similar to the mudstone) and greensish-grey. Bedding is vertical (Figure 2.10), with local flame structures and channel fill deposits (conglomerate) that records general younging to the west (towards the Ordovician volcanic rocks).

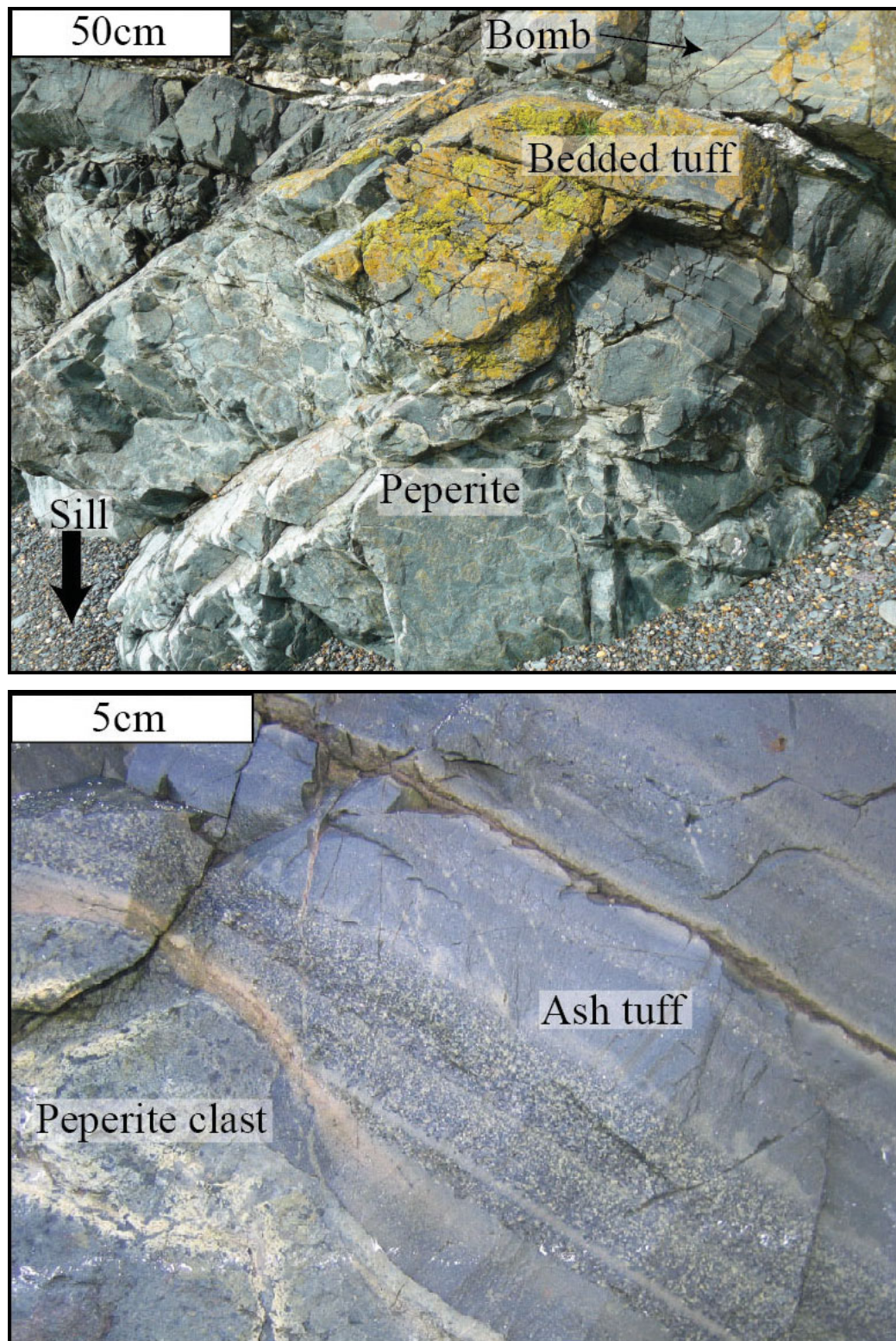


Figure 2.7: Peperite, exposed at the western end of Trawnamoe, consists of (a) separated clasts from an underlying mafic sill in the overlying bedded tuff, with (b) some clasts disrupting the laminations of the overlying tuff.

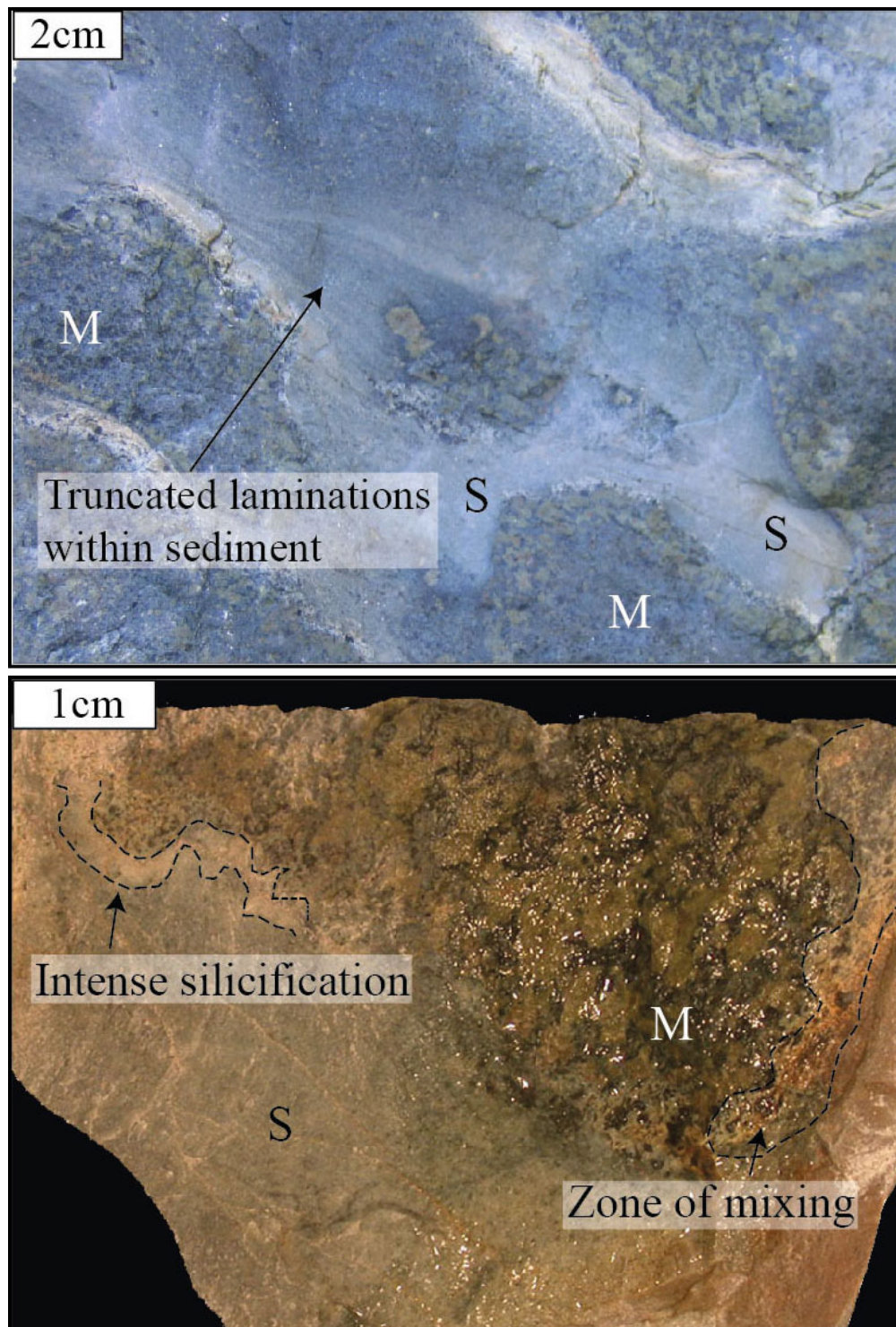


Figure 2.8: Various features within peperite including (a) truncation of laminations against clasts in peperite and (b) the irregular, undulating contact between the magmatic and sedimentary components, with silicification of the sedimentary matrix at clast margins and a zone of mixing between the magmatic and sedimentary component at the clast contact. M = magmatic, S = sedimentary.

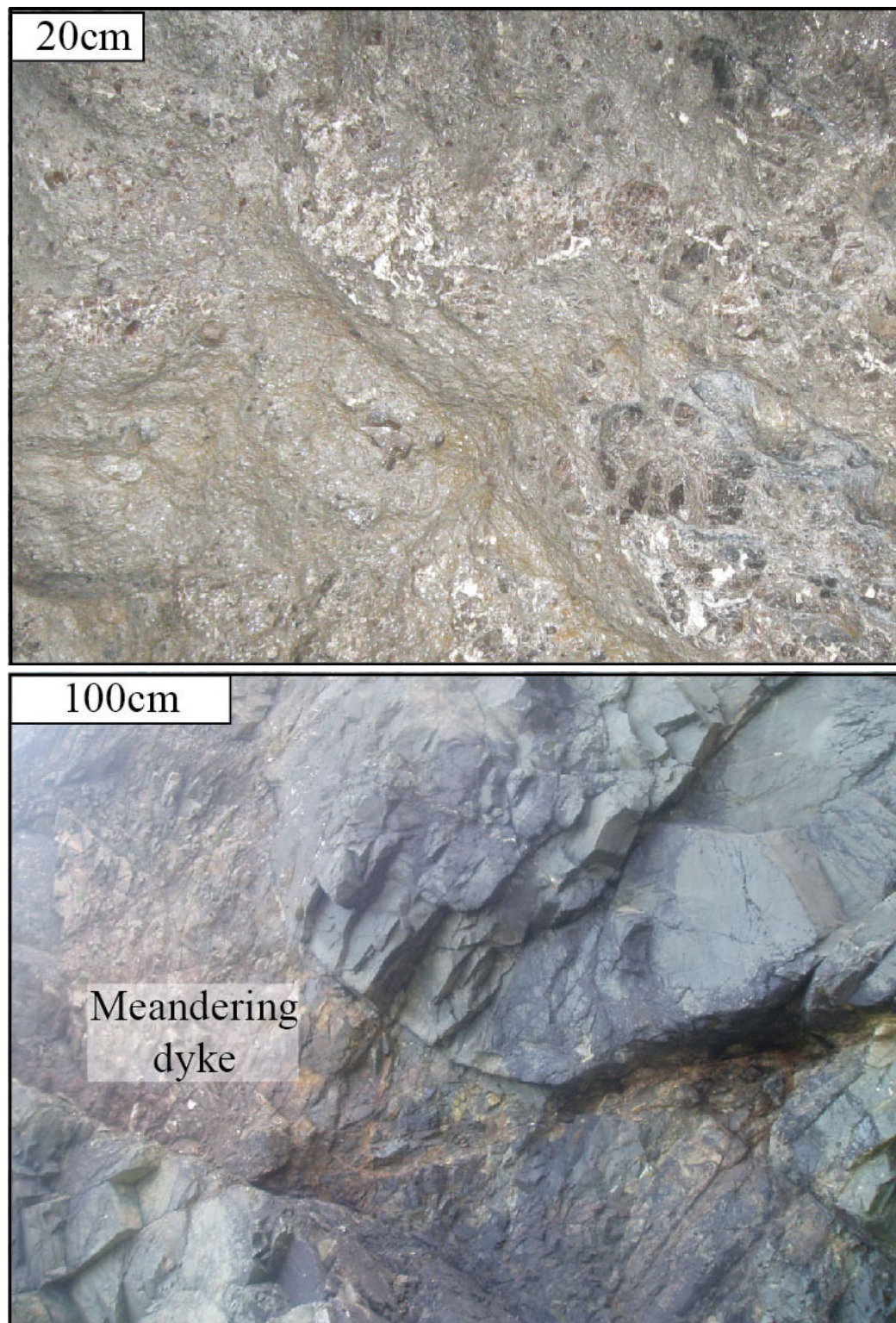


Figure 2.9: Late stage felsic intrusive rocks including quartz feldspar porphyry with (a) cataclastite developed as a result of fault movement and brecciation and (b) meandering dyke within mafic-intermediate composition host rock.



Figure 2.10: Alternating beds of mudstone and conglomerate of the Old Red Sandstone in Trawnamoe, displaying vertical bedding.

2.4 Volcanological features of the Bunmahon and Dunabrattin Formations at Stradbally Cove

Stradbally Cove is located approximately 7km westwards along the coast from Bunmahon (Figure 2.1). The accepted stratigraphy of the area places Stradbally Cove within the Dunabrattin Formation (Sleeman and McConnell, 1995), which is contemporaneous with the Bunmahon Formation. The Dunabrattin Formation is composed predominantly of shales, mudstones and volcanogenic fine-grained sedimentary rocks (Figure 2.11).

Field relationships of the South Waterford volcanic rocks

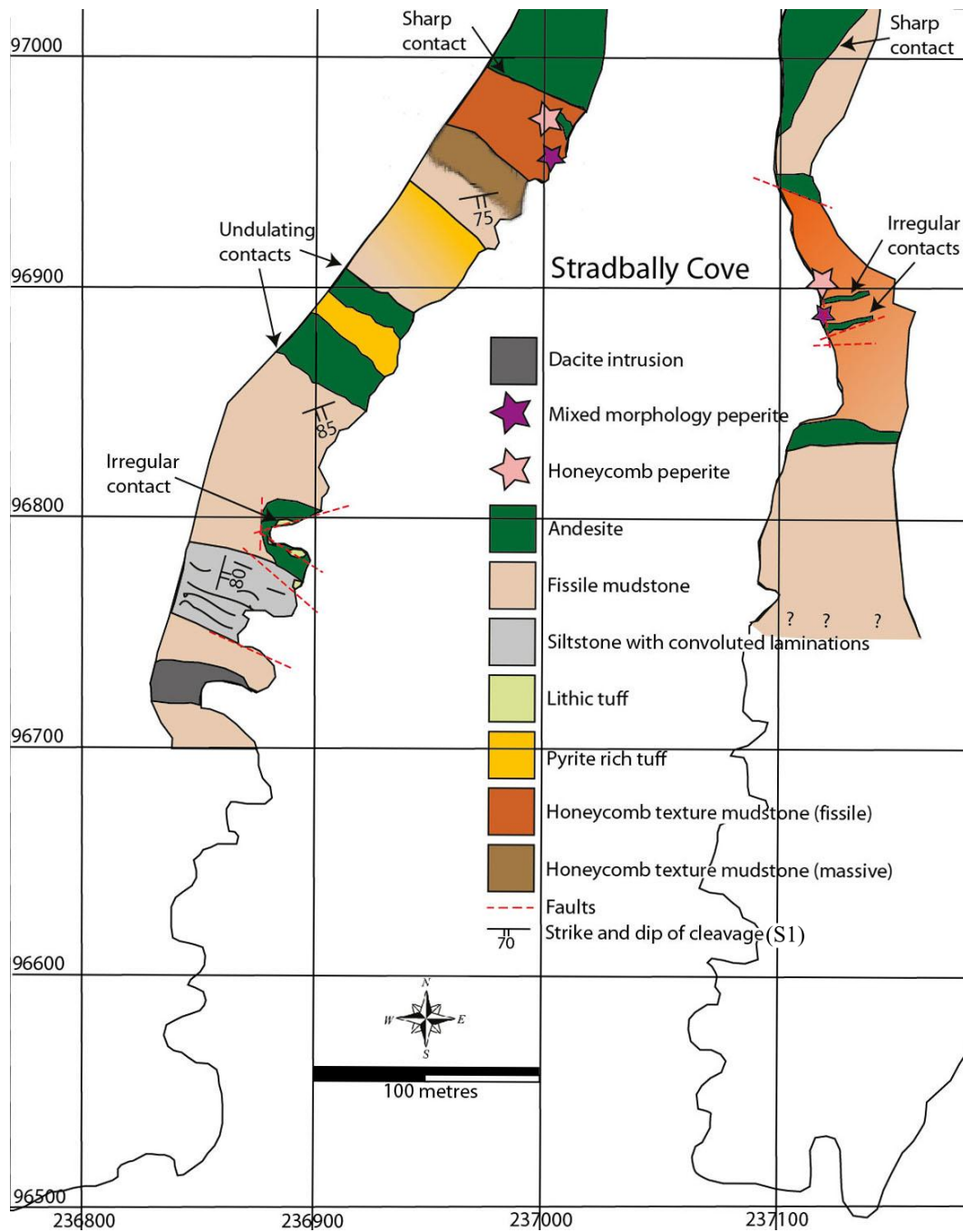


Figure 2.11: Geological map of Stradbally Cove (a) showing the location of the major lithologies and faults. (Figure 2.11 continued overleaf).

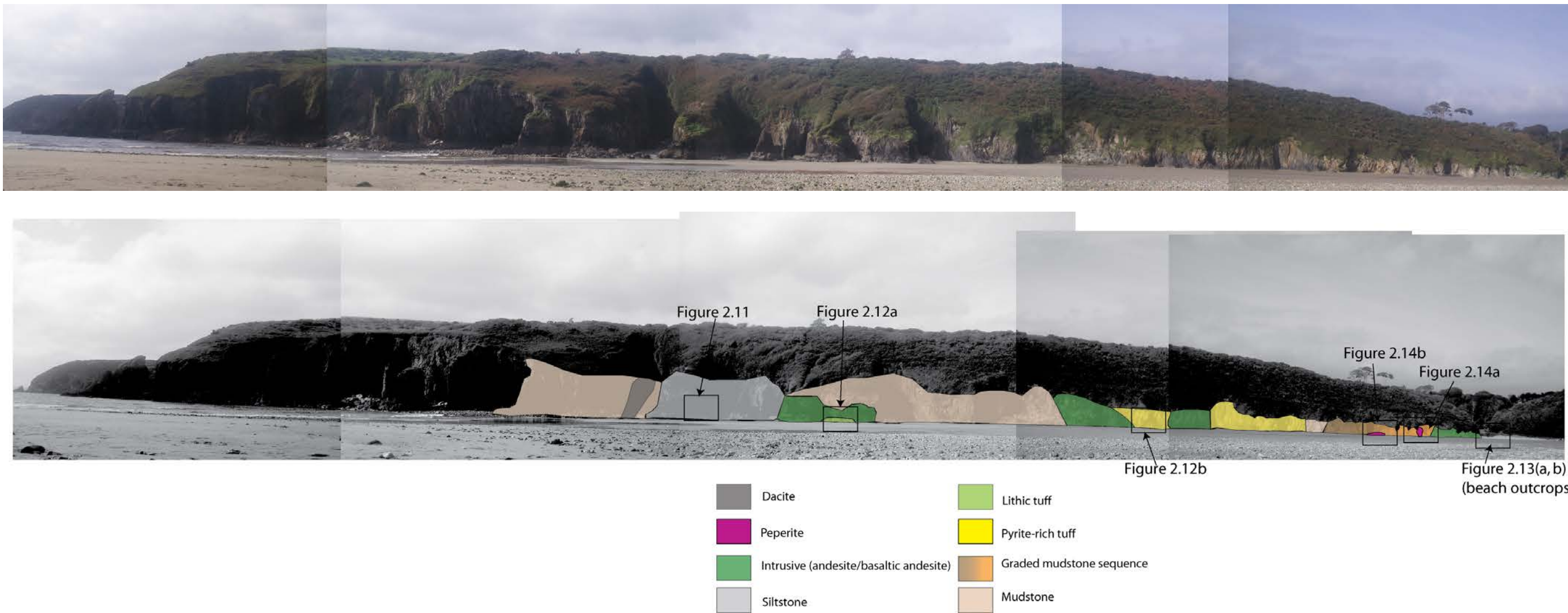


Figure 2.10 (continued): (b) panoramic view of the west side of Stradbally Cove cliff section and (c) geological features of this cliff section with the location of field photographs shown. Figure 2.14 is at contacts of minor intrusive rocks and therefore cannot be shown on the small scale geological map or photographs.

2.4.1 Siltstone

A graded siltstone – fine-sandstone sequence contains abundant convoluted laminations, micro folds and crenulation cleavage (Figure 2.12a). The sequence displays lenticular heterolithic bedding between siltstone and fine sandstone, interspersed occasionally with coarser layers of sandstone. Coarse-grained sandy layers commonly exist as nodules representing isolated fold cores that are often completely replaced by pyrite (Figure 2.12b). Randomly orientated, reworked clasts (up to 10cm long axis) of more competent siltstone display parallel laminations and weather proud within the deformed sequence. The siltstone is cut by a fault (X 36875 96756), with way up structures of the southern section indicating younging to the SSW and way up structures of the northern section indicating younging to the NNW, suggesting either rotation of the sequence or a faulted fold with both limbs exposed.

2.4.2 Mudstone

The sedimentary succession comprises fine-grained, reddish brown, fissile mudstone and a more competent, jointed mudstone. Light buff coloured spots, small cracks and iron-rich veinlets are developed within the fissile mudstone resulting in a honeycomb texture, and these are particularly well developed close to irregular intrusive contacts (e.g. X 37020 96972). Rounded clasts (50-100µm) of siltstone and fine-grained sandstone within the host mudstone are augened by laminations in the mudstone.

2.4.3 Tuffs

The lithic tuff (X 36896 96779) is laterally discontinuous, and has an irregular contact with adjacent rocks. The tuff is composed of angular clasts (1-2cm) of siltstone and fine-grained sandstone that weather proud within a light to medium grey, fine-grained, occasionally glassy, matrix (Figure 2.13a).

The pyrite-rich tuffs (X 36962 96904) display normal grading, from a coarse-grained, jointed tuff to a fine-grained, fissile tuff. Individual disseminated pyrite crystals are abundant, while pyrite nodules (~1mm-4mm), consisting of individual crystals (<0.1mm) of pyrite are rarer, evenly dispersed and oxidised at the rim (Figure 2.13b).

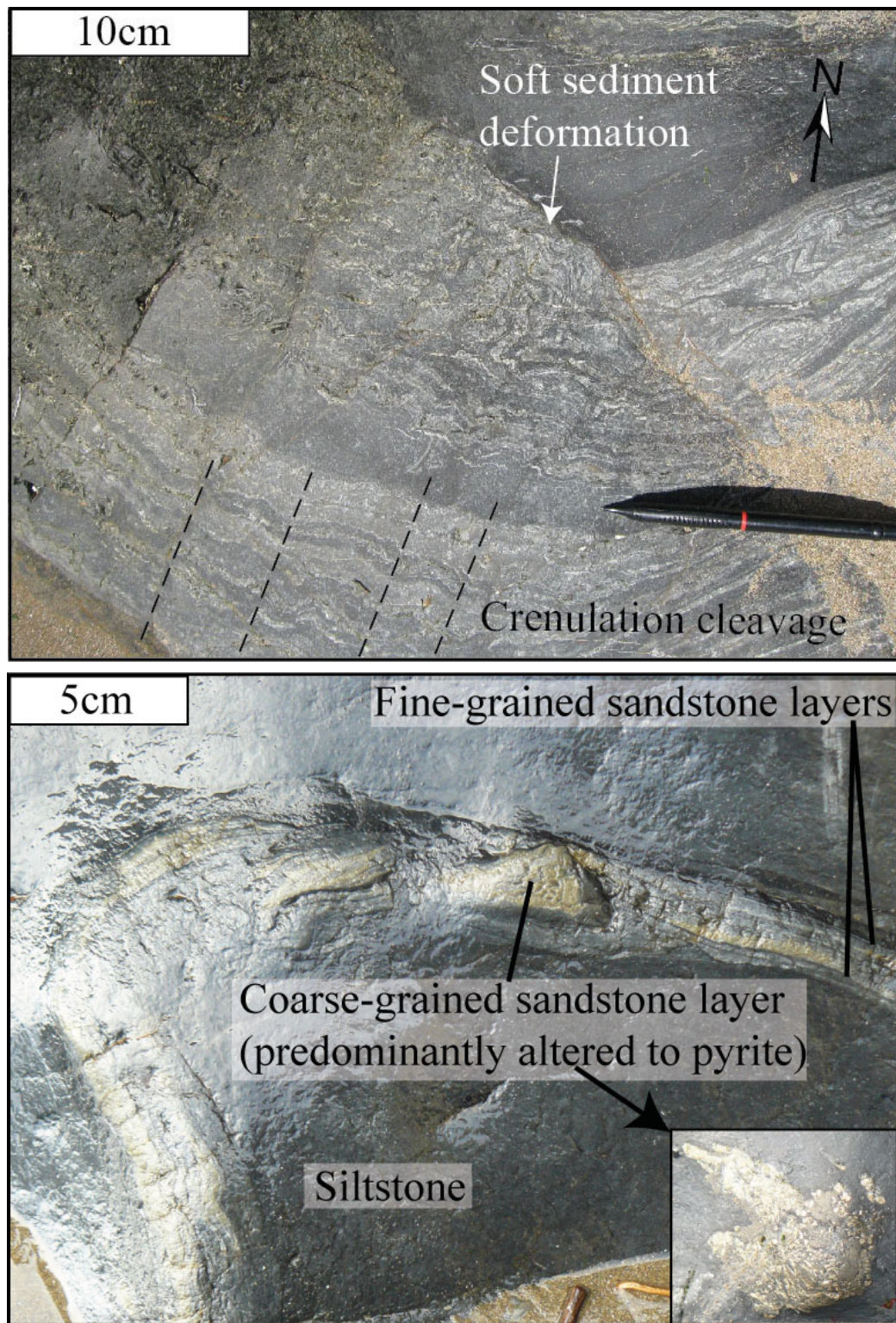


Figure 2.12: Siltstone and fine sandstone sequence containing (a) convoluted laminations as a result of soft sediment deformation and later developed crenulation cleavage associated with regional deformation and (b) folded coarser-grained sandstone layers replaced by pyrite, some of these layers occurring in tighter folds where only the fold core is exposed (inset).

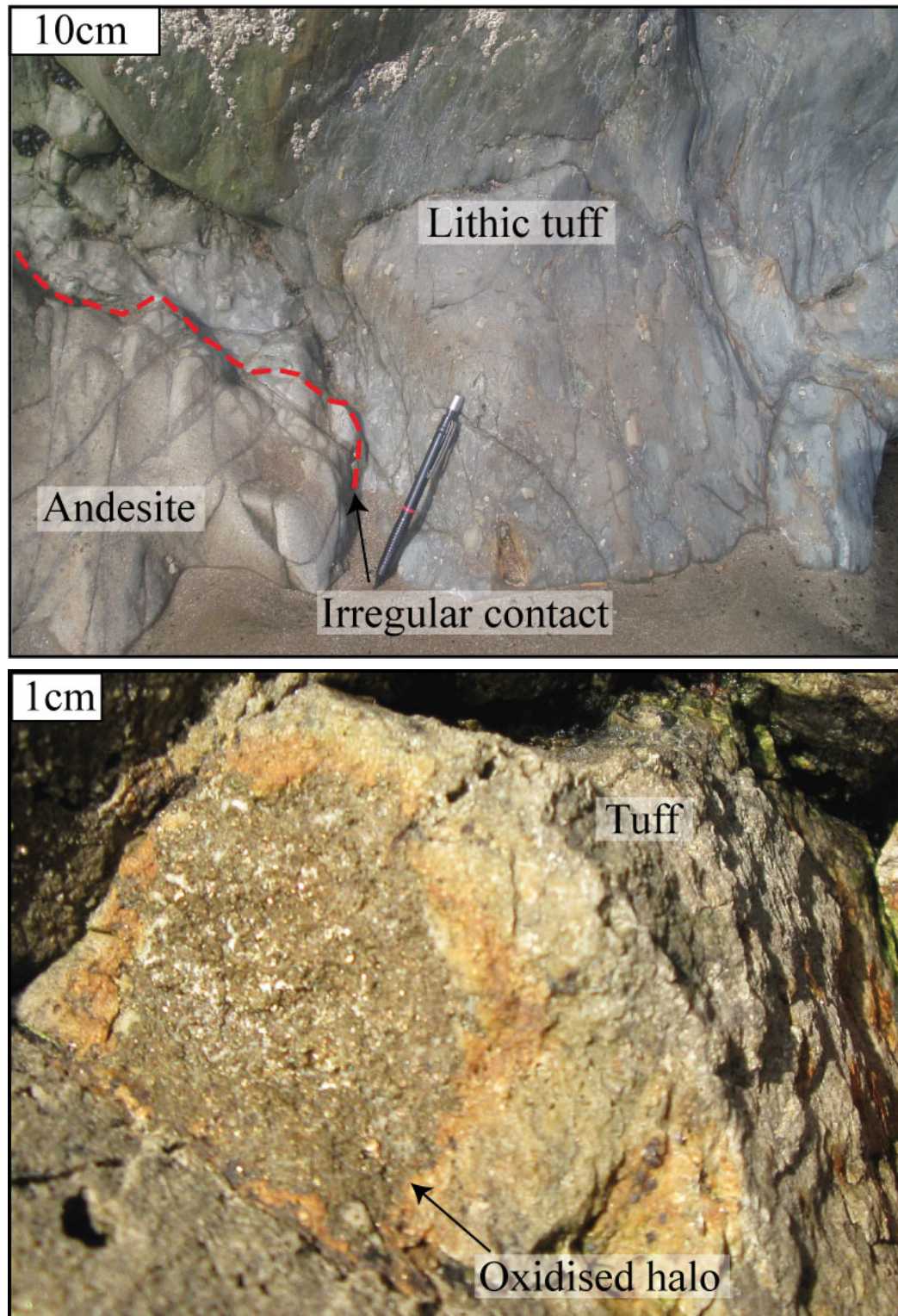


Figure 2.13: Tuff sequences in Stradbally Cove including (a) lithic tuff, containing angular lithic fragments up to 4cm long and (b) pyrite-rich tuff containing disseminated pyrite and rare pyrite nodules.

2.4.4 Intrusive rocks

The nature of intrusive contacts varies greatly from complete fragmentation of magma into clasts (X 37019 96964) to irregular, undulating contacts with rare fragmentation (Figure 2.14), coherent but lobate or bulbous contacts (Figure 2.15a; X 37002 96956) and straight contacts (X 37123 96886). Well jointed, greenish-grey, coarse-grained intrusive rocks (X 37027 96994 and X 37104 97019), comprise a phenocryst assemblage (<1mm) of predominantly quartz and plagioclase. Porphyritic dykes (Figure 2.15b), with a similar phenocryst assemblage within a feldspar and chlorite-rich groundmass, are exposed at regular intervals within the host sedimentary succession, (e.g. X 37123 96886), and range in thickness from 6 to 30cm.

2.4.5 Peperite lithologies

The honeycomb texture mudstone was intruded by a fine-grained, greenish grey sill, with angular peperite developed in a 3m x 0.75m area (X 37019 96964). Peperite clasts are larger (~6cm), more abundant and close-packed adjacent to the intrusive contact, with some clasts showing jigsaw-fit texture (Figure 2.16a). Further away from the intrusive contact clasts decrease in abundance and size (0.5cm-4cm). On the eastern side of the cove (X 37110 96903) a similar composition peperite contains larger clasts (4x10cm, elongated in the vertical) but the coherent intrusive body that formed the peperite is not exposed. Due to the texture developed within the host mudstone adjacent to this peperitic intrusion, this is described as honeycomb peperite.

At X 37005 96956, peperite is formed as a result of andesite intrusion into fine-grained mudstone. The outcrop of peperite is approximately 2.5m long and 0.5m high, with the base covered by beach deposits. Larger and more abundant clasts occur adjacent to an irregular intrusive contact. Several barbed apophyses, finger-like protrusions and wispy fragments of volcanic material extend into the sedimentary component that have remained attached to the main intrusive body (Figure 2.16b). Due to the range of clast shapes and sizes (sub-rounded to angular clasts, with wispy tendrils, from mms up to 10cm) this is described as a mixed morphology peperite.

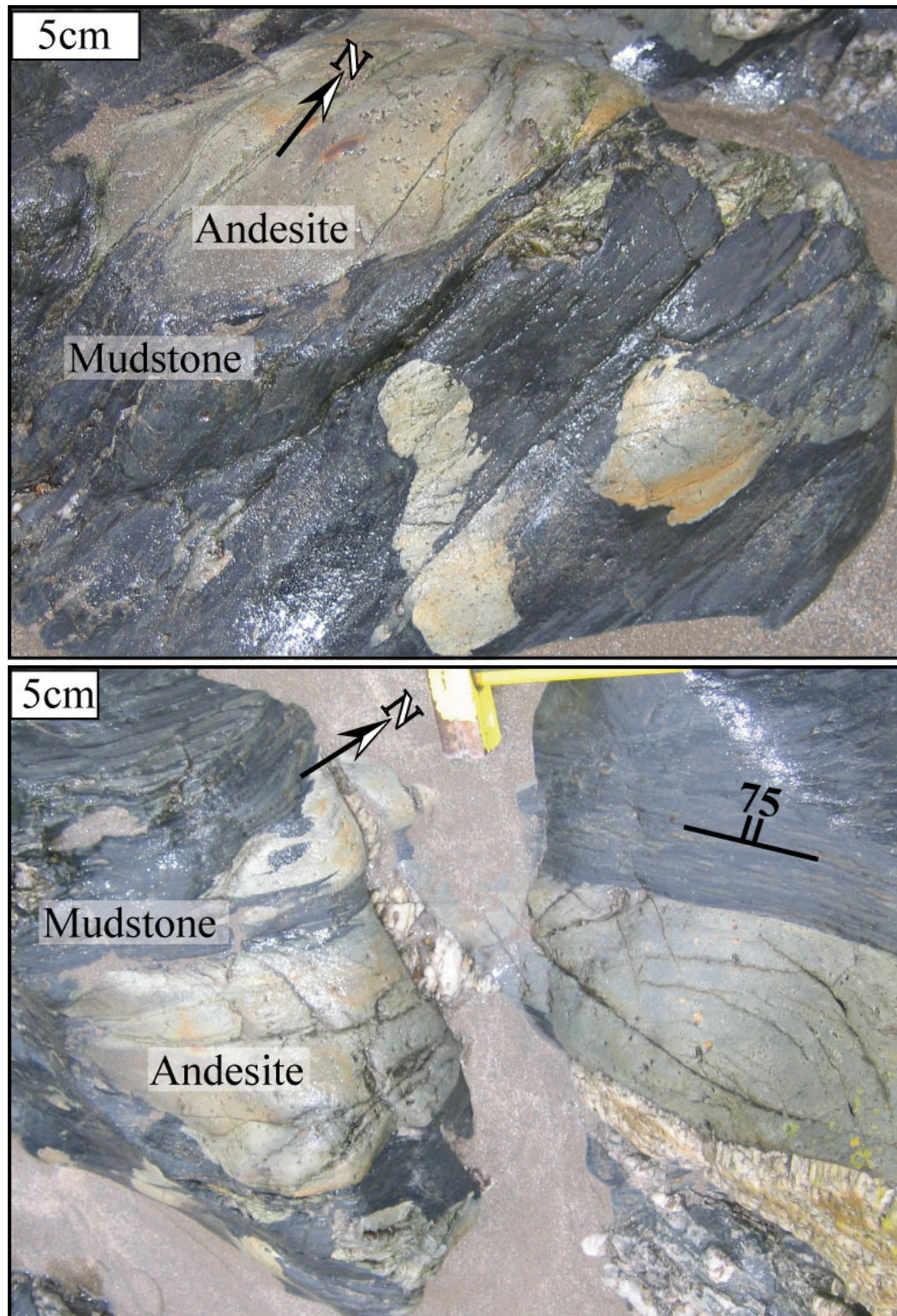


Figure 2.14: Field photographs of intrusive contacts from Stradbally Cove including (a) rare peperite clasts that have spalled from the main intrusion into the host mudstone and (b) an irregular contact with rare clasts of both magmatic and sedimentary material.

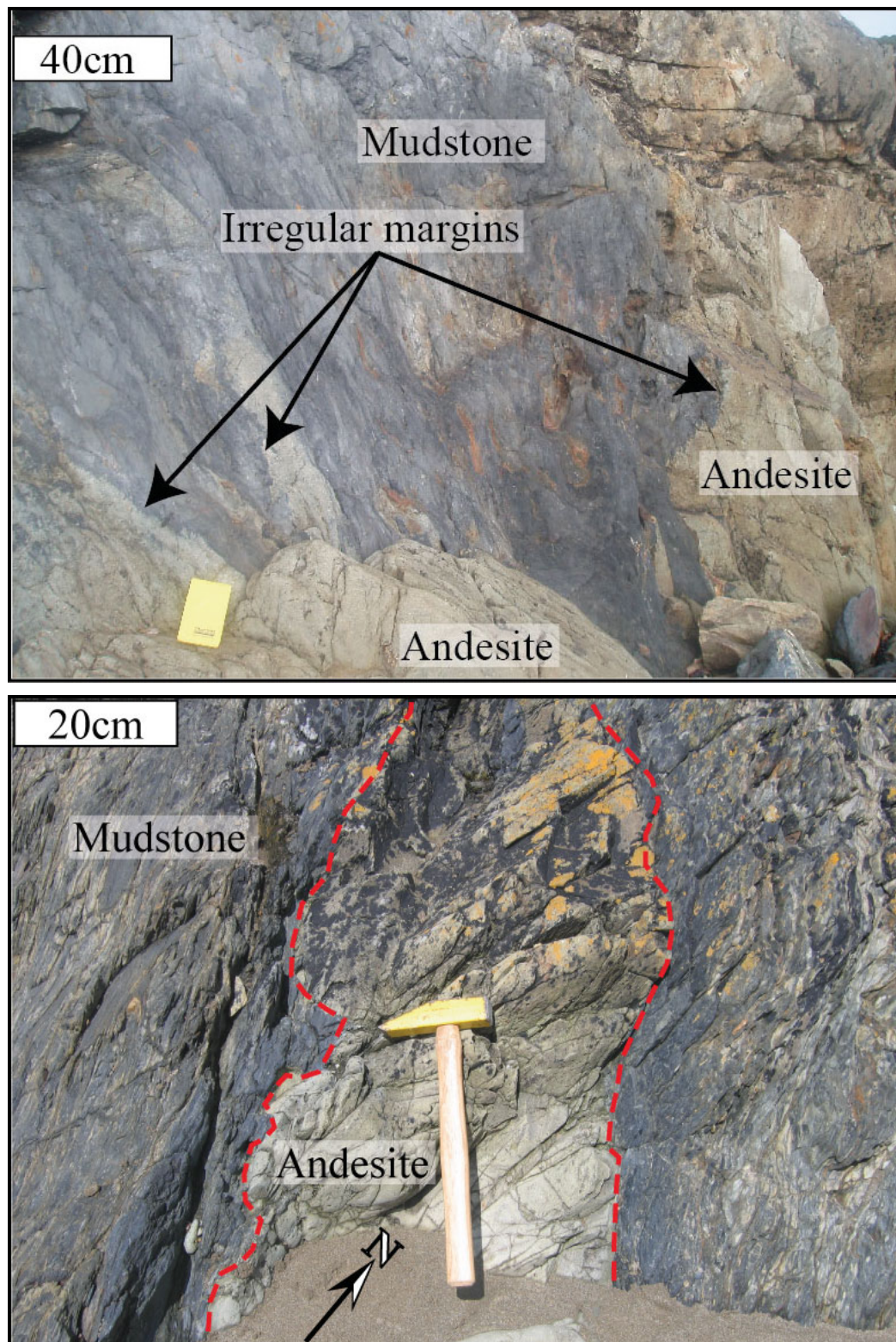


Figure 2.15: Intrusions at Stradbally Cove, with (a) a ragged, irregular intrusive contact between mudstone and andesite, and (b) boudinage dyke of andesite in cleaved mudstone host rock.

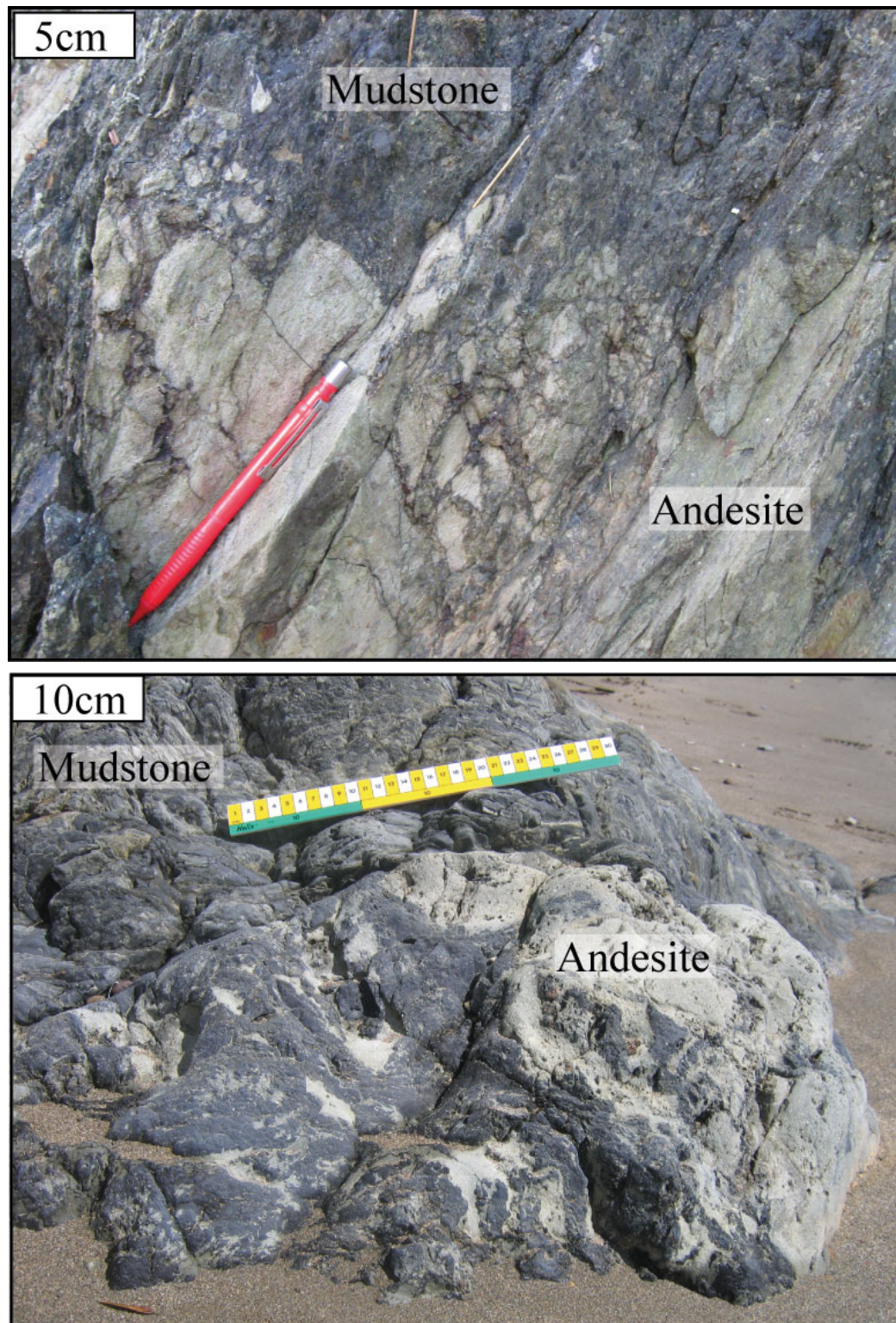


Figure 2.16: Peperite formed as a result of interaction between andesite and unconsolidated mudstone resulting in (a) close-packed, angular jigsaw-fit clasts close to the intrusive contact in honeycomb peperite and (b) a range of clast morphologies including barbed apophyses and wispy tendrils attached to the main intrusive body in the mixed morphology peperite.

2.5 Additional coastal and cored localities in the Bunmahon Formation

Several small outcrops are present in and around the village of Bunmahon, some within road cuttings and some with topographic relief due to preferential weathering of surrounding host rocks. A highly weathered and oxidised intrusive rock at X 45044 03802 consists of a very pale grey, fine-grained groundmass comprised of altered feldspars and rare clay minerals hosting rounded to sub-rounded phenocrysts of quartz and feldspar and some large iron oxides. The mineralogical assemblage is indicative of a dacitic to rhyolitic rock type. Outcrops at both ends of Bunmahon beach (X 43044 98587 and X 43805 98726) and within roadside outcrops at X 43903 98928, X 43841 98849 and X 43514 98883 are well jointed, medium grey-green in colour and porphyritic. At the eastern end of Bunmahon beach, the lava grades into hyaloclastite, likely a continuation of those in Trawnamoe, displaced by later faulting.

Kilmurrin Cove is located approximately 3Km to the east of Bunmahon, (X 246500 98750; Figure 2.1); the exposed section is composed entirely of intrusive and extrusive igneous rocks (Figure 2.17a). Fine-grained greyish-green sheet flows dominate the cove, which commonly grade into an outer hyaloclastite rim, similar to those observed at Trawnamoe and Bunmahon. Irregular and faulted contacts are preserved between the lava flows and an agglomerate containing mafic and felsic clasts. The groundmass of the agglomerate grades from greenish-grey (similar to andesite) to an oxidised purplish-red colour (e.g. X 46549 98794). Several mafic dykes cross cut this sequence of lithologies, some of which are associated with quartz veining (Figure 2.17b). Tuff deposits are exposed at both the western and eastern end of the cove, with faulted relationships between these and the surrounding lithologies.

At Ballydowane Bay, small outcrops of alternating coherent andesite and friable hyaloclastite (Figure 2.18a) are present surrounded by later deposits of Old Red Sandstone. The andesitic sheet flows and associated hyaloclastite have complex relationships and are commonly interdigitating and as a result individual sheet flow identification cannot be made from separate outcrops. However, the similarity between this andesite/hyaloclastite and those observed in Trawnamoe and Kilmurrin Cove suggests that these represent successive sheet flows with hyaloclastite margins. The majority of the rest of the cliff section is composed of

Field relationships of the South Waterford volcanic rocks

Old Red Sandstone with an alternating sequence of conglomerate and mudstone, similar to that seen in Trawnamoe. As at Trawnamoe, the conglomerate section of the Old Red Sandstone contains clasts of the andesite/hyaloclastite (Figure 2.18b).

One core section (WYR-1) within the Bunmahon Formation (Ballyristeen, X 24395 10115; Figure 2.1) was examined to correlate coastal and inland geology (Appendix A2). The top section (~65m) of the core predominantly consists of heavily altered, fine-grained, iron-rich tuff deposits. The fine-grained sedimentary rocks towards the base of the section were intruded by a fine-grained andesite that resulted in soft sediment deformation directly adjacent to the contact. Large quartz veins bisect the sedimentary rock in contact with the intrusive rock.

Field relationships of the South Waterford volcanic rocks

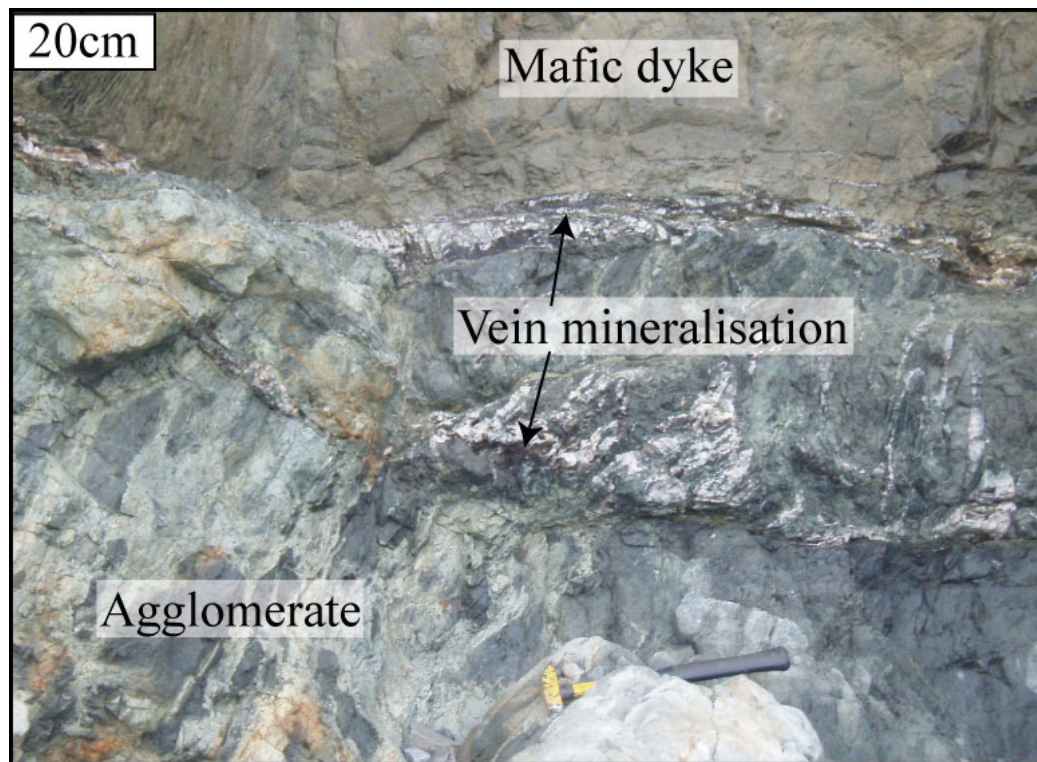
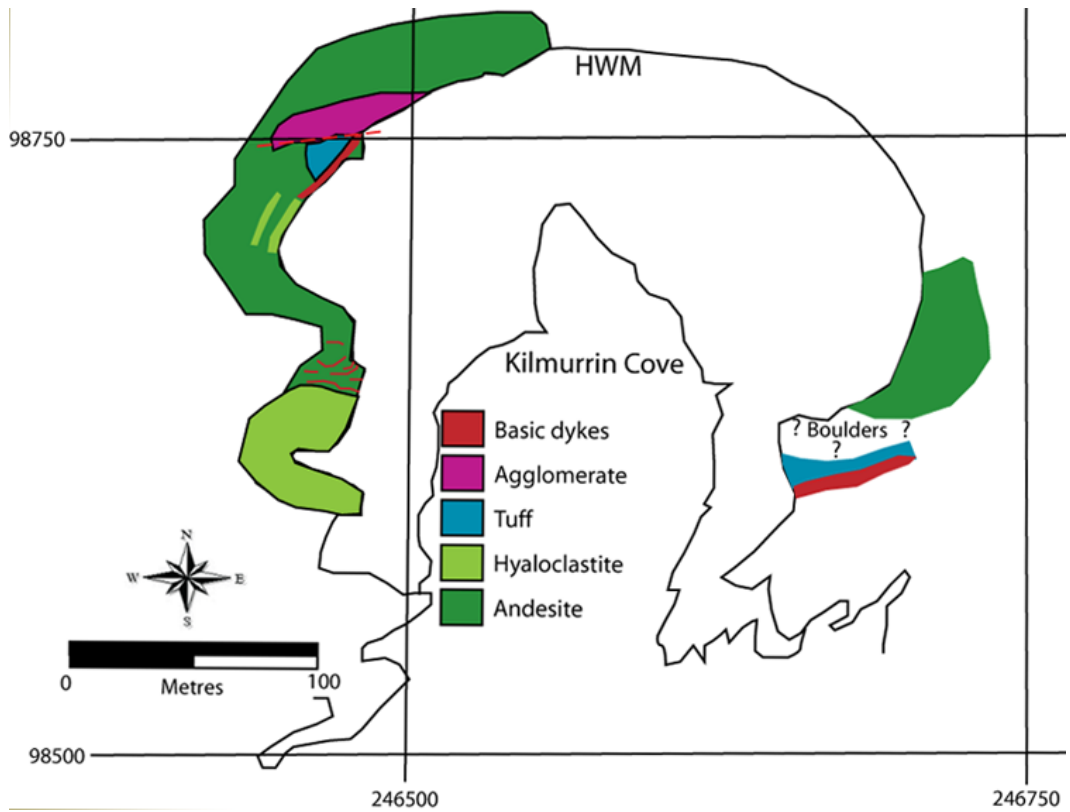


Figure 2.17: Geological map of the main lithologies of Kilmurrin Cove (a) and (b) field photograph of a mafic dyke cross-cutting agglomerate with associated quartz veining at Kilmurrin Cove.

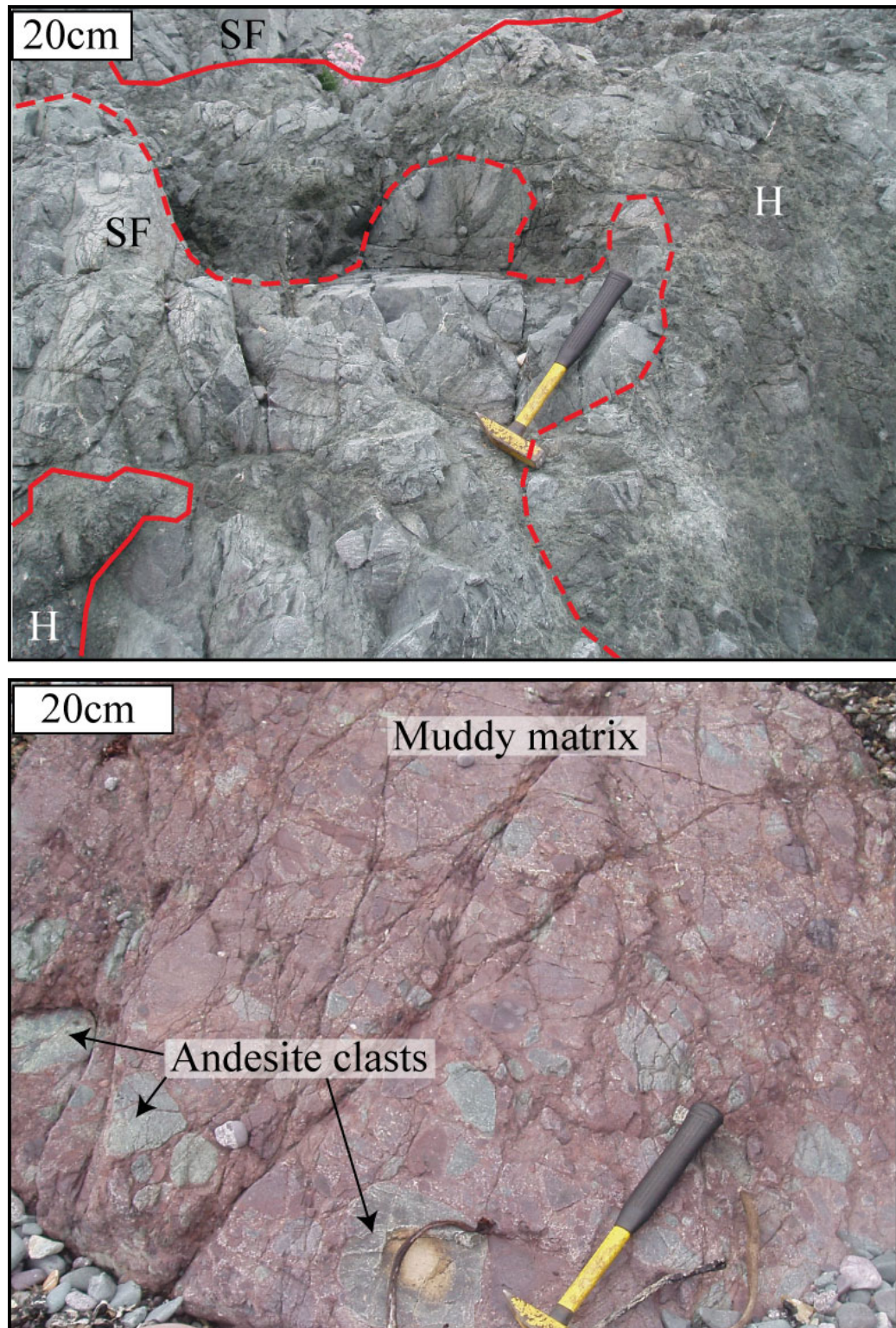


Figure 2.18: The dominant rock types exposed in Ballydowane Bay are (a) andesite sheet flows (SF) and interdigitating hyaloclastite (H) and (b) conglomerate of Old Red Sandstone containing clasts of the underlying Ordovician andesites.

2.6 Coastal and core localities in the Campile Formation

Kilfarrasy Strand, within the Campile Formation, (X 52420 98230) is comprised of intensely cleaved and folded mudstones (Figure 2.19a), with some soft sediment deformation preserved. The contacts of the mudstones with adjacent intrusive rocks are obscured due to fallen material from the cliff face. Contacts are observed at X 52824 98133 between underlying highly altered, fine-grained intrusive rocks and an overlying coarse-grained tuff containing crystals of quartz and feldspar in a feldspar rich matrix.

Garrarus Strand is also located within the Campile Formation (X 54570 98350), one kilometre east of Kilfarrasy Strand. The entire cliff section is composed of igneous lithologies. Contacts are generally obscured due to fault movement, but those contacts which are preserved are highly irregular. At X 54749 98391 an outcrop of agglomerate containing angular basaltic clasts is overlain by an irregular mafic lava flow. The matrix of the agglomerate is very fine-grained hosting angular, elongated, vesicular basalt clasts, ranging in size from two centimetres up to ten centimetres. The rest of the section is composed of fine-medium grained intermediate intrusive rocks, fine-grained tuffs and irregular basalt dykes within the host sedimentary sequence (Figure 2.19b). The complicated nature of the contacts is attributed to the intrusion of magma into soft, unconsolidated sediment resulting in soft sediment deformation and disrupted bedding (Stillman and Sevastopulo, 2005).

Five core sections (WLK-3, WLK-7, WFN-3, WFN-12, WFN-14; Figure 2.1), from inland localities within the Campile Formation, were also examined. All core sections are composed predominantly of interbedded pyrite-rich black shales and intermediate to felsic tuffs (Appendix A2). Minor rhyolitic and basaltic intrusions also occur (WFN-3, WFN-14) and display irregular intrusive contacts with the host sedimentary rocks. Sulphide-bearing vein mineralisation is recorded within the host sedimentary sequence (e.g. WFN-3, WFN-14), commonly associated with irregular intrusive rocks and brecciation of the host rocks.

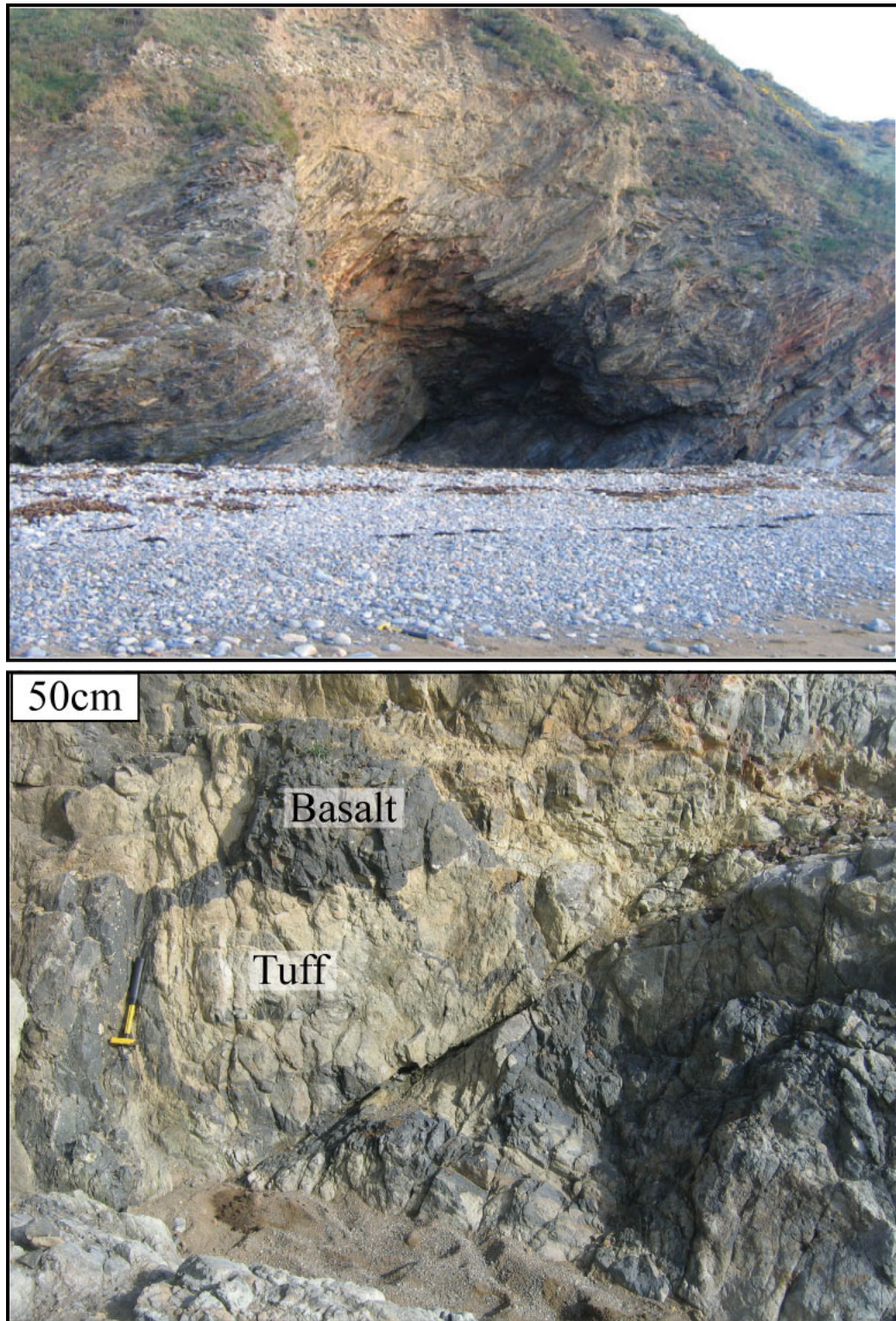


Figure 2.19: Main lithologies exposed in (a) Kilfarrasy Strand include cleaved and deformed mudstones and in (b) Garrarus Strand include mafic and intermediate intrusive rocks with highly irregular contacts as a result of intrusion into unconsolidated or poorly consolidated host sediments.

2.7 Mineralisation

Much of the sequence has been altered from its primary composition and the most common secondary or replacement mineral is chlorite, which occurs in the majority of intrusive and volcanoclastic rocks. Generally vein mineralisation throughout the sequence is composed of calcite and/or quartz. Two distinct types of vein mineralisation are identified on the basis of both their structural relationship with the host rock and their mineral assemblage.

Swarms of irregular, sulphide-bearing quartz and calcite veins are hosted by the alternating sheet flow/hyaloclastite lithology in Trawnamoe at X 42683 98159, X 42786 98180, X 42806 98178 and X 42820 98178, with associated wall rock alteration. The majority of veins comprising these swarms range in thickness from a few millimetres to 5cm, have little variation in strike, ranging between 355° and ~25°, and are vertical to sub-vertical (Figure 2.20a). The thicker veins often contain angular fragments of brecciated host rock. Individual veins are composed of quartz or intergrowths of quartz and calcite. The larger quartz veins tend to exhibit a syntaxial growth pattern with smaller anhedral quartz crystals towards the margin of the vein and larger subhedral crystals within the centre of the vein. Sulphide minerals present include pyrite and chalcopyrite, occurring in isolated clusters within the host veins (Figure 2.20b) and are commonly associated with abundant malachite alteration. Similar pyrite to that found in the vein deposits is present in the host hyaloclastite adjacent to these veins. A similar swarm of irregular quartz veins, approximately 40-50cm wide, and composed of individual veins 8-10cm thick along with minor veinlets, is hosted by the siltstone at the southern end of Stradbally Cove (X 36876 96736). Individual veins are irregular, with an overall strike direction of ~100°, and are dipping sub-vertically. Lenses of the host siltstone, with disrupted laminations, have been incorporated into the vein system; some of these laminations outline the irregular contact with the quartz vein (Figure 2.21a). Pyrite is the only sulphide mineral recorded, occurring in stringers, adjacent to or along the contact between the quartz vein and the incorporated siltstone. The term sheeted vein system is applied here, as this is often used to describe similar swarms or clusters of steeply-dipping, sub-parallel, narrow and closely spaced veins (e.g. Dominy *et al.*, 1995). The sheeted vein systems in Trawnamoe and Stradbally Cove are classed as sulphide-bearing veins.

Veins utilising weaknesses such as bedding or fault planes are composed of quartz or calcite, or are zoned quartz-calcite. These planar veins are generally much thicker than the irregular sheeted veins. At Trawnamoe, the largest vein occurs parallel to bedding within the tuff at the western end of the cove (X 42770 98180). The vein varies from 20cm to 40cm in thickness and is composed of a calcite core with an outer margin of quartz (Figure 2.21b). Several smaller veins of apparently the same composition occur approximately ten metres up the vertical cliff face and perpendicular to bedding. These veins are all aligned in the same direction, dipping approximately at 45°N and appear to be utilising a similar weakness, perhaps pull apart fractures or tension gashes. Planar veins, following bedding or fault planes, are abundant in Stradbally Cove. Numerous barren quartz veins (~5cm thick) cross-cut mudstone in contact with andesite (X 36896 96779). Individual veins meander through the mudstone, originating at the fault plane; these probably outline planes of drag folding associated with fault movement. Similar irregular veins are recorded within the fissile mudstone, following bedding planes that are disturbed across a fault plane. The planar veins do not contain any sulphide minerals and are classified as barren.

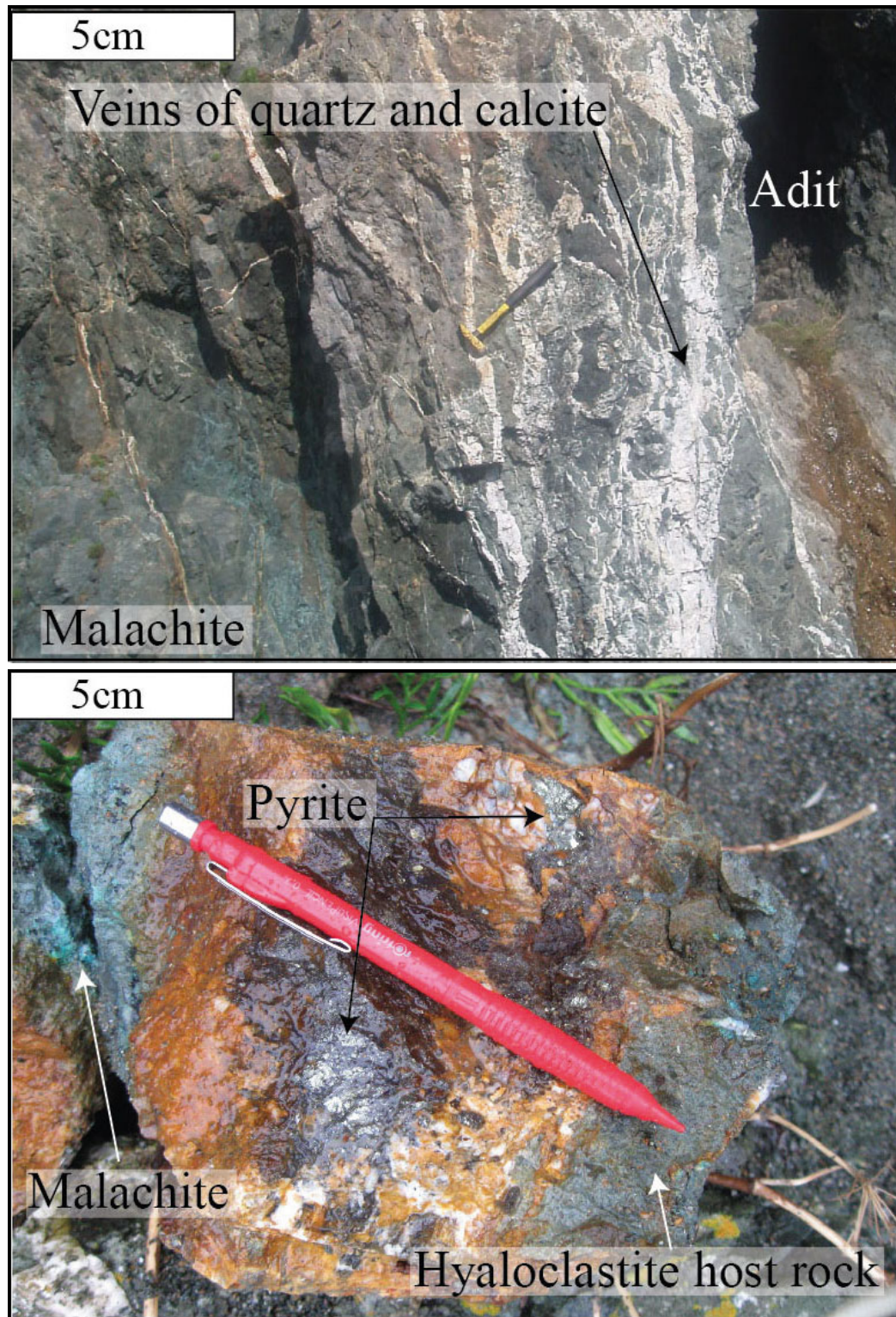


Figure 2.20: Sheeted vein mineralisation at Trawnamoe consists of (a) irregular networks of steeply dipping veins containing (b) disseminated and stringer deposits of pyrite.

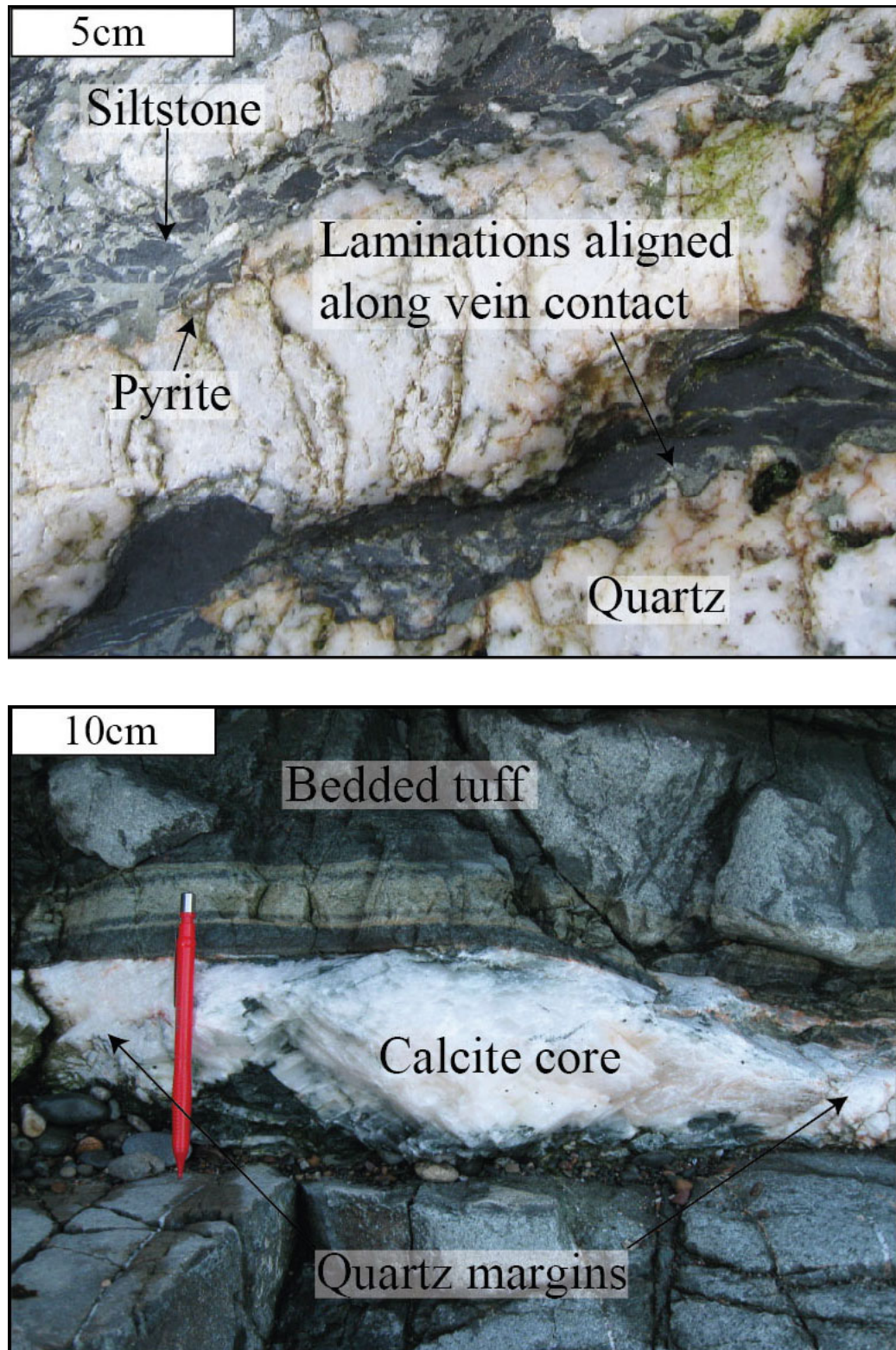


Figure 2.21: Field photographs of (a) the sulphide-bearing sheeted vein system at Stradbally Cove in siltstone host rock, with siltstone laminations aligned parallel to the vein contact and (b) the barren zoned quartz-calcite vein from Trawnamoe in the bedded tuff host rock.

2.8 Peperite rock textures

Classification in terms of juvenile clast morphology (Skilling *et al.*, 2002) is a useful tool for the description of peperites, given the occurrence of peperite in nearly all geological settings and in many different lithologies (Appendix A1). Peperite lithologies at Trawnamoe and Stradbally Cove have been described as fluidal (Figure 2.7), blocky or angular with jigsaw-fit textures (Figure 2.16a) or mixed morphology (Figure 2.16b). Sketches of the clast morphology within the context of outcrops at Trawnamoe and Stradbally Cove are illustrated in Figure 2.22. Field photographs have been further enhanced by converting these to binary images, in order that pixel counting may be used to quantify relative volumes of magmatic and sedimentary components in peperite. Techniques used in computer assisted image analysis and determination of errors is given in Appendix A4 and results are given in Figure 2.23.

2.8.1 Fluidal Peperite

The peperite consists of fluidal clasts of magmatic material, rounded to sub-rounded in shape but with irregular margins. Features such as necking of the clasts and wispy margins are common. Clast sizes range from one centimetre up to as large as 25 centimetres. The majority of clasts are densely packed together with the thickness of the intervening sediment ranging from a few millimetres up to four centimetres (Figure 2.22). Alteration to chlorite is pervasive in the sill but more intensely developed in the peperite clasts. The tuff matrix is silicified, predominantly occurring within very narrow tracts or in sedimentary fragments incorporated into magmatic clasts. Delicate laminations are commonly preserved within the silicified matrix curving around magmatic clasts. The magmatic component comprises approximately 67% total area of peperite exposed (Figure 2.23). As two adjacent sections of the peperite are exposed, both of which contain the boundary limits of peperite, a minimum peperite volume of 45m^3 was determined for the exposure. Therefore, extrapolating total area percentage of magmatic clasts to volume, a minimum of 30m^3 of magma interacted with sediment to produce this peperite. An absolute minimum volume of 15m^3 of sediment interacted to form peperite, as the total volume of fluidised sediment entrained away from the magmatic contacts cannot be determined.

Analysis of clast orientation and elongation is presented in Figure 2.24. Measurements of aspect ratio of clasts (horizontal/vertical) indicate that the majority of clasts are slightly elongated in the horizontal, yielding an aspect ratio of >1 . The angle of clast orientation was measured as the angle between the longest axis and the horizontal reference frame. The majority of clasts are sub-parallel to the overlying bedded tuff, orientated between 5 and 30° from the horizontal (Figure 2.24). The degree of elongation and the orientation of clasts may be related to “tectonic flattening” (e.g. Schaffalitzky, 1982) as a result of subsequent regional deformation.

2.8.2 Honeycomb Peperite

An irregular, light coloured basaltic andesite dyke in contact with the overlying mudstone produced peperite clasts over an exposed area of two metres in height and 0.75 metres in width. Magmatic clasts are closely packed adjacent to the magmatic contact, becoming more dispersed within the sedimentary host rock approximately 8cm from the contact, resulting in a rough grading pattern. Clasts are evenly dispersed within the main body of peperite and are randomly orientated with approximately two centimetres of sedimentary matrix separating clasts (Figure 2.22). The host rock is a fine-grained iron rich mudstone, with a network of darker veins and cracks. Clasts vary considerably in shape and size, from 0.5cm up to 6cm, however most are in the range of 1-3cm. All clasts are best described as angular (following sedimentary classification of angular clasts), with irregular, well-defined edges. A high proportion of clasts have extremely straight edges and are approaching square or rectangular in shape. Conversion of peperite field photographs to binary images (Figure 2.23) yields total area coverage of the magmatic component of approximately 27% of the outcrop. Extrapolation to total volume is not viable as only one face of the outcrop is exposed.

2.8.3 Mixed Morphology Peperite

Mixed morphology peperite is exposed over an area of one metre long and 30 cm high. Coherent basaltic andesite is preserved at the eastern extremity of the peperite exposure and the number of magmatic clasts decreases toward the west. The magmatic component is a fine-grained basaltic andesite intrusion, and the sedimentary component is a fine-grained mudstone. Magmatic clasts are generally fluidal in nature, with some angular clasts. Commonly fragments of magmatic

Field relationships of the South Waterford volcanic rocks

material have jagged outlines, the majority of which have become separated from fingers of magmatic material extending into the sediment (Figure 2.22). These numerous apophyses, some of which are barbed, are joined to larger clasts. Some elongated tendrils of magma (~10cm) with wispy margins completely surround sedimentary clasts. Analysis of binary images (Figure 2.23) yields an approximate magmatic percentage of 34%.

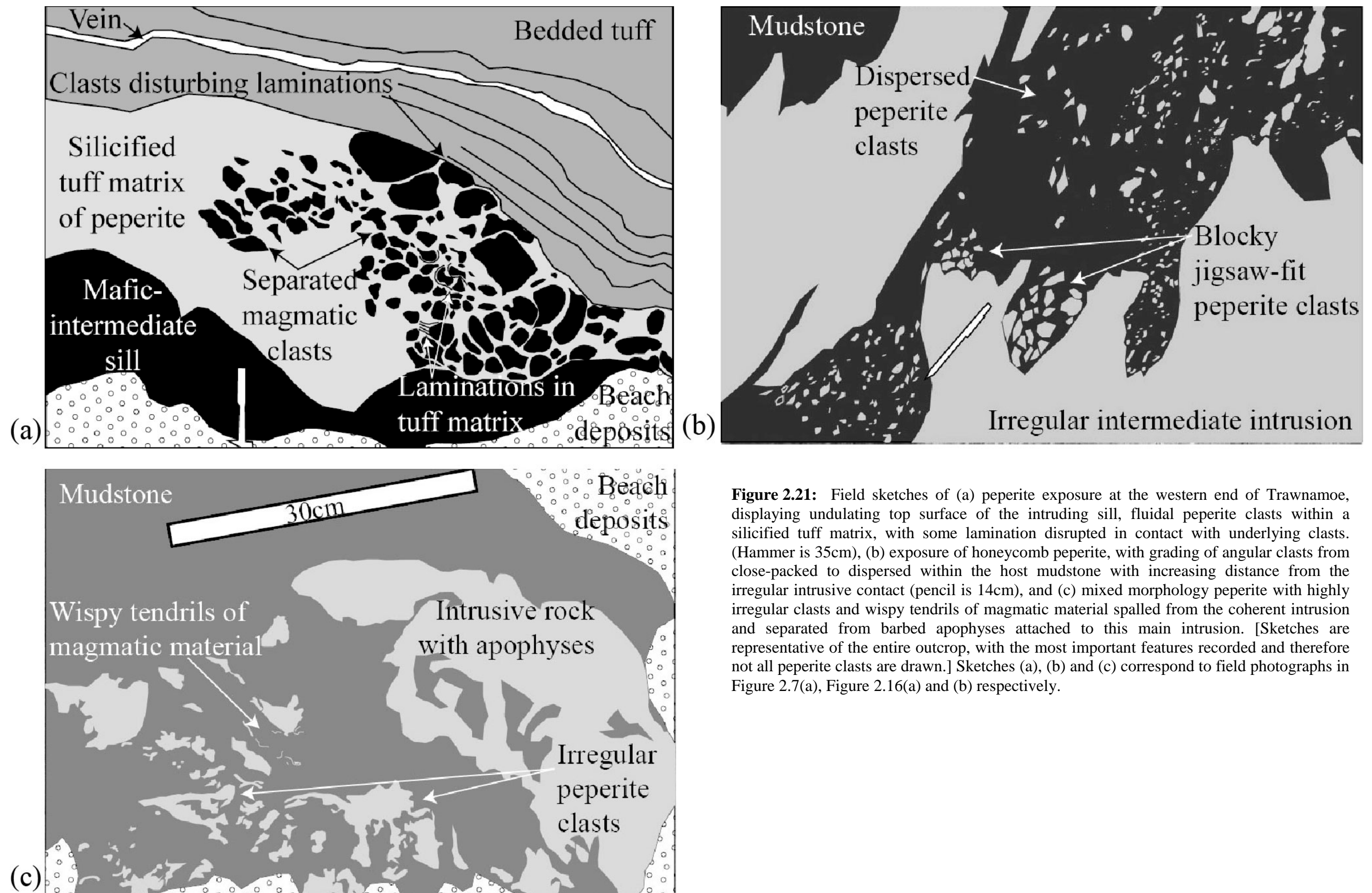


Figure 2.21: Field sketches of (a) peperite exposure at the western end of Trawnamoe, displaying undulating top surface of the intruding sill, fluidal peperite clasts within a silicified tuff matrix, with some lamination disrupted in contact with underlying clasts. (Hammer is 35cm), (b) exposure of honeycomb peperite, with grading of angular clasts from close-packed to dispersed within the host mudstone with increasing distance from the irregular intrusive contact (pencil is 14cm), and (c) mixed morphology peperite with highly irregular clasts and wispy tendrils of magmatic material spalled from the coherent intrusion and separated from barbed apophyses attached to this main intrusion. [Sketches are representative of the entire outcrop, with the most important features recorded and therefore not all peperite clasts are drawn.] Sketches (a), (b) and (c) correspond to field photographs in Figure 2.7(a), Figure 2.16(a) and (b) respectively.

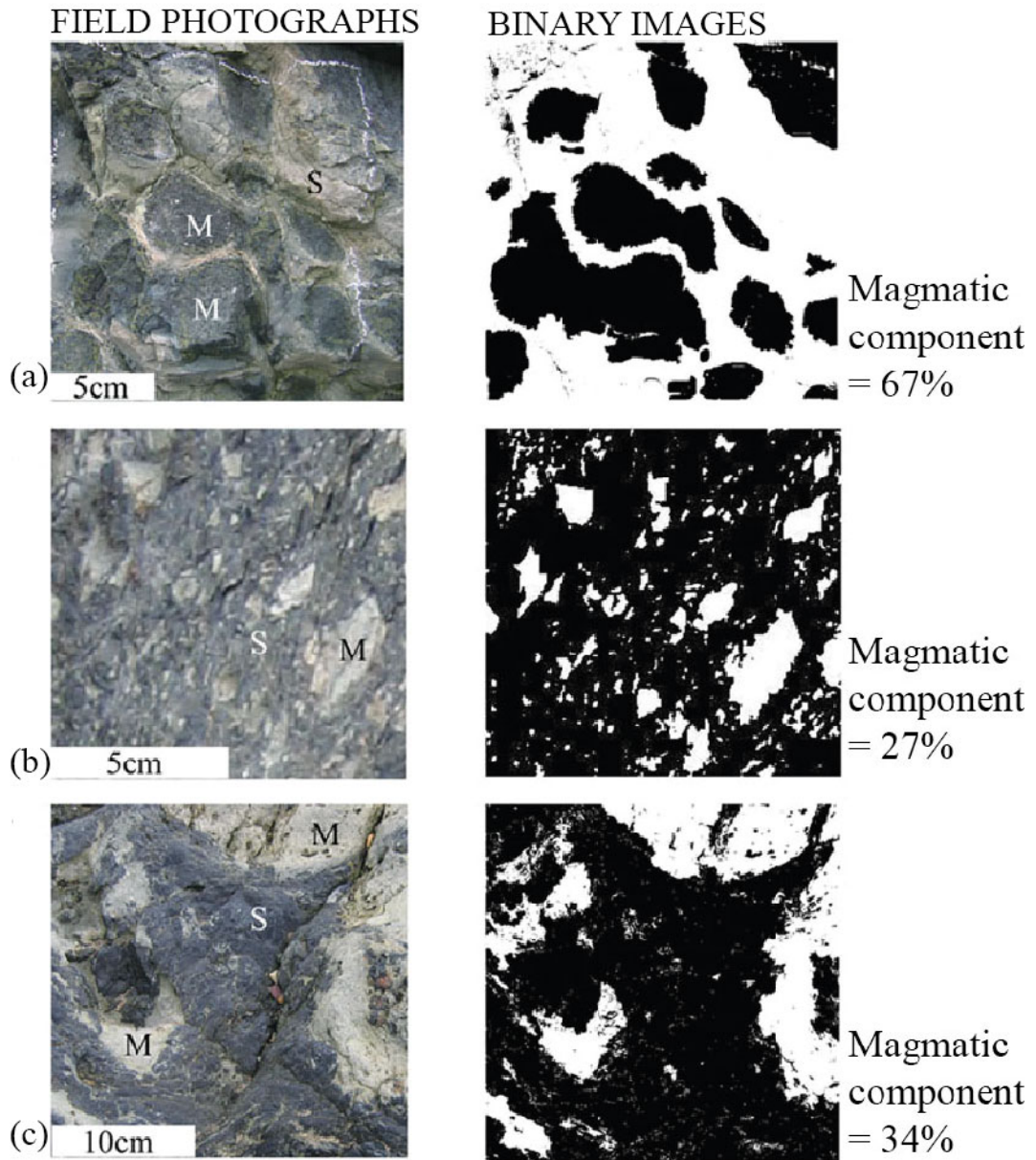


Figure 2.23: Field photographs and corresponding binary images of (a) fluidal peperite, (b) honeycomb peperite and (c) mixed morphology peperite, with the calculated percentage area coverage of the magmatic volume given.

Field relationships of the South Waterford volcanic rocks

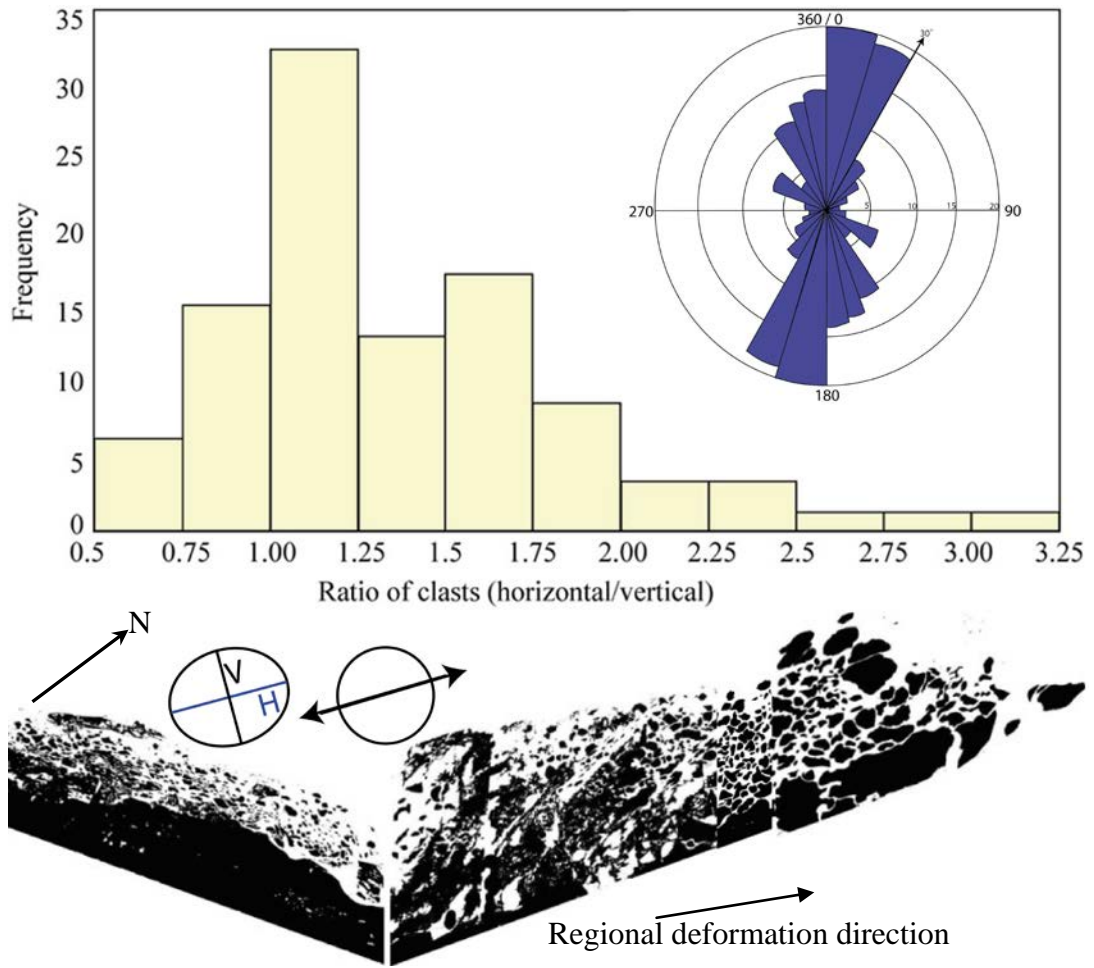


Figure 2.24: Frequency distribution histogram of aspect ratio of clasts in fluidal peperite from Trawnamoe, with inset rose diagram of angle of orientation of clasts from the horizontal reference frame, corresponding to the regional deformation direction of NW-SE. Clast orientation and elongation directions are summarised in the binary image of peperite, with the ellipse showing the degree of elongation in the horizontal (H) compared to the vertical (V) and the arrowed circle showing the dominant degree of clast orientation.

2.9 Discussion

2.9.1 Temporal volcano and volcano-sedimentary associations

Volcanic, volcanoclastic and volcano-sedimentary rocks of the Bunmahon Formation occur in an extensively faulted and folded sequence so that their temporal associations can only be established where volcanic contacts and way up criteria are preserved within individual fault bounded blocks. Draping of lapilli tuff over the surface of pillow lavas at Trawnamoe suggests a conformable sequence with a minimal time lapse between effusive and explosive volcanic behaviour (Figure 2.25). Similarly, grading from the lapilli tuff into the overlying hyaloclastite indicates coeval deposition. The build up of volcanic material resulted in mass flow deposits (e.g. massive tuff, Trawnamoe; agglomerate, Kilmurrin Cove), which prevented the subsequent extrusion of magma and resulted in sill emplacement into the unconsolidated sediment pile (McBirney, 1963) (Figure 2.25). Consequently, irregular sills and thin sheets resulted in peperite formation (Trawnamoe and Stradbally Cove), suggesting that there was a limited time interval between sediment deposition and magmatic intrusion. The range of peperite morphologies, irregular margins and planar contacts of intrusive rocks indicates that the physical nature of the host varied with increasing magmatic intrusion. Thus, the relative sequence of events can be determined, from intrusion into unconsolidated sediment (peperite) to intrusion into poorly consolidated sediment (irregular contacts) and intrusion into lithified sediment (planar contacts). Compaction and subsequent consolidation of the host sediment was facilitated as a result of continued magmatic intrusion (Martin and White, 2002), as pore water was rapidly converted to steam and moved away from the magmatic contact resulting in heat transfer directly to the sediment.

Porphyritic felsic intrusive rocks display faulted relationships with their mafic-intermediate host rocks. The lack of interaction with either water or wet sediment and cataclastite developed along the faulted contact of the porphyry, indicates that the felsic intrusive rocks were emplaced into consolidated rock and later faulted into their current position. Age relationships of felsic intrusive rocks are generally obscured due to faulted contacts, but they cut across andesite and associated sedimentary rocks suggesting that they post-date much of the andesitic activity in the Bunmahon Formation (Stillman, 1971) and are probably related to the Campile Formation phase of volcanic activity (Boland, 1983).

Primary volcanic deposits are preserved in and around the Bunmahon area, with a complete absence of sedimentary rocks suggesting these products were proximal to the central vent (Downes, 1975). In the more distal regions (e.g. Stradbally Cove, Kilmurrin Cove) there is a predominance of reworked and sedimentary deposits that occurred simultaneously with primary volcanic deposits. The change in volcanic facies represents lateral variations across the volcanic pile, with a decreasing volume of magma with increasing distance from the central vent. The greater influence of deep water sedimentation and secondary volcanoclastic deposits suggests deposition on the outer flanks of the volcano (Németh and Martin, 2007). Therefore, the temporally equivalent Bunmahon and Dunabrattin Formations represent proximal and distal volcanic successions of the same volcano respectively (Figure 2.26).

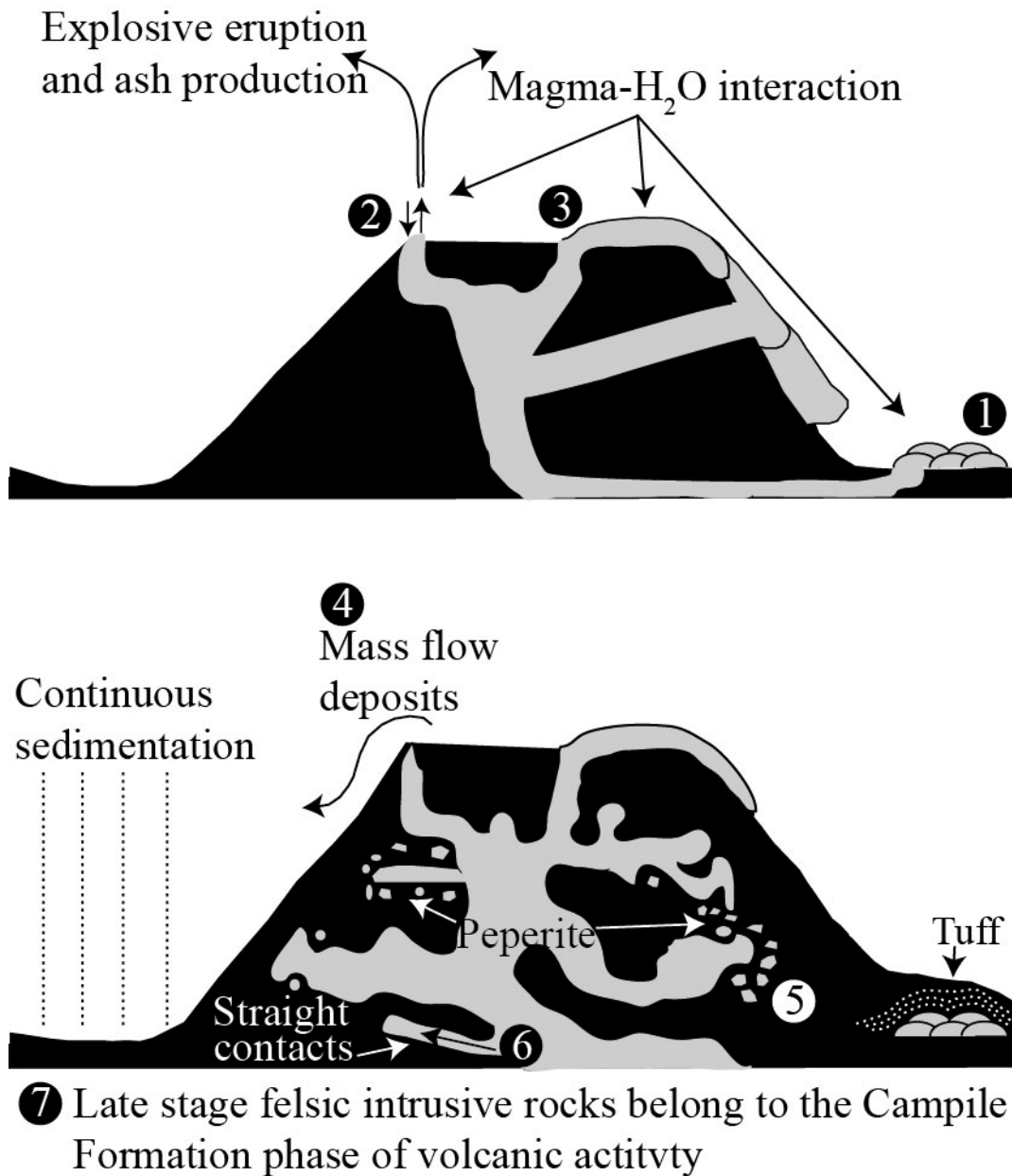


Figure 2.25: Summary of the sequence of events and relative location of types of lithologies with reference to the central vent and flanks of the volcano. Numbers 1-7 represent the order of events.

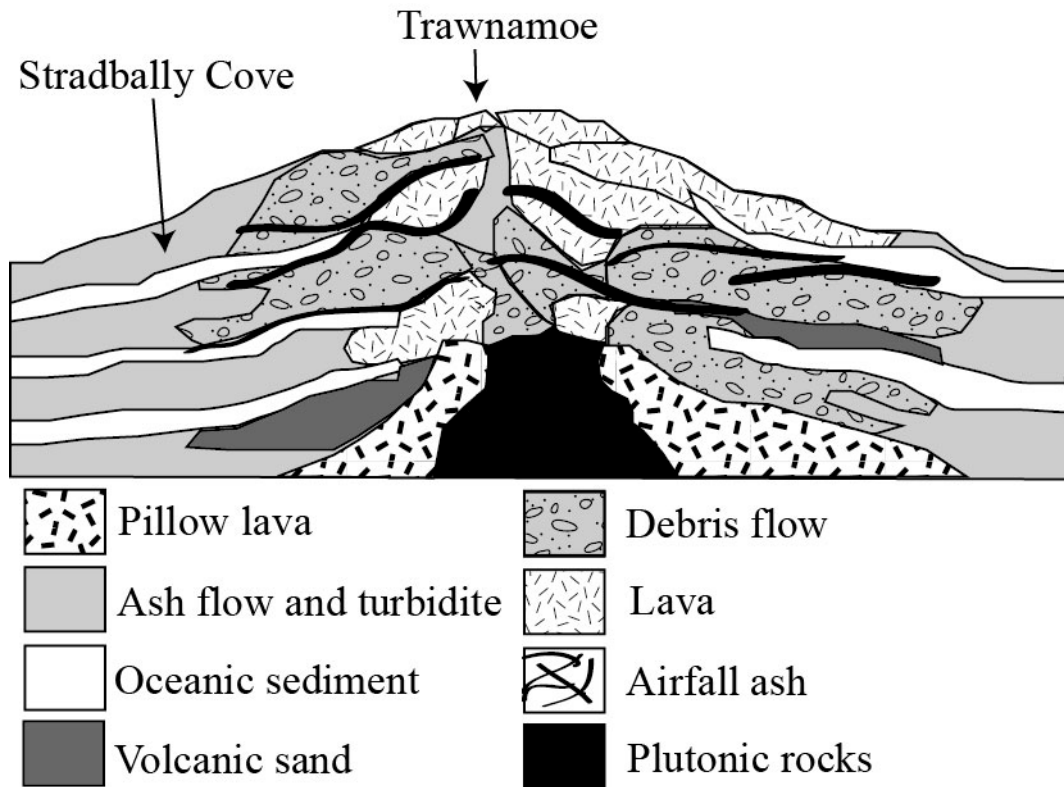


Figure 2.26: Cross-section of typical arc volcano showing the distribution of rock types (modified from Stillman and Sevastopulo, 2005) with relative locations of Trawnamoe (central vent) and Stradbally Cove (flanks of volcano).

2.9.2 Fragmentation processes

Although pillow lavas and hyaloclastite are formed due to interaction between magma and water and as a result are commonly associated with one another (Walker, 1992), pillow lavas in the Bunmahon Formation have only been found in isolation in one outcrop (east Trawnamoe). The size and limited occurrence of these pillow lavas indicates a dramatically lower magma eruption rate than that required for sheet flow formation (Figure 2.27). Thermal contraction of the lava surface resulted in the formation of the outer glassy rim, where cracking of this outer surface occurred as a result of cooling contraction granulation. Individual pillows are sparsely vesicular, with small, spherical vesicles evenly distributed suggesting an initially low dissolved volatile content combined with high confining pressure.

Andesitic sheet flows comprise a large proportion of the Bunmahon volcanic pile and are aurally extensive within the Bunmahon Formation (e.g. Ballydowane Bay, Trawnamoe, Bunmahon and Kilmurrin Cove). Hyaloclastite, occurring as a carapace up to 30cm thick, was formed on the outer margin of the sheet flows upon contact with seawater. Non-explosive fragmentation of the surface magma occurred as a result of cooling contraction granulation (Kokelaar, 1986; Head and Wilson, 2003), while the interior of the lava flow was insulated from direct chilling against seawater and remained coherent (Silvestri, 1963). Irregular interfingering of the coherent inner portions of the sheet flows and the marginal hyaloclastite is common in Ballydowane Bay (e.g. Figure 2.18a), resulting from breaking of the outer solidified crust due to continued movement in the flow interior. As a result of this autobrecciation, it can be inferred that flow or eruption rate of the lava was relatively high, where the magma could expand relatively freely before the crust attained sufficient strength to prevent further growth (Fridleifsson *et al.*, 1982). An increased eruption rate from the earlier pillow lavas resulted in an increase in pillow diameter (Figure 2.27) and as a result the pillows tend to flatten out to form sheet flows (Klingelhöfer *et al.*, 1999). The high eruption rate of these sheet flows accounts for their ability to breach the sediment surface and the large volumes of extruded magma (up to 30m height of successive sheet flows in Trawnamoe). Such rapid eruption rates commonly promote a change from clastic dominated to flow dominated eruptive behaviour (Smith and

Batiza, 1989) and aids in thermal contraction fragmentation and the formation of hyaloclastite (Fouquet *et al.*, 1998).

Where magma did not attain sufficient velocity to breach the sediment surface, probably due to increased confining pressure, the magma invaded and interacted with the unconsolidated sediment pile to form peperite (e.g. fluidal peperite at Trawnamoe and honeycomb peperite and mixed morphology peperite at Stradbally Cove). The fragmentation processes that occurred to produce both hyaloclastite and pillow lavas as a result of magma-water interaction are applicable to the formation of peperite as a result of the similar thermal gradient experienced between intruding magma and wet sediment. Differences in juvenile clast morphology of peperites, from fluidal to angular to wispy, are attributed to differences in the fragmentation mechanism upon contact with the host sediment. Low magmatic volumes (e.g. 27% and 34% in honeycomb peperite and mixed morphology peperite respectively) and a subsequent lower heat capacity of the invading magma, resulted in rapid quenching of the magma surface and the formation of angular clasts, with jigsaw-fit texture representing in-situ fragmentation (e.g. Carr and Jones, 2001). Higher magmatic volumes with a higher heat capacity (e.g. 67% in fluidal peperite) resulted in heat transfer to the host sediment. The increased temperature of the host sediment resulted in a more gradual cooling of the magma surface and the formation of fluidal peperite clasts. Grading from close-packed to dispersed clasts in all peperite types indicates that the clasts were derived from finger-like protrusions originating from the coherent magma that progressively detached and separated within the sediment (Vezzoli *et al.*, 2009). Necking of clasts, clasts attached to the main body of magma with barbed apophyses and wispy tendrils of magma within the sedimentary matrix represents cooling and solidification of the magma while detachment was in progress.

Early and complete fragmentation of magma resulted in the formation of ash particles and produced ash-fall or ash-flow deposits (see section 2.9.1). Only the primary volcanic products (lapilli tuff and bedded tuff at Trawnamoe) can be examined with respect to fragmentation mechanisms because secondary processes may have obscured some of the original features in ash-flow tuffs. Cyclic bedding with normal grading within ash-fall tuff deposits suggests successive eruptions

occurred with deposition through a water column. Both tuff deposits contain volcanic bombs that suggests the tuffs were formed from high energy, explosive events, where the energy required for fragmentation was either the result of magmatic fragmentation or phreatomagmatic fragmentation (Németh and Martin, 2007). There is no evidence (e.g. pumice, scoria, stretched vesicles) to suggest that rapid volatile exsolution occurred to result in magmatic explosivity and therefore phreatomagmatic activity is inferred as the primary mechanism of magma fragmentation. Sub-aerial formation of accretionary lapilli suggests that the eruption intensity was large enough to breach the water surface to produce eruption clouds (White *et al.*, 2003), thus indicating that phreatomagmatic explosions probably occurred within a shallow sub-aqueous setting.

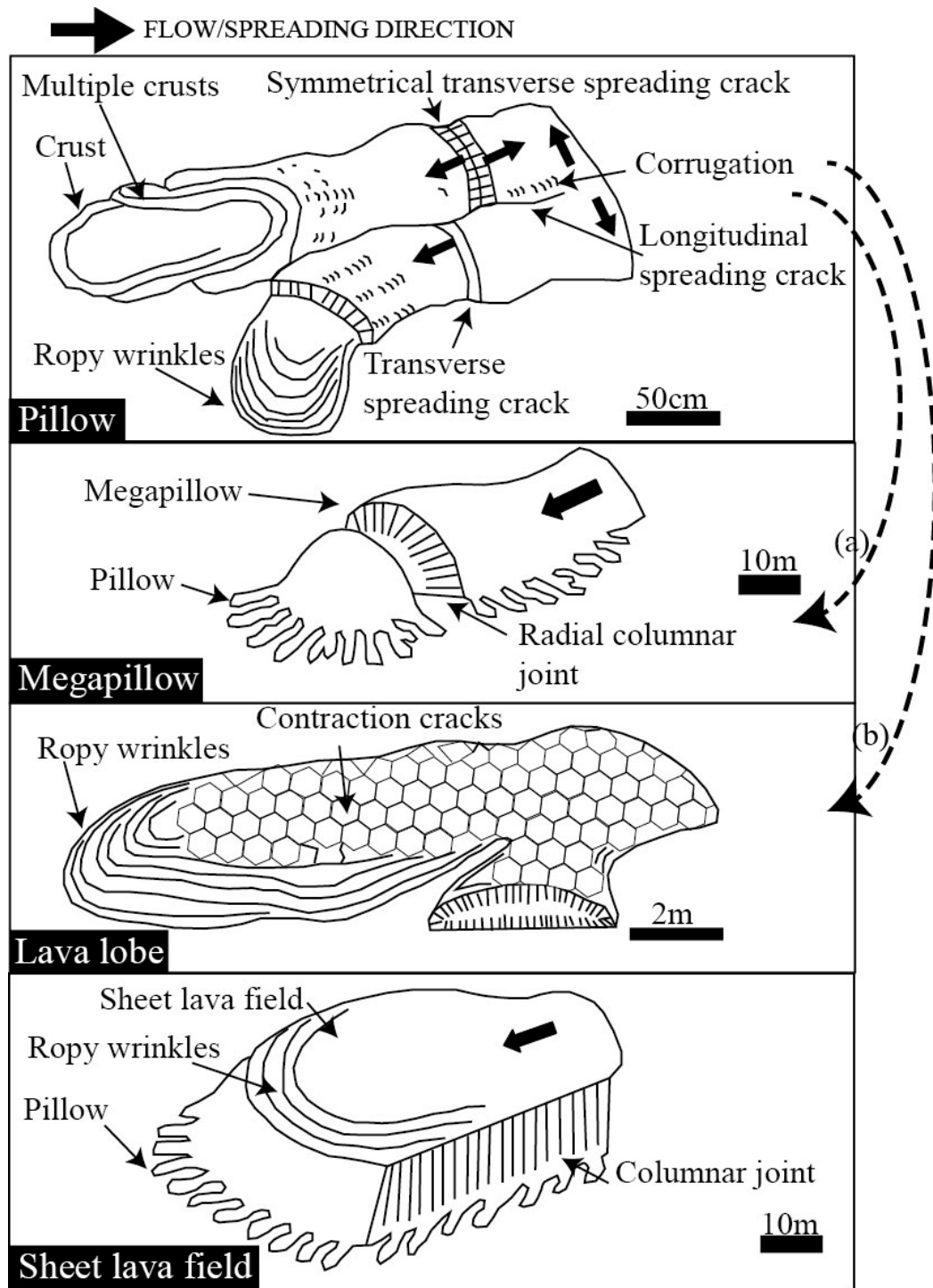


Figure 2.27: Evolution of extrusive products with increasing rate of eruption and an increase in magmatic volume (adapted from Németh and Martin, 2007). Low eruption rates result in pillow lava formation where a progressive increase in eruption rate results in larger pillow lavas (mega-pillows). For more rapid rates of eruption pillow lavas flatten out to form lava lobes and eventually, due to a significant increase in the volume of magma extruded, successive sheet flows form extensive sheet lava fields. No megapillows have been recorded in Waterford, indicating either scenario (a) where these were present and are now eroded away, or scenario (b) these were bypassed and led straight from the formation of pillow lavas to lava lobes.

2.9.3 Effects of magma and sediment properties on juvenile clast morphology

Intrusion of magma into wet, unconsolidated sediment resulted in the disintegration of magma and the formation of peperite, with variation in the juvenile clast morphology due to variation in the properties of magma and/or sediment. Composition of the intruding magma within all peperite examples shows little variation (SiO_2 range = 54.33wt% to 56.89wt%; appendix A3), while grain size of the host sediment remains relatively constant. The primary mechanism by which the properties of either the magmatic or sedimentary component vary is therefore due to the large differences in volumes of intruding magma. Fluidal peperite, (Trawnamoe), comprising rounded to sub-rounded magmatic clasts with highly irregular margins, was formed as a result of intrusion of a much larger volume of magma than that which interacted to form either the honeycomb or mixed morphology peperite. Reconstitution of the host sediment and loss of sedimentary structures in fluidal peperite indicates that sediment fluidisation occurred during peperite formation (Kokelaar, 1982) as a result of heating of the sediment pore water. Sediment fluidisation dramatically decreases sediment viscosity and the result is mixing of two low viscosity components (Figure 2.28). Heating of the water saturated host sediment resulted in conversion of pore water to steam, which formed a vapour film that enveloped separated magmatic clasts. Due to rapid conversion to steam, combined with sediment fluidisation, the vapour films were unstable and continuously oscillating and induced further tearing and fragmentation of the magma. Smaller magmatic volumes were unable to sustain the same level of heat transfer to the host sediment and sediment fluidisation was limited, so that a higher viscosity contrast between the two components was retained. Textures observed at the magma:sediment interface in peperite and at the margins of irregular intrusive rocks are reminiscent of the range of textures produced in experimental simulations of mixing of two liquids of varying viscosities (Perugini and Poli, 2005). A progressive increase in the viscosity contrast resulted in an evolving pattern from spherical magmatic clasts to irregular, elongated magmatic clasts, representing the development of Shaffman-Taylor instabilities between fluids of varying viscosities. The lower viscosity contrast at Trawnamoe (due to sediment fluidisation) promoted the generation of spherical clasts, while a higher viscosity contrast at Stradbally Cove facilitated unsteady and chaotic motion (Koyaguchi, 1987) to produce finger like protrusions and wispy margins.

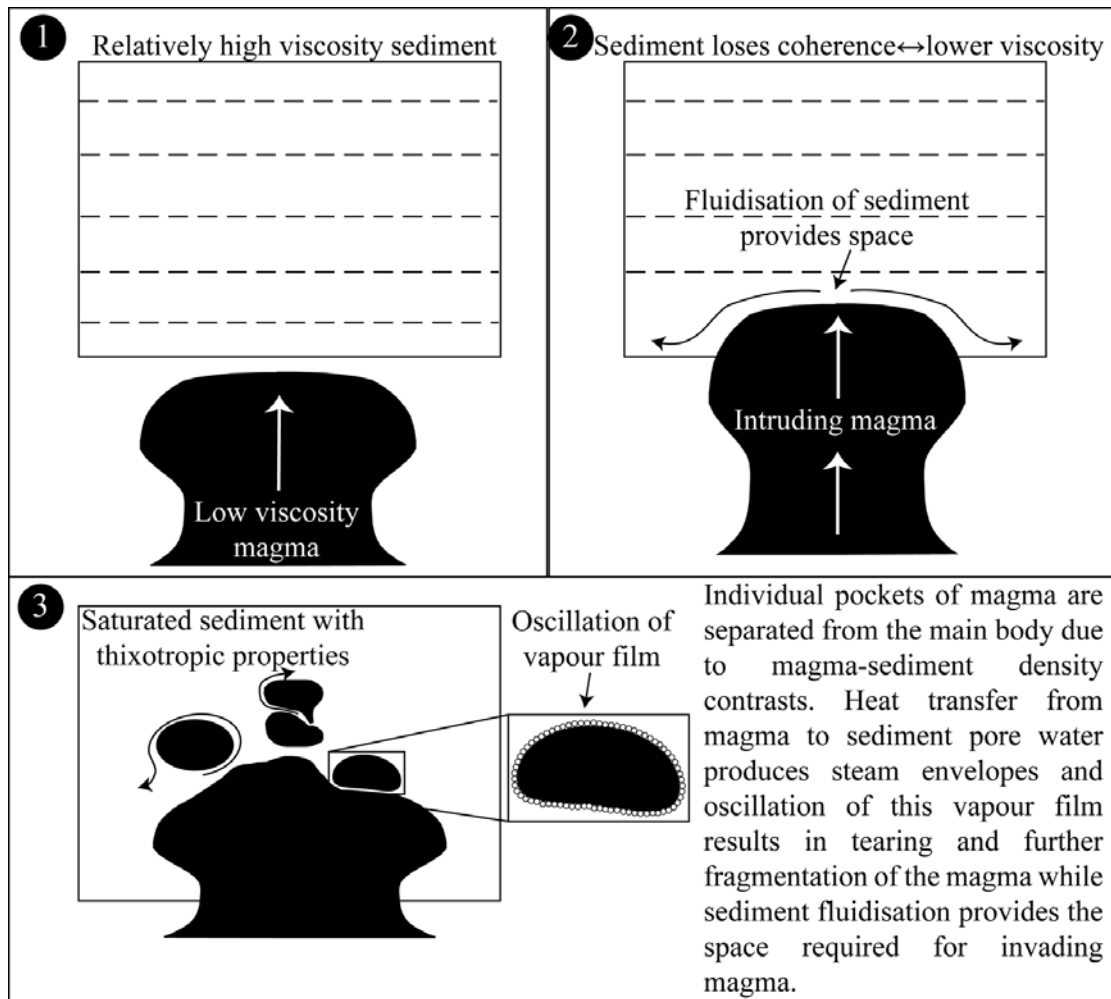


Figure 2.28: Processes involved in the formation of peperite: (1) a low viscosity magma intrudes unconsolidated sediment of higher viscosity, with the magmatic component providing heat energy to the saturated sediment until (2) the sediment begins to fluidise and as a result loses coherence and the viscosity decreases. (3) Oscillation of vapour films and the movement of fluidised sediment results in tearing and fragmentation of the magma. The ability of sediment to fluidise is more pronounced in fine-grained sediment (Bareschino *et al.*, 2007; Cagnoli and Romano, 2010), indicating fluidisation is a likely mechanism for the provision of space in peperite formed from tuff and mudstone. Upon cooling the separated blobs of magma solidify to form peperite clasts, and with the heat transfer from magma to sediment cut off, the host sediment again increases in viscosity.

2.9.4 Mineralisation

Vein mineralisation occurs as sulphide-bearing, sheeted vein systems and planar, barren veins at both Trawnamoe and Stradbally Cove. The sheeted vein systems contain fragments of brecciated host rock (Trawnamoe) or have lenses of host rock incorporated into the vein system (Stradbally Cove). Fluid infiltration and heat loss to the host rocks resulted in intense wall rock alteration of the host lava sheet flows/hyaloclastite adjacent to the sheeted vein systems at Trawnamoe. The efficient circulation and heat loss of the fluid resulting in such intense wall rock alteration was probably the result of the high permeability of the host rock, as fluid circulation rate increases proportionally with permeability (Cathles, 1977). Fragments of the brecciated host rock incorporated into the vein system are highly angular, indicating that some degree of lithification of the host had taken place prior to vein formation. Therefore, the sheeted vein system at Trawnamoe was probably formed post-lithification but the mineralisation event is classed as early epigenetic. The lenses of host rock incorporated into the sheeted vein system at Stradbally Cove are evidence that the host rock behaved as a ductile material during vein formation (Figure 2.21a). The deformation of these lenses may have occurred as a result of disaggregation of the lithified host rock. Disaggregation indicates that the host siltstone and fine sandstone was broken along individual grain boundaries and that the degree of cementation was probably 'patchy', which is commonly the case during early stages of lithification (Parnell and Kelly, 2003). Therefore, vein formation was subsequent to the consolidation of the sediments, probably early epigenetic, similar to the sheeted vein systems at Trawnamoe. Structurally controlled planar veins from both localities, not associated with alteration, are probably of a later stage than the sulphide-bearing sheeted vein systems. Such planar veins represent classic epigenetic mineralisation (Wilkinson *et al.*, 2003).

2.10 Conclusions

The main features of the volcanic and intercalated sedimentary rocks suggest that:

- The range of mafic-intermediate intrusive rocks, lavas and tuff deposits had a bimodal eruption style.
- The formation of sheet flows, pillow lavas etc. all occur as a result of similar fragmentation processes, where the main difference resulting in different lithologies is the eruption rate.
- Early lithologies show evidence of either interaction with water (pillow lavas, hyaloclastite) or sediment (peperite).
- The volume of magma intruded into the wet sediments resulted in extensive alteration of the magmatic component, while heating of the sediment pore waters resulted in sediment fluidisation and silicification of the sediment.
- Various levels of interaction between intrusive rocks and the surrounding host sediment (Figure 2.29) represent a time-line of volcanic activity, where magmas were continually emplaced during consolidation or lithification of the host sediment, and the heat generated from these probably contributed to more rapid consolidation of the host.
- Lateral variation across the volcanic sequence is a result of deposition in proximal or distal regions. Primary volcanic and sedimentary deposits are contemporaneous with secondary volcanoclastic deposits and these are commonly inter-bedded or inter-fingered with one another.
- Late stage felsic magmas (Campile Formation) were probably intruded into the now consolidated upper part of the Bunmahon Formation and were later faulted downwards to the same level as the sheet flows and shallow intrusive rocks.

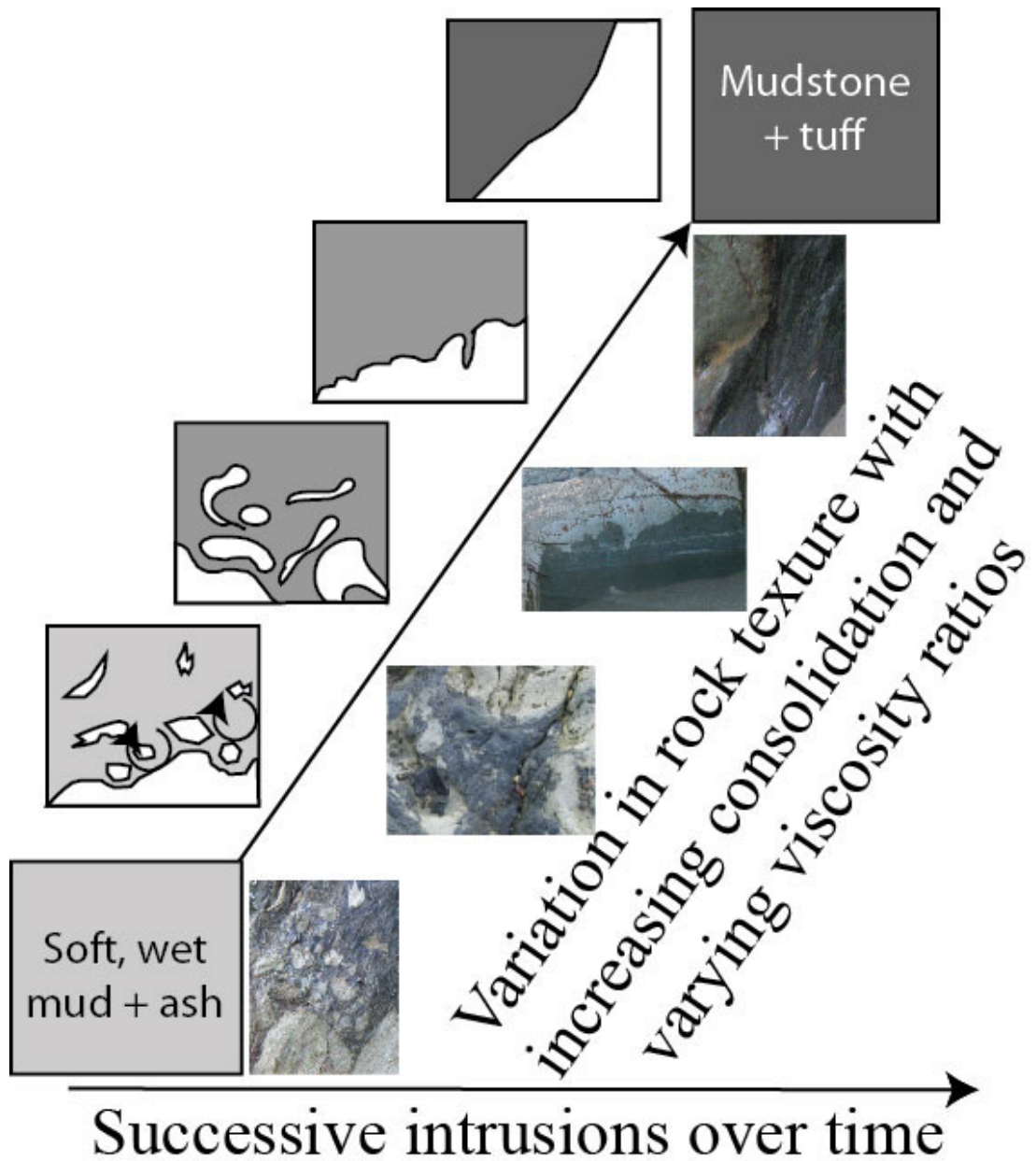


Figure 2.29: Summary of main factors controlling the type of intrusive contact as a result of increasing consolidation of the host sediment sequence through time.

Chapter Three:

Petrography of the major volcanic and sedimentary lithologies in south County Waterford

3.1 Introduction

Petrographic descriptions of the main volcanic and sedimentary lithologies of south Waterford were carried out to determine both the primary, and the subsequent alteration, mineral assemblages. The composition of the dominant alteration minerals were then used to constrain the cause and extent of alteration.

3.2 Petrography of major rock types in Trawnamoe

3.2.1 Tuff units

The lapilli tuff is composed of graded coarse and fine-grained beds with planar contacts. The fine-grained groundmass is heavily altered, and comprises devitrified glass and chlorite, with angular to sub-rounded crystals of quartz and K-feldspar (Figure 3.1a). Spherical or oval accretionary lapilli and ash pellets occur in one layer and consist of an unstructured ash core with rare concentric laminations comprising the outer margin. Accessory lithic lapilli (up to 4mm) are extensively replaced and contain crystals completely altered to chlorite. Smaller lithic fragments (~2mm) are composed of acicular plagioclase crystals.

The crystal tuff located at X 42690 981812 consists of alternating coarse, medium and fine-grained layers that show normal grading, with an abrupt contact between the top fine layer and the overlying coarse-grained layer. The crystals embedded in the matrix of the tuff are predominantly feldspar and quartz, with a size range of 0.1-2.5mm. The fine layers of the crystal tuff consist of an aphanitic groundmass with a felsitic texture. Approximately 30% of the groundmass of the tuff is altered to chlorite, and contains individual larger crystals of K-feldspar. The coarser layers consist of a much darker matrix with larger grains of feldspars and quartz, with chlorite occurring as pseudomorphs or in veins. Quartz grains are sub-rounded and unaltered, with a small proportion showing crystal embayments (Figure 3.1b). Where crystals are elongated the long axis is aligned parallel to bedding. The bedded tuff grades upwards to a massive tuff, extending upward for 20m. (Due to the height of the exposure, individual tuff deposits, if

present within the massive tuff, cannot be readily identified). The massive tuff deposit contains epidote pseudomorphs of pyroxene crystals (up to 2mm), chlorite pseudomorphs and rare feldspar crystals within a dark fine-grained matrix, similar to the coarse-grained layers in the bedded tuff.

3.2.2 Mafic-intermediate intrusive rocks

The large intrusive rock at the western end of the cove (X 42665 98119), the sill at X 42687 98155 and magmatic clasts of the associated overlying peperite are all of a similar composition. The coherent intrusive rocks consist of a microcrystalline groundmass containing microphenocrysts of K-feldspar (1mm) and plagioclase feldspar, with smaller quartz crystals displaying undulose and polygonal extinction. Minor epidote is present in glomeroporphyritic clusters, with individual crystals up to 0.3mm. Clasts within the peperite are composed of a microcrystalline groundmass containing phenocrysts of rounded to sub-rounded feldspar, lath shaped plagioclase and clusters of epidote. Finely crystalline masses of epidote are commonly developed close to clast contacts and disseminated iron oxides occur throughout.

Within both the coherent intrusive rock and the sill underlying peperite, alteration has affected the majority of larger crystals, and secondary veinlets of calcite occur throughout the groundmass. While chlorite alteration is pervasive within the sill, alteration is much more extensive within peperite clasts of the same composition (Figure 3.2a). Chlorite occurs with both a ropy or wavy texture and is commonly zoned (Figure 3.2b). Inclusions of quartz are common within the chlorite alteration indicating that free silica was produced during the alteration reaction to form chlorite. Glomeroporphyritic crystals of epidote pseudomorph original clinopyroxene. Chlorite and epidote are better developed at the margins of peperite clasts, occurring within the glassy components of the chilled margins. Occasional large calcite crystals contain inclusions of feldspar. Similar textures and mineralogies observed within the sill and peperite clasts are summarised in Table 3.1.

Petrography of the major volcanic and sedimentary lithologies in south County Waterford

	SILL	PEPERITE CLASTS
Groundmass	Plagioclase + K-feldspar	Plagioclase + K-feldspar
Microphenocryst assemblage	Plagioclase	Plagioclase
Secondary mineral (chlorite, epidote and rare pumpellyite) distribution	Preferentially associated with larger phenocrysts. Pseudomorphs of clinopyroxene	Pervasive

Table 3.1: Differences observed between the mineral assemblages of the intruding sill and magmatic clasts of the same lithology in peperite. No interaction with sediment has occurred within the coherent sill, while the peperite clasts have undergone mingling with wet sediment and were quenched as a result of this interaction.

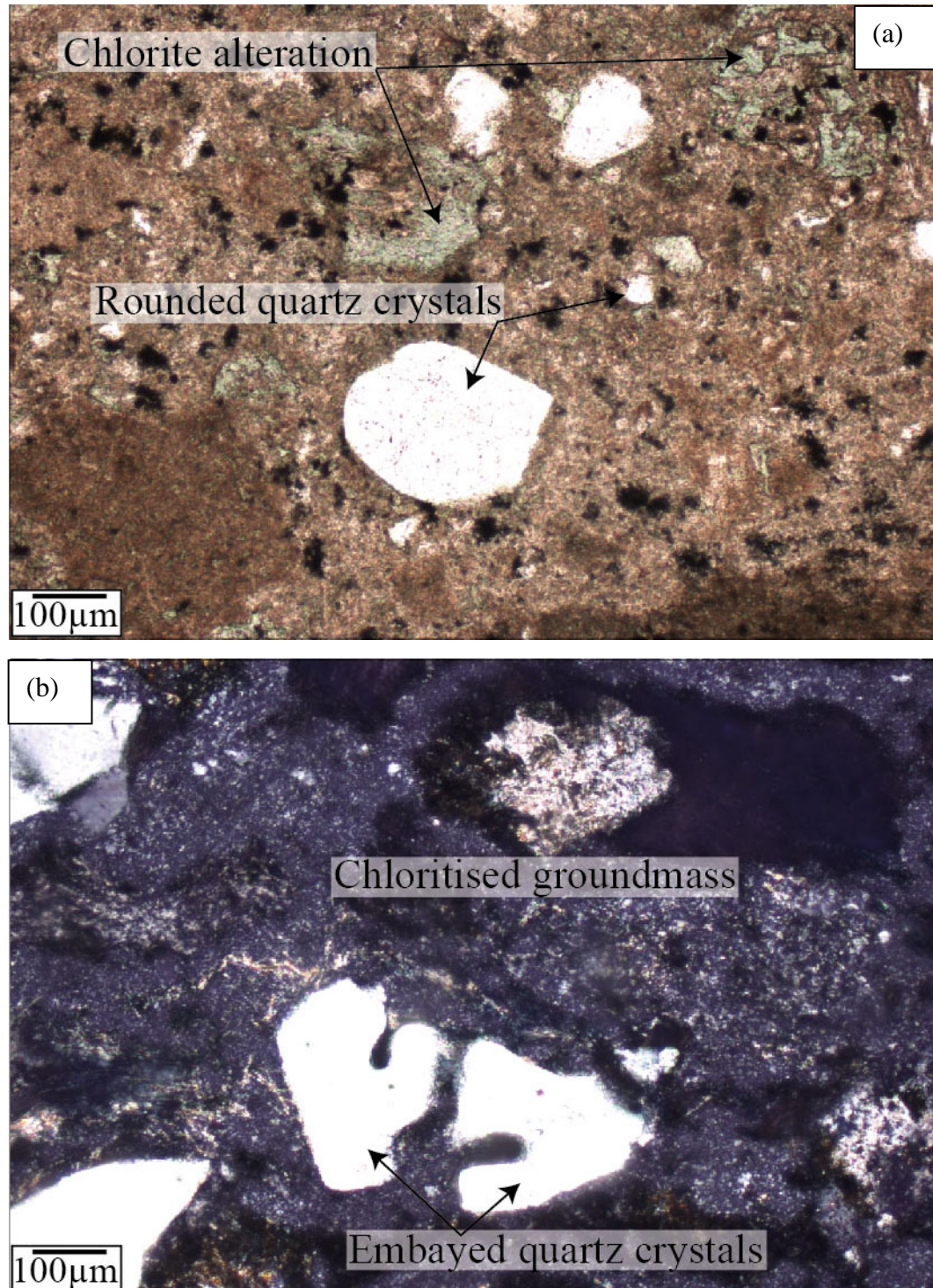


Figure 3.1: Photomicrographs of tuff deposits from Trawnamoe: (a) typical lapilli tuff (sample T8) with sub-rounded to rounded quartz crystals and chlorite alteration in a fine-grained groundmass (PPL) and (b) typical texture of the laminated tuff (sample T9), with a feldspar rich microcrystalline groundmass and embayed quartz crystals (XPL).

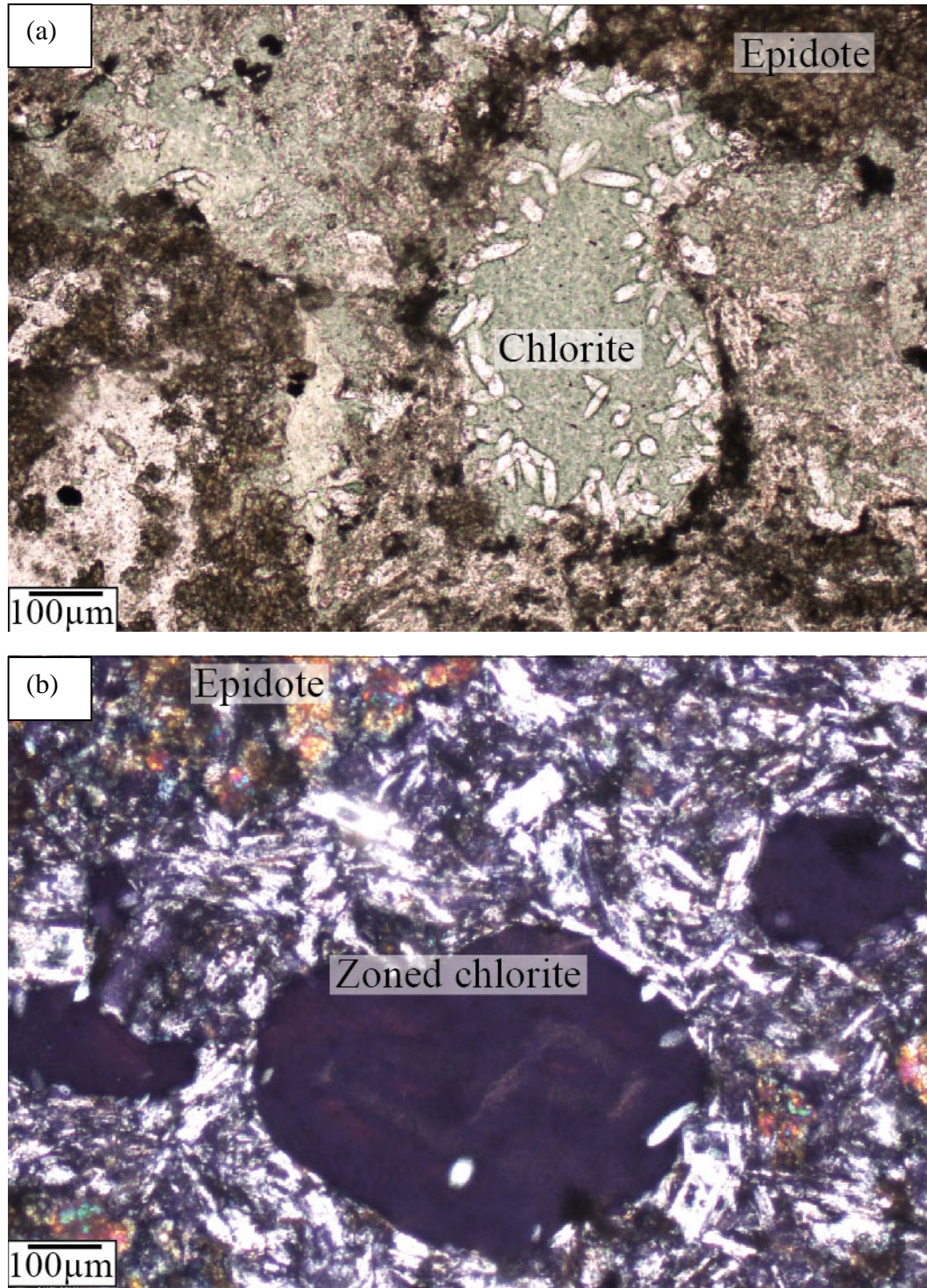


Figure 3.2: Photomicrographs of the typical texture within mafic-intermediate intrusive rocks with (a) the main alteration minerals including chlorite and epidote (sample T15) (PPL), where (b) chlorite is commonly zoned and is hosted within a fine-grained groundmass composed predominantly of plagioclase feldspars (sample T2) (XPL).

3.2.3 Lava flows

The sheet flow within the lava/hyaloclastite volcanic unit contains a microphenocryst assemblage dominated by plagioclase laths (0.35-0.4mm), with less common alkali feldspars. Chlorite, epidote, minor sericite and a high proportion of smaller sized opaque minerals are also present in the microcrystalline groundmass (Figure 3.3a). All phenocrysts are heavily altered to chlorite. The hyaloclastite of the same unit (although similar in composition and texture to the lava) is visibly more altered, with a higher proportion of epidote and chlorite within a fine-grained groundmass composed of devitrified glass (Figure 3.3b).

3.2.4 Felsic intrusive rocks

The quartz-feldspar porphyry (X 42752 98188) is composed of approximately equal volumes of quartz and feldspar. Granophyric texture is commonly developed throughout the porphyry (Figure 3.4a), indicating simultaneous crystallisation of quartz and feldspar. Phenocrysts comprise large euhedral crystals of alkali feldspar and plagioclase feldspar, approximately 0.5 to 1.5mm in size. Some of the larger crystals of feldspar contain inclusions of sericite and epidote (Figure 3.4b). Minor amounts of chlorite alteration and thin quartz veins occur throughout.

The dacite, at X 42778 98179, has a mineral assemblage dominated by feldspars. The groundmass is composed of alkali feldspars with minor quartz, containing crystals of secondary chlorite (up to 0.4mm). Acicular plagioclase crystals are up to 0.5mm long.

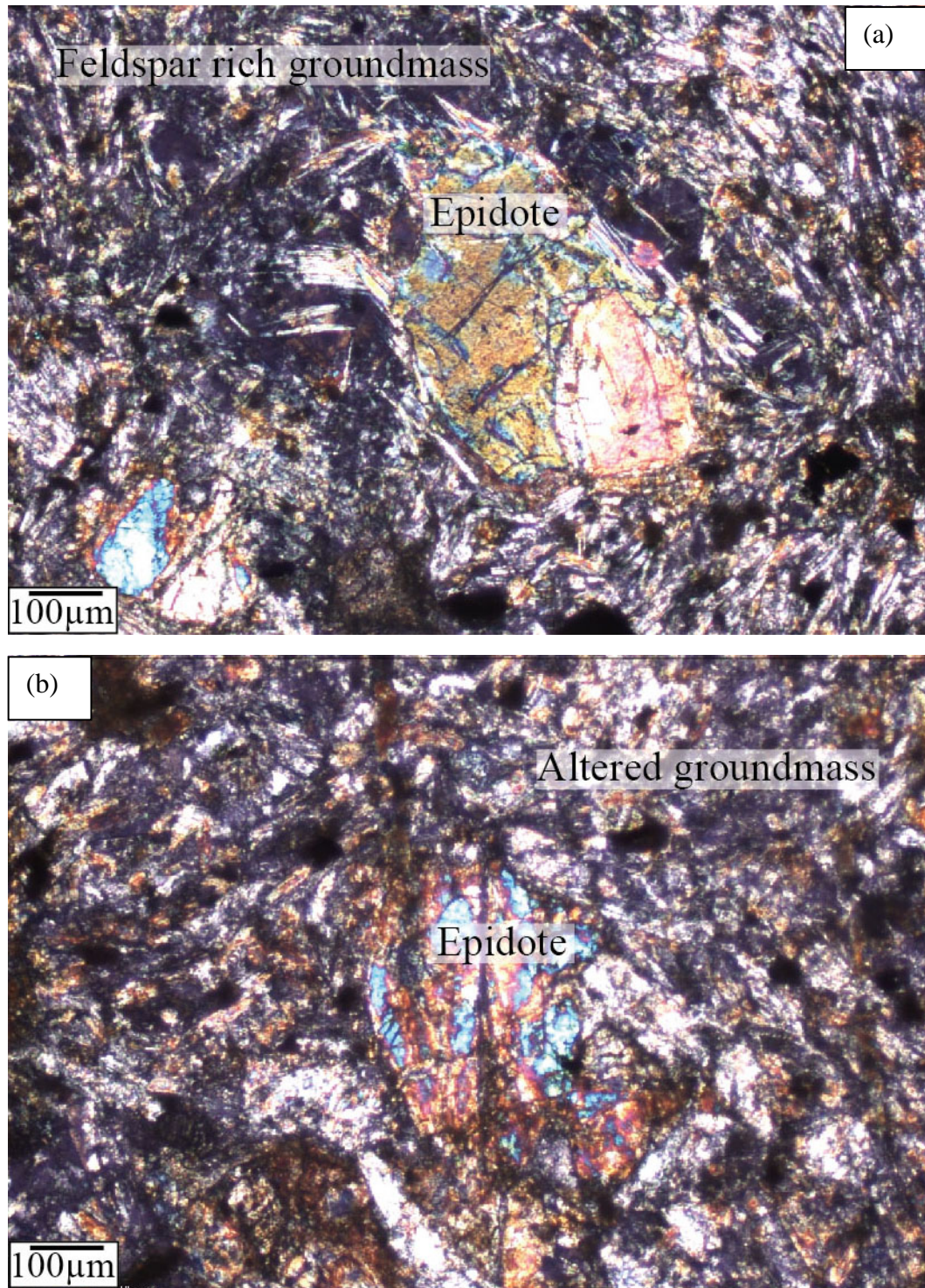


Figure 3.3 Photomicrographs of the sheet flow-hyaloclastite lithology with (a) phenocrysts of epidote hosted within a fine-grained feldspar rich groundmass in the coherent sheet flow (sample T3) (XPL) and (b) similar epidote crystals within the more altered groundmass of the hyaloclastite (sample T1) (XPL).

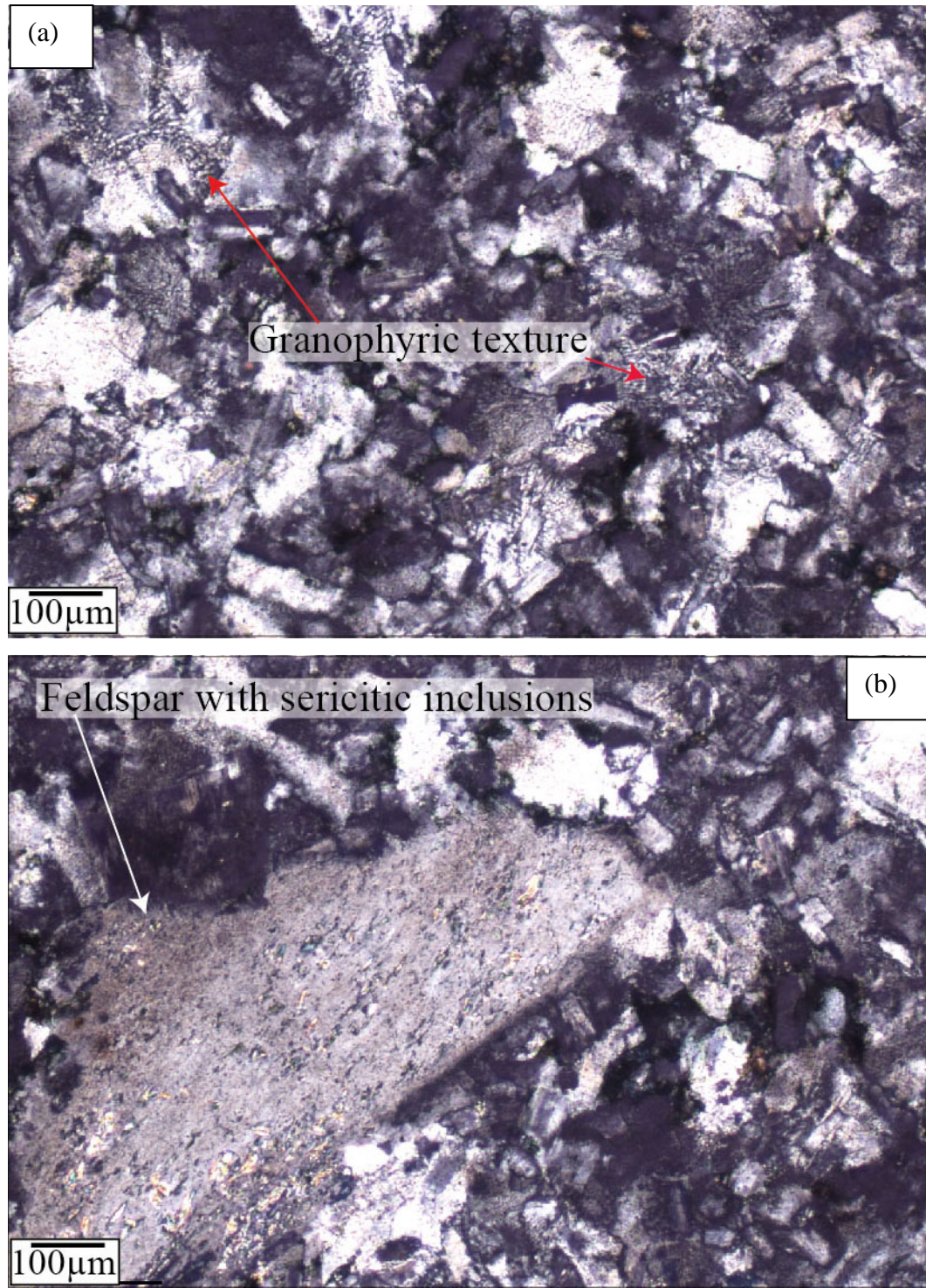


Figure 3.4: Photomicrographs of the quartz feldspar porphyry (sample T6) at X 42752 98188 containing (a) granophyric texture (XPL) and (b) altered alkali feldspars hosting inclusions of sericite within a groundmass of quartz and feldspar (XPL).

3.3 Petrography of major rock types in Stradbally Cove

3.3.1 Sedimentary rocks

The siltstone (X 36879 96761) consists of alternating light and dark layers, with a mineral assemblage dominated by quartz and feldspar with minor sericite. Cubic pyrite crystals (100µm) are developed along planes or laminations while smaller anhedral pyrite crystals (~10µm) are disseminated throughout the rock (Figure 3.5a).

All mudstones are dominated by quartz and feldspar, but petrographic differences include randomly orientated veinlets of oxidised iron within the honeycomb textured mudstone, compared to iron oxides disseminated throughout the competent mudstone. Sericite is aligned along cleavage planes within the honeycomb textures mudstone. Clasts (50-100µm) comprising fine-grained quartz and feldspar are recorded within the fissile mudstone associated with minor disturbance of underlying laminations. The competent, pyrite-rich mudstone (X 36975 69420) contains plagioclase feldspar and interconnected, tendrils of elongated muscovite crystals, which define cleavage planes. Cubic crystals (up to 2mm) of haematite and pyrite are disseminated throughout the rock, with the majority of iron oxides and pyrite crystals associated with chlorite alteration and/or minor quartz veining (Figure 3.5b).

The pyrite tuff (X 36962 96904) consists of a fine-grained, feldspar-rich groundmass, which is dominantly altered to chlorite, and contains crystals of K-feldspar (100µm) and plagioclase feldspar (1mm), which hosts sericite inclusions. Cubic pyrite crystals occur in clusters with haloes of oxidised iron. The coarse-grained and fine-grained pyrite tuffs have essentially the same mineral composition.

The lithic tuff (X 36896 96779) consists of a fine-grained matrix, dominated by quartz and feldspar, with isolated lithic fragments up to 2cm. The lithic fragments are fine to medium-grained and are composed of quartz, alkali feldspar and minor muscovite, similar to the siltstone (Figure 2.14d). Rare spherulites, formed by devitrification of glassy components of the tuff, are developed close to the contact with an overlying intrusive rock.

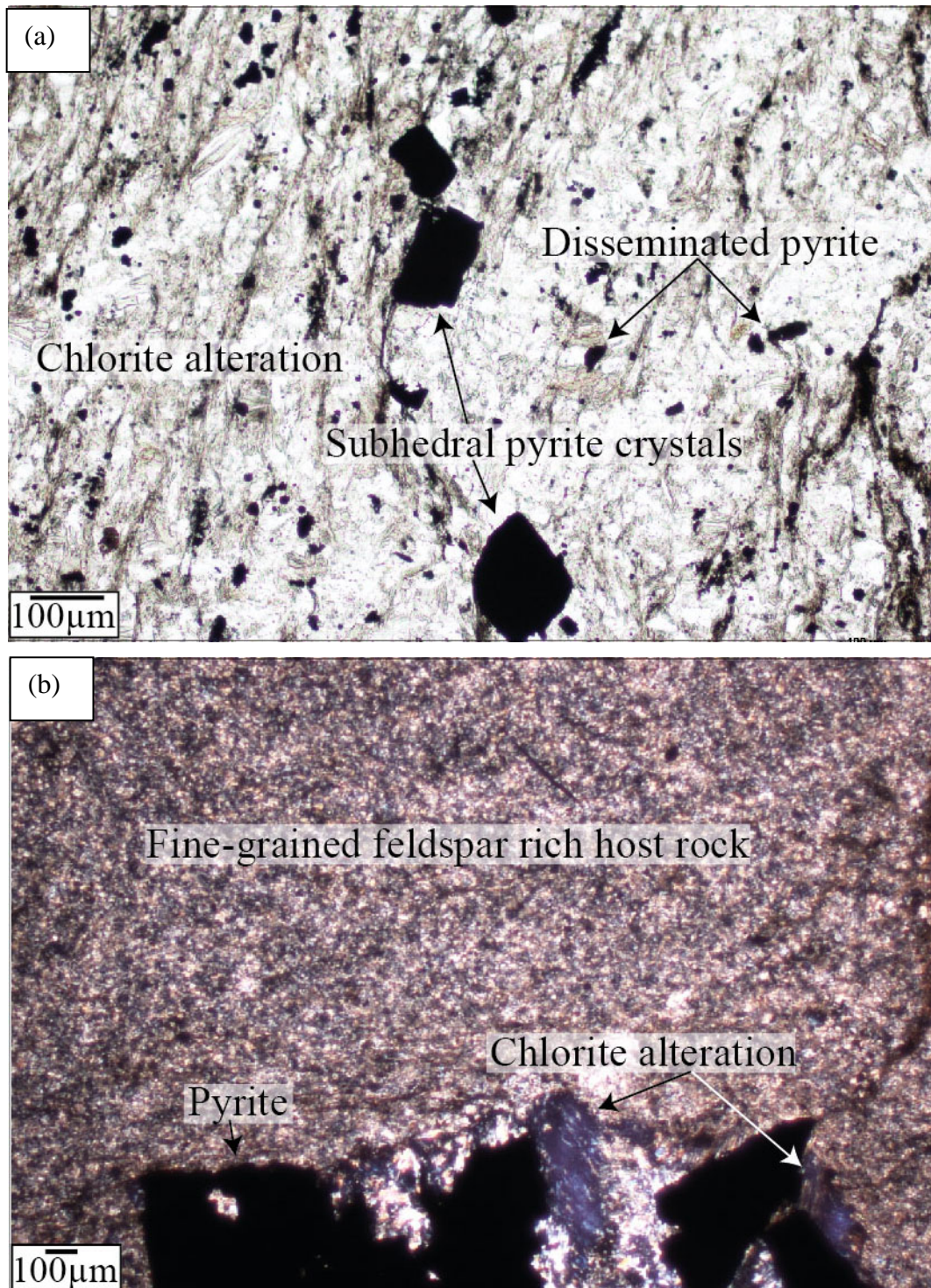


Figure 3.5: Photomicrographs of fine-grained sedimentary rocks including (a) siltstone with disseminated pyrite (sample S26) (PPL) and (b) feldspar rich mudstone containing subhedral pyrite crystals and associated chlorite alteration (sample S4) (XPL).

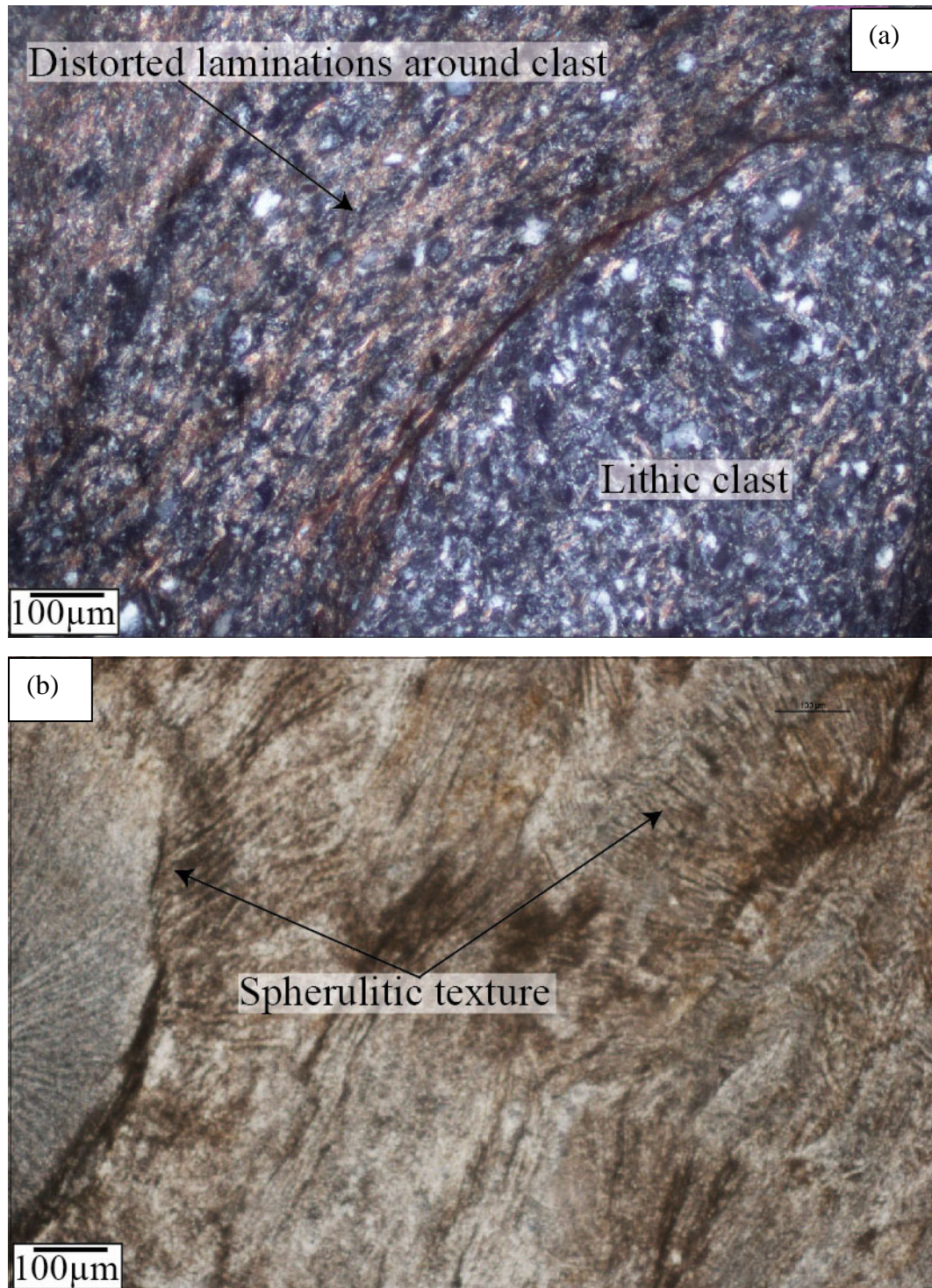


Figure 3.6: Photomicrographs of lithic tuff (sample S9 and S14) from Stradbally Cove with (a) laminations within the fine-grained groundmass deformed around lithic clasts (XPL) and (b) spherulites of radiating quartz and K-feldspar developed within devitrified glass at the margin of the tuff (PPL).

3.3.2 Mafic-intermediate intrusive rocks

Abundant thin sheets of porphyritic intrusive rocks (e.g. X 37019 96964, X 37110 96903 and X 37005 96956) all have similar mineral assemblages comprising microphenocrysts of plagioclase and alkali feldspar, pyroxene and minor sericite within a fine-grained to microcrystalline groundmass (Figure 3.7a). Clasts of magmatic material trapped in the sedimentary host during peperite formation, although more extensively altered, are similar in composition, consisting predominantly of plagioclase feldspar within a microcrystalline groundmass.

Coarse-grained intrusive rocks have a mineral assemblage dominated by plagioclase feldspar (0.5-1mm), alkali feldspar and clinopyroxene within a microcrystalline groundmass of feldspar and minor sericite. Extensive chlorite alteration occurs within the groundmass and phenocrysts of ferromagnesian minerals, while alteration to epidote only occurs within larger phenocrysts of pyroxene (Figure 3.7b). Sericite often occurs as inclusions within larger feldspar phenocrysts.

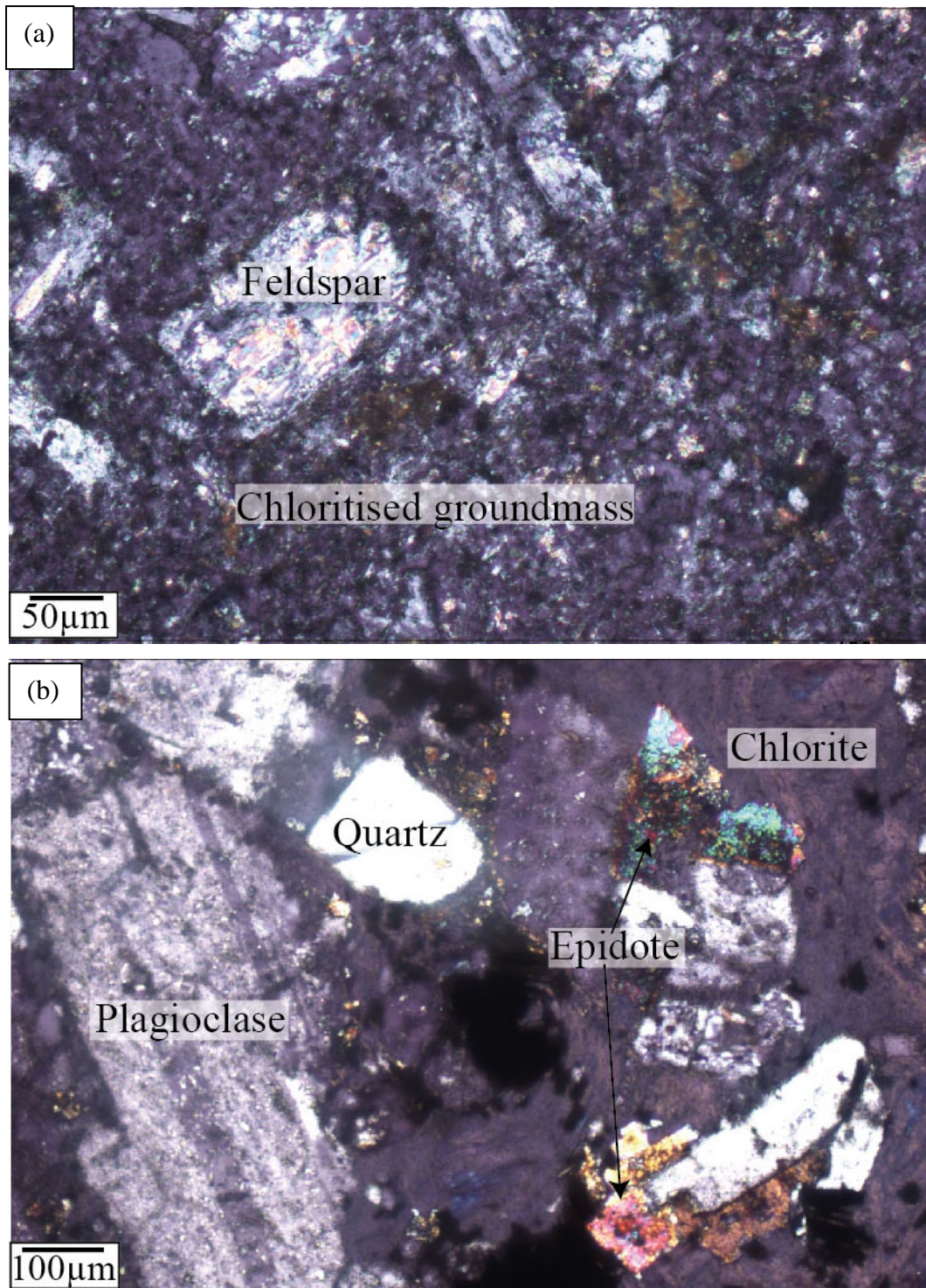


Figure 3.7: Photomicrographs of mafic-intermediate rocks of Stradbally Cove ranging from (a) porphyritic intrusive rocks containing phenocrysts of alkali feldspar within a chloritised groundmass (sample S23) (XPL) to (b) coarse grained intrusive rocks comprising phenocrysts of quartz, alkali feldspar, plagioclase and epidote within a fine-grained groundmass of quartz and feldspar with extensive chlorite alteration (sample S6) (XPL).

3.4 Discussion

The majority of volcanic rocks from Trawnamoe and Stradbally Cove are porphyritic, mafic-intermediate sub-volcanic or extrusive in origin with a primary mineral assemblage of plagioclase feldspar, clinopyroxene, alkali feldspars and quartz. Late stage felsic intrusive rocks consist almost entirely of plagioclase, alkali feldspars and quartz. Boland (1983) described the volcanic units of the Bunmahon Formation in detail and observed that the primary mineral assemblage of feldspar, pyroxene and quartz is dominant within all mafic-intermediate composition volcanic rocks, which comprise approximately 50% of the surface bedrock in Waterford (Stillman and Williams, 1979). The intercalated volcanoclastic and volcano-sedimentary rocks are of a similar composition to the intruded volcanic rocks, with some of the coarser grained units containing clasts of volcanic material. Purely sedimentary rocks (e.g. siltstone and mudstone, Stradbally Cove) are very iron-rich and commonly contain volcanic clasts suggesting a significant volcanic input or influence during deposition. The epiclastic content of sedimentary rocks and lateral facies changes from tuffs to sedimentary deposits, such as those at Stradbally Cove, are attributed to reworking of volcanic material (e.g. Swennan, 1984). Thus, intrusive and extrusive volcanic rocks and intercalated sedimentary rocks are all derived from the same original source.

The lithologies examined have all been subject to extensive alteration, resulting in a mineral assemblage of chlorite, epidote, sericite and albite, characteristic of spillitisation (Cann, 1969). This alteration mineral assemblage corresponds to that observed by Boland (1983) (albite and chlorite, with associated epidote and calcite) throughout the entire volcanic sequence. The term spillite is therefore applied to the volcanic rocks of Trawnamoe and Stradbally Cove, where the mineral assemblage is interpreted to result from seawater-basalt interactions during diagenesis on or near the seafloor (Gifkins *et al.*, 2005). Shannon (1979) recorded a similar mineral assemblage of chlorite, albite and calcite in the volcanic rocks in County Wexford, where alteration in the entire southeastern volcanic belt appears to have been the result of syn- or immediately post-emplacement submarine weathering and hydrothermal metasomatism (Stillman and Williams, 1979). Hydrous alteration minerals are most extensively developed within the vitreous components of volcanic rocks as a result of preferential

degradation of glass, either associated with syn-emplacement quenching or post-emplacement diagenesis. Although disseminated pyrite is a common constituent within many of the volcanic and sedimentary lithologies, larger clusters or nodules of pyrite are formed from secondary processes, with associated chlorite alteration haloes and adjacent quartz veining indicative of fluid flow. The formation of secondary pyrite in association with albite, epidote, chlorite and calcite is consistent with propylitization, where late stage alteration is a result of altering fluids derived from either later intrusive bodies or vein forming solutions (Coats, 1940). Therefore, the range and combination of alteration minerals is indicative of both early stage metasomatism and later stage hydrothermal alteration or metamorphism. Crystallinity studies of regionally developed chlorite and white mica indicates that formation of such minerals is attributed to both contemporaneous shallow level intrusions and later tectonic deformation (Diskin, 1997).

3.5 Conclusions

Sub-marine volcanic activity resulted in the development of a volcanic pile comprising a range of lithologies including shallow level intrusive and extrusive mafic-intermediate volcanic rocks, primary and reworked tuff deposits and sedimentary rocks. Alteration to spillites or propylites is dominant within the volcanic rocks. The extent of alteration is greater for those lithologies that have a greater glass component, either as a result of the readiness at which glass alters, or as a result of the increased interaction of that magma with external water. Two main phases of alteration are recorded: syn-volcanic metasomatism and later metamorphism; however the relative timing of these events cannot always be discerned.

Chapter Four

Bulk Rock and Mineral Geochemistry

4.1 Introduction

Published geochemical analysis has shown that both the northern and southeastern volcanic belts of Ireland were generated as a result of island arc volcanism on the margins of a continental plate above a southeasterly dipping subduction zone (Stillman *et al.*, 1974; Downes, 1975; Stillman and Williams, 1979; McConnell, 1987). The majority of the northern belt is dominated by tholeiitic basalts and andesites, while calc-alkaline rhyolites were the main eruption product of the southeastern belt, indicating that the northern belt represents the outer immature arc and the southeastern belt represents the inner mature arc (Stillman and Williams, 1979). The volcanic rocks exposed in Waterford comprise approximately equal proportions of mafic-intermediate and felsic rocks with a calc-alkaline (approaching shoshonitic) signature that resulted from formation in a mature continental arc (Stillman and Williams, 1979). Although various models are proposed for each specific area (e.g. Lake District; Branney and Soper, 1988), the orientation of the Iapetus suture (Phillips *et al.*, 1976), the general NE-SW trend of all associated Ordovician terranes and the geochemical variation between the northern and southeastern volcanic belts suggests that the southeastward subduction of oceanic lithosphere (Fitton *et al.*, 1982) is probably the most plausible explanation to account for both the preserved volcanic rocks and their structural relationships (Kokelaar, 1988).

Previous published analyses of bulk rock geochemistry were predominantly used to discriminate tectonic setting (e.g. Downes, 1975; Stillman and Williams, 1979). In contrast, new analyses of samples from south Waterford were used to determine the geochemical affinities of rocks from the Bunmahon, Campile and Dunabrattin Formations and to assess the relationship between emplacement styles and the geochemical composition of the volcanic rocks. Comparisons between a variety of compositional and tectonic discrimination diagrams were used to determine the overall reliability of major (and trace) elements and hence elucidate the extent of alteration. The alteration mineral assemblage (descriptions in Chapter Three) was analysed using micro-analytical techniques such as Electron Probe Micro Analysis (EPMA) and Scanning Electron Microscopy (SEM) in order to assess the relationship of alteration with magma-sediment

interaction, metasomatism and/or regional metamorphism. The nature of the chemical interaction at the magma-sediment interface in peperite was examined, using both EPMA and SEM (fitted with Energy Dispersive X-ray Spectroscopy (EDS)) elemental maps in order to distinguish the alteration pattern. This alteration pattern was then subsequently used as a proxy for the distribution of secondary minerals in similar volcanic rocks in order to investigate the significance of hydrothermal alteration due to magma-sediment or magma-water interaction, and later metamorphic events, in particular within the Bunmahon Formation.

4.2 Sampling and analytical techniques

Samples for bulk rock and mineral geochemical analysis were primarily collected from Trawnamoe and Stradbally Cove (21 samples), as these localities were identified as type localities of the Bunmahon and Dunabrattin Formation (with one sample representing the Campile Formation), comprising a range of rock types representative of both the central vent and the flanks of the volcano (Chapter Two). A further four samples from the Bunmahon Formation and five samples from the Campile Formation were collected from other coastal and inland localities. Details of samples and reference materials analysed for bulk rock compositions using inductively coupled plasma mass spectrometry (ICP-MS) are given in Table 4.1 (refer to Figure 2.1 for localities).

Samples for bulk rock geochemistry were prepared in the discipline of Earth and Ocean Sciences, NUIG, using a multi-acid technique and analysed by ICP-MS at OMAC laboratories in Loughrea, Co. Galway. Reference materials were selected to complement the lithologies observed in the Bunmahon and Campile Formations (Chapter Two). ICP-MS is the synergistic combination of an inductively coupled plasma with a quadrupole mass spectrometer. ICP-MS uses the ability of the argon ICP to efficiently generate singly charged ions from the elemental species within a sample. These ions are then directed into a quadrupole mass spectrometer. The mass spectrometer separates the ions introduced from the ICP according to their mass-to-charge ratio. Ions of the selected mass/charge are directed to a detector which quantitates the number of ions present. Detection limits of the X series ICP-MS used by OMAC laboratories are given in Appendix A5.

In order to test the reliability of bulk rock geochemical results, each batch that was sent for analysis contained a duplicate sample. The standard deviation was up to 5% for Si, with an average standard deviation for major elements ranging from 0.15 to 1.3. The R^2 test (the square of the Pearson product moment correlation) was used to test the reliability of bulk rock geochemistry results. The test was applied to determine the errors between the published and measured values of the certified reference material (CRM), by defining the linear trend between X values (published) and Y values (measured). The majority of samples analysed for major, trace and rare earth elements using ICP-MS have an R^2 value of 0.93 – 1 (errors given in Appendix A5). Those samples with lowest R^2 values, were reanalysed with different CRM and returned values of >0.96 . The average R^2 values are 0.9999 (oxides), 0.982 (trace elements) and 0.9995 (REE), indicating the measured CRM values had a 98.2%–99.9% similarity to the published values.

A total of 21 samples from Trawnamoe and Stradbally Cove were prepared for micro-analysis (Table 4.2): 13 samples across the magma-sediment interface in peperite and eight samples representing intrusive rocks, tuffs, mudstone and vein mineralisation. Polished slabs of each sample were mounted on an aluminium stub and carbon coated. SEM and EPM analyses were carried out in two research visits, the first to the Universitat de Barcelona, Spain, and the second to Camborne School of Mines, Cornwall, UK. Preliminary mineral analysis completed in Barcelona was carried out using a Quanta 200 SEM equipped with a Genesis (EDAX) EDS; element mapping in Barcelona was carried out using a JEOL JSM 840 equipped with an Inca series 250 EDS. Preliminary mineral analysis in Camborne School of Mines was completed using a JEOL JSM-5400LV equipped with an Oxford ISIS EDS system. Detailed microprobe analysis in Barcelona was carried out using a Cameca SX-50 equipped with four wavelength-dispersive spectrometers and automated with SAMx software and hardware, using an accelerating voltage of 20kV. Detailed mineral analysis in Camborne was carried out using a JEOL JXA-8200 Superprobe, using an accelerating voltage of 15kV. The major mineral phases were predominantly silicates and reference materials were chosen accordingly.

Bulk rock and Mineral Geochemistry

Name	Type	Grid Reference	Name	Type	Grid reference
BT1	H	X 42685 98184	BS6	I	X 37019 96983
BT2	I	X 42687 98155	BS7	I	X 36896 96779
BT3	SF	X 42730 98192	BS8	I	X 37113 96967
BT4	I	X 42660 98143	BS9	T	X 36896 96779
BT5	I	X 42778 98179	BS10	T	X 36962 96904
CT1	I	X 42752 98198	BS11	T	X 36963 96907
BT7	T	X 42685 98152	BBW1	I	X 41016 97887
BT8	T	X 42810 98180	BB1	I	X 43514 98883
BT9	T	X 42696 98170	BB2	SF	X 43903 98298
BT10	T	X 42696 98179	BK1	SF	X 46481 98684
BS1	M	X 36965 96896	CKS1	SF	X 52824 98133
BS2	M	X 37020 96958	CB1	I	S 41332 01893
BS3	M	X 37019 96954	CB2	I	S 41332 01893
BS4	M	X 36931 96896	CK1	I	S 45044 03802
BS5	I	X 37100 96982	CC1	I	S 41903 00349

Reference materials:

Name	Type	Name	Type
W-2	Diabase	UCGB	Basalt
BHVO-1	Basalt	SY-3	Syenite
Sco-1	Shale	SY-4	Syenite

Table 4.1: List of samples, and corresponding reference materials, analysed for whole rock geochemistry. Prefix B = Bunmahon Formation, C = Campile Formation. Rock types include mudstone (M), intrusive rocks (I), tuff (T), hyaloclastite (H) and sheet flows (SF).

Bulk rock and Mineral Geochemistry

Name	Type	Locality	Grid Reference
BT9	Bedded tuff	Trawnamoe	X 42696 98170
BT10	Sill	Trawnamoe	X 42696 98179
BT15	Peperite (5 probe sections)	Trawnamoe	X 42617 98174
BT16	Barren vein	Trawnamoe	X 42770 98180
BT18	Sulphide-bearing vein	Trawnamoe	X 42810 98175
BS4	Mudstone	Stradbally Cove	X 36931 96896
BS6	Intrusive rock	Stradbally Cove	X 37019 96983
BS13	Peperite (2 probe sections)	Stradbally Cove	X 37019 96964
BS14	Intrusion/tuff contact	Stradbally Cove	X 36896 96779
BS28	Intrusive rock	Stradbally Cove	X 36923 69841
BS29	Peperite (4 probe sections)	Stradbally Cove	X 36999 96964
BS31	Peperite	Stradbally Cove	X 37008 96966
BS32	Peperite	Stradbally Cove	X 37006 96965

Table 4.2: List of samples analysed using a SEM and an EPMA.

4.3 Results

4.3.1 Whole rock analysis

Bulk rock geochemical analyses of major, trace and rare earth elements (REE) are presented in Appendix A5. The Ordovician volcanic rocks have compositions ranging from basaltic through to rhyolitic, with a differentiation occurring between the mafic-intermediate Bunmahon Formation and the more felsic Campile Formation (Figure 4.1 and Figure 4.2). Compositions determined from bulk rock analysis in this study correspond to those determined in previously published results (e.g. Downes, 1975; Stillman and Williams, 1979) (see Appendix A5). Classification of the volcanic rocks was made in the first instance using the total alkalis versus silica (TAS) diagram of Le Bas *et al.* (1986). Samples from the Campile Formation are spread between two fields, with five samples plotting within the rhyolite field and one sample (Carrighalia – sample CC1) plotting within the andesite field. Samples from the Bunmahon Formation plot predominantly in the basalt, basaltic andesite and andesite fields (Figure 4.1), with two out of twenty samples plotting outside these fields. The intrusive rock classified as a dacite (Trawnamoe – sample BT5) represents late stage felsic volcanic activity (Chapter Two) that Boland (1983) suggested may be attributed to the Campile Formation phase of volcanic activity, hence the more felsic signature. The tuff sample from the Bunmahon Formation (Trawnamoe – BT7) that is classified as a rhyolite is the bedded tuff that interacted with intruding magma to form peperite, while a sample of the same tuff further away from the contact with peperite plots as an andesite.

Further classification was made using the $\text{SiO}_2\text{-Zr/TiO}_2$ diagram (Figure 4.2a) and the $\text{Zr/TiO}_2\text{-Nb/Y}$ diagram (Figure 4.2b) of Winchester and Floyd (1977), where Zr/TiO_2 is used as a discriminator as this ratio increases with progressive evolution of a mafic magma. Samples from the Campile Formation are tightly constrained when plotted using SiO_2 , with the majority of samples plotting within the rhyolite field and one sample plotting within the andesite field (similar to TAS diagram). However, when using more immobile trace elements as discriminators (e.g. Nb/Y ratio) the samples from the Campile Formation are more evenly spread between the fields from andesite through rhyodacite/dacite to rhyolite, suggesting mobility of some of the major elements such as Si. Samples from the Bunmahon Formation display a trend of compositions from sub-alkaline basalt through to

rhyolite when using SiO_2 in conjunction with the Zr/TiO_2 ratio, whereas when the more immobile Nb/Y ratio is used the samples show a tighter cluster within the sub-alkaline basalt, basalt and andesite fields (Figure 4.2b). The apparently rhyolitic tuff sample in Figures 4.1 and 4.2a is classified as a trachy-andesite using the more reliable discrimination diagram of Nb/Y vs. Zr/TiO_2 (Figure 4.2b). This tuff matrix in peperite has been reported in both field observations (Chapter Two) and petrographic descriptions (Chapter Three) to have undergone silicification, probably as a result of peperite formation. The increased SiO_2 content may be a result of major element mobility and therefore represents a secondary feature. Sample BT9, part of the same section of bedded tuff, was not involved in peperite formation and is classified as sub-alkaline basalt.

The mobility of alkalis during weathering and alteration indicates that the reliability of these elements within altered rocks may be in question, and as a result the more immobile elements are considered more reliable for use in discrimination diagrams (e.g. Figure 4.2b). Seven samples are classified as sub-alkaline basalts using solely trace elements whereas in the TAS diagram the majority of samples are considered sub-alkaline, with eleven of these samples classified as basalts and basaltic andesites. Therefore, it appears that in the majority of samples the alkalis (K and Na) are highly mobile and are possibly depleted during alteration, while Si is enriched in a limited number of samples. Those samples that are accurately classified as sub-alkaline (using trace elements) are highlighted in grey in the results table (Appendix A5). Classification diagrams displayed in this chapter are also shown in Appendix A5 with additional data from previous published results.

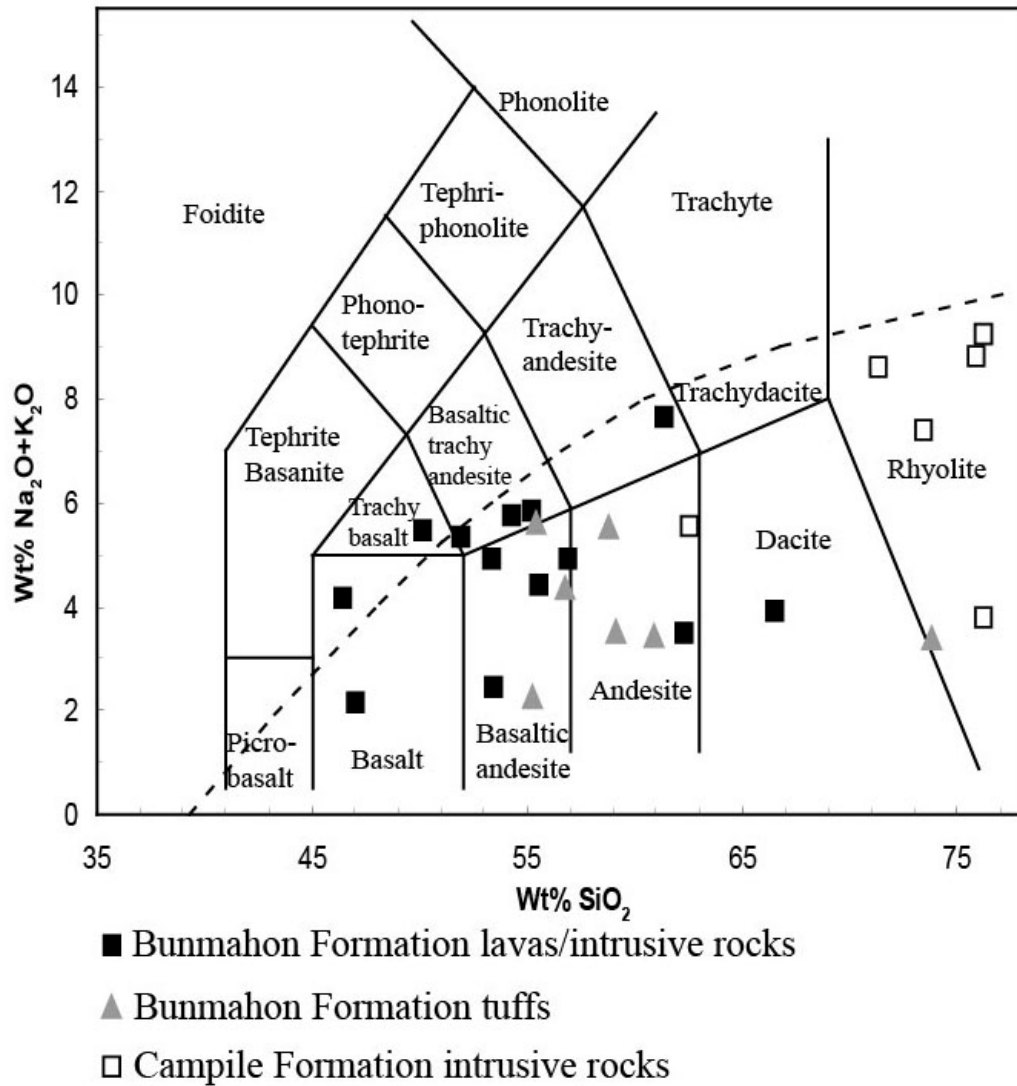


Figure 4.1: Total alkalis versus silica classification diagram after Le Bas *et al.* (1986) showing the predominantly intermediate composition of the Bunmahon Formation and the more felsic nature of the Campile Formation. The dashed line divides alkalic (high $\text{Na}_2\text{O} + \text{K}_2\text{O}$) and sub-alkalic (low $\text{Na}_2\text{O} + \text{K}_2\text{O}$).

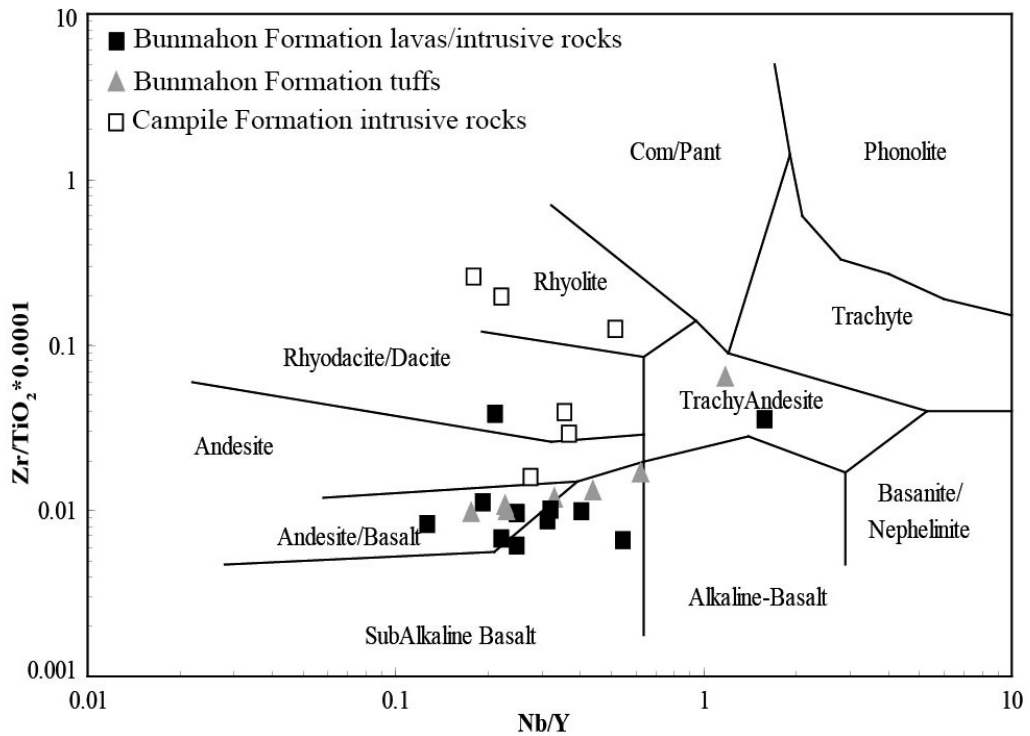
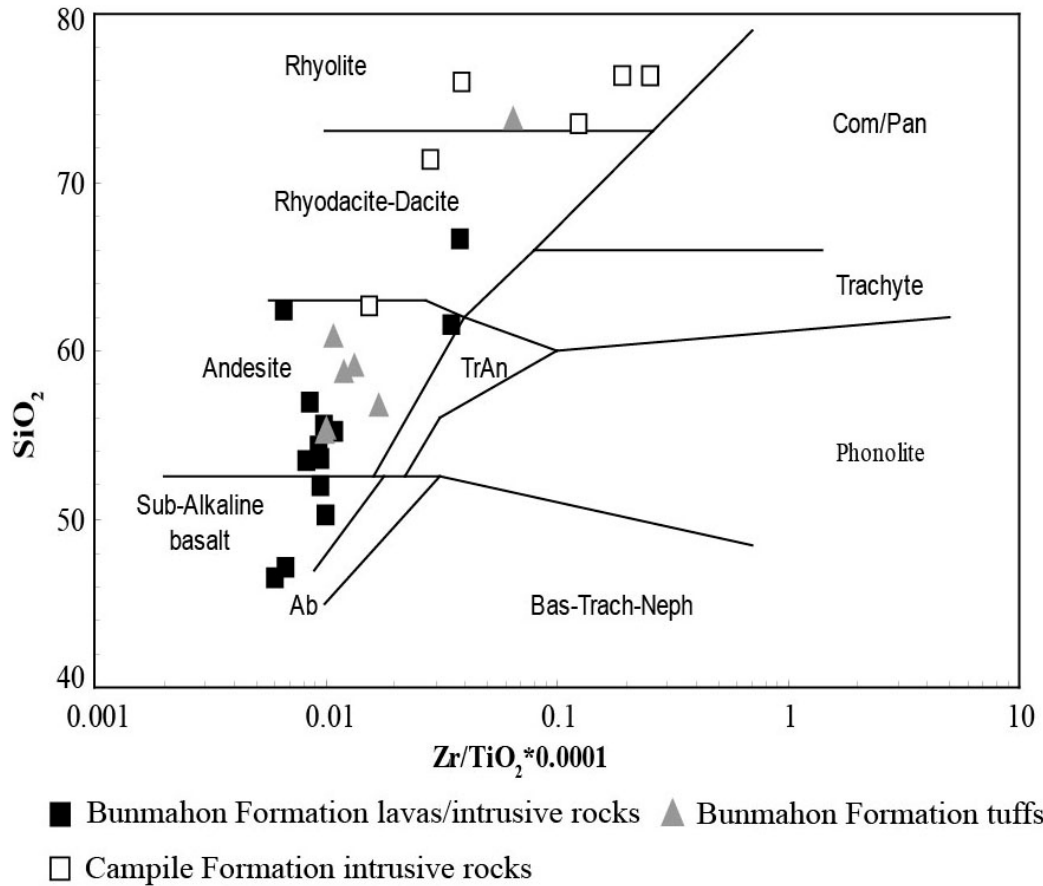


Figure 4.2: Igneous classification diagrams of Winchester and Floyd (1977) using $\text{Zr}/\text{TiO}_2 \times 0.0001$ against (a) SiO_2 and (b) Nb/Y . TrAn = trachyandesite, Bas-Trach-Neph = basanite-trachyte-nephelinite, Com/pant = comendite/pantelerite.

Harker diagrams (Figure 4.3) show that no correlation exists between Na_2O and SiO_2 and a very loose correlation exists between K_2O and SiO_2 (predominantly in the more felsic samples of the Campile Formation), thus indicating that Na was probably the most mobile of the alkalis, with possible depletion occurring within the majority of samples (see Figure 4.1). A slight negative correlation is observed between SiO_2 and TiO_2 . A steep negative linear trend is recorded between SiO_2 and Fe_2O_3 concentrations, while SiO_2 vs. MgO appears to follow a very similar pattern (Figure 4.3). The negative linear trend of Fe_2O_3 and MgO with SiO_2 indicates continuing fractionation of ferromagnesian minerals probably occurred within the magma source. The original or primary mineral assemblage within the majority of mafic-intermediate rocks includes clinopyroxene and plagioclase feldspar, whereas plagioclase becomes a more dominant phase in the more felsic samples (Chapter Three). Therefore, clinopyroxene was probably one of several fractionating ferromagnesian minerals, and contributed to the decreasing Ca concentrations with increasing Si (Appendix A5).

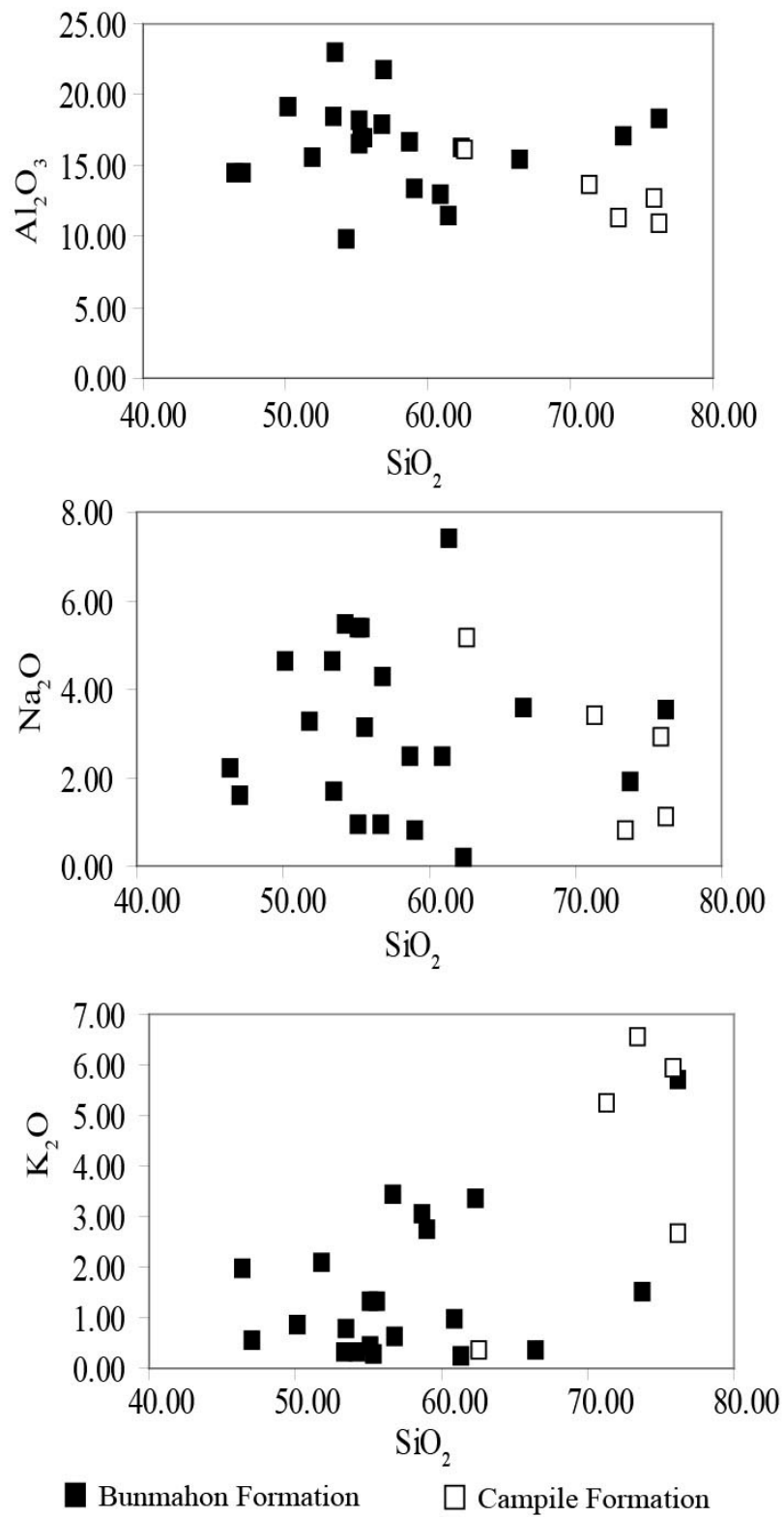


Figure 4.3: Harker diagrams of oxides Al_2O_3 and Na_2O showing a broad scatter, and K_2O showing enrichment with increasing SiO_2 .

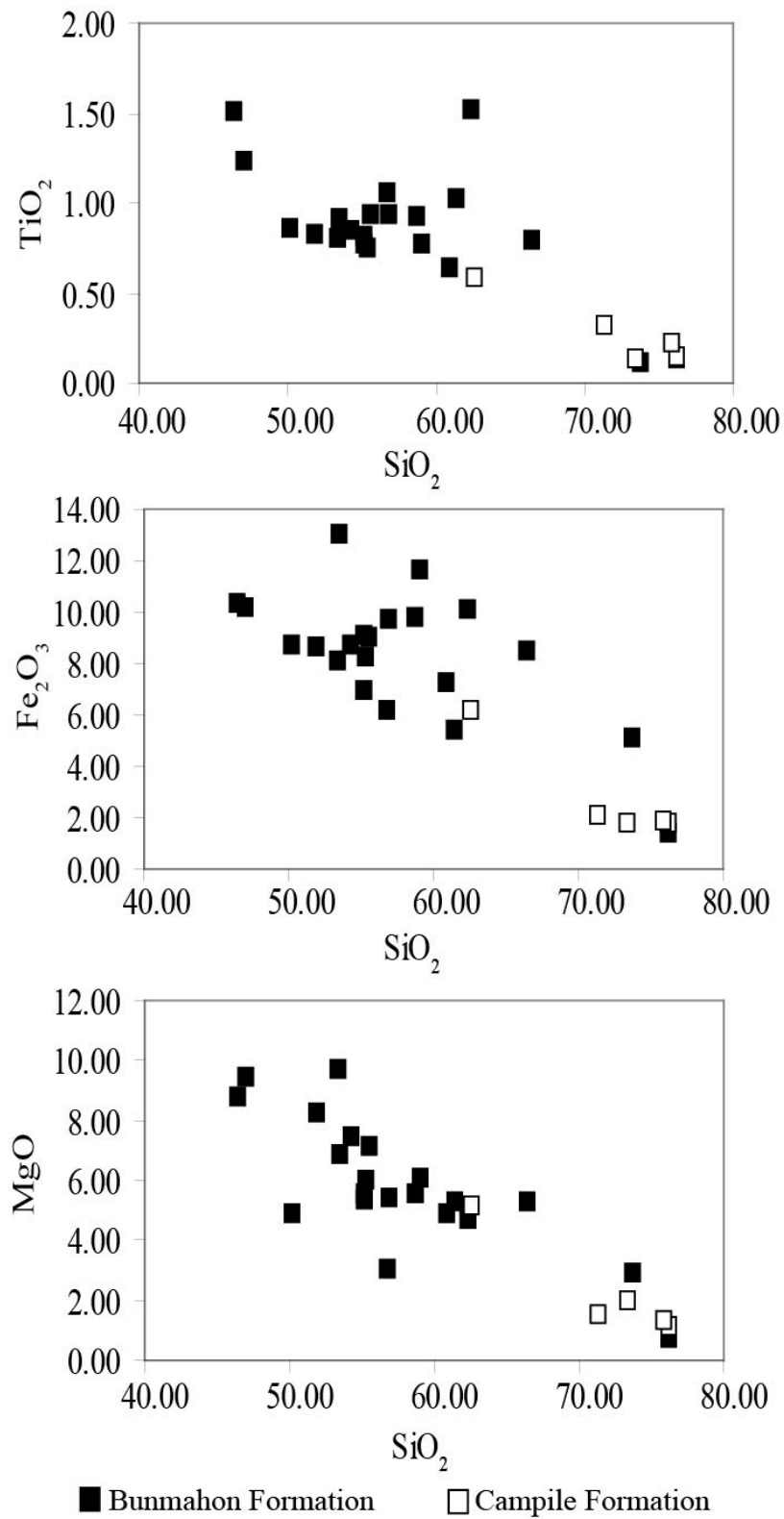


Figure 4.3 (continued): Harker diagrams of oxides TiO₂, Fe₂O₃, MgO, all of which display a negative linear relationship with SiO₂.

Bulk rock geochemical analysis has been used along with the secondary mineral assemblage (Chapter Three) to determine the alteration index or alteration extent of the suite of volcanic rocks of south Waterford (Figure 4.4). The ‘alteration box plot’ of Large *et al.* (2001a) compares the Ishikawa Alteration Index (AI) and the Chlorite-Carbonate-Pyrite Index (CCPI). The alteration box plot is primarily used to characterise the different alteration trends related to volcanic hosted massive sulphide (VHMS) ores and to assist in the distinction of VHMS-related hydrothermal alteration from regional diagenetic alteration. The majority of the south Waterford samples are located towards the higher end of the CCP index and towards the right hand side of the alteration index. The hydrothermal trend is adhered to, indicating a pronounced development of chlorite and pyrite, that corresponds to the secondary mineral assemblage as determined from petrographic descriptions (Chapter Three). The development of chlorite is ubiquitous within all volcanic rocks and is particularly well developed in the most intensely altered samples (e.g. peperite and hyaloclastite). Secondary pyrite is also recorded within the more extensively altered volcanic rocks, commonly associated with chlorite, where the concentration of pyrite layers or nodules (see Chapter Two) is commonly attributed to ore forming hydrothermal events (Large *et al.*, 2001a)). Of the other mineral phases that are suggested to occur as a result of hydrothermal alteration of volcanic rocks, epidote and sericite are present as the dominant phases with minor development of secondary calcite. Those samples following the diagenetic trend are predominantly from the Campile Formation, indicating a more pronounced effect of diagenesis on the later volcanic rocks. The later diagenetic alteration corresponds to an observed mineral assemblage dominated by albite, where albite is a more common mineral phase in the felsic volcanic rocks. Diagenetic alteration may have overprinted the original hydrothermal alteration mineral assemblage to some extent in the mafic-intermediate volcanic rocks (formation of albite) but the stronger signature of hydrothermal alteration was retained.

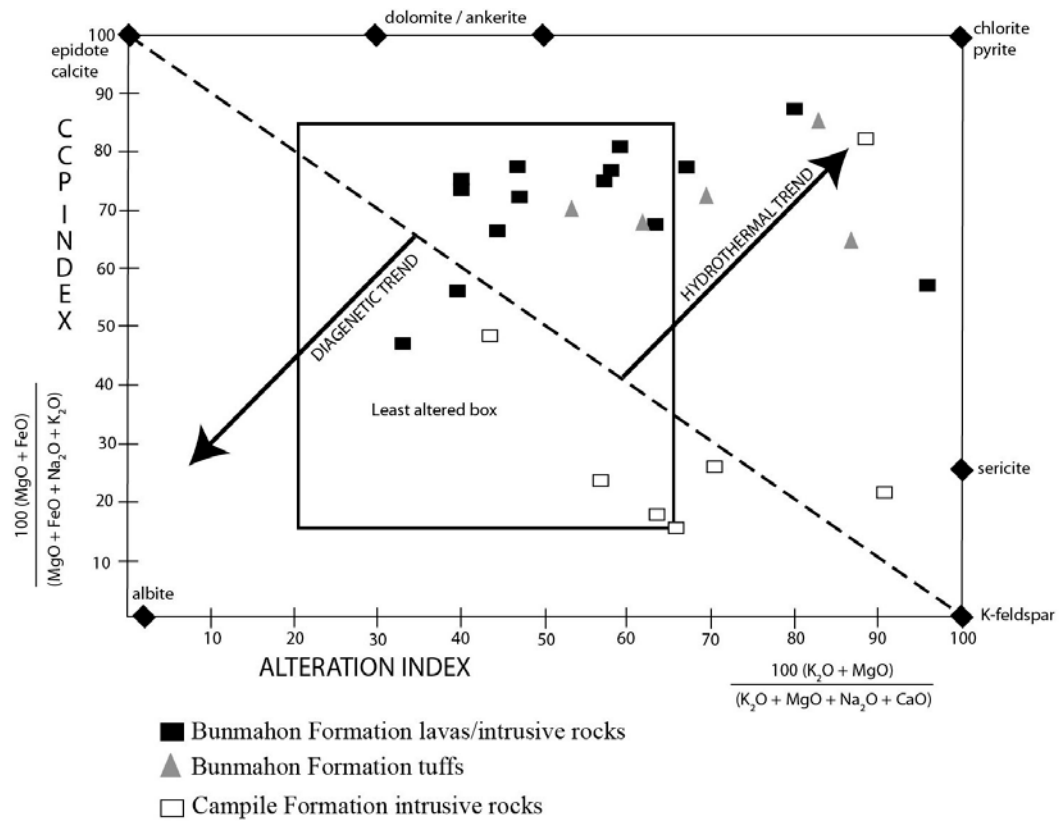


Figure 4.4: Alteration box plot of Large *et al.* (2001) showing the majority of samples follow a hydrothermal trend of alteration, with the more felsic samples of the Campile Formation affected by diagenetic alteration.

4.3.2 Trace Element Geochemistry

The trace element geochemistry of volcanic rocks from the Bunmahon and Campile Formations is presented in MORB normalised (Pearce, 1983) plots (Figure 4.5). Elements from Rb to Ta are enriched relative to MORB in all rock types from both the Bunmahon and Campile Formations. The mobile elements have more variable concentration in the tuffs than in associated lavas and intrusive rocks. Depletion of Nb and Ta relative to Th is observed in the majority of samples. Negative Sr anomalies are recorded within intrusive rocks and tuffs. Ba is depleted relative to Rb within the majority of rocks, although to a lesser extent within the Campile Formation. A large negative anomaly is recorded for Ti in the Campile Formation (predominantly felsic rocks), in the silicified tuff matrix of peperite at Trawnamoe and in the late stage felsic dyke at Trawnamoe (Figure 4.5 and 4.6).

Trace element profiles were also plotted for the sedimentary rocks of the Bunmahon/Dunabrattin Formation, normalised to both MORB (Figure 4.6b) and to the upper crust values (Figure 4.7) of Rudnick and Gao (2003). The MORB normalised sedimentary rocks show a similar trace element profile to the volcanic rocks, with depletions in Sr, Ba and Nb (Figure 4.6). Two of the four sedimentary samples have flat profiles in all elements relative to upper crust values (Figure 4.7). The two remaining samples have anomalously low concentrations in mobile elements with a steep profile as a result of higher concentrations in the immobile elements.

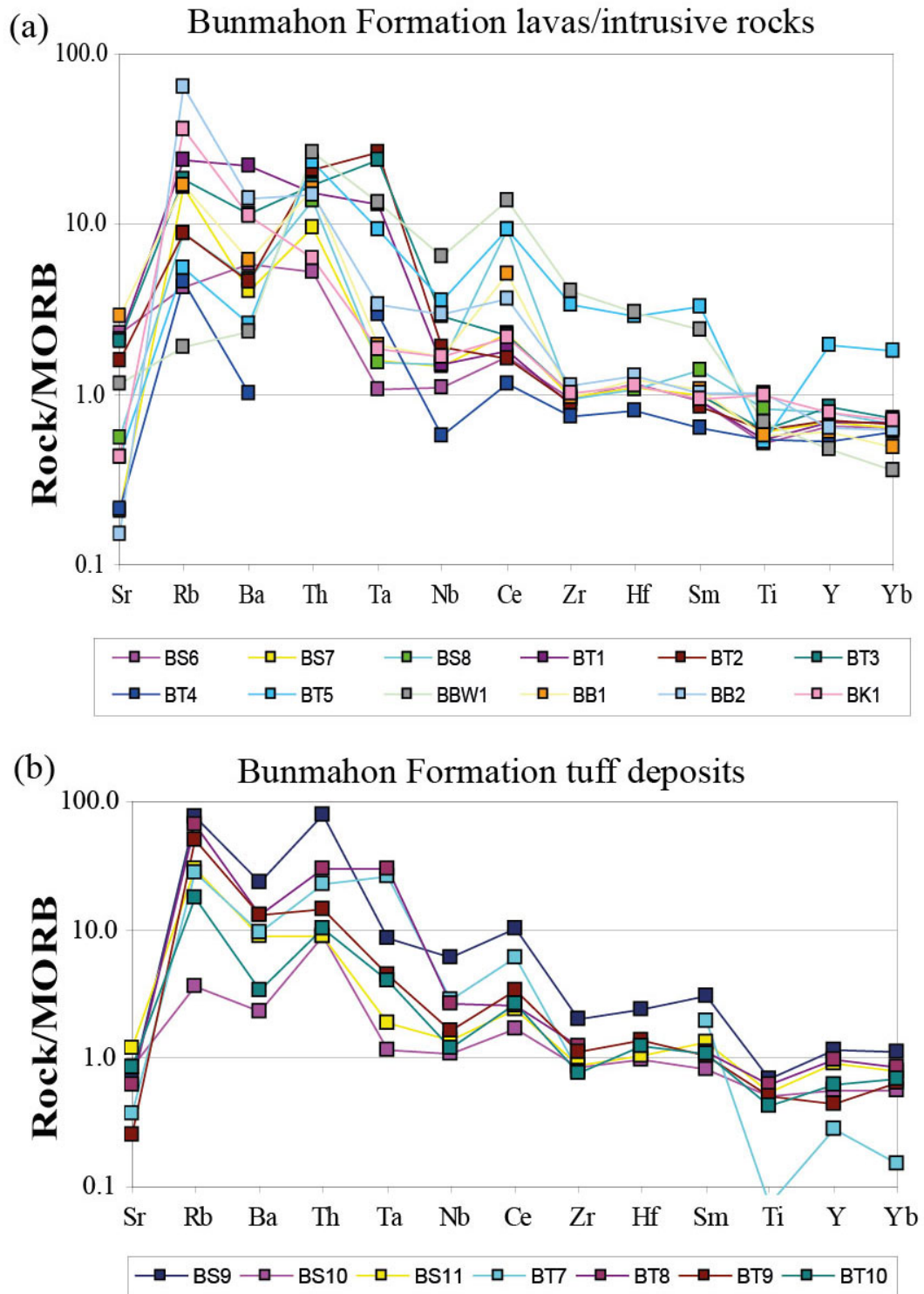


Figure 4.5: Multielement profiles of (a) lavas and intrusive rocks from the Bunmahon Formation and (b) tuffs from the Bunmahon Formation, normalised to MORB values of Pearce (1983) and plotted using Geoplot (Zhou and Li, 2006).

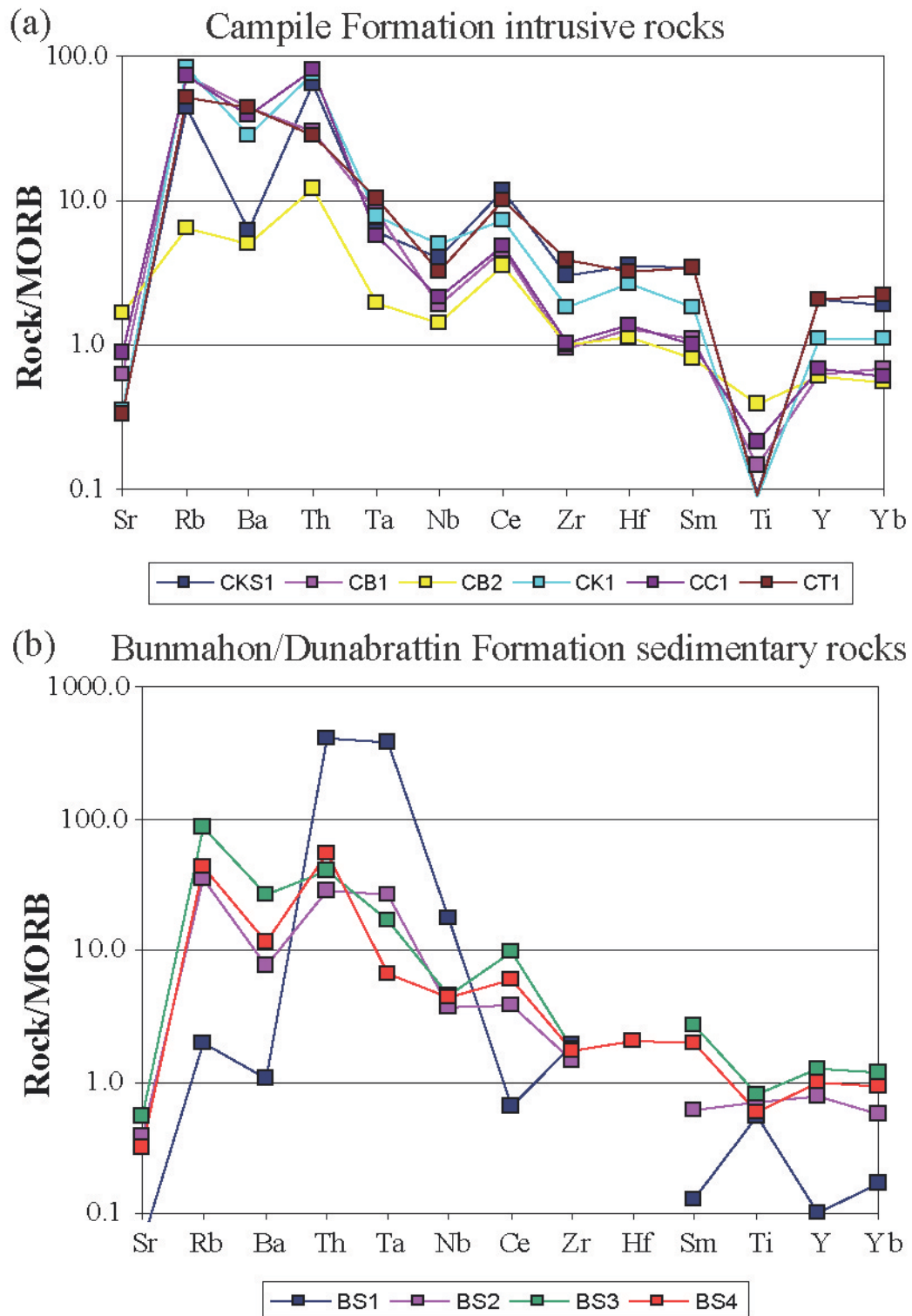


Figure 4.6: Multielement profiles of (a) intrusive rocks from the Campile Formation and (b) sedimentary rocks from the Bunmahon/Dunabrattin Formation, normalised to MORB (Pearce, 1983).

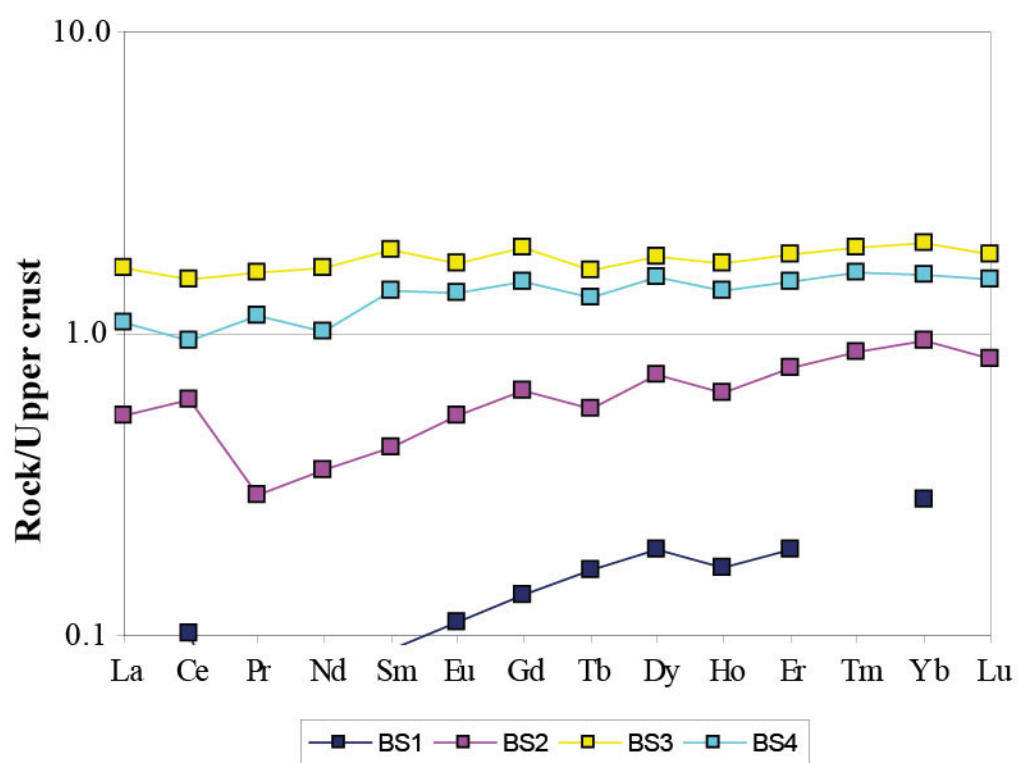


Figure 4.7: Upper crust normalised (Rudnick and Gao, 2003) trace element profile for sedimentary rocks of the Bunmahon/Dunabrattin Formation from Stradbally Cove.

4.3.3 Rare Earth Element Geochemistry

Rare Earth Element concentrations from the south Waterford volcanic and sedimentary rocks were normalised to the N-type MORB values of Sun and McDonough (1989). All samples, apart from BS1 (mudstone), are slightly enriched in light REE relative to MORB with a flat profile observed for the heavy REE (Figure 4.8 and Figure 4.9). The steepness of the profile is measured using the La_N/Yb_N ratio (normalised to chondrite) (Table 4.3). The most significant light to heavy REE enrichment is recorded in the Campile Formation (average $La_N/Yb_N = 7.09$); the greater average value for the tuffs of the Bunmahon Formation is due to significant enrichment in LREE and depletion in HREE in the silicified tuff sample BT7 ($La_N/Yb_N = 37.7$). This tuff sample is from directly above the peperite, where interaction with magma has occurred, whereas another sample stratigraphically higher in this section of tuff exhibits an enrichment in LREE and flat HREE profile similar to the majority of samples ($La_N/Yb_N = 5.7$). The highest concentration of both LREE and HREE in the Bunmahon Formation is within the most felsic sample (BT5). The largest Eu anomaly is observed in the Campile Formation ($Eu/Eu^* = 0.53$). Sedimentary rocks of the Bunmahon/Dunabrattin Formation (three of four samples) have similar concentrations in all rare earth elements to the volcanic rocks, with a corresponding Eu depletion ($Eu/Eu^* = 0.68$).

Formation – rock type	Eu/Eu*	La_N/Yb_N	La_N/Sm_N	Gd_N/Yb_N
Bunmahon Formation – lavas/intrusive rocks	0.93	8.67	3.26	1.55
Bunmahon Formation – tuffs	0.85	9.4	2.46	2.12
Bunmahon/Dunabrattin Formation - sedimentary rocks	0.68	7.66	4.12	1.26
Campile Formation - intrusive rocks	0.53	7.09	4.05	1.27

Table 4.3: Results from REE profiles using chondrite normalised values. Eu/Eu^* = europium anomaly; La_N/Yb_N = measure of light REE to heavy REE; La_N/Sm_N = measure of fractionation in LREE; Gd_N/Yb_N = measure of fractionation in HREE.

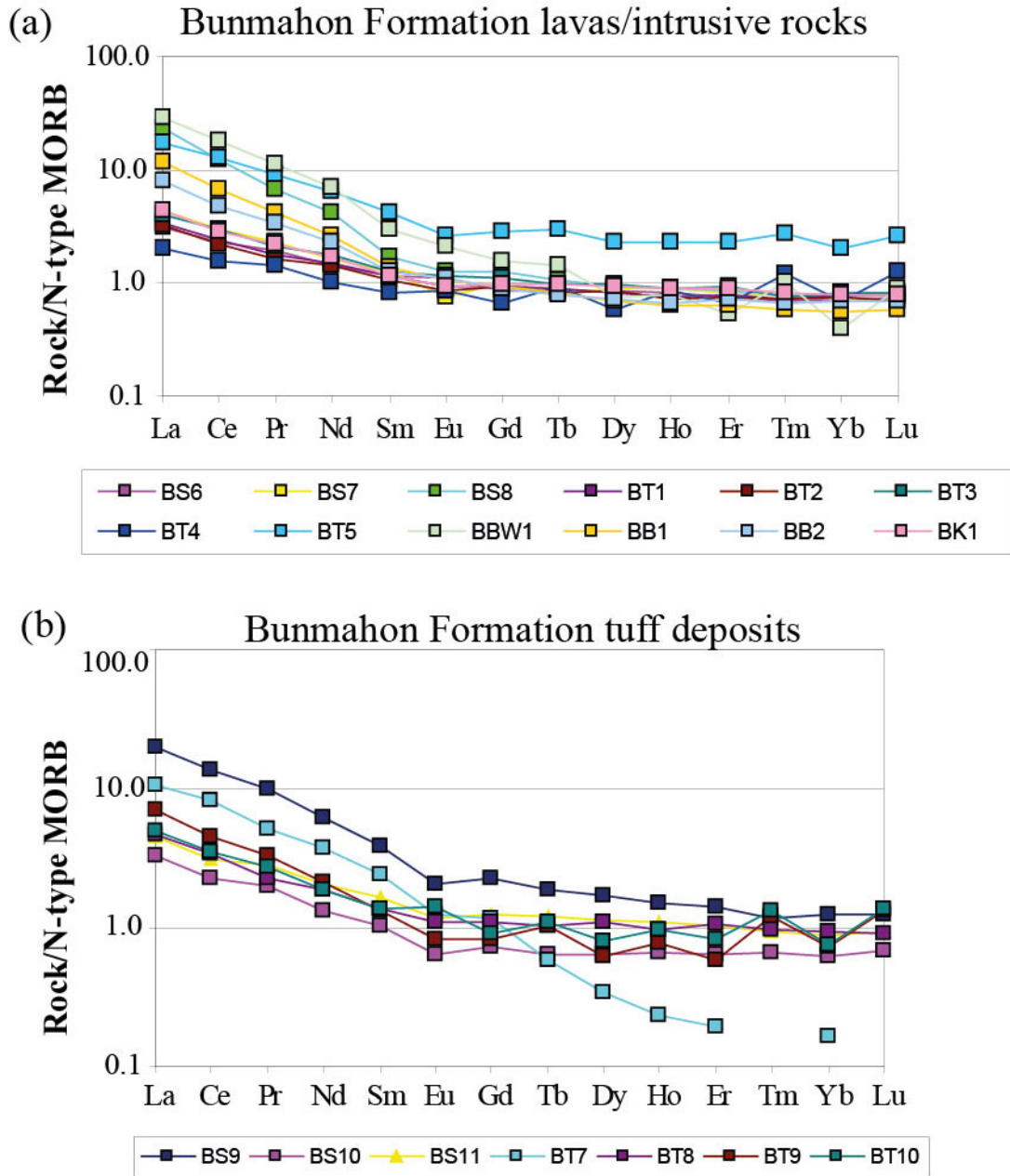


Figure 4.8: Rare Earth Element plots of (a) lavas and intrusive rocks from the Bunmahon Formation and (b) tuff deposits from the Bunmahon Formation, normalised to the N-type MORB values of Sun and McDonough (1989).

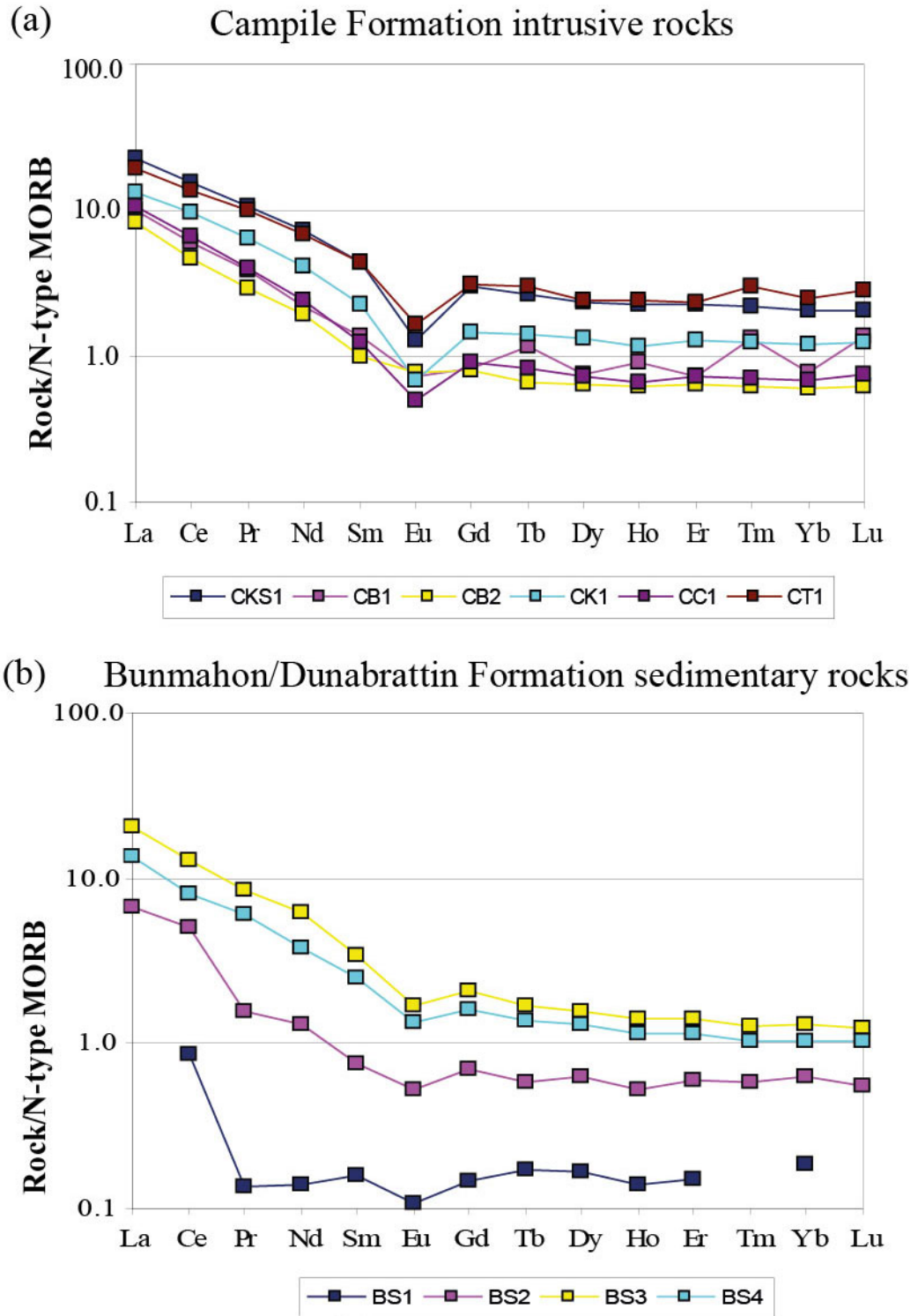


Figure 4.9: Rare Earth Element plots of (a) intrusive rocks from the Campile Formation and (b) sedimentary rocks from the Bunmahon/Dunabrattin Formation.

4.3.4 Volcanic discrimination diagrams

A simple binary plot of TiO_2 versus the Y/Nb ratio is used to differentiate between tholeiitic and alkaline compositions (Winchester and Floyd, 1976). Apart from two anomalous samples plotting within the alkaline field, all samples have a tholeiitic composition (Figure 4.10), which is associated with an island arc signature (Winchester and Floyd, 1976). Due to the altered nature of the volcanic rocks, discrimination diagrams that utilise immobile elements are considered the most reliable. A bivariate plot of Ti against Zr (Pearce, 1983) is recognised as the most reliable discriminator for intermediate composition rocks (Pearce and Norry, 1979; Pearce, 1983) and the majority of samples plot as arc lavas (Figure 4.11). Th and Ta tend to become enriched in volcanic arc settings (Pearce, 1982) and are incompatible elements so that they are also good discriminators for altered rocks. Th and Ta values are normalised to Yb as this is not enriched in island arc or active continental magmatism and all samples plot in or close to the field of oceanic island arcs (Figure 4.12). Six samples plot within the MORB field, which may be due to post-emplacement alteration or more likely is a result of the common overlap between island arc tholeiites and MORB on this discrimination diagram. K generally gives a better discrimination than Th between arc lavas and mid-ocean ridge basalts but in the case of altered rocks such as those from Waterford, Th is a more reliable element due to being much less mobile in aqueous solutions (Pearce, 1982). There is no distinction between rock types or between formations. The ternary TiO_2 -MnO- P_2O_5 diagram of Mullen (1983) was the only discrimination diagram used that is based on major element data, but these elements are also unlikely to be mobilised during alteration. The majority of samples plot in the Island Arc Tholeiite or Calc-Alkaline Basalt fields (Figure 4.13). A comparison between discrimination diagrams is given in Table 4.4.

Graph	Setting/type determined	Reference
Ti versus Zr (Fig. 11)	Arc lavas with few outliers	Pearce, 1983
Th/Yb versus Ta/Yb (Fig. 12)	Calc-alkaline – active continental margin and “alkalic” oceanic arcs	Pearce, 1982
Ternary plot of MnO, TiO_2 and P_2O_5 (Fig. 13)	Island Arc Tholeiite with few outliers	Mullen, 1983
TiO_2 wt% versus Nb/Y ratio (Fig. 10)	Tholeiitic magmas (island arc related)	Winchester and Floyd, 1976

Table 4.4: Correlation between various discrimination diagrams plotted using major and trace elements.

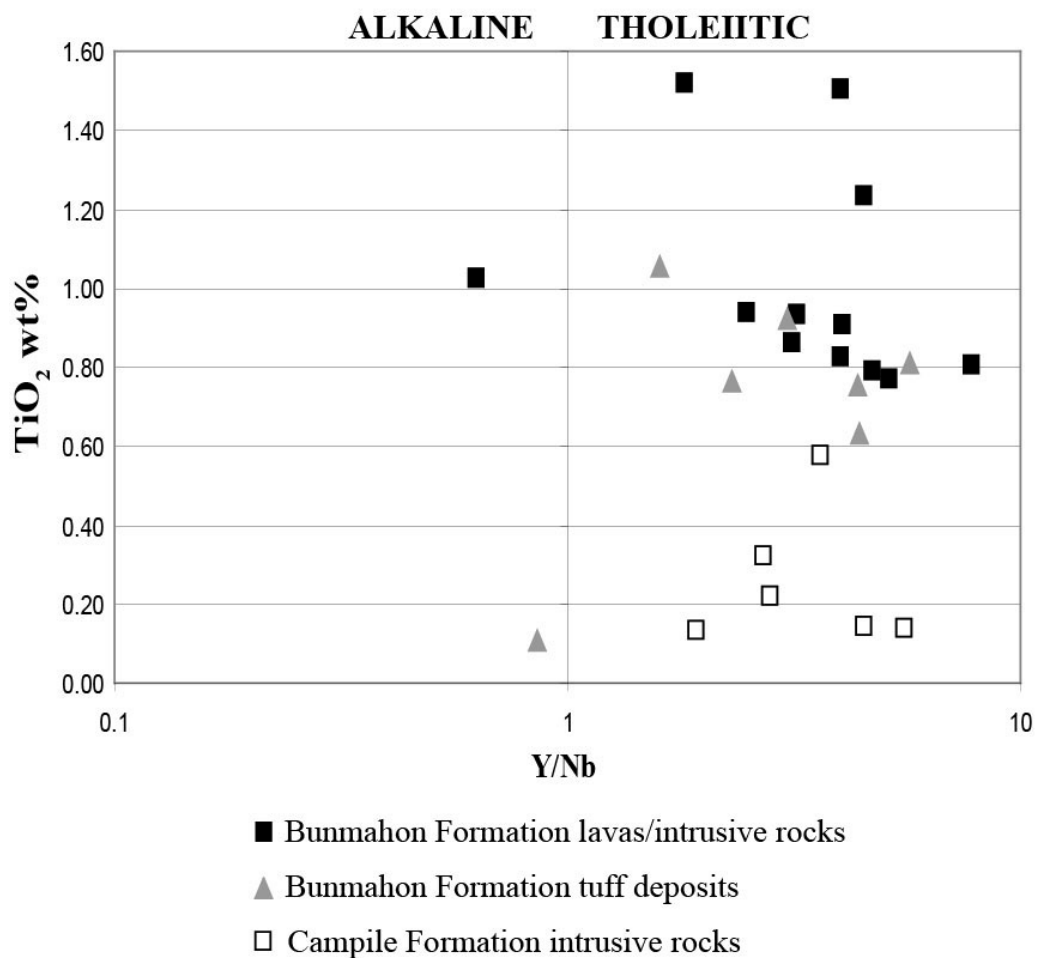


Figure 4.10: Bivariate discrimination diagram after Winchester and Floyd (1976) used to determine between alkaline and tholeiitic compositions, showing the majority of volcanic samples from south Waterford are tholeiitic.

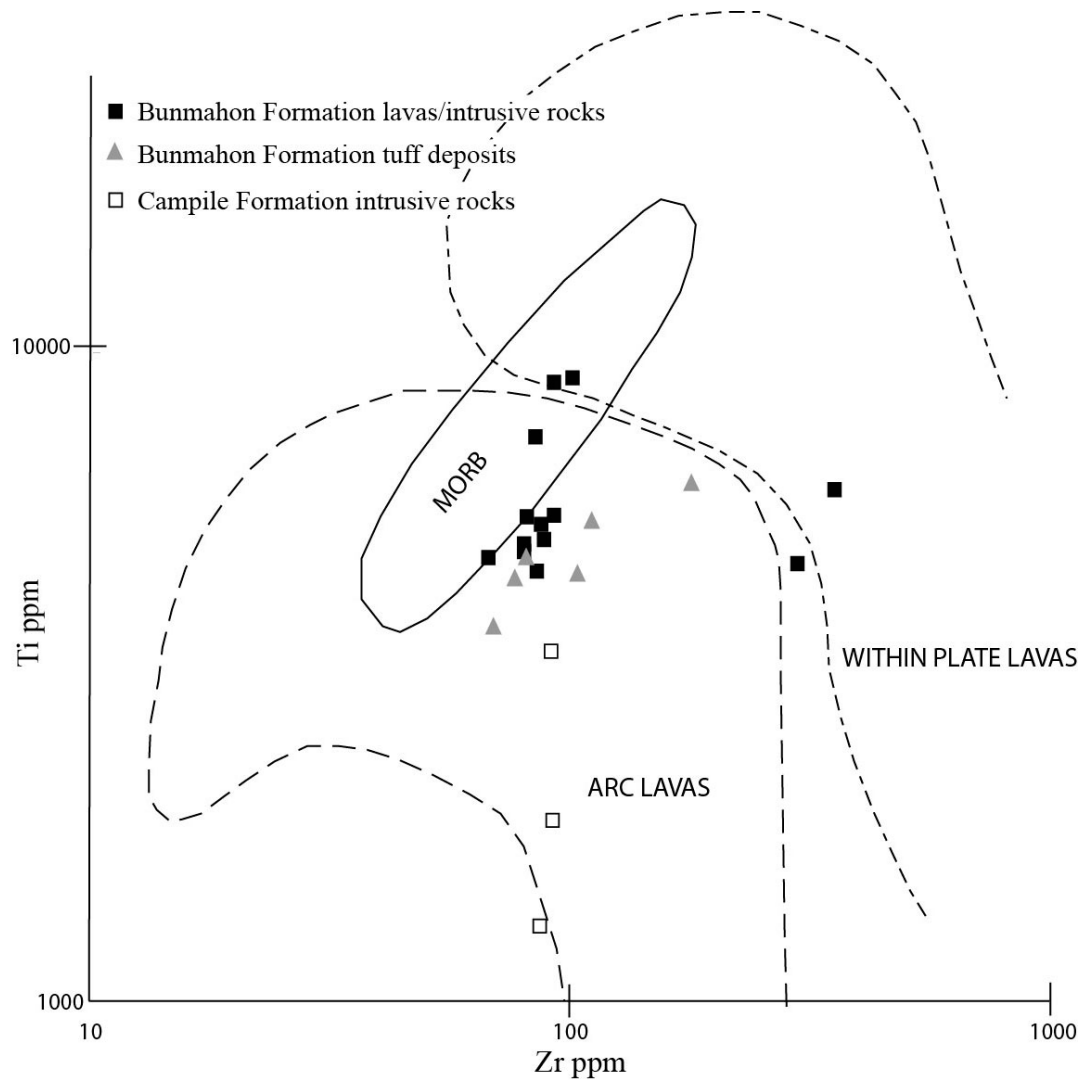


Figure 4.11: Bivariate plot of trace elements Ti against Zr (after Pearce, 1983) for the volcanic rocks of the Bunmahon and Campile Formations, with the majority of samples plotting as arc lavas.

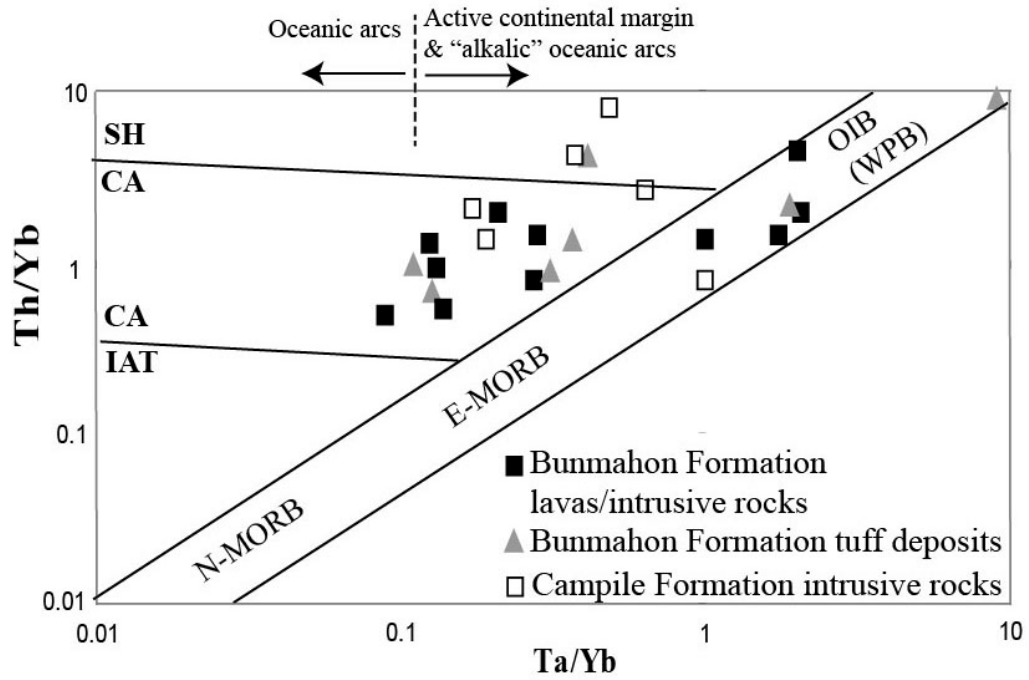


Figure 4.12: Bivariate diagram of Ta/Yb versus Th/Yb (after Pearce, 1982) for volcanic rocks from the Bunmahon and Campile Formation. Island arc tholeiitic = IAT; calc-alkaline = CA; shoshonitic = SH.

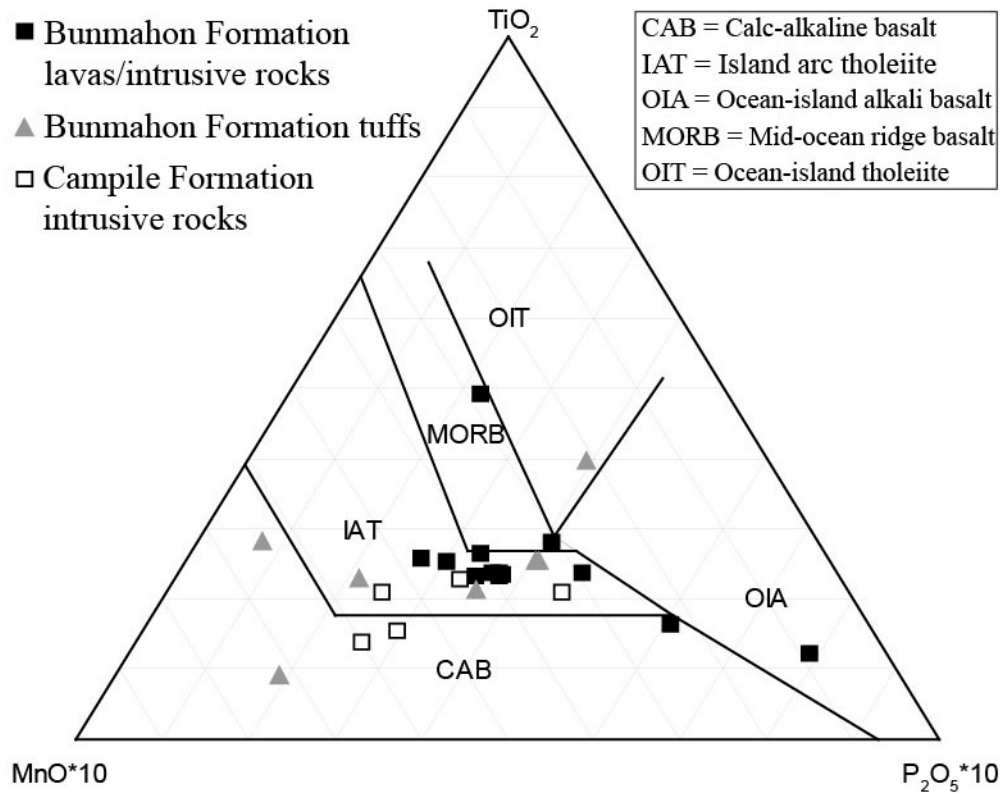


Figure 4.13: Ternary plot of $\text{MnO-TiO}_2\text{-P}_2\text{O}_5$ after Mullen (1983) displaying volcanic rocks from the Bunmahon and Campile Formations.

Discrimination diagrams, using major and trace elements, were used to differentiate the geochemical signature of the sedimentary rocks from Stradbally Cove. The sediment classification scheme of Herron (1988) uses a graph of $\log(\text{SiO}_2/\text{Al}_2\text{O}_3)$ versus $\log(\text{Fe}_2\text{O}_3/\text{K}_2\text{O})$, where the $\text{SiO}_2/\text{Al}_2\text{O}_3$ ratio differentiates between Si-rich quartz-arenites and Al-rich shales and the $\text{Fe}_2\text{O}_3/\text{K}_2\text{O}$ ratio separates lithic sands, feldspathic sands and Fe-rich sands and shales. The four sedimentary samples analysed from Stradbally Cove are identified as iron-rich shales and sands (Figure 4.14a). The sediment provenance discrimination of Roser and Korsch (1986) uses wt% SiO_2 versus $\log(\text{K}_2\text{O}/\text{Na}_2\text{O})$ to determine between three distinct settings: passive margin, active continental margin and oceanic island arc margin (Figure 4.14a). Passive margin sediments are derived from stable continental areas and deposited in sites away from active plate boundaries. Active continental margin sediments and oceanic island arc sediments consist of sediments derived from continental margin magmatic arcs and oceanic island arcs respectively (and are deposited in a variety of basin settings including trench, fore-arc, intra-arc and back-arc). Settings determined for the Stradbally Cove sedimentary rocks indicate derivation from an oceanic island arc margin bordering an active continental margin (Figure 4.14b). One sample (BS1), with low K_2O and Na_2O values, cannot be plotted on this diagram as the \log of $(\text{K}_2\text{O}/\text{Na}_2\text{O})$ yields a negative value. Sample BS1 is a pyrite-rich mudstone that grades over a distance of 3-4m from the pyrite-rich tuff. The graded nature between the mudstone and tuff may be the principal factor in influencing the resultant composition of the mudstone, where element mobility resulting in low K_2O and Na_2O values, combined with SiO_2 enrichment (78wt.%), is probably a result of hydrothermal fluid migration.

Bhatia (1983) constructed four bivariate discrimination diagrams for classification of sedimentary provenance. The most useful discriminating parameters are $\text{Fe}_2\text{O}_3 + \text{MgO}$, TiO_2 wt%, $\text{Al}_2\text{O}_3/\text{SiO}_2$, $\text{K}_2\text{O}/\text{Na}_2\text{O}$ and $\text{Al}_2\text{O}_3/(\text{CaO} + \text{Na}_2\text{O})$ ratios, which are used to determine between oceanic island arcs, continental island arcs, active continental margins and passive margins. Due to alkali mobility, all of the Waterford volcanic rocks analysed plot outside fields defined in the discrimination diagrams using K and Na and are therefore not used in this study. For fields defined by more reliable elements, particularly Ti (more immobile), the sedimentary samples plot in or close to the oceanic island arc field (Figure 4.15).

Bulk rock and Mineral Geochemistry

The larger scatter in the $\text{Al}_2\text{O}_3/\text{SiO}_2$ graph as compared to the TiO_2 graph is a result of the large variation in Si in particular (58 – 78wt.%) due to the effect of later alteration and/or metamorphism, whereas immobile Ti yields more consistent values.

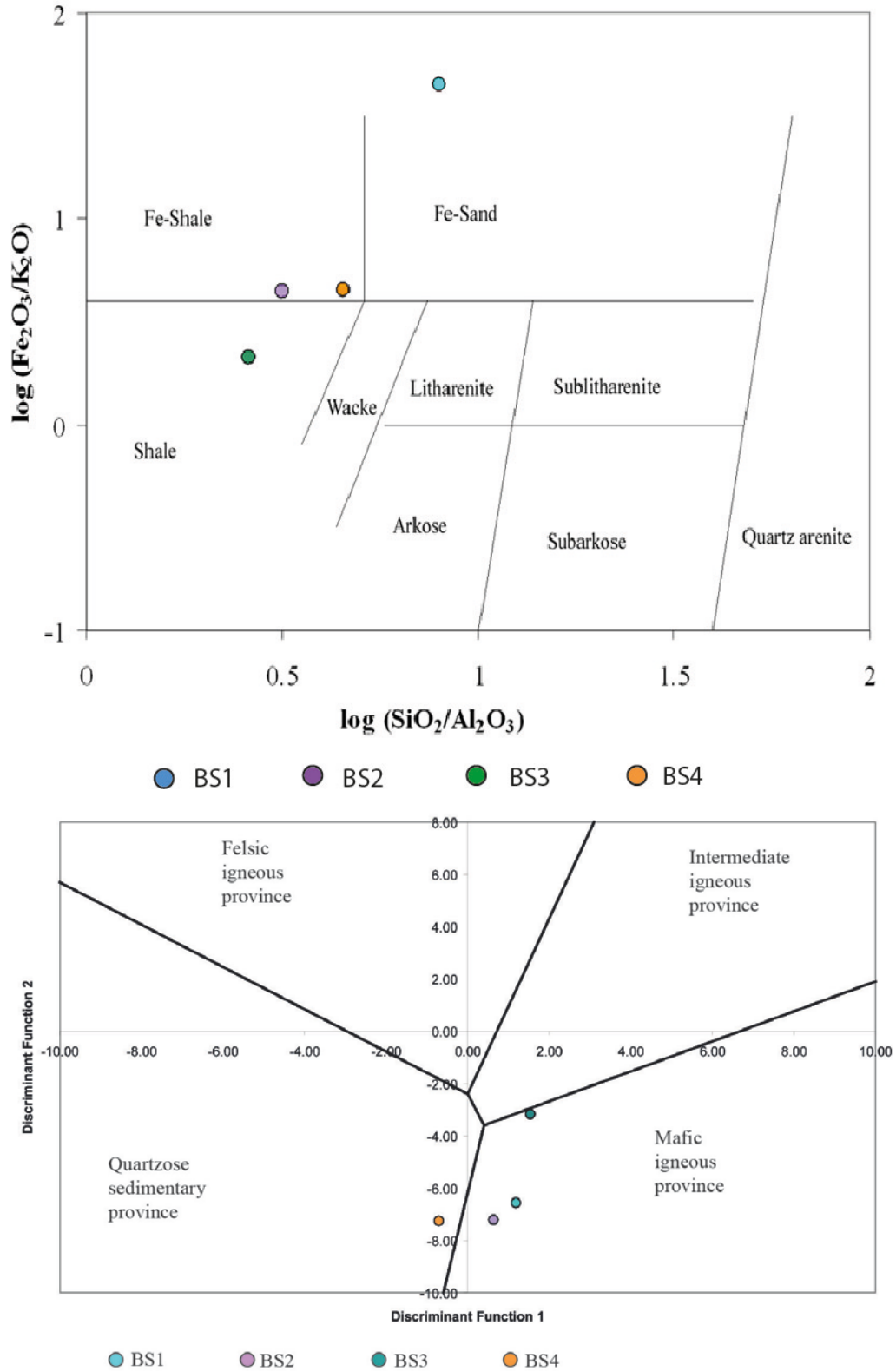


Figure 4.14: Sediment classification diagram of (a) $\log(\text{SiO}_2/\text{Al}_2\text{O}_3)$ versus $\log(\text{Fe}_2\text{O}_3/\text{K}_2\text{O})$ differentiating the Stradbally sediments into iron rich sand, iron rich shale and shale (after Herron, 1988) and (b) sediment provenance determination graphs of Roser and Korsch (1988) where discriminant function 1 = $((-1.773 \cdot \text{TiO}_2) + (0.607 \cdot \text{Al}_2\text{O}_3) + (0.76 \cdot \text{Fe}_2\text{O}_3) - (1.5 \cdot \text{MgO}) + (0.616 \cdot \text{CaO}) + (0.509 \cdot \text{Na}_2\text{O}) - (1.244 \cdot \text{K}_2\text{O}) - 9.09)$ and discriminant function 2 = $((0.445 \cdot \text{TiO}_2) + (0.07 \cdot \text{Al}_2\text{O}_3) - (0.25 \cdot \text{Fe}_2\text{O}_3) - (1.142 \cdot \text{MgO}) + (0.438 \cdot \text{CaO}) + (1.475 \cdot \text{Na}_2\text{O}) + (1.426 \cdot \text{K}_2\text{O}) - 6.861)$.

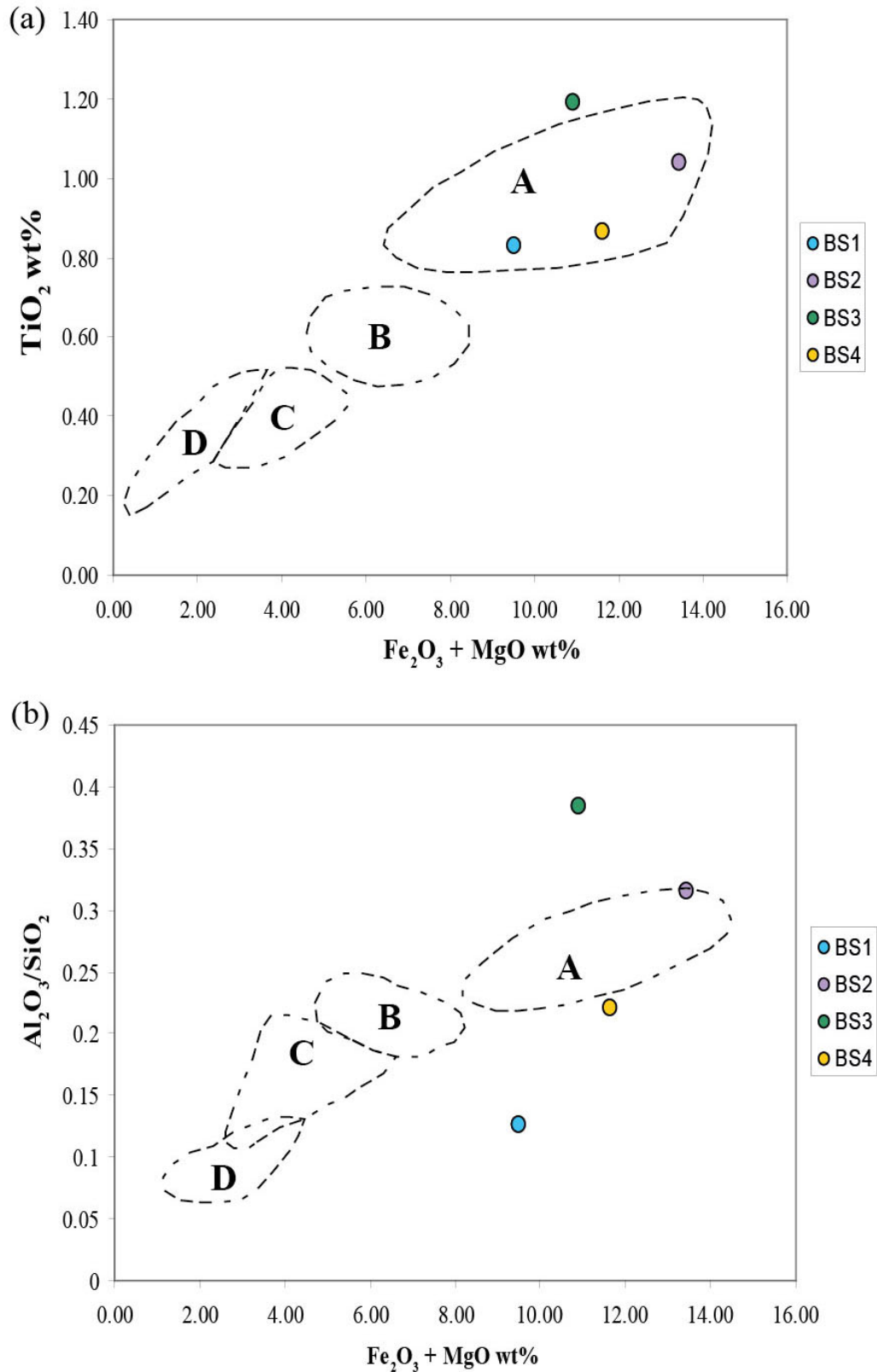


Figure 4.15: Bivariate discrimination diagram of (a) TiO_2 versus $\text{Fe}_2\text{O}_3 + \text{MgO}$ and (b) $\text{Al}_2\text{O}_3/\text{SiO}_2$ versus $\text{Fe}_2\text{O}_3 + \text{MgO}$ after Bhatia (1983) differentiating the tectonic setting of sedimentary samples. A = Oceanic Island Arc; B = Continental Island Arc; C = Active Continental Margin; D = Passive Margin.

4.3.5 Mineral chemistry

The mineral chemistry of the major primary and secondary minerals in the volcanic and sedimentary rocks is presented in Tables 4.5, 4.6, 4.9 and 4.10. The only primary minerals recorded are quartz and feldspar, though these also occur in abundance as secondary minerals. The main chemical and textural features of specific mineral phases, as identified through micro-analysis, are discussed below.

Quartz

Quartz from all volcanic and sedimentary samples was analysed. Quartz generally occurs as small sub-rounded crystals (50-100µm) within the sedimentary rocks and in the sedimentary components of peperite and commonly in the groundmass of volcanic lithologies (Figure 4.16a). Larger quartz crystals (200µm) occur within the tuff, or are accompanied by pyrite and/or chlorite in both tuff and magmatic clasts in peperite. These larger quartz crystals are commonly observed overgrowing or replacing primary minerals and surrounding or hosting inclusions of other secondary minerals (e.g. chlorite). Homogenous patches of quartz associated with the development of pyrite nodules represent secondary fluid flow, mineral growth and vein deposition.

Feldspar

Feldspar predominantly occurs within the groundmass of both sedimentary and volcanic lithologies (Figure 4.16a); with larger degraded, isolated, sub-rounded to rounded crystals (500µm-1mm) occurring in association with alteration minerals such as chlorite. The majority of plagioclase feldspar crystals analysed have an albite composition (Table 4.5), ranging from oligoclase to pure albite, indicating that these are secondary compositions probably formed as a result of spillitization. The alkali feldspars are influenced significantly by the presence of Na, with rare crystals of a pure orthoclase composition and the remainder ranging from Na-rich orthoclase to anorthoclase (average molar percent = Ab:76.3 An:5.1 Or:18.6).

Calculated Mineral Formula:

Albite	$\text{Na}_{(0.6-0.8)}\text{Ca}_{(0.01-0.05)}[\text{AlSi}_3\text{O}_8]$
Na-rich orthoclase	$\text{Na}_{0.4}\text{K}_{0.1}[\text{Al}_{1.1}\text{Si}_{2.9}\text{O}_8]$
Anorthoclase	$\text{Na}_{0.26}\text{K}_{0.15}[\text{Al}_{1.1}\text{Si}_{2.9}\text{O}_8]$
Orthoclase	$\text{K}_{0.92}\text{Na}_{0.01}[\text{AlSi}_3\text{O}_8]$

Feldspar						
Oxide wt%	<i>1</i>	<i>2</i>	<i>3</i>	<i>4</i>	<i>5</i>	<i>6</i>
SiO₂	62.85	67.11	71.2	62.79	69.99	71.42
TiO₂	0.16	0.02	0.01	0.01	0	0.02
Al₂O₃	23.67	24.74	20.31	24.67	19.82	21.03
FeO	3.81	0.79	0.1	0.85	0.3	0.32
MnO	0.01	0	0.01	0.01	0	0.03
MgO	1.74	0.2	0	0.76	0.03	0
CaO	0.05	0.74	0.07	0.47	0.02	0.14
Na₂O	0.07	6.21	8.02	4.84	8.14	7.4
K₂O	6.93	2.48	0.03	4.27	0.03	0.37
Total	99.34	102.34	99.82	98.77	98.42	100.73

Table 4.5: Representative major element composition of feldspar from (1) tuff matrix and (2, 3) basaltic andesite and (4-6) peperite clasts.

Chlorite

Chlorite is present within all samples and varies from magnesium to iron-rich (Table 4.6). Chlorite occurs within veins, overgrowths, within the groundmass/matrix, as alteration rims around phenocrysts, as inclusions within other secondary minerals (e.g. epidote; Figure 4.16b) and as complete crystals (pseudomorphs) up to 1mm in size. The abundance of chlorite, dominantly pycnochlorite and ripidolite (Figure 4.17), throughout all lithologies, particularly within veins and as overgrowths indicates this is a dominant alteration product throughout the whole succession. Fe numbers ($\text{Fe}/(\text{Fe} + \text{Mg}) = \sim 0.5$) for pycnochlorite and ripidolite do not vary significantly, as it is the Si cation value that controls the defined field of chlorite compositions in this case (Figure 4.17). The variations in the Mg and Fe content of chlorite do not seem to be controlled by the host rock type or position within any of the samples i.e. whether it is associated with iron or magnesium rich minerals (Figure 4.16, 4.17), such that there must be an alternative reason for chemical variation such as variable temperatures of alteration (Kranidiotis and MacLean, 1987) or variation in the composition of the hydrothermal fluid (Teagle and Alt, 2004). Textural variations within chlorite vary between samples and location within samples (e.g. adjacent to magma-sediment contact). Widespread amorphous chlorite alteration in homogenous patches occurs in all samples but is particularly well developed close to magma-sediment contacts due to the higher

glass content (Figure 4.16a) while inclusions of chlorite crystals within masses of epidote only occurs in peperite (Figure 4.16b). Other chlorite textures include zoned or ropy chlorite, chlorite needles and chlorite pseudomorphs, with all samples containing some combination of these. The variation in chlorite texture appears to be in part controlled by the variation in chemical composition. Although the Fe number does not vary significantly, the larger crystals of chlorite have a higher Fe content than needles, smaller crystals and homogenous patches of chlorite in the groundmass/matrix (Table 4.7)

Calculated Mineral Formula:

Low Mg content → $\text{Mg}_{(3.5)}\text{Fe}_{(4.6)}\text{Al}_{(3.3)}\text{Mn}_{(0.05)}[\text{Si}_{(5.2)}\text{Al}_{(2.8)}]\text{O}_{20}\text{OH}_{16}$

Medium Mg content → $\text{Mg}_{(4.4)}\text{Fe}_{(4.6)}\text{Al}_{(3.3)}\text{Mn}_{(0.09)}[\text{Si}_{(5.4)}\text{Al}_{(2.6)}]\text{O}_{20}\text{OH}_{16}$

High Mg content → $\text{Mg}_{(4.8)}\text{Fe}_{(4.3)}\text{Al}_{(2.7)}\text{Mn}_{(0.09)}[\text{Si}_{(5.5)}\text{Al}_{(2.5)}]\text{O}_{20}\text{OH}_{16}$

[The variation in Fe number, as controlled by the ratio of Mg to Fe, is predominantly influenced by the amount of Mg as Fe levels do not fluctuate between samples with high or low Fe numbers.]

Chlorite						
Oxide wt%	1	2	3	4	5	6
SiO ₂	28.52	29.74	27.18	25.08	27.71	23.26
TiO ₂	0.05	0.02	0.01	0.09	0.02	0.02
Al ₂ O ₃	20.51	17.81	21.46	23.54	22.2	23.25
FeO	25.39	20.2	24.92	27.85	25.56	31.53
MnO	0.41	0.34	0.55	0.38	0.47	0.32
MgO	16.36	22.99	15.54	12.56	11.92	11.53
CaO	0.05	0.09	0.06	0.06	0.04	0.01
Na ₂ O	0.05	0.01	0.02	0.04	0.02	0.04
K ₂ O	0.01	0.05	0.02	0.02	0.46	0.01
Total	91.37	91.29	89.86	89.69	88.41	90.01

Table 4.6: Representative major element composition of chlorite from (1-4) groundmass and phenocrysts in intrusive rocks and magmatic clasts in peperite, (5) tuff and (6) mudstone associated with pyrite.

TEXTURE	SAMPLE	FE #
Needle-like crystals	Basaltic andesite sill (BT10)	0.45
Needle-like crystals	Basaltic andesite sill (BT10)	0.47
Fibrous crystals	Peperite (BT15)	0.51
Fibrous crystals	Peperite (BT15)	0.55
Rosette crystals	Peperite (BT15)	0.53
Rosette crystals	Peperite (BT15)	0.55
Groundmass	Peperite (BT15)	0.46
Groundmass	Bedded tuff (BT9)	0.49
Alteration halo of pyrite	Mudstone (BS4)	0.62

Table 4.7: The variation in Fe number ($\text{Fe}/(\text{Fe} + \text{Mg})$) or the Fe to Mg ratio in various chlorite forms within different samples show that smaller crystals and chlorite within the groundmass/matrix are Mg-rich (low Fe numbers), larger crystals have approximately equal proportions of Fe and Mg or are Mg-poor and chlorite associated with Fe-rich minerals such as pyrite are extremely Mg-poor.

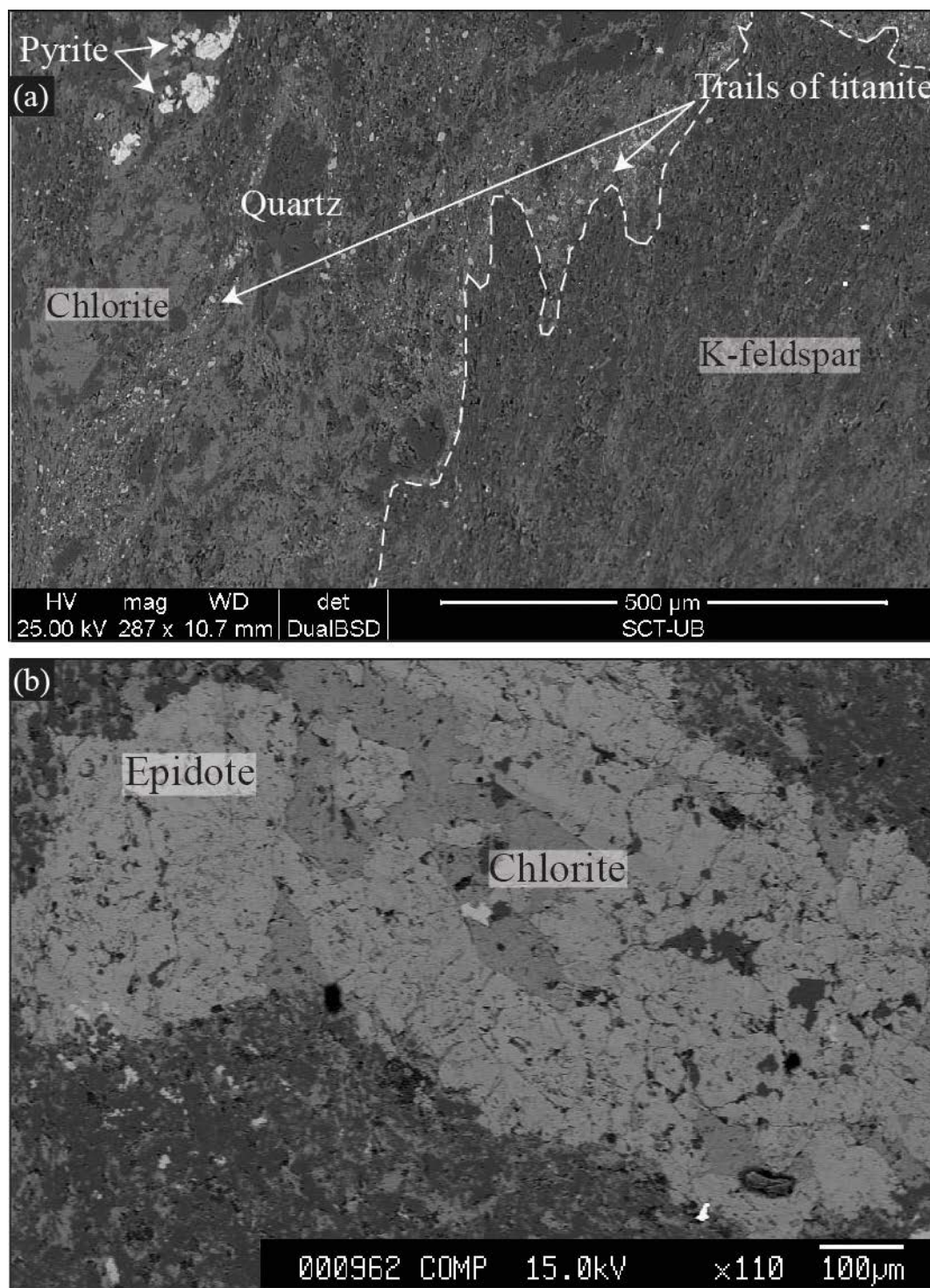


Figure 4.16: Backscatter electron images of (a) homogenous, feldspar-rich mudstone and chlorite-rich basaltic andesite, with associated minor quartz and rare pyrite and titanite (dashed line represents contact between mudstone and basaltic andesite; sample BS31) and (b) mass of epidote surrounding chlorite crystals in peperite clast (sample BT15).

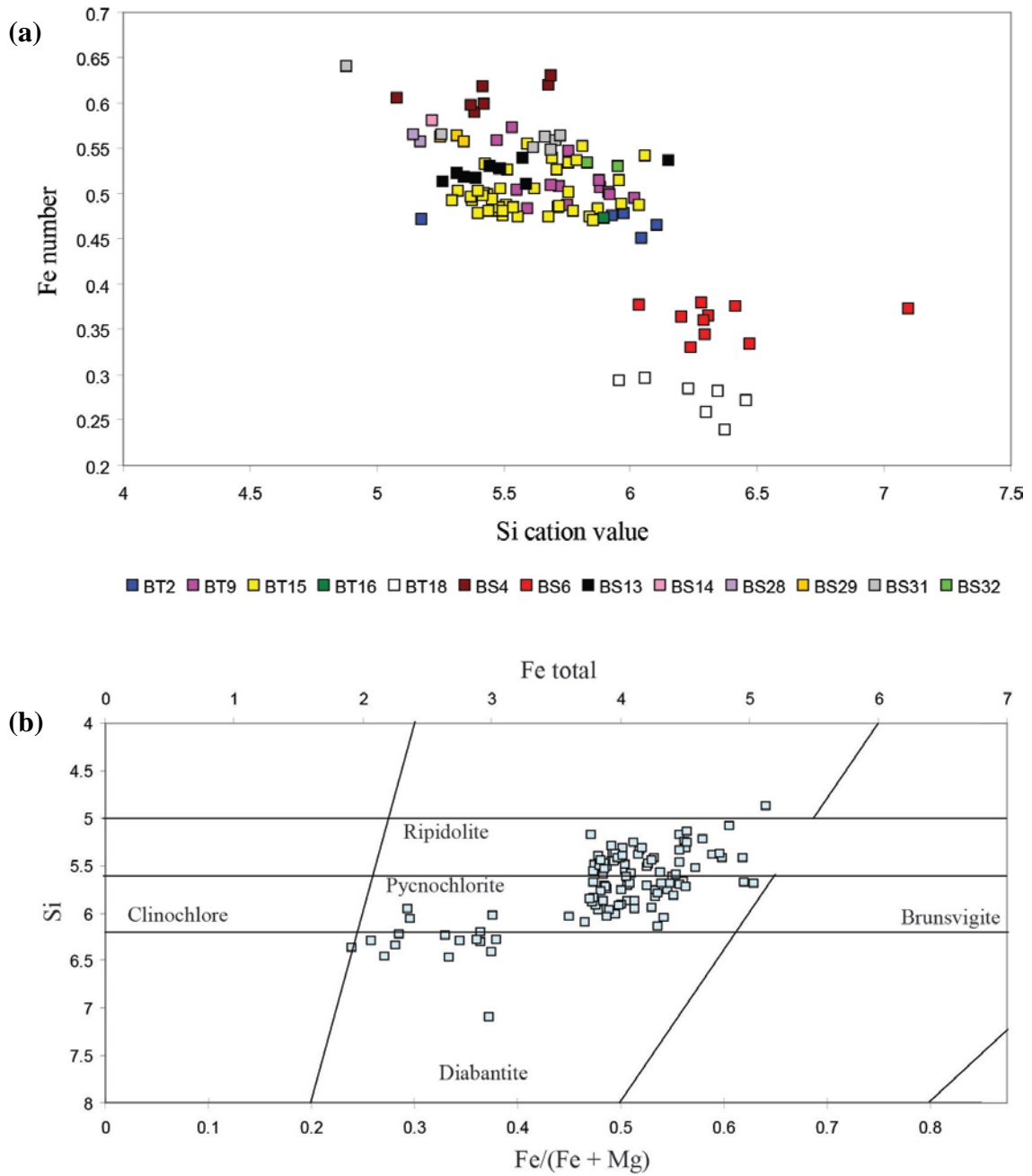


Figure 4.17: Graphs of the chemical composition of chlorites showing (a) the relationship between Fe number ($\text{Fe}/\text{Fe} + \text{Mg}$) and Si (details of samples and sample descriptions are given in Table 4.2) and (b) the variation in chlorite type based on the Si and Fe content and the Fe number (plotted on a Hey (1954) diagram). The majority of chlorites analysed in this study are ripidolite and pycnochlorite.

Variations in the chemical composition of chlorite (e.g. Figure 4.17) are proposed to reflect variation in the temperature of chlorite formation (e.g. Reed, 1997). Chlorite geothermometry has thus been applied to a variety of rock types to determine formation conditions (Cathelineau and Niveau, 1985; Kranidiotis and MacLean, 1987; Cathelineau, 1988; Jowett, 1991, with a summary of techniques given in Zhang *et al.*, 1997). Many authors have recognised the variation in chlorite composition relating to relative distances from VHMS deposits (Hendry, 1981; Gifkins *et al.*, 2005), with chlorite close to the deposit predominantly Mg-rich and a general increase in Fe/Mg ratio from the deposit centre to the margins. Three different chlorite geothermometry techniques were employed in order to determine the temperature of formation of chlorite and hence constrain the temperature at which hydrothermal alteration took place (Table 4.8). The calculations used by Kranidiotis and MacLean (1987) and Jowett (1991) take into account a variation between Fe and Al_{iv} content, whereas the calculation used by Cathelineau (1988) suggests there is no relationship between these. Each of the three methods used yields a wide temperature range (310°C-360°C - Kranidiotis and MacLean, 1987; 624°C-860°C – Jowett, 1991; 620°C-860°C – Cathelineau, 1988) with the most likely temperatures in the range of 300°C-400°C, indicating the last two geothermometers are less reliable. The range of temperatures calculated and averages of each sample set are given in Figure 4.18.

	T1 (°C)	T2 (°C)	T3 (°C)
Trawnamoe:			
BT15-1	332.66	782.95	783.76
BT15-2	320.86	749.79	750.52
BT15-3	326.67	763.31	764.50
BT15-4	328.88	774.58	775.02
BT15-5	321.62	746.57	748.11
BT15-6	328.34	768.14	769.32
BT15-7	339.27	800.66	801.64
BT15-8	318.47	743.67	744.30
BT15-9	312.10	724.68	725.43
BT15-10	317.96	739.49	740.52
BT15-11	320.54	747.86	748.74
BT15-12	318.73	743.35	744.13
BT15-13	333.14	783.60	784.51
BT15-14	324.59	761.06	761.69
BT15-15	340.90	808.07	808.63
BT15-16	279.12	622.29	624.30
BT15-17	324.20	756.87	757.97
BT15-18	328.73	769.75	770.86
BT15-19	330.34	766.86	769.09
BT15-20	330.96	775.55	776.74
BT15-21	314.95	730.79	731.84
Stradbally Cove:			
BS13-1	338.12	793.58	795.13
BS13-2	332.74	777.48	779.14
BS13-3	341.10	801.95	803.52
BS13-4	311.46	714.37	716.40
BS14-1	355.94	833.50	836.69
BS29-1	351.01	822.88	825.55
BS29-2	323.17	746.25	748.51
BS29-3	344.19	801.95	804.84
BS29-4	340.81	792.93	795.74
BS28-1	358.99	848.32	850.58
BS28-2	362.62	857.65	860.07

Table 4.8: Temperature of chlorite formation calculated from a range of geothermometers, with temperatures ranging from 311°C to 857°C, dependant on sample analysed and geothermometer used. $T1 = 106Al^{iv} + 18$, where $Al_{iv} = Al^{iv} + 0.7(Fe/Fe + Mg)$ (Kranidiotis and MacLean, 1987); $T2 = -61.92 + 321.98(Al^{iv})$ (Cathelineau, 1988) and $T3 = 319Al_c^{iv} - 69$, where $Al_c^{iv} = Al^{iv} + 0.1(Fe/Fe + Mg)$ (Jowett, 1991). Samples BT15 = fluidal peperite clast; BS13 = honeycomb peperite clast; BS14 = coherent intrusive rock; BS29 = mixed morphology peperite clast; BS28 = intrusive rock with irregular margins.

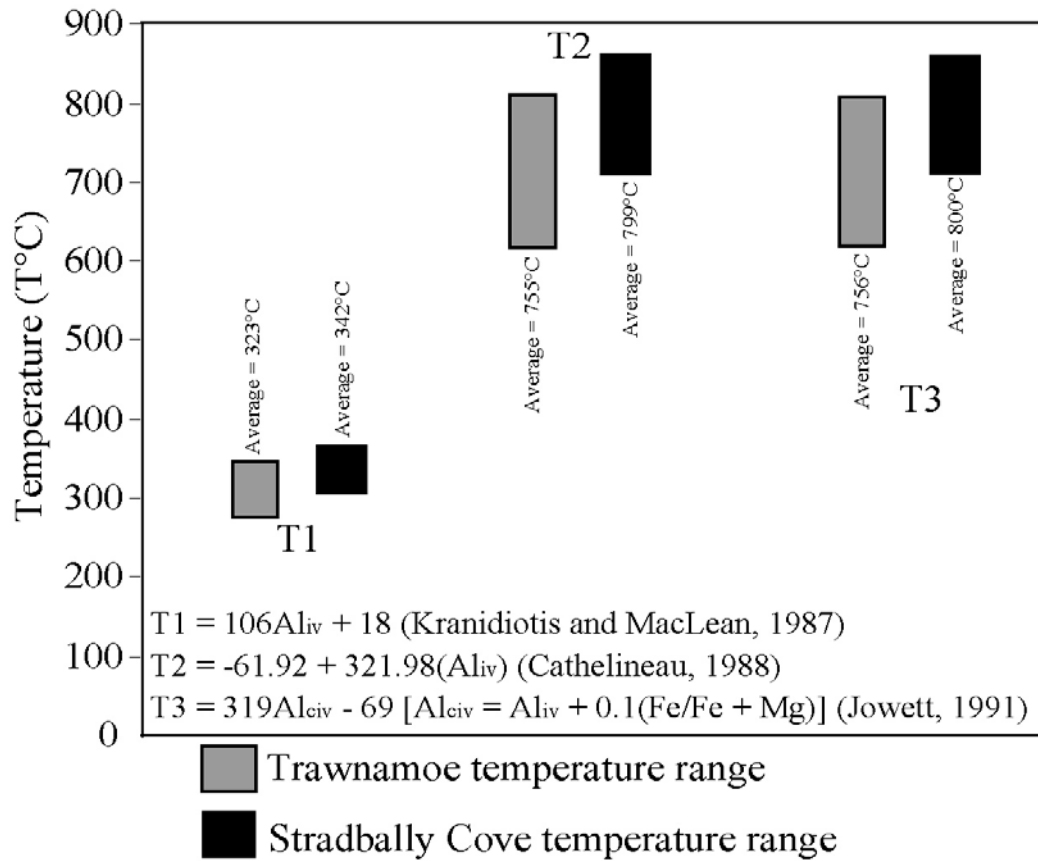
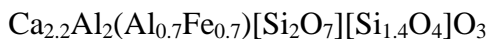


Figure 4.18: Temperature variations as determined by chlorite geothermometry in all samples analysed using the methods of Kranidiotis and MacLean (1987), Cathelineau (1988) and Jowett (1991). The calculation of Kranidiotis and MacLean, taking Fe and Mg content of chlorites into account, yields a much lower, and probably more realistic, temperature estimate.

Pumpellyite

Whereas chlorite is ubiquitous in all lithologies, pumpellyite is only locally developed within intrusive rocks, peperite clasts and bedded tuff (samples BT2, BT9 and BT15) in Trawnamoe. The dominant occurrence of pumpellyite is within magmatic clasts in peperite (close to the magma-sediment interface) and commonly associated with other hydrous alteration minerals. Pumpellyite crystals occur as inclusions within phenocrysts of epidote, as alteration rims around phenocrysts of chlorite and as elongate and occasionally stubby crystals (up to 100µm) within the groundmass. This is a typically common association of minerals (chlorite-epidote-pumpellyite) within sub-greenschist facies metabasalts (Deer *et al.*, 1992).

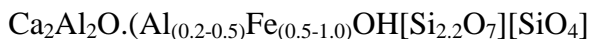
Calculated Mineral Formula:



Epidote

Epidote is present within the sills and other intrusive rocks from both Trawnamoe and Stradbally Cove that have interacted with wet sediment to form peperite but occurs most extensively within the magmatic clasts of the peperite at Trawnamoe. Small epidote phenocrysts that are stubby to elongated are common within peperite clasts and those that have ragged, altered edges are generally found associated with abundant chlorite alteration and rare pumpellyite (Figure 4.18). Epidote abundance decreases rapidly from peperite clast margins to the centre of peperite clasts and within the coherent sill. Glomeroporphyritic masses of epidote are Ca and Fe rich (Table 4.9) and probably (along with Fe-Mg chlorite) represent secondary replacement of original clinopyroxene. Occasional crystals of epidote are incorporated into the host tuff matrix of peperite, probably representing incorporation of minor mafic glass fragments during peperite formation.

Calculated Mineral Formula:



Accessory minerals

Apatite is only present within a peperite clast from Stradbally Cove (sample BS31). Two separate occurrences have been recorded of apatite from the magmatic clast, one isolated crystal and one trail of small crystals. Anhedral crystals within the trail are approximately 5µm in size are surrounded by chlorite

crystals, approximately 400µm from the contact with homogenous mudstone (Table 4.10). Fe-oxides are disseminated throughout all lithologies and, similar to pyrite, are associated with Fe-rich chlorite (Figure 4.19). Sphene occurs as inclusions within chlorite (Figure 4.20), commonly associated with pyrite, in intrusive rocks and peperite clasts. Ti-oxides (rutile) usually appear as large (200µm), cracked crystals and are commonly associated with sphene.

Pumpellyite				Epidote		
Oxide wt%	1	2	3	4	5	6
SiO ₂	37.84	38.57	39.27	38.17	38.49	39.27
TiO ₂	0.08	0.029	0.073	0.04	0.03	0.073
Al ₂ O ₃	23.87	26.71	26.593	22.59	24.65	26.59
FeO	13.65	9.99	10.012	14.1	12.75	10.01
MnO	0.535	0.105	0.295	0.12	0.57	0.29
MgO	0.381	0	0	0.01	0.05	0
CaO	22.62	23.654	23.511	23.78	23.27	23.51
Na ₂ O	0	0	0	0.01	0.01	0
K ₂ O	0.01	0.028	0.007	0.01	0	0.01
Total	99.016	99.104	99.786	98.84	99.84	99.78

Table 4.9: Representative major element composition of pumpellyite from peperite clasts (1-3) associated with chlorite alteration, and epidote from intrusive rocks (4-5) and peperite clasts (6).

Apatite				Sphene		
Oxide wt%	1	2		Oxide wt%	1	2
FeO	0.26	0.21		SiO ₂	31.28	34.2
MnO	0.05	0.05		TiO ₂	34.12	30.3
MgO	0.02	0		Al ₂ O ₃	4.32	7.55
CaO	54.63	54.18		FeO	1.07	0.8
SrO	n.a.	n.a.		MnO	0.02	0.01
Na ₂ O	0	0		MgO	0	0.22
K ₂ O	0.01	0.03		CaO	29.48	24.09
P ₂ O ₅	43.35	43.87		Na ₂ O	0.03	0.01
				K ₂ O	0	1.27
Total	98.94	98.64		Total	100.32	98.6

Table 4.10: Representative major element composition of apatite in inclusion trails in peperite clast and sphene occurring as inclusions in albite (3) and chlorite (4) crystal in peperite clast.

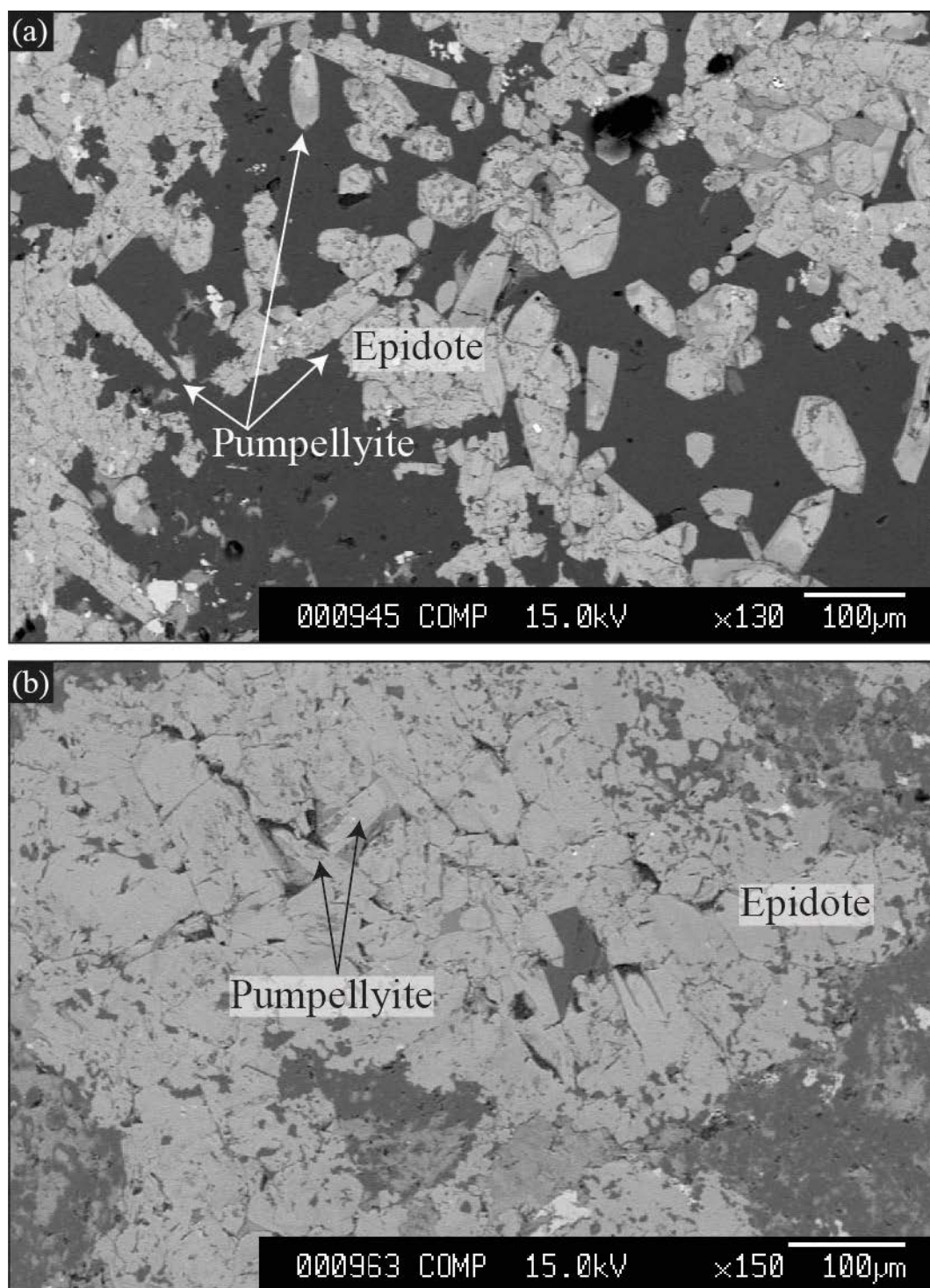


Figure 4.19: Backscatter electron images of (a) abundant epidote crystals within the fine-grained groundmass of a peperite clast (sample BT15) and (b) pumpellyite crystals hosted within a glomeroporphyritic cluster of epidote in basaltic andesite (sample BT2).

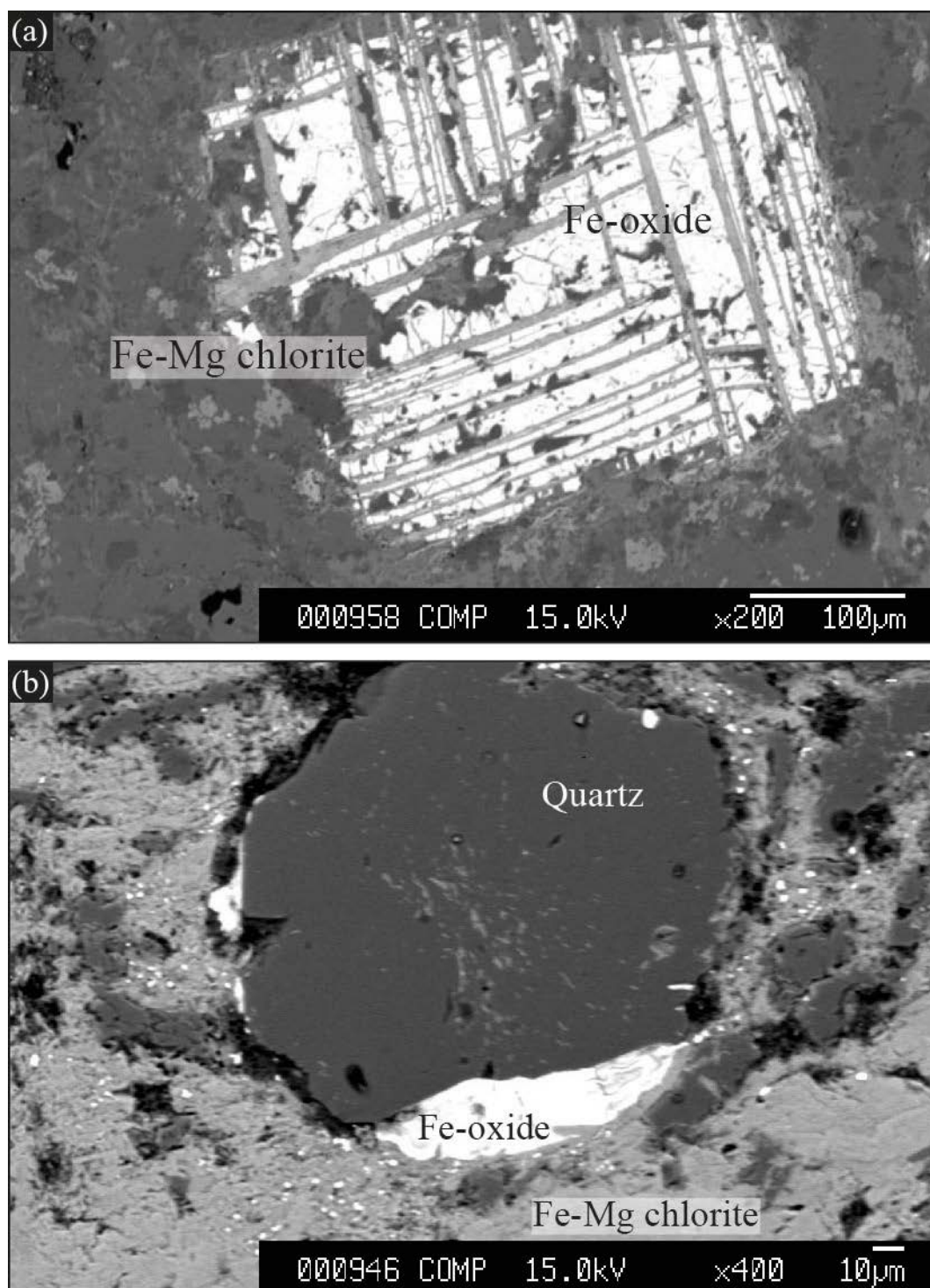


Figure 4.20: Backscatter electron image of (a) fractured iron oxide crystal with associated Fe-Mg chlorite alteration in basaltic andesite (sample BS6) and (b) halo of iron oxide surrounding quartz crystal in basaltic andesite peperite clast (sample BS31). Note the trail of chlorite crystals within the quartz crystal.

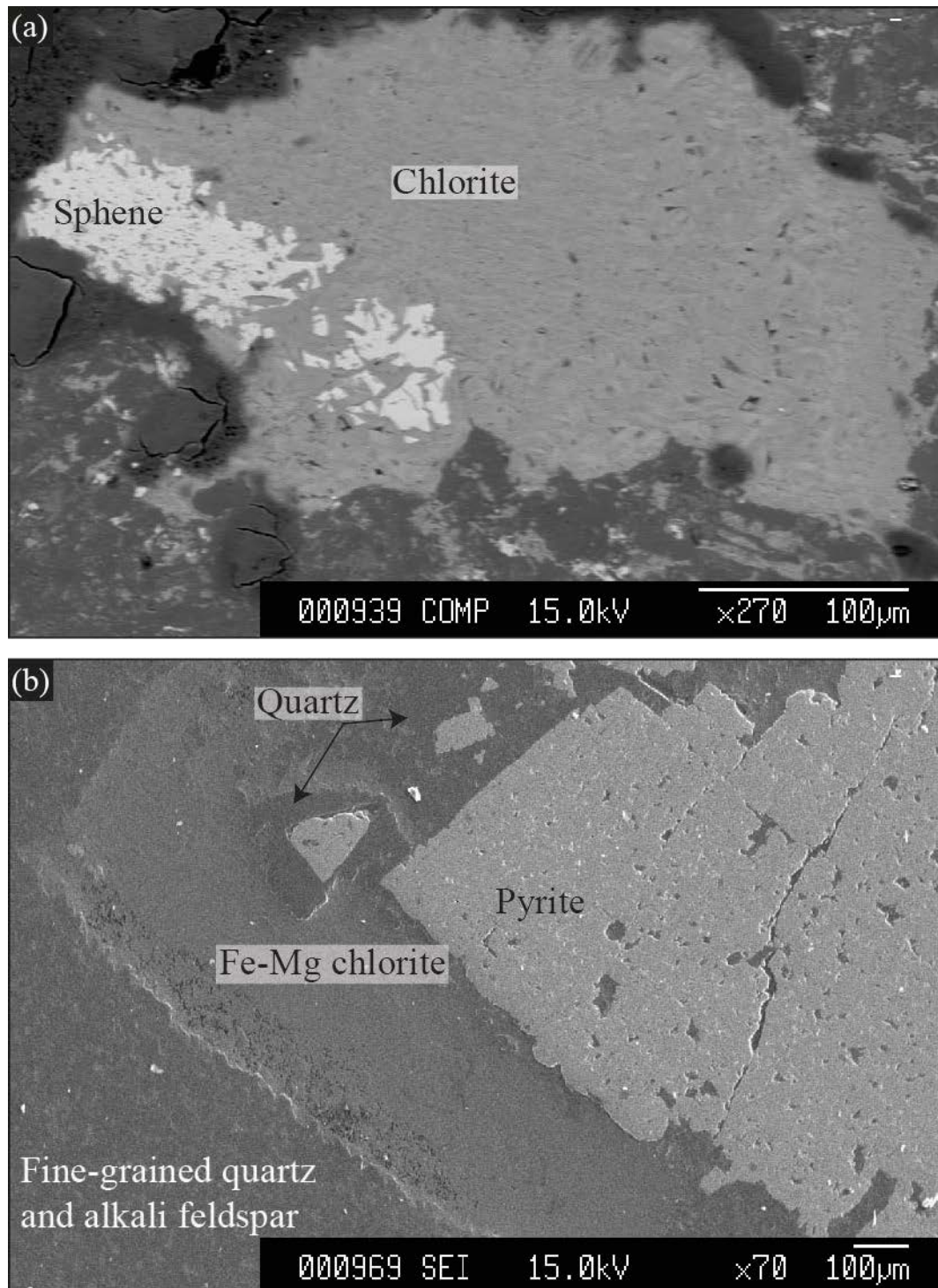


Figure 4.21: Backscatter electron images of (a) inclusions of sphene within chlorite in peperite clast (sample BT15) and (b) cluster of pyrite crystals within fine-grained mudstone with associated quartz veining and chlorite alteration (sample BS4).

4.3.6 Element mapping

Element mapping across the magma-sediment interface in peperite was carried out to determine the nature of any chemical exchange between the end member components. Element maps were produced by combining SEM (backscatter and secondary electron) imaging with EDS analysis. Figures 4.22 to 4.24 show the nature of the magma-sediment interface in fluidal peperite, honeycomb peperite and mixed morphology peperite respectively, in terms of their chemical components.

BT15:

Peperite sample BT15 (Trawnamoe, Table 4.2) consists of roughly spherical basaltic andesite clasts with ragged margins separated by up to 2cm silicified andesitic ash tuff (Figure 4.22a). The contrast in Si and Al (Figure 4.22a, b) concentrations across the magma/sediment boundary helps to define the nature of the interface, which is a sharp contact with small scale interfingering of the magmatic and sedimentary components in places. The difference in composition between magmatic clast and tuff matrix is illustrated best by Si content (~57wt% for the basaltic andesite and 73.7wt% for the silicified ash tuff, Appendix A5) and is clearly visible within the element maps (Figure 4.22b). The tuff is extremely Si-rich, with quartz a dominant mineral phase as a result of silicification. Al is present in greater abundances within the magmatic clasts (sill: $\text{SiO}_2 = 56.9\text{wt}\%$, $\text{Al}_2\text{O}_3 = 18.2\text{wt}\%$; tuff: $\text{SiO}_2 = 73.75\text{wt}\%$, $\text{Al}_2\text{O}_3 = 11.4\text{wt}\%$).

Bright areas on the Ca map (Figure 4.22d) highlight the presence of alteration minerals such as epidote (\pm rare pumpellyite) within the margin of the magmatic clast that are rare or absent in the interior of magmatic clasts. The distribution of epidote and pumpellyite within magmatic clasts indicates that the formation of these minerals is a consequence of chemical interactions at the magma-sediment interface, either at the time of formation or subsequently. Figure 4.22e and 4.22f shows greater abundance of Fe and Mg-rich minerals in the magmatic clast than the tuff matrix, in keeping with bulk rock composition (sill: $\text{Fe}_2\text{O}_3 = 9.71\text{wt}\%$, $\text{MgO} = 5.4\text{wt}\%$; tuff: $\text{Fe}_2\text{O}_3 = 5.1\text{wt}\%$, $\text{MgO} = 2.9\text{wt}\%$). Alteration of the mafic minerals has resulted in the formation of Fe-Mg chlorite. Thus the element distribution maps of Ca, Fe and Mg (Figure 4.22) reflect the shape, occurrence

and distribution of alteration minerals (epidote, pumpellyite and chlorite) within the mafic end member of peperite.

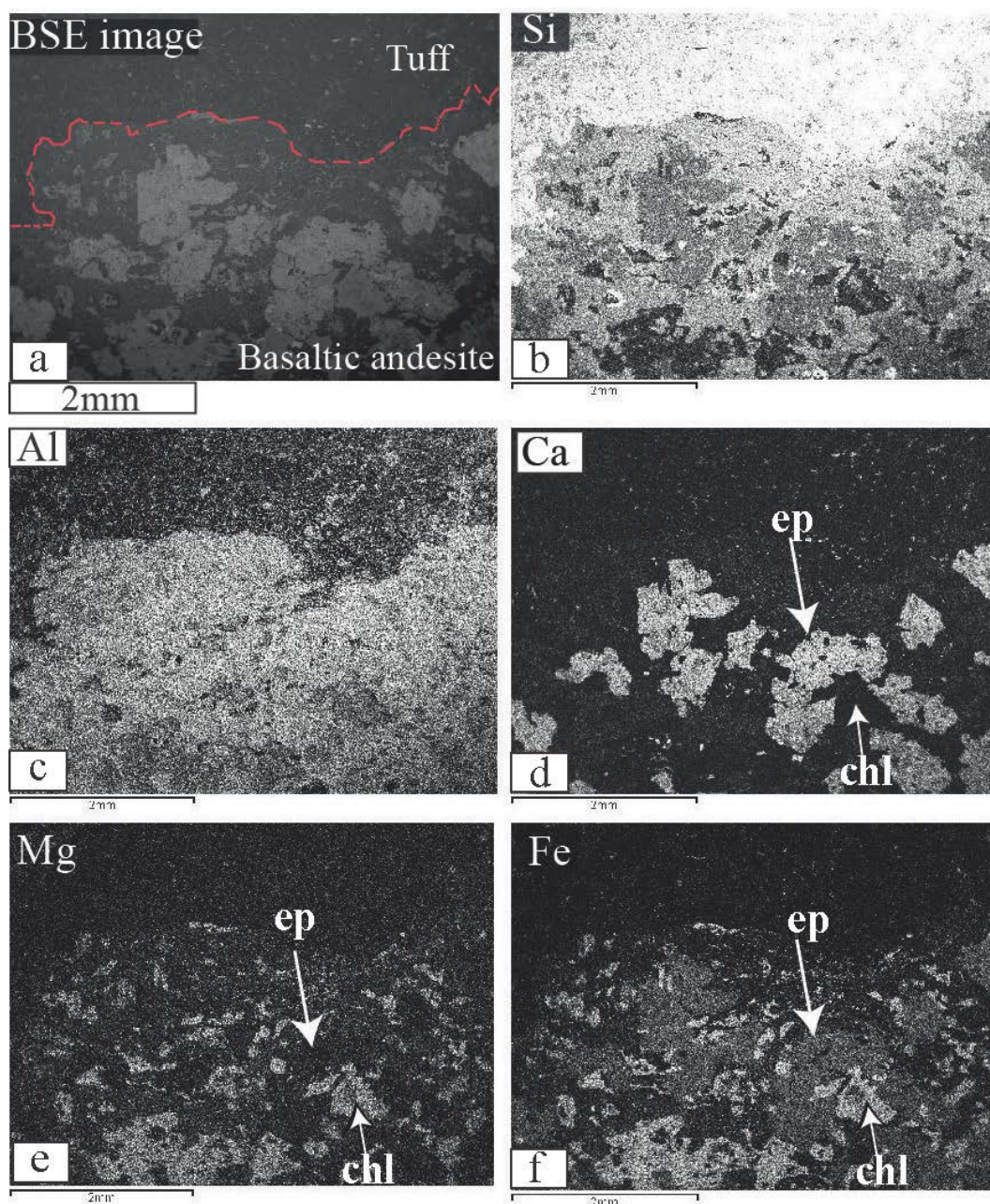


Figure 4.22: Backscatter electron image (a) of the magma-sediment interface in fluidal peperite from Trawnamoe (sample BT15) and element distribution maps, b-f (Si, Al, Ca, Mg and Fe) across the contact. Concentrations are shown in greyscale, ranging from black (low concentrations) to white (high concentrations). Note arrowed areas in maps of Ca, Mg and Fe distribution displaying the high Ca, medium Fe epidote (ep) mantling Fe-Mg chlorite (chl).

BS32:

Peperite sample BS32 (honeycomb peperite, Stradbally Cove, Table 4.2) consists of basaltic andesite clasts in a mudstone matrix, obtained approximately 3cm from the contact with a coherent basaltic andesite intrusion. The contact between magmatic clast and sedimentary host is sharp but irregular in shape (Figure 4.23a). The element distribution maps for Si, Al and K (Figure 4.23b-d) emphasise the textural differences between the fine-grained, more chemically homogeneous sedimentary component and the crystal controlled distribution of elements in basaltic andesite. The similar distribution patterns of Si, Al and K within the mudstone probably represent clay minerals and feldspar. Mg and Fe concentrations (Figure 4.23e and Figure 4.23f) have very similar spatial distributions, reflecting the presence of chlorite within the magmatic clast, in which mineral the average Mg : Fe : Al : Si ratio is 4 : 4.3 : 5.8 : 5.4. Those areas with high Mg and Fe contents combined with a lower Al content are representative of the margins of chlorite crystals where the heavier elements (Mg + Fe) have been leached and are deposited in veinlets between crystals (oval area in Figure 4.23).

BS31:

Peperite sample BS31 (mixed morphology peperite, Stradbally Cove, Table 4.2) consists of porphyritic basaltic andesite magmatic clasts within mudstone. Si content is highest within the mudstone, suggesting a dominance of quartz. The higher K concentrations that correlate with Si within the mudstone indicate the presence of K-feldspar/sericite. Local mobilisation of Si is observed where a narrow quartz vein cross-cuts both sedimentary host and magmatic clast (Figure 4.24b). Bulk rock analysis of the basaltic andesite and mudstone yields iron concentrations of approximately 7 wt% and 13 wt% respectively (Appendix A5). However, the high iron content in the mudstone is due to abundant pyrite crystals that are not evenly dispersed throughout the lithology, such that the element maps display a lower iron concentration in mudstone (Figure 4.24e). Mg and Fe have an inverse relationship with Si, and are the dominant elements within the magmatic clasts, once more reflecting the more mafic nature of the basaltic andesite and associated chlorite alteration.

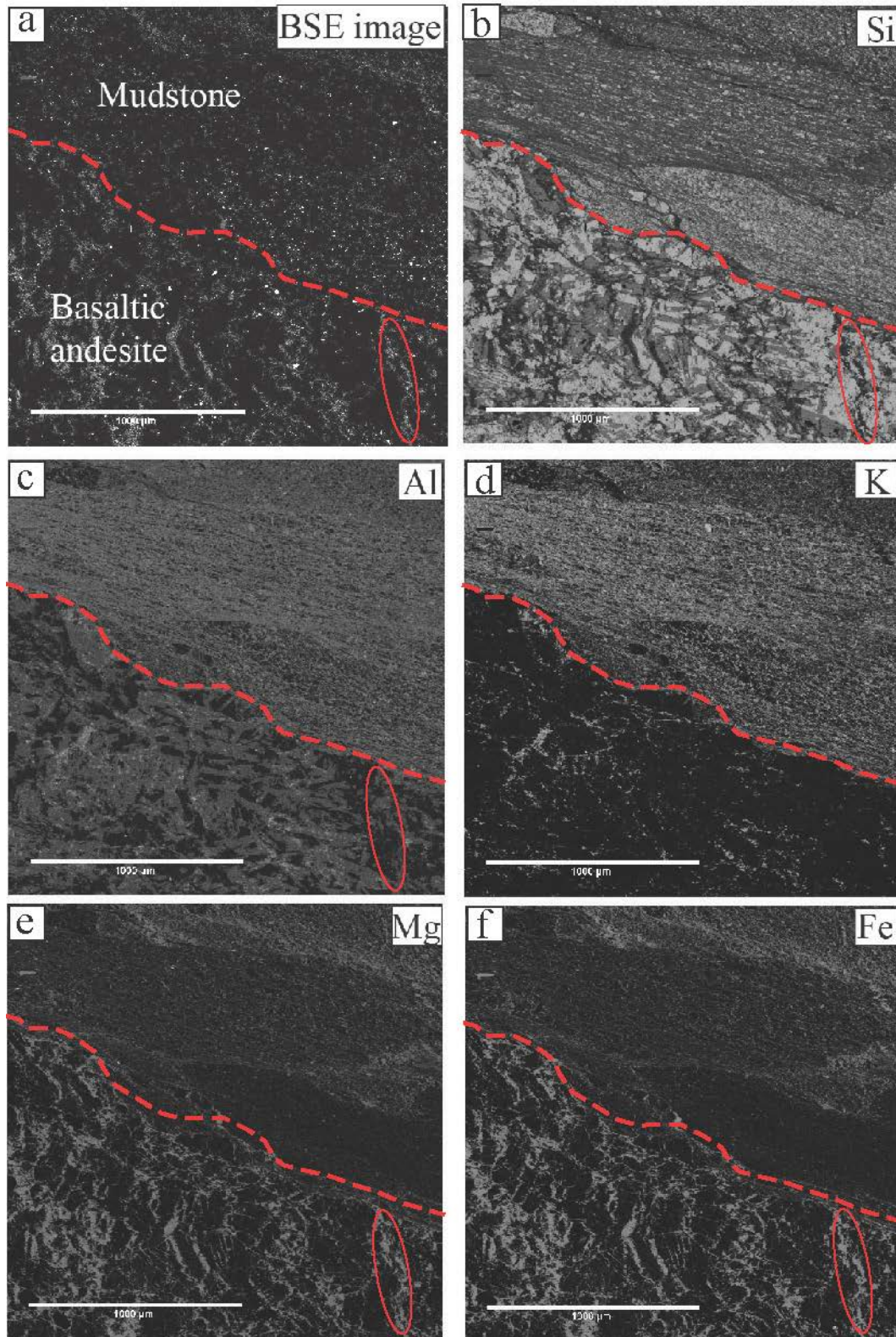
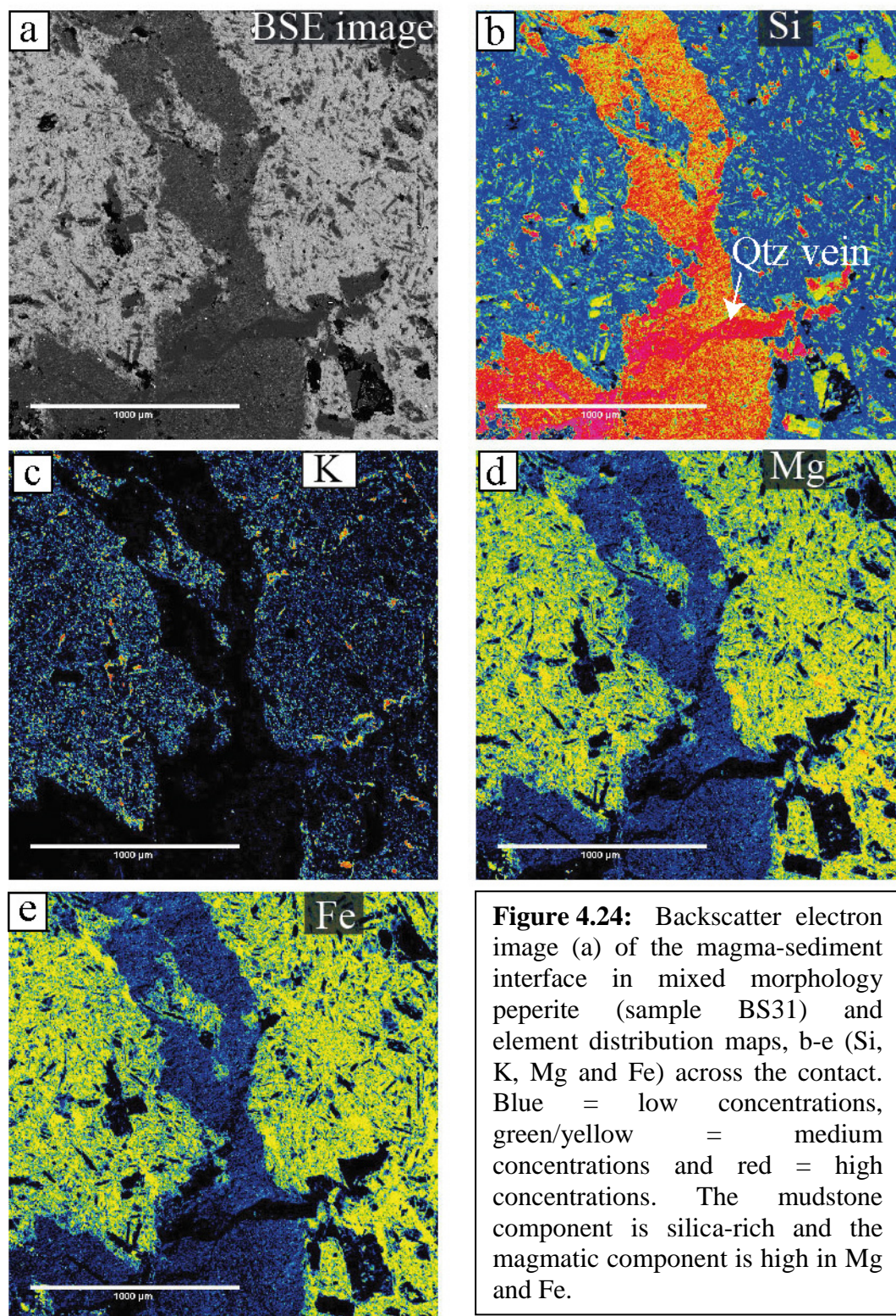


Figure 4.23: Backscatter electron image (a) of the magma-sediment interface in honeycomb peperite (sample BS32) and element distribution maps, b-f (Si, Al, K, Mg and Fe) across the contact. Concentrations are shown in greyscale, ranging from black (low concentrations) to white (high concentrations).



4.4 Discussion

4.4.1 Tectonic setting, magmatic source and provenance

Major and trace element analyses of the volcanic rocks from south Waterford show that magma compositions were tholeiitic basalt/sub-alkaline basalt to rhyolite (Figure 4.2, 4.3 and 4.10) generated at an island arc subduction zone (Figure 4.11). Approximately 92% of the samples analysed plot as tholeiitic using trace elements (Figure 4.10) and therefore, the majority of these samples should be classified as sub-alkaline as tholeiites are an iron-enriched variety of sub-alkaline rocks (Bardintzeff and McBirney, 2000). A negative Nb anomaly is observed within the majority of magmas (Figure 4.5 and 4.6), a feature characteristic of subduction related magmatic arcs (Kelemen *et al.*, 1993) because rocks from non-arc settings characteristically have very high Nb values (Wilson, 1989). The negative niobium-tantalum anomaly commonly occurs as a result of preferential partitioning of these elements into Al-rich clinopyroxene due to their extremely low solubility in the water-rich shallow parts of a subduction zone (Baier *et al.*, 2008). However, McCulloch and Gamble (1991) suggested that, as immobile Nb is sourced from the mantle wedge, the Nb depletion in arc magmas is due to partial melting of an already depleted mantle wedge, where more mobile elements (e.g. Rb) occur in higher concentrations (Figure 4.5 and 4.6) as these are derived from the subducted slab. The Campile Formation intrusive rocks show significantly greater depletion in incompatible elements, such as Nb and Ti, than the Bunmahon Formation (Figure 4.6). The more extensive depletion of the magma source for the Campile Formation was probably caused by prior melting events such as that resulting in the Bunmahon Formation phase of volcanic activity, whereas mobile elements are continuously provided through melting of the subducted slab (McCulloch and Gamble, 1991; Woodhead *et al.*, 1993).

Although sedimentary geochemical discrimination diagrams are not entirely reliable when used in isolation (Armstrong-Altrin and Verma, 2005), the combination of several discrimination diagrams with multi-element profiles and petrographic study is useful in determining tectonic setting and/or sedimentary provenance (Ryan, 2005). Multi-element plots of sedimentary rocks normalised to MORB (Figure 4.6b), show a similar profile to the surrounding volcanic rocks (e.g. enrichment in Rb and Th and depletion in Sr, Ba and Nb). The significant enrichment, particularly of mobile elements, relative to MORB rules out

derivation of these sediments from a MORB parent while flat profiles in the upper crust normalised plots (Figure 4.7) suggests upper or continental crustal involvement (Rudnick and Gao, 2003). Major element discrimination diagrams assign an ocean island arc provenance for the sedimentary rocks (Figure 4.15), where TiO_2 vs. $\text{Fe}_2\text{O}_3 + \text{MgO}$ is a measure of the mafic component and the $\text{SiO}_2/\text{Al}_2\text{O}_3$ ratio is a measure of quartz content (Bhatia, 1983). The REE profiles of sedimentary rocks (normalised to MORB) display a similar trend to that of the volcanic rocks, with enrichment in the LREE and a decreasing trend towards the HREE (Figure 4.9b). Sample BS1 (Fe-sand, Figure 4.14), however, is significantly more depleted in all REE, where the lower REE concentrations in sand fractions is attributed to depletion of heavy minerals and enrichment in the quartz-feldspar fraction (Cullers *et al.*, 1987). The combination of discrimination diagrams based on the content of major and trace elements and REE indicates that the sedimentary rocks were derived from a similar source as the surrounding volcanic rocks. Therefore, these sedimentary components testify to long-lived volcanic activity, where the first volcanic products as a result of arc volcanism were being eroded and deposited as sediment while volcanic eruptions continued.

4.4.2 Fractionation

Negative linear trends of MgO and Fe_2O_3 associated with a slight negative correlation between CaO and SiO_2 (Figure 4.1) suggest that clinopyroxene was one of several fractionating ferromagnesian minerals. Fractionation trends of initial clinopyroxene crystallisation (decreasing Ca, Mg and Fe) followed by later plagioclase crystallisation correspond to the observed mineralogy, where clinopyroxene and plagioclase microphenocrysts occur in the mafic-intermediate lavas and sills, while plagioclase is dominant (along with K-feldspar and quartz) within the more felsic end members. The contrasting behaviour of Sr and Rb (enrichment in Rb coupled with a depletion in Sr; Figure 4.5 and 4.6) indicates that plagioclase fractionation has taken place, where Sr tends to be concentrated in plagioclase whereas Rb remains in the residual magma (Wilson, 1989). The negative europium anomaly, particularly developed in the Campile Formation ($\text{Eu}/\text{Eu}^* = 0.58$; Table 4.3, Figure 4.9a), suggests that plagioclase fractionation was dominant in the more felsic samples.

4.4.3 Alteration

Alteration of the volcanic rocks, either by hydrothermal alteration or diagenesis, was examined using a combination of the Ishikawa alteration index and the chlorite carbonate pyrite index (Large *et al.*, 2001a). The more extensively altered samples, as indicated by the alteration box plot (Figure 4.4), have the highest abundance of chlorite (e.g. samples BT9 and BS7) or extensive pyrite enrichment with associated chloritisation (e.g. sample BS11). The more mafic samples of the Bunmahon Formation are affected predominantly by hydrothermal alteration (Figure 4.4), resulting in ubiquitous chlorite and epidote with minor pyrite. The more felsic samples of the Campile Formation are more affected by later diagenetic alteration. There are several possible reasons why hydrothermal alteration affects the more mafic composition volcanic rocks to a greater extent: (1) hydrothermal alteration was concomitant with exhalative activity on the seafloor during formation of the Bunmahon Formation mafic rocks (2) hydrothermal activity occurred after formation of the Bunmahon rocks and prior to the Campile Formation (3) the contrasts in the extent of alteration between lithologies are due to variations in the permeability of the host rock (e.g. Gillis and Robinson, 1988) or (4) hydrothermal activity was local and post-dated formation of all rocks, but pre-dated faulting of felsic rocks adjacent to the mafic rocks. As the exact timing of hydrothermal alteration cannot be constrained and the field relations suggest the felsic intrusive rocks were probably later faulted into place (Chapter Two), alteration predominantly affecting the more permeable rock types of the Bunmahon Formation prior to (or even during) the Campile Formation phase of volcanic activity seems the most likely scenario.

The alteration mineral assemblage chlorite + epidote + quartz + sericite + calcite + Fe-Ti-oxides (e.g. samples BT1, BT9 and BS7) is common in chlorite zones of volcanic rocks associated with hydrothermal alteration and mineralisation (Gifkins *et al.*, 2005). Furthermore, the sulphide-bearing sheeted vein systems at Trawnamoe and Stradbally Cove are similar to pyrite and chalcopyrite stringer deposits hosted within these chlorite zones (Gifkins *et al.*, 2005) and may represent pathways of hydrothermal fluid flow leading to base metal deposits. Extensively altered volcanic rocks (pervasive chlorite and albite) are commonly host to sulphide deposits (Richards *et al.*, 1989), where the associated alteration mineral assemblage is formed at low water/rock ratios and moderate temperatures

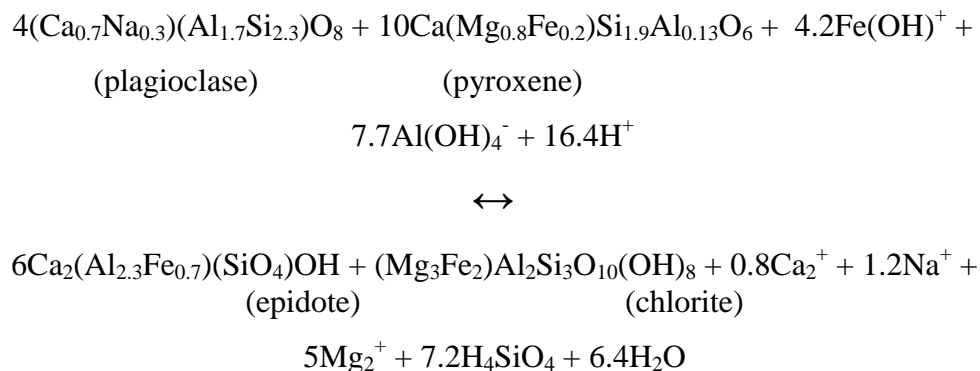
of 100-250°C (Gillis and Robinson, 1988). Thus, formation of the sulphide-bearing feeder channels (quartz + chlorite + pyrite) and the hydrothermal alteration of the host volcanic rocks may have occurred during the same hydrothermal event.

Enrichment in SiO₂ and Na₂O with a slight depletion in K₂O within the host tuff sequence to peperite in Trawnamoe (Table 4.3) reflects silicification of the sedimentary matrix as a result of peperite-driven fluid migration. Similar silicification of tuff at Arklow Head is attributed to autometasomatism by the condensed volcanic gases trapped in the tuff (Stillman and Maytham, 1973). The silicified tuff (BT7) also has a more irregular REE pattern than other tuff samples, where such REE mobility is often attributed to hydrothermal alteration of host rocks to massive sulphide deposits (McConnell, 1991). REE mobility is only recorded within the peperite matrix and would therefore appear to indicate that element mobility is due to fluid circulation initiated by peperite formation (e.g. Michard and Albarède, 1986; Yongliang and Yusheng, 1991; Zhiwei and Zhenhua, 2003). REE mobility is commonly attributed to migration of hydrothermal fluids containing large amounts of sulphur (Gieré, 1990; Gieré, 1993), suggesting that interaction between magma and wet sediment during peperite formation may have released sulphur into the pore fluid. The mobility of REE in sulphur rich environments can be related to the precipitation of base-metal sulphides (Gieré, 1993), where preliminary data suggest the degree of REE mobility increases with the size of the deposit (Campbell *et al.*, 1984). The pattern of REE enrichment and mobility, and enrichment of Si and Na, within the tuff matrix of peperite may be related to peperite-driven fluid migration and local hydrothermal fluid circulation, limited to the outcrop extent of peperite.

4.4.4 Secondary mineral compositions

The alteration mineral assemblage consists of chlorite ($\text{Fe}/(\text{Fe} + \text{Mg}) = 0.33 - 0.63$), albite, epidote, pumpellyite, pyrite and Fe- and Ti-oxides, typical of low temperature alteration. The identities and relative quantities of minerals that constitute various alteration assemblages depend on five factors: (1) temperature, (2) pressure, (3) primary rock composition, (4) primary fluid composition and (5) the ratio of fluid to rock in the reaction that produced the alteration (Reed, 1997). Epidote and pumpellyite formation within volcanic or volcanoclastic rocks may be

a result of either large fluxes of Ca-rich fluids into the host rock or, where fluid/rock ratios are low, Ca is an original component of the host rock (Metcalf *et al.*, 1996). The concentration of epidote and pumpellyite at the boundaries between magmatic clasts and sedimentary host in peperite (Figure 4.22) suggests that peperite-driven fluid migration, as a result of magmatic heat input, was locally important with pre-cursor minerals such as clinopyroxene providing additional Ca to the system. Humphries (1976) suggested the reaction:



where hydrothermal alteration of associated clinopyroxene and plagioclase resulted in chlorite and epidote formation.

Chlorite is pervasive throughout the volcanic sequence, but is more common within glassy components of hyaloclastite and along peperite clast margins. Alteration processes, such as those induced by fluid, are facilitated by increased contact area in rocks with a high permeability or porosity (Büchl and Gier, 2003; Franzson *et al.*, 2008). The origin of chloritic alteration may be due to interaction with Mg-rich fluids, such as seawater (generally with a large water/rock ratio) (Reed, 1997), with chlorite dominant in the alteration assemblage at water/rock ratios of >30, whereas epidote is dominant at water/rock ratios of <30 (Reed, 1983). More abundant chlorite with associated epidote indicates the water/rock ratios in the Waterford volcanic rocks were >30. The composition of chlorite varies significantly between lithologies, with substitution occurring between Si and tetrahedral Al (Al^{iv}) and between Mg and Fe, with Fe/(Fe + Mg) of chlorite (0.33-0.63) interpreted to reflect the relative proportions of hydrothermal fluid (Fe-rich) and seawater (Mg-rich) (Teagle and Alt, 2004). In seawater-rock interactions at 300°C seawater always loses Mg and SO₄²⁻ to the rock, regardless of rock type (Chiba, 1995) with Mg enrichment usually associated with seawater alteration (Lécuyer *et al.*, 1995). Therefore, chlorite with a higher Mg content was probably significantly more influenced by circulating seawater while chlorite

with a higher Fe content was influenced by the hydrothermal fluid. Therefore, the compositional variation in chlorite appears to be directly related to the ratio of hydrothermal fluid/seawater and the water/rock ratio rather than dependant wholly on the precursor mineral assemblage.

The wide range of chlorite alteration temperatures (311°C to 860°C; Table 4.8, Figure 4.18), depends on the formula used for the calculation, where the empirical equations to determine temperature of Kranidiotis and MacLean (1987) and of Jowett (1991) take into account a systematic variation between Al^{iv} and Fe number ($Fe/(Fe + Mg)$), whereas the calculation used by Cathelineau (1989) suggests that only Al^{iv} varies with temperature. Chlorite compositions from the south Waterford volcanic rocks show a negative linear trend between Al^{iv} and Fe number (Figure 4.17) and as the Fe number is not related to host lithology, the composition of the hydrothermal fluid is probably the dominant influence. Therefore, the geothermometers taking Mg and Fe content into account are more reliable for use with chlorite compositions calculated within the south Waterford volcanic rocks. However, the calculation used by Jowett (1991) has been designed for use with chlorite of relatively low Fe numbers and it is suggested that corrections to this formula are employed to determine a more realistic temperature range (Esteban *et al.*, 2007). Zang and Fyfe (1995) used a similar technique, where they rearranged the original formula of Cathelineau (1989) and taking into account Fe and Mg contents (but at higher Fe ratios) they proposed a formula that only uses approximately half of the tetrahedral aluminium. Therefore, temperature values yielded using this equation are approximately half of those calculated by the original Cathelineau (1989) equation (and corresponding to those of Kranidiotis and MacLean, 1987). The temperatures calculated from both the original Cathelineau (1989) geothermometer and the Jowett (1991) geothermometer are at the upper end of stable chlorite temperatures (>750°C), where transition to spinel would probably occur (Bucher and Frey, 2002), whereas the temperatures calculated by combining Al^{iv} and Fe number, in the range 300°C - 400°C, are more plausible. The use of chlorite geothermometers is best used in conjunction with other methods to determine temperatures, such as fluid inclusion studies, but the mineral assemblage indicates that the volcanic rocks represent a transitional assemblage between prehnite/pumpellyite and sub-greenschist facies, which correlates with calculated chlorite temperatures. Similar temperatures are

also recorded in the same region from illite crystallinity (~300°C; Diskin, 1997) and conodont alteration index (300-400°C; Bergström, 1980). As the intercalated sedimentary sequence retains much of the original texture and occurs as mudstone transitional to phyllite, the pressure estimate is probably at the lower range of greenschist facies (2-3 kbar). Gallagher *et al.* (1994) noted that a diagnostic mineral assemblage is not generally present and agreed with Pointon (1979) who deduced that prehnite-pumpellyite to lower greenschist facies occurs throughout the area. Shannon (1979) also suggests that similar rocks (within the same volcanic belt) in Wexford have undergone at most a chlorite-grade greenschist facies metamorphism and that this grade of metamorphism is regionally developed. The presence of epidote (Table 4.9) without any development of lawsonite, aragonite or glaucophane indicates metamorphism took place at pressures of 1.5 to 3.0 kbar (Deer *et al.*, 1962).

4.5 Conclusions

The geochemical characteristics of the volcanic suite have an island arc subduction zone affinity. The volcanic rocks and intercalated iron-rich volcano-sedimentary sequence have similar trace element and REE concentrations. The kinship between volcanic, volcanoclastic and sedimentary rocks indicates that the sedimentary rocks were probably sourced from the weathered detritus of initial mafic-intermediate volcanism, with geochemical characteristics of arc magmatism preserved in the sedimentary record. The interspersed and graded tuff deposits are tholeiitic and genetically related to the intermediate composition lava flows and shallow intrusive rocks. Progressive fractionation and evolution of the magma source occurred, resulting in a change from early mafic-intermediate compositions to a later dominance of intermediate with minor felsic compositions in the Bunmahon Formation. Felsic lithologies predominate in the Campile Formation.

Hydrothermal alteration is more significantly developed within the more permeable, upper section of the volcanic pile, consisting of mafic-intermediate volcanic rocks (summary of syn-volcanic hydrothermal alteration given in Figure 4.25). Circulation of a hydrothermal fluid and subsequent alteration was probably a result of both fracture controlled fluid flow (e.g. veins- possibly associated with the development of VHMS deposits) and contact alteration associated with

shallow intrusive activity (e.g. peperite) (Figure 4.25). Hydrothermal alteration probably occurred prior to the Campile Formation phase of volcanic activity. Later overprinting by diagenetic alteration has a more pronounced effect within the unaltered felsic intrusive rocks than the hydrothermally altered mafic-intermediate volcanic rocks. The variation in the extent, and type, of alteration is therefore attributed to the location in the stratigraphic sequence and the permeability or degree of consolidation of the host rock. Local variations in alteration occur as a result of minor fluctuations in temperature and/or composition of the circulating fluid. Variations in the temperature and composition of the fluid are a result of the degree of mixing of magmatic fluid, pore fluid and seawater. Some lithologies, such as hyaloclastite, have interacted to a greater degree with seawater, while others, such as peperite, have interacted to a greater degree with sediment pore water. The limited extent of REE mobility associated with Si, Na and K mobility within an area confined to peperite formation suggests that the migration pattern was limited to directly adjacent to the peperite.

Temperature of alteration, calculated using the more reliable empirical calculations of Kranidiotis and MacLean (1987) from compositional variations in chlorite, ranges from ~300°C to 400°C. Local variation in alteration minerals is a consequence of the primary mineral assemblage (e.g. clinopyroxene → epidote), variations in the composition of the hydrothermal fluid (e.g. Mg- vs. Fe-rich chlorite) and the water/rock ratio. Where larger influxes of Ca occur within the Fe-rich hydrothermal fluid, or where the primary mineral assemblage contains moderate amounts of Ca, hydrous alteration minerals such as epidote, pumpellyite and chlorite are abundant (summary of alteration given in Figure 4.26). For very high water/rock ratios (at similar temperatures calculated for Waterford volcanic rocks) REE are mobile and chlorite is a much more dominant alteration mineral than epidote, where the highest ratios occur within more permeable rocks (hyaloclastite) or within areas of high heat flow and fluid circulation (peperite).

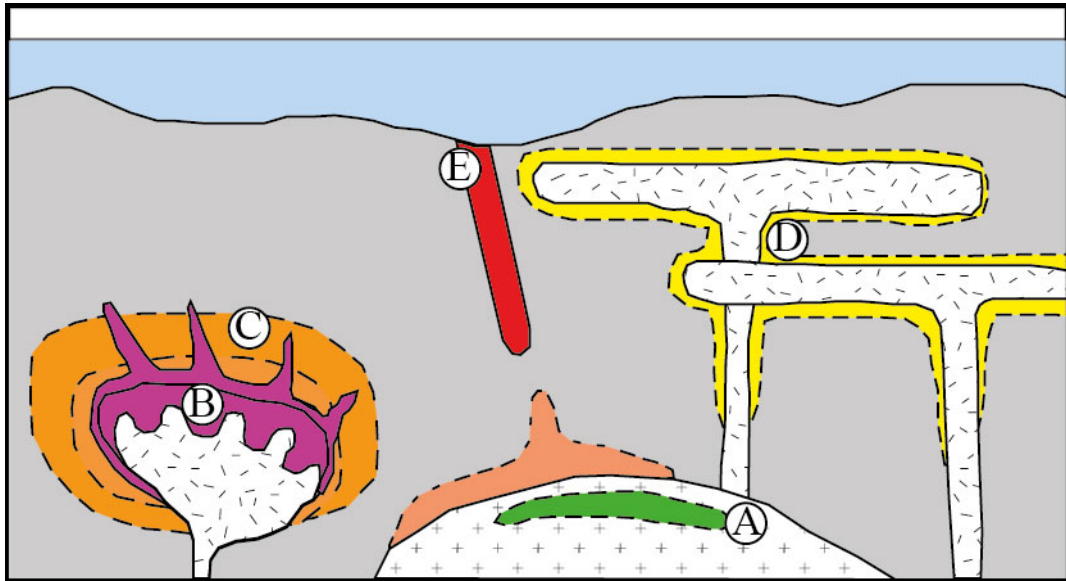


Figure 4.25: Cartoon of the variety of syn-volcanic alteration zones (from Gifkins *et al.*, 2005). A = deuteritic alteration zone within the top of a large volume intrusion; B = fracture-controlled hydrothermally altered zone at the margins of an intrusion and in the surrounding host rock; C = concentric zones of contact alteration around a large volume intrusion; D = contact-altered zones around sills emplaced into unconsolidated sediment; E = footwall alteration pipe beneath a VHMS deposit. Scenario D and possibly B are the most likely to account for the alteration styles observed within the south Waterford volcanic rocks.

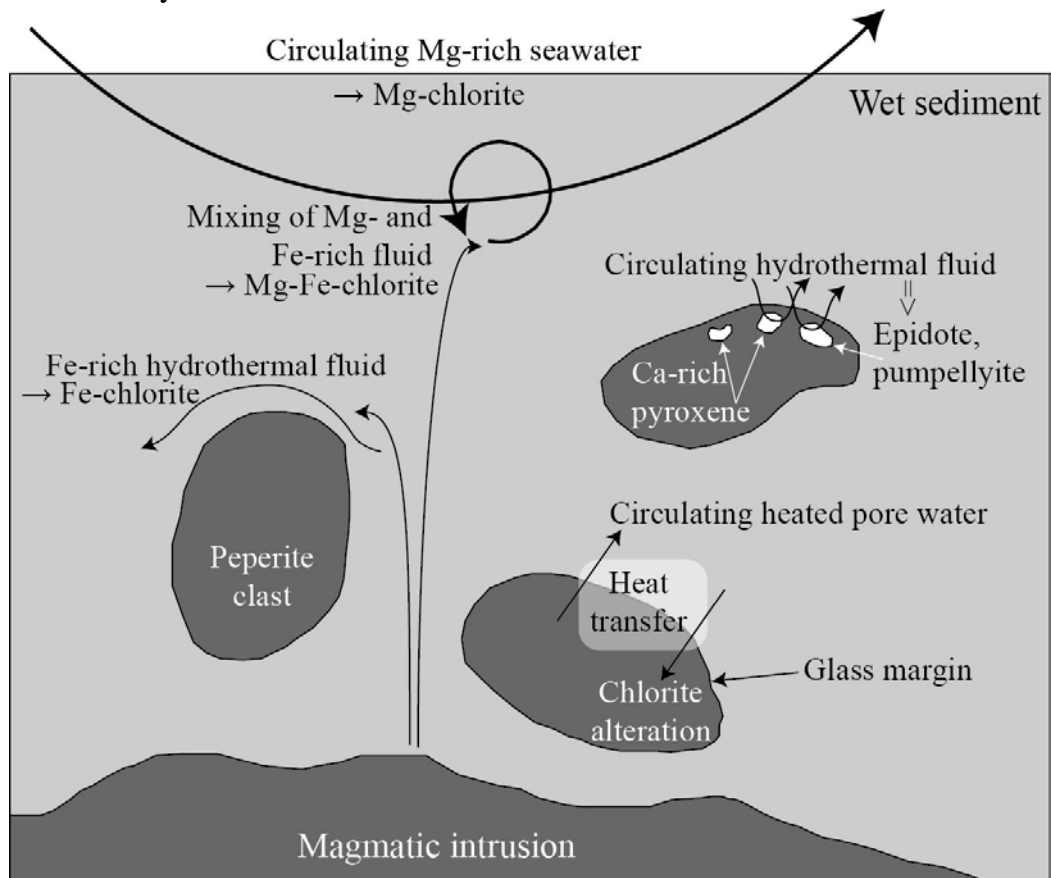


Figure 4.26: Circulation of Fe-rich hydrothermal fluid and Mg-rich seawater resulting in the range of secondary minerals recorded. Limited mobility of Si, Na, K and REE also occur within the sedimentary matrix of peperite as a result of intrusion into unconsolidated sediment.

Chapter Five:

Fluid Inclusion studies of vein mineralisation

5.1 Introduction

Fluid inclusion studies of vein quartz (seven samples) and calcite (one sample) from Trawnamoe and Stradbally Cove were carried out to determine:

- 1) The true trapping temperature, composition and salinity of vein forming fluids
- 2) The mineralisation style and how it compares with other base metal mineralisation in the region such as the Avoca Pb-Zn deposit and the Carboniferous Irish-type Zn-Pb deposits in the Irish midlands.

5.2 Sampling for fluid inclusion studies

At Trawnamoe, two samples were taken from a ~20cm vein which parallels bedding within a laminated ash and crystal tuff. Sample T16 is composed entirely of calcite from the centre of the vein, while T20 is composed of quartz from the margins of the vein. A further four samples were taken from sheeted vein systems hosted by andesite sheet flows and hyaloclastite at the eastern end of Trawnamoe – T17 and T26 are composed of vein quartz from the margin of the vein system, while T22 and T24 are composed of vein quartz from the centre of the vein system.

At Stradbally Cove, two quartz veins that parallel bedding were sampled, i.e. S17 from a quartz vein hosted by mudstone and S30 from a quartz vein at the contact between andesite and mudstone. A sheeted vein hosted by siltstone was also sampled (S27).

A summary of vein types is given in Table 5.1 and sample distribution is shown in Figure 5.1.

Sample	Grid Reference	Host lithology	Type	Host
T16	X 42670 98180	Laminated ash tuff	Barren	Cct
T17	X 42786 98180	Hyaloclastic margins of sheet flows	Mineralised	Qtz
T20	X 42693 98181	Laminated ash tuff	Barren	Qtz
T22	X 42807 98177	Hyaloclastite	Mineralised	Qtz
T24	X 42807 98179	Hyaloclastite	Mineralised	Qtz
T26	X 42813 98179	Hyaloclastite (associated with malachite)	Mineralised	Qtz
S17	X 36979 96928	Graded pyrite-rich mudstone/tuff sequence	Barren	Qtz
S27	X 36878 96736	Siltstone	Mineralised	Qtz
S30	X 36896 96779	Mudstone in contact with andesite	Barren	Qtz

Table 5.1: Location, composition and host lithology data for vein samples used for FI studies. (Cct = calcite, qtz = quartz. Sample labels: T = Trawnamoe, S = Stradbally Cove).

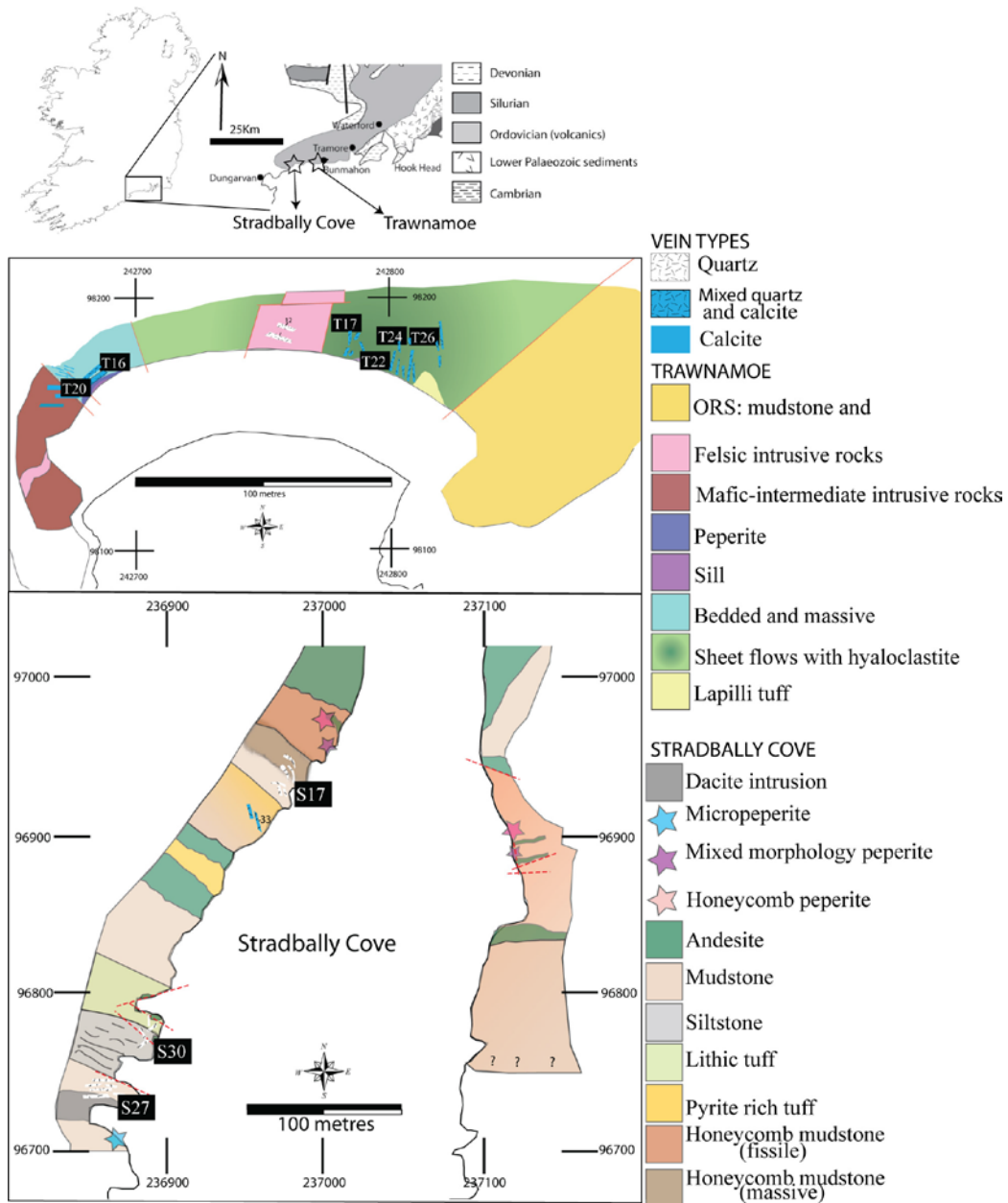


Figure 5.1: Geological map of (a) Trawnamoe and (b) Stradbally Cove showing the location, host lithologies and vein types sampled for fluid inclusion studies.

5.3 Fluid Inclusions – an introduction

Fluid inclusions (FIs) occur in crystals and can be simply considered as sealed microscopic (usually <50 microns in longest dimension) vacuum flasks that contain a sample of fluid trapped during, or after, formation of the host crystal. Solid, liquid and vapour phases are commonly observed in FIs under the petrological microscope. Determination of the chemistry of the fluid components trapped in the crystal cavity provides fundamental information which can facilitate the reconstruction of the conditions of mineral growth. This in turn leads to a better understanding of the physical and chemical environment of economically important geological processes such as ore deposition.

5.4 Analytical techniques used in fluid inclusion studies

5.4.1 Fluid inclusion petrography

Fluid inclusion petrography is vital to the correct interpretation of microthermometric analysis. Both thin sections (30µm thick) and doubly polished wafers (~100µm thick) are used to examine and classify the fluid inclusions. Fluid inclusion petrography facilitates the generation of a paragenetic classification and a morphological/compositional classification. In the paragenetic classification FIs are described according to their origin:

- Primary (P) inclusions were formed during crystal growth (Figure 5.2). These inclusions are commonly found in trails parallel to the growth zones of the crystal, or as large, isolated or randomly distributed inclusions (Roedder, 1984; Shepherd *et al.* 1985).
- Secondary (S) inclusions are incorporated in the host mineral after the crystal has been formed (Figure 5.2). These inclusions are commonly found delineating postcrystallisation fractures, which form due to either mechanical or thermal stress (Shepherd *et al.* 1985).
- A third genetic FI type, consisting of inclusions intermediate between P and S inclusions, is termed pseudosecondary (PS) inclusions. These inclusions are similar to S inclusions, except that they are trapped in trails along annealed fractures which were formed *before* the crystal growth has terminated.

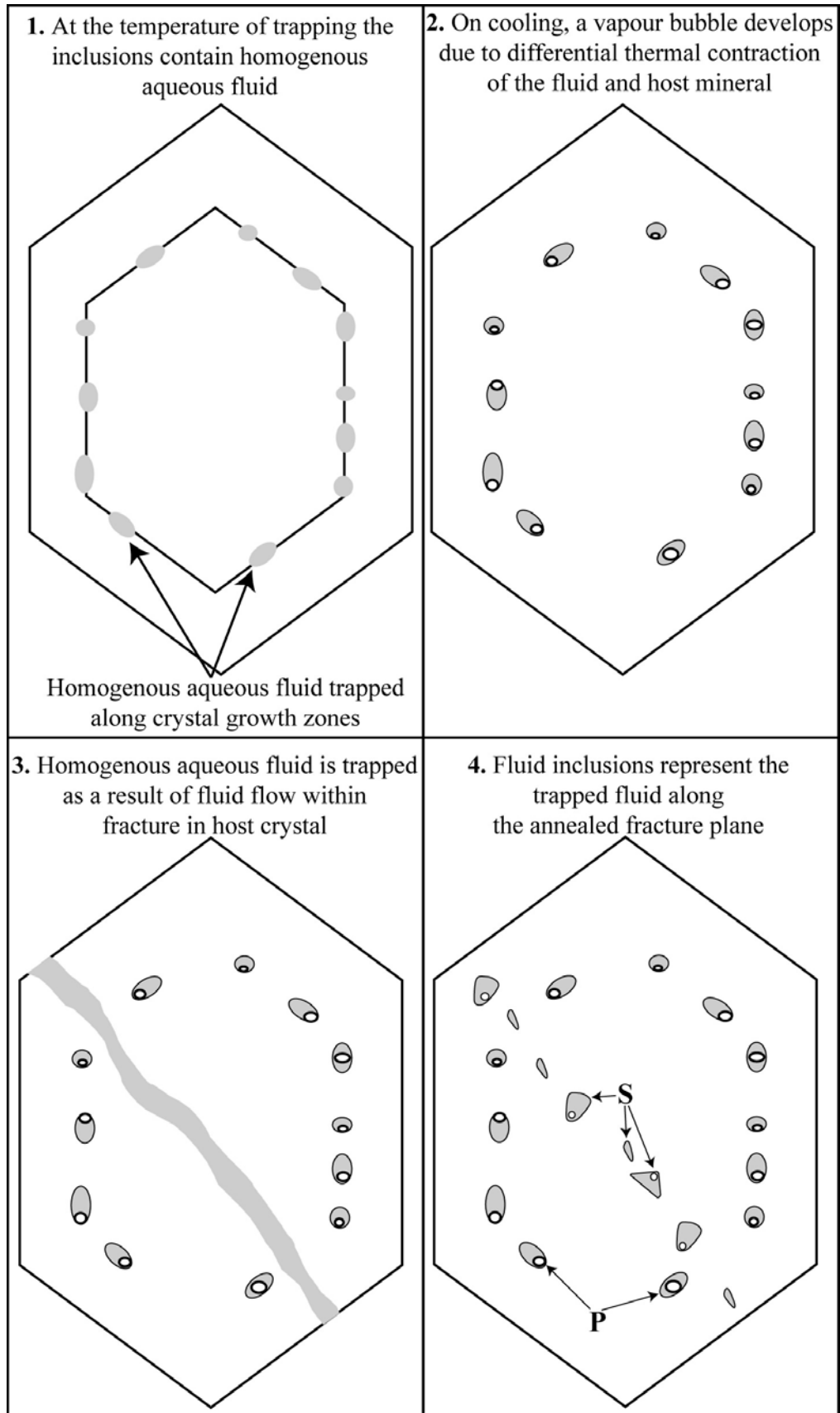


Figure 5.2: Development of Primary (P) and Secondary (S) fluid inclusions during the growth and later fracturing of the host crystal.

Morphological and phase classifications are based on the optical characteristics of fluid inclusions, including shape, degree of fill (F) and phases present. Fluid inclusion morphologies can be highly variable, ranging from irregular to spherical shapes. In some cases FIs can also take the form of negative crystal shapes, adopting the crystallographic shape of the host mineral. Morphological classification of FIs was carried out using Lucia Archive Software, recording length and area using polygon and line tools. F ($F = V_L / (V_L + V_V)$, where V_L is the volume of the liquid phase and V_V is the volume of the vapour phase) was also calculated. Shape of FIs ranges from elongate and tabular to spherical.

Paragenetic classification involves the recognition of primary, secondary or pseudosecondary FIs, while morphological and phase classification of FIs involves grouping of inclusions based on shape and phases present at room temperature (Figure 5.3).

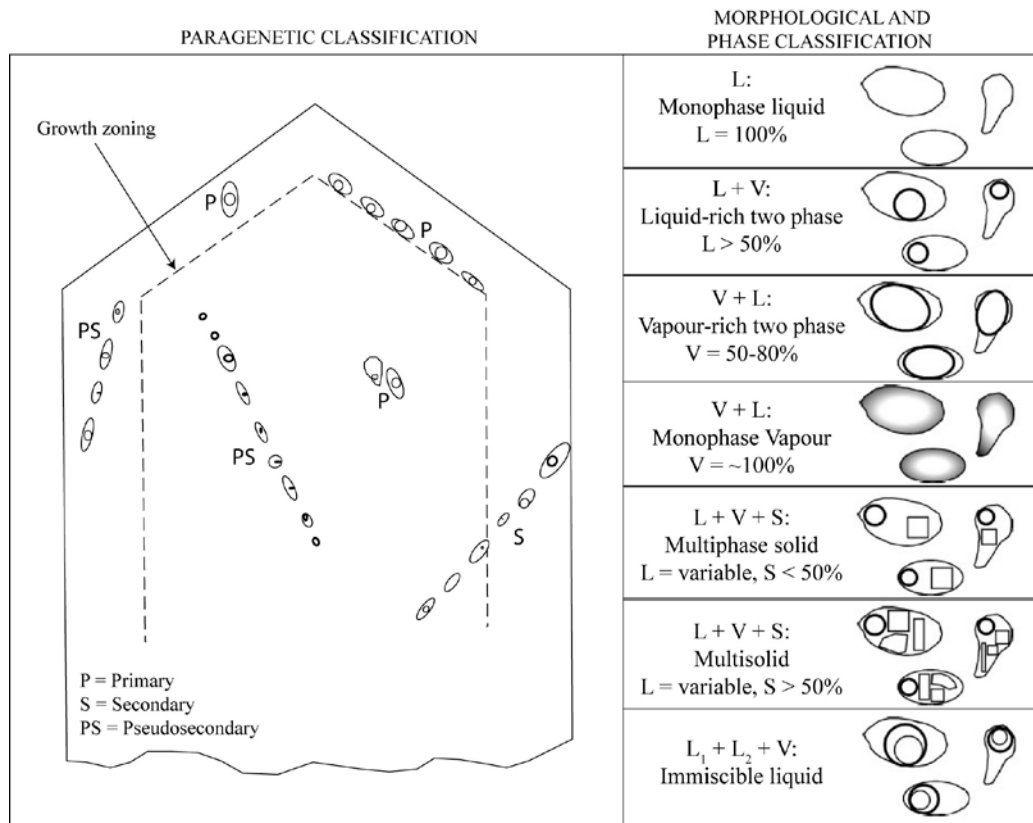


Figure 5.3: Sketch of paragenetic fluid inclusion classification, based on Roedders (1984) criteria, and morphological and phase classification based on shape of the inclusion and phases present at room temperature (from Shepherd *et al.*, 1985).

5.4.2 Microthermometry

Microthermometric analysis of fluid inclusions involves the observation of the phase changes which occur in the inclusion during heating and cooling. Microthermometric analysis was carried out using a Linkam THMSG 600 heating-freezing stage mounted on an Olympus transmitted light microscope (x10 to x100 lenses) with digital camera feeding to a dedicated computer loaded with the Linksys 32DV imaging and heating control software. Calibration of the stage was carried out using synthetic FI standards (pure CO₂ and water). The temperatures at which phase changes occur within an inclusion reflect the pressure, temperature, composition and density (P-T-X-D) of the fluid at the time of trapping, assuming the inclusions have not undergone any post-entrapment modifications (e.g. leakage or stretching of FIs). By comparing observed phase transition temperatures to published values for simple fluid systems (e.g. H₂O-NaCl, H₂O-NaCl-CaCl₂) deductions about fluid chemistry and trapping conditions can be made. A detailed discussion of the theory and practical aspects of FI microthermometry is given by Shepherd *et al.* (1985).

Saline Aqueous Inclusions - Freezing

In saline aqueous systems two phase changes are recorded during cooling (Figure 5.4). The temperature at which liquid first appears after ice formation is termed the temperature of first ice melting (T_{FM}). This temperature corresponds to the eutectic points determined by the composition of the end member components (Table 5.2). Freezing studies of saline aqueous fluid inclusions are used to estimate salinity. The temperature of last ice melting (T_{LM}) is directly proportional to the amount of salt present. Salinity values are referred to as “equivalent weight % NaCl” (eq. wt.% NaCl), as it equates to an experimentally determined amount of NaCl in a solution (Shepherd *et al.*, 1985).

Saline Aqueous Inclusions – Heating

The temperature of homogenisation (T_H) is the minimum trapping temperature of the FI, and can be used in conjunction with the density of the fluid to give minimum trapping pressures (T_P) (Figure 5.4 and 5.5). Homogenisation can occur in three ways:

1. To the liquid state (L+V → L)
2. To the vapour state (L+V → V) and

3. Critical homogenization characterized by the fading of liquid vapour meniscus ($L+V \rightarrow$ supercritical fluid)

Salt system	Eutectic temperature (°C)
H ₂ O-MgCl ₂	-33.6
H ₂ O-NaCl-KCl	-23.5 (-22.9)
H ₂ O-NaCl-Na ₂ SO ₄	-21.7
H ₂ O-NaCl	-21.2 (-20.8)

Table 5.2: Salt systems and corresponding eutectic temperatures of Borisenko (1977) and Crawford (1981) (*italics*) relevant to aqueous FIs in this study.

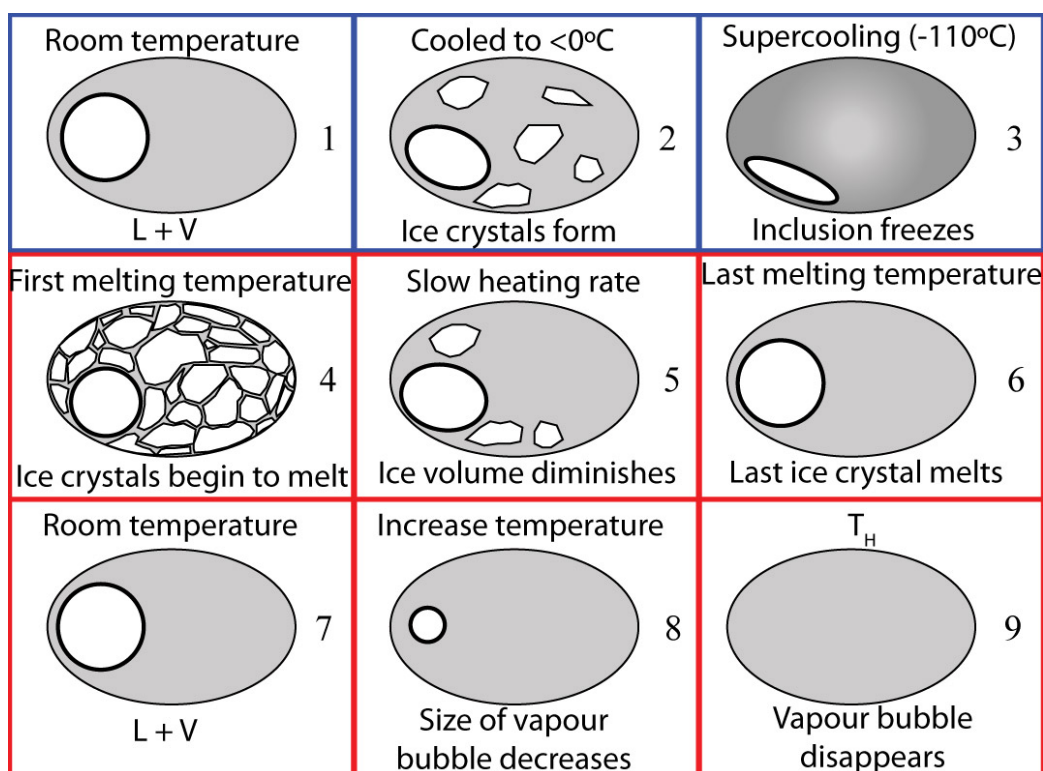


Figure 5.4: Steps involved in microthermometric analyses of two phase (L + V) FIs including cooling and subsequent reheating. From room temperature the inclusion is supercooled to -110°C , and once the liquid freezes forming solid ice, collapse of the vapour bubble is observed. First ice melting (T_{FM}) occurs after slow heating, producing a fine-grained mixture of solid and liquid. T_{FM} is used to determined chemical composition of the fluid. Upon further heating the volume of ice diminishes and breaks into several smaller ice crystals. Disappearance of the last ice crystal is recorded as T_{LM} , which is used to calculate salinity. Heating of the inclusion above room temperature results in a decrease in the vapour bubble size until it disappears. This measurement represents temperature of homogenisation (T_H) to the liquid phase. (Steps at 7, 8 and 9 correspond to points A, B and C respectively in Figure 5.5).

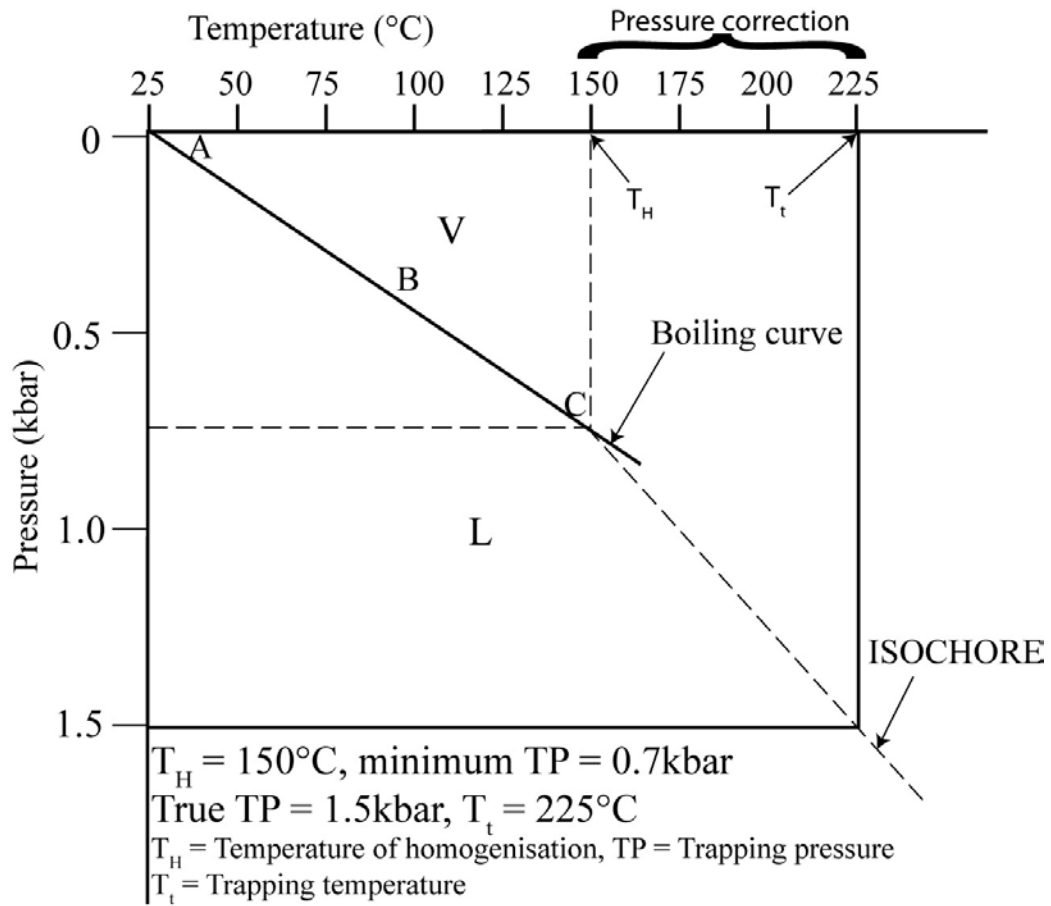


Figure 5.5: Graphical representation of the relationship between T_H , T_t and trapping pressure. V = vapour, L = liquid. (A, B and C represent stages of the inclusion shown in Figure 5.3).

5.5 Results

Fluid inclusions hosted in quartz and calcite are predominantly two phase, liquid-rich ($L + V$, $L > V$) and are either primary, secondary or pseudosecondary in origin. Type 1 are two phase liquid-rich inclusions and are recognised as primary based on criteria such as their larger size ($\sim 6\text{--}20\mu\text{m}$) and their isolation within a crystal (Roedder, 1984). Secondary two phase liquid-rich FIs (Type 2) are usually smaller than primary inclusions ($2\text{--}9\mu\text{m}$). They occur as trails within annealed fractures (Figure 5.6). Type 3 are secondary monophasic liquid inclusions. These are rare and occur in samples T20, T22 and S17 within the same trails as Type 2. Rare two phase (Type 4), liquid-rich pseudosecondary inclusions were recorded in samples T22 and S30 – they occur in trails that do not cut crystal boundaries.

(a)	Primary Type 1	Secondary		Pseudosecondary Type 4
		Type 2	Type 3	
Phases present	$L + V$, $L > V$	$L + V$, $L > V$	Monophase L	$L + V$, $L > V$
Size	$3 - 25\mu\text{m}$	$2 - 4\mu\text{m}$	$\sim 2\mu\text{m}$	$< 3\mu\text{m}$
F	$0.73 - 0.96$	$0.8 - 0.9$	–	~ 0.9
Shape	Variable	Oval, irregular	Spherical	Spherical
Occurrence	Isolated, clusters	Trails that cut crystal boundaries	Within trails of Type 2	Trails terminate within crystal
Mineralised samples	T17, T22, T24, T26	T17, T22, T24, T26	T22	T22
Barren samples	T16, T20	T16, T20	T20	–

(b)	Primary (Type 1)	Secondary		Pseudosecondary (Type 4)
		(Type 2)	(Type 3)	
Phases present	$L + V$, $L > V$	$L + V$, $L > V$	Monophase L	$L + V$, $L > V$
Size	$3 - 27\mu\text{m}$	$2 - 9\mu\text{m}$	$< 3\mu\text{m}$	$< 4\mu\text{m}$
F	$0.70 - 0.97$	$\sim 0.8 - 0.9$	–	$0.8 - 0.95$
Shape	Variable	Oval, irregular	Spherical, oval	Spherical
Occurrence	Isolated, clusters, growth zones	Trails that cut crystal boundaries	Trails	Trails terminate within crystal
Mineralised Samples	S27	S27	–	–
Barren samples	S17, S30	S17, S30	S17	S30

Table 5.3: Description and characteristics of FIs recorded from (a) Trawnamoe and (b) Stradbally Cove.

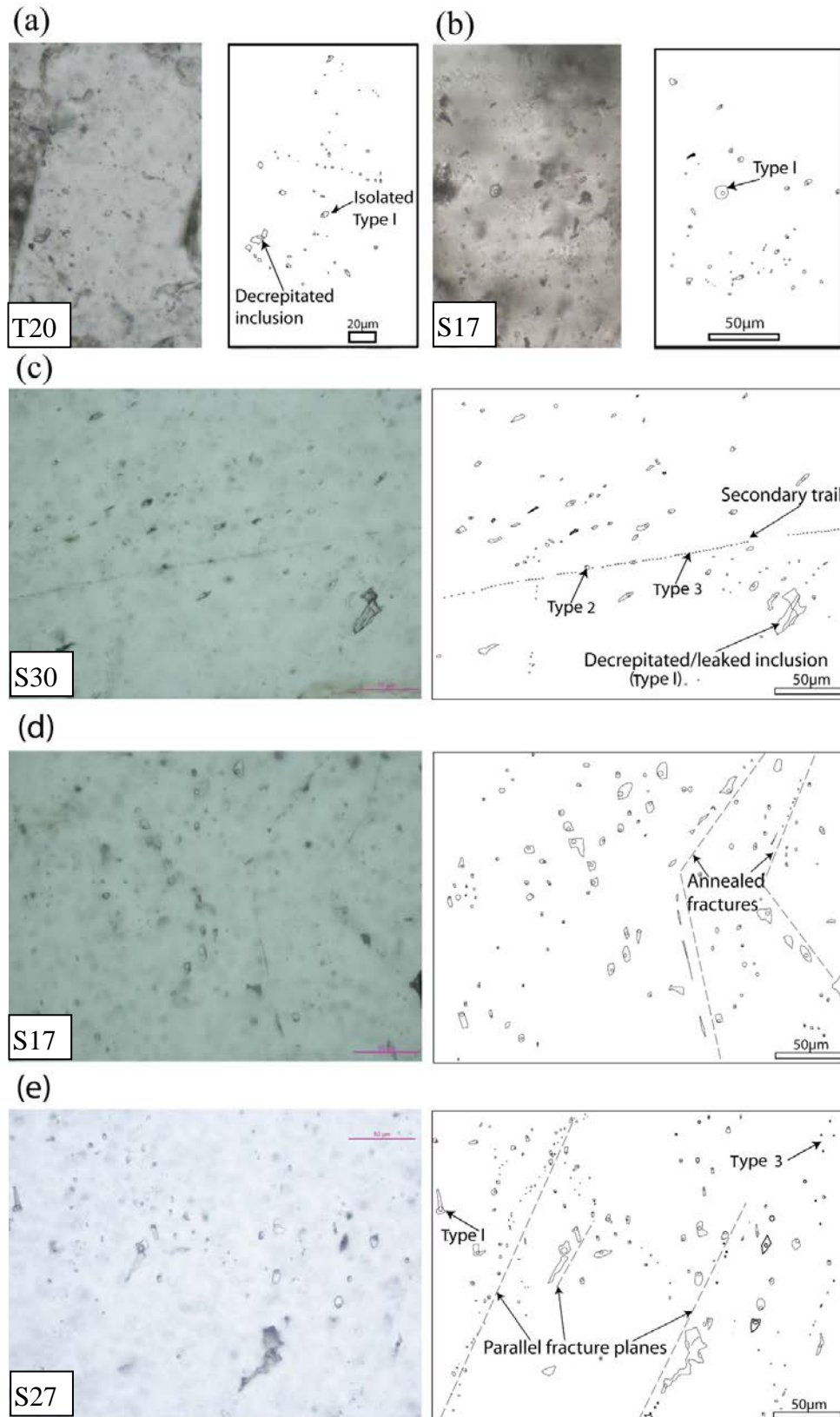


Figure 5.6: Range of inclusion types present in quartz: (a) and (b) isolated primary Type 1 inclusions, (c) trails of secondary inclusions (Type 2), (d) inclusions formed along annealed fracture planes (Type 2) and (e) parallel fracture planes. Sample numbers shown in photomicrographs, T20 = barren, S17 = barren, S30 = mineralised, S27 = barren.

5.5.1 Trawnamoe

A total of 225 primary Type 1 FIs were analysed from sulphide-bearing, sheeted veins and barren, linear veins from Trawnamoe. Temperature of homogenisation (T_H) ranges from 105°C to 286°C, with an average of 154°C (Figure 5.7). Salinities range from 5 up to 20.1 eq. wt.% NaCl with an average of 13.5 eq. wt.% NaCl (Figure 5.8). At Trawnamoe a range of compositions have been recorded, corresponding to T_{FM} values, from H₂O-NaCl-KCl to H₂O-MgCl₂.

5.5.2 Stradbally Cove

A total of 170 primary Type 1 FIs were analysed from quartz within the sulphide-bearing sheeted vein and barren, linear veins from Stradbally Cove. T_H ranges from 100°C to 270°C, with an average of 172°C (Figure 5.7). Salinities are highly variable, from 3 to 19 eq. wt.% NaCl, with a mean of 12 eq. wt.% NaCl (Figure 5.8). Temperature of first ice melting (T_{FM}) ranges between -22.5°C and -31°C, corresponding to a range of compositions including H₂O-NaCl-NaSO₄, H₂O-NaCl-KCl and H₂O-MgCl₂.

A broad overlap occurs between FIs in vein samples from Trawnamoe and Stradbally Cove in terms of T_H , with dominant peaks occurring between 125°C and 200°C (Figure 5.7). The majority of salinity values ranges between 10 and 16 eq. wt.% NaCl (Figure 5.8). An inverse relationship between salinity and T_H is recorded for FIs in the sulphide-bearing veins, representing a trend of fluid mixing between a high temperature, low salinity magmatic fluid and a lower temperature, high salinity meteoric fluid (Figure 5.9a). The majority of FIs in barren veins are of medium salinity and temperature (Figure 5.9b), with no definite trend recorded between the two parameters.

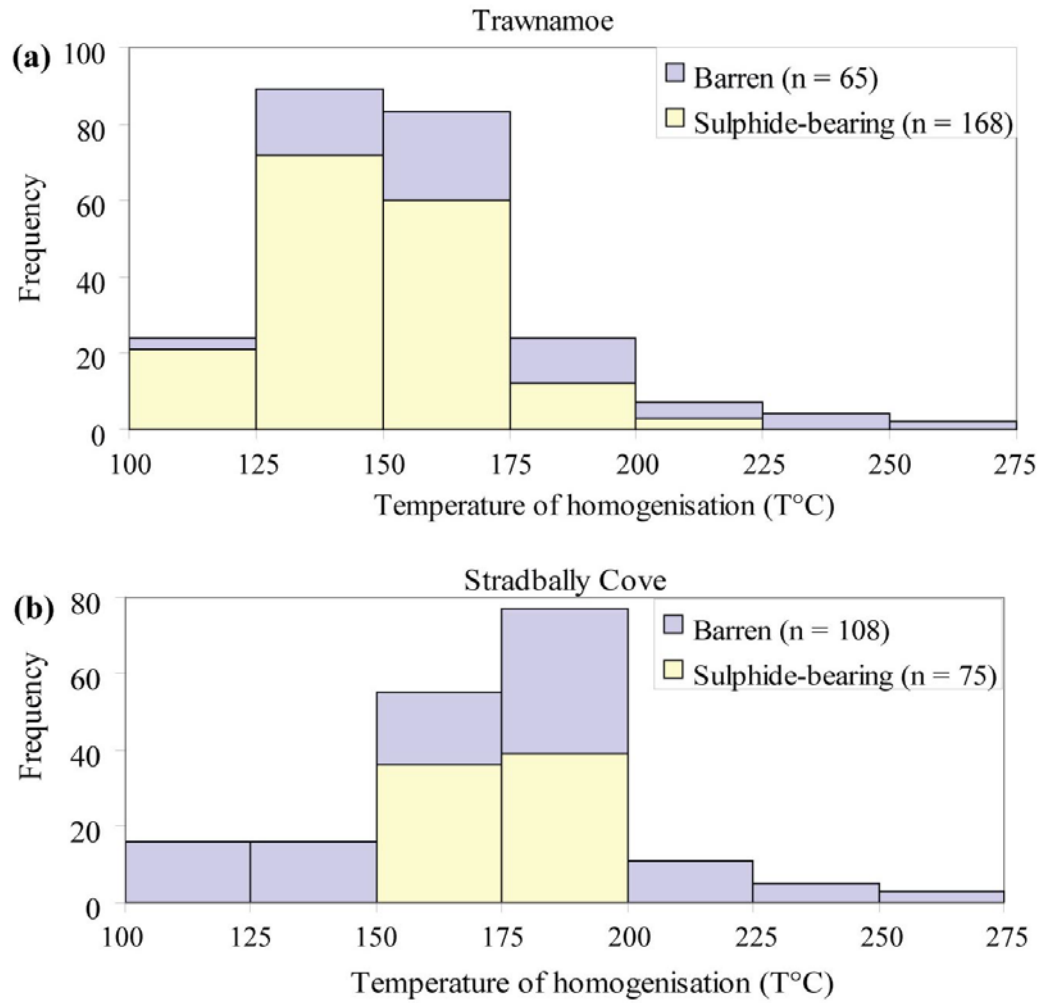


Figure 5.7: Frequency distribution histograms showing the range of T_H for primary Type 1 FIs hosted in vein samples from (a) Trawnamoe and (b) Stradbally Cove. (All FIs hosted in quartz except six calcite hosted FIs in Trawnamoe veins).

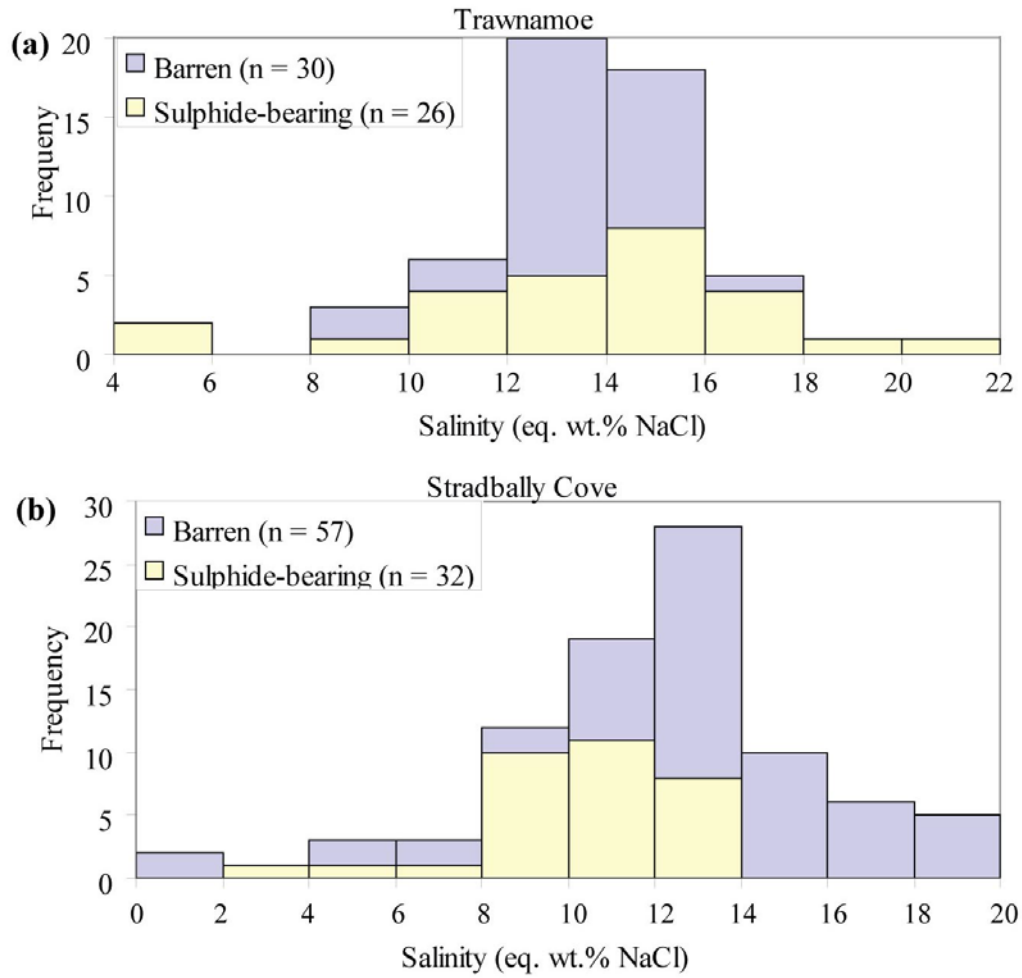


Figure 5.8: Frequency distribution histograms showing the range of salinities for primary Type 1 FIs hosted in quartz in veins from (a) Trawnamoe and (b) Stradbally Cove.

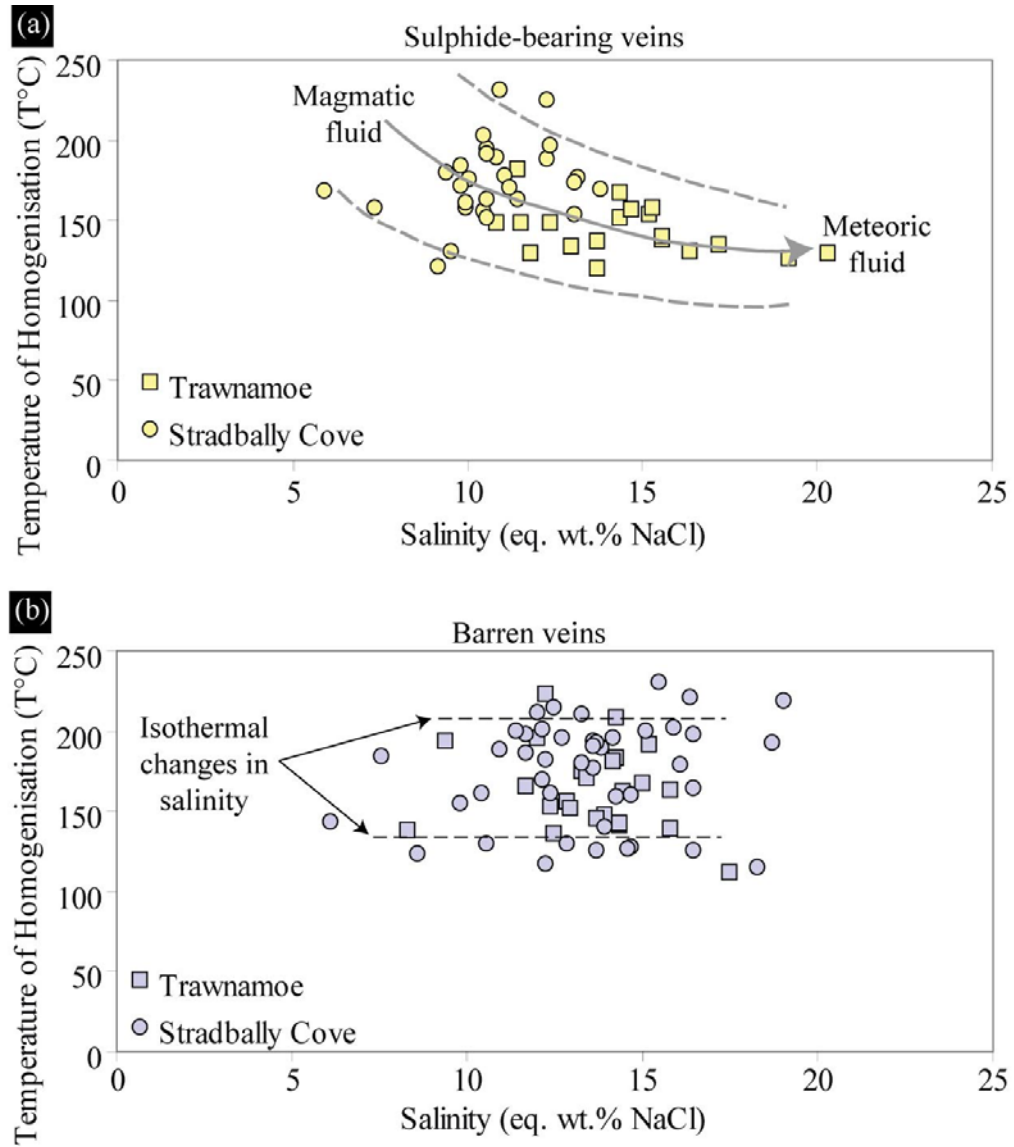


Figure 5.9: Bivariate diagrams showing the range of T_H and corresponding salinities estimated from fluid inclusion studies of (a) sulphide-bearing sheeted vein systems and (b) linear barren veins.

5.6 P-T-X trapping conditions

Fluid inclusions trapped at temperatures $> \sim 50^\circ\text{C}$ commonly show two phases (L + V) at room temperature and pressure. An inclusion trapped at P_t and T_t will follow the P-T cooling path defined by a line of equal fluid density (isochore). The inclusion remains homogeneous until the isochore meets the vapour-liquid equilibrium curve, at which point a vapour bubble nucleates, corresponding to the homogenisation temperature (T_H) (Figure 5.10) which represents the minimum P-T trapping conditions. However, trapping could have occurred anywhere within the single-phase region above this curve along the P-T path defined by the isochore. The difference between T_t and T_H is often referred to as the pressure correction. An estimate of P_t (and salinity) is required to determine T_t and in order to calculate these values either an independent geothermometer or geobarometer is needed, or intersecting isochores from coeval inclusions. Pressures for vein deposits in this study were chosen to correlate with the sub-greenschist facies of the host volcanic rocks (Chapter Two and Three).

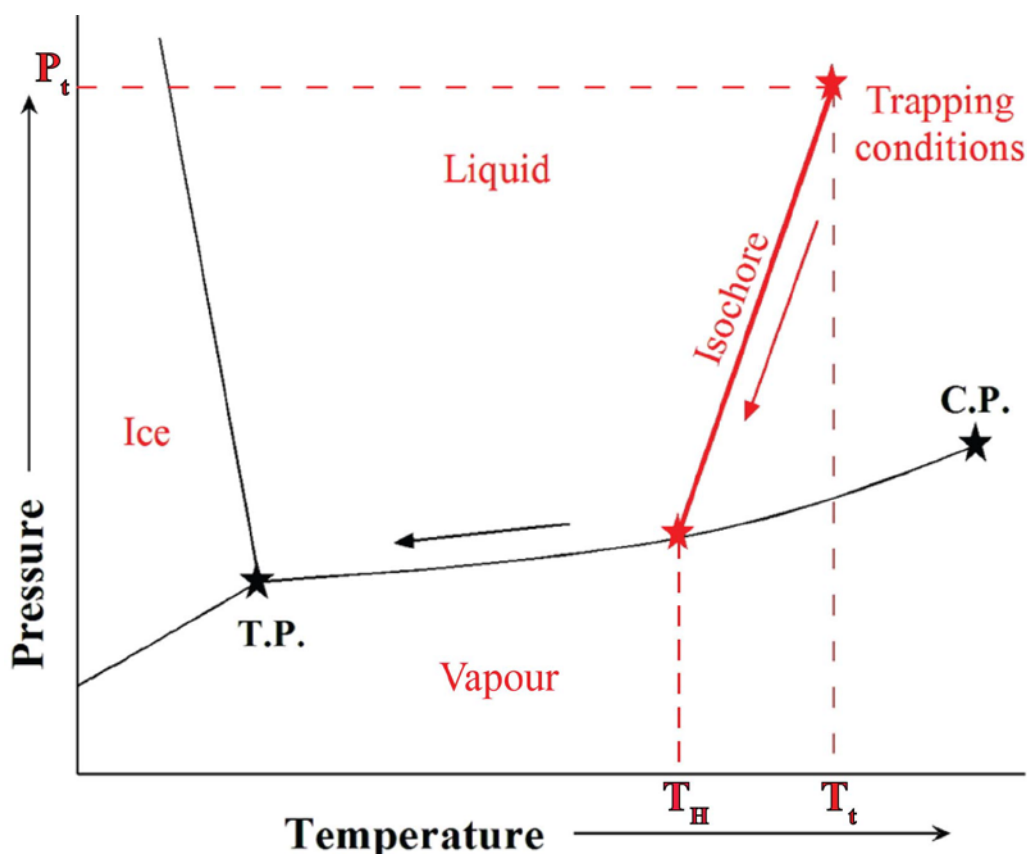


Figure 5.10: Schematic P-T phase diagram for aqueous fluid. T.P.: triple point; C.P.: critical point; T_H : homogenisation temperature; T_t : true trapping temperature; P_t : trapping pressure.

Isochores were plotted using programmes BULK (uses information obtained from FIs to calculate fluid density and composition; Bakker, 2003) and ISOC (calculates isochores corresponding to the bulk density and composition; Bakker, 2003). Values required for input to the BULK programme were determined directly from FI analysis i.e. salt composition, salinity, T_H , mode of phase change and type of aqueous system (e.g. H_2O -NaCl; Archer, 1992). The results of these calculations, along with T_H , are used in the ISOC programme to determine the slope of the isochore. A minimum, mean and maximum isochore was calculated for the magmatic and meteoric fluids involved in the formation of sulphide-bearing veins and for fluids associated with barren veins. If pressures were at a maximum at the time of vein formation, determination of T_i requires a pressure correction to T_H , using a pressure value of 1.5 - 3kbar (average 2kbar), corresponding to the observed mineral assemblage (Figure 5.11). Pressure corrected temperatures range between $\sim 190^\circ\text{C}$ and 370°C for both vein types, with a mean T_i of 300°C and 210°C calculated for the magmatic and meteoric fluids respectively associated with the sulphide-bearing veins. A mean T_i of 270°C was calculated for the fluids associated with barren veins (Figure 5.12).

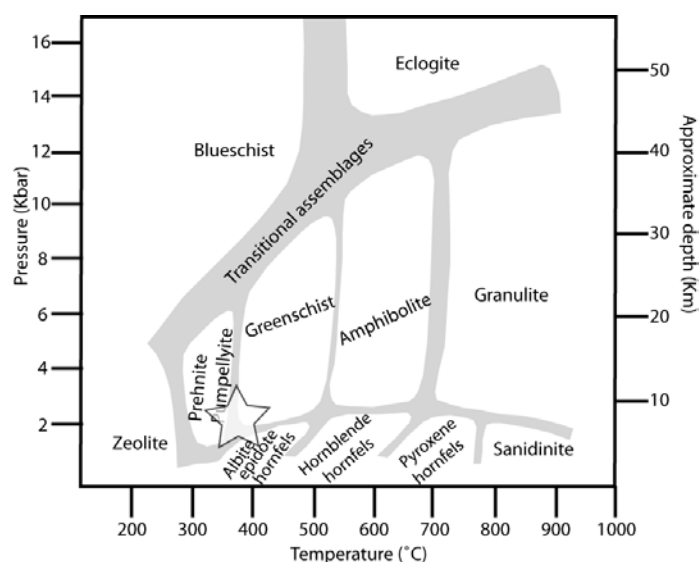
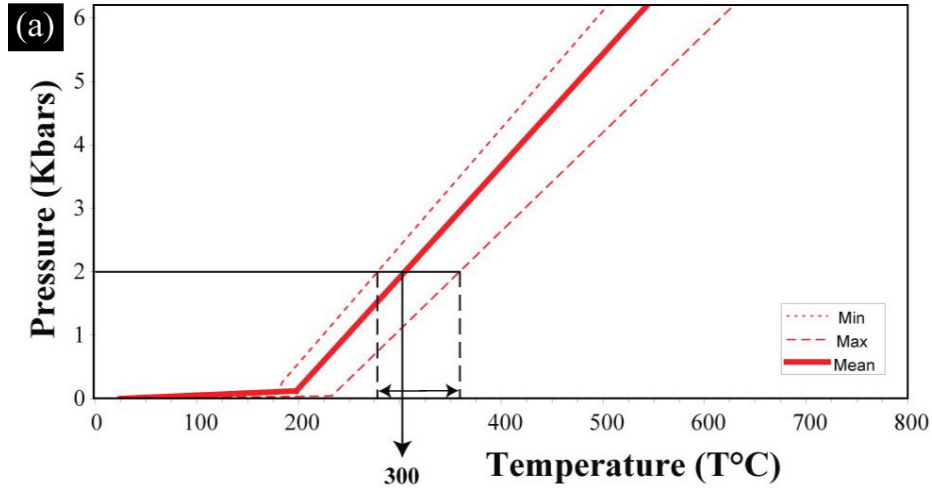
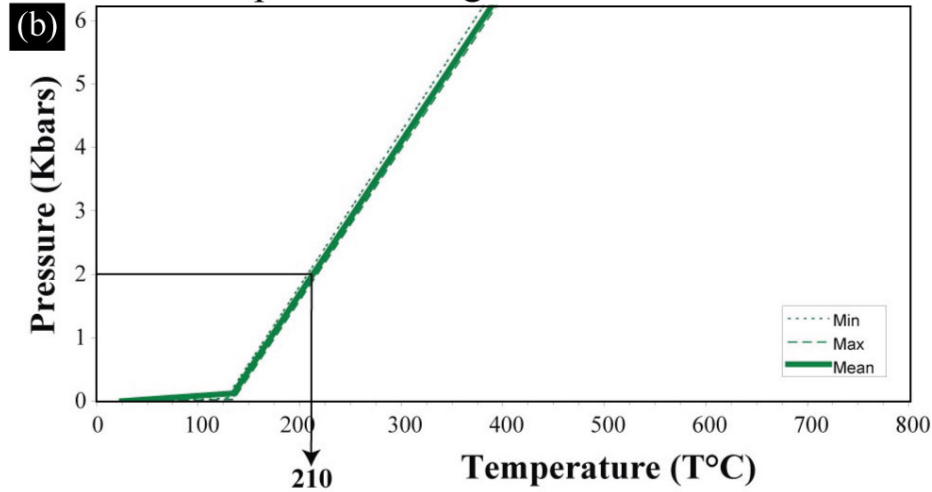


Figure 5.11: Pressure estimate of 1.5--3kbar, used to determine T_i , corresponds to the observed alteration mineral assemblage in volcanic host rocks. (Pressure-temperature fields from Best, 2006).

Sulphide-bearing - magmatic fluid



Sulphide-bearing - meteoric fluid



Barren

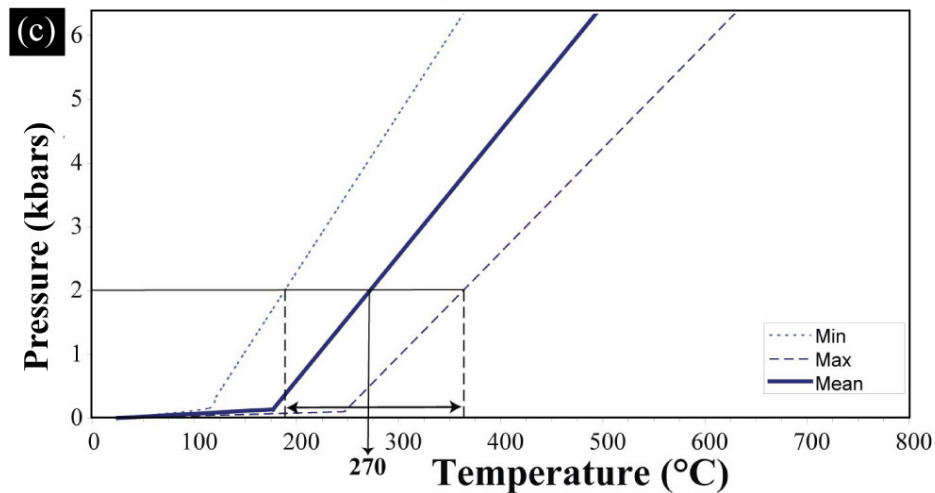


Figure 5.12: Minimum, mean and maximum isochores plotted for (a) the magmatic fluid component and (b) the meteoric fluid component in the sulphide-bearing veins, and (c) the barren veins of Trawnamoe and Stradbally Cove, with a pressure correction of 2kbar yielding a range of true trapping temperatures (T_1) of 300°C, 210°C and 270°C respectively.

5.7 Discussion

Two distinct styles of vein mineralisation have been recorded from field observations (Chapter Two) at Trawnamoe and Stradbally Cove: 1) sulphide-bearing, sheeted vein systems and 2) barren, linear veins. Fluid inclusions from both styles of vein deposits show a wide range of T_H (~100°C to 245°C). In FIs from sulphide-bearing veins, the negative correlation between T_H and salinity (Figure 5.9) is attributed to fluid mixing between a high temperature (300°C) low salinity (~11 eq. wt% NaCl) magmatic fluid and a lower temperature (210°C) high salinity (~18 eq. wt% NaCl) meteoric fluid. Fluids associated with barren veins show no correlation between T_H and salinity possibly indicating isothermal changes in salinity or isothermal mixing of different composition fluids (Figure 5.13).

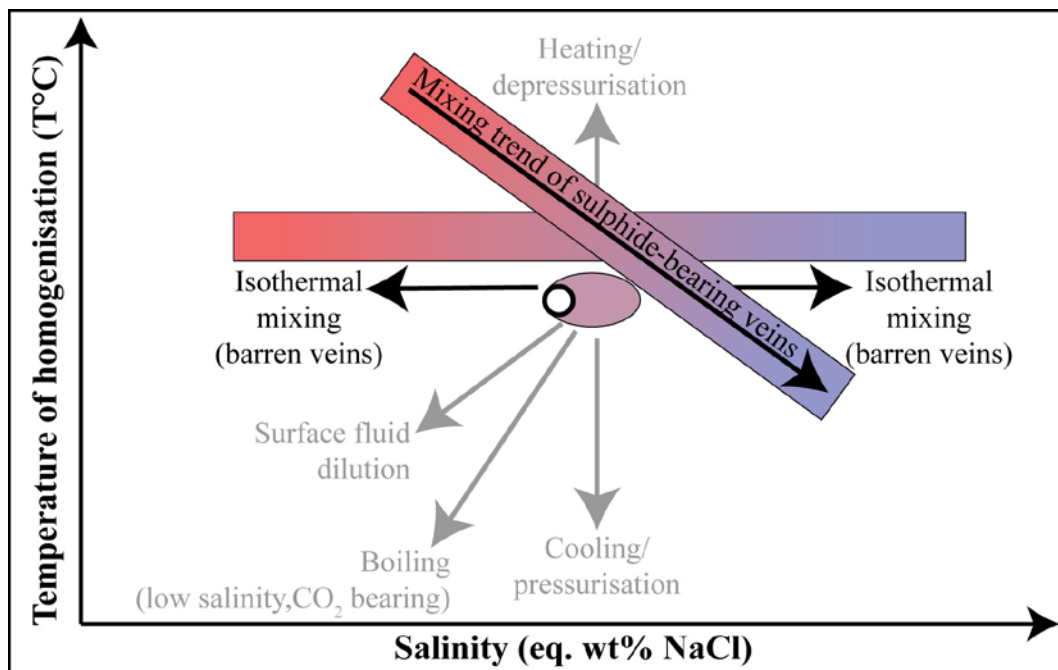


Figure 5.13: Typical trends in T_H -salinity space due to various fluid evolution processes (modified from Wilkinson, 2001). The temperature and salinity of fluids associated with sulphide-bearing veins record a mixing trend between a high temperature low salinity fluid and a low temperature high salinity fluid. Conversely, fluids associated with barren veins show isothermal changes in salinity or isothermal mixing of different composition fluids.

Primary, two phase, liquid-rich FIs from hydrothermal veins at Trawnamoe and Stradbally Cove are similar to FIs recorded from the Carboniferous Irish-type Zn-Pb mineralisation (Wilkinson, 2001), where ore genesis resulted from a combination of exhalative processes, diagenesis and later hydrothermal fluid activity (Wilkinson *et al.*, 2003). FIs recorded in veins within Lower Palaeozoic rocks have similar salinities to fluids from Carboniferous Irish-type mineralisation (Figure 5.14). This indicates that the fluids within the Lower Palaeozoic basement may be linked to the fluids involved in Carboniferous mineralisation (Everett *et al.*, 1999). The fluid mixing trend suggested for sulphide-bearing veins in Trawnamoe and Stradbally Cove (Figure 5.9) is similar to multi-source fluid models in Carboniferous Irish-type mineralisation (Figure 5.15). Mixing of separate fluids containing the different chemical components (e.g. S, Fe) required for ore deposition (Samson and Russell, 1987; Banks and Russell, 1992, Banks *et al.*, 2002) was the primary control of mineralisation in the Carboniferous (Hitzmann and Beaty, 2003). A similar trend of sulphide precipitation in vein mineralisation in Waterford was probably controlled by mixing of metal-rich hydrothermal fluids with cooler, high salinity meteoric fluids.

The sheeted vein systems at Trawnamoe and Stradbally Cove have similar characteristics to feeder channels that transect chlorite zones, leading to Volcanic Hosted Massive Sulphide (VHMS) deposits (Gifkins *et al.*, 2005). The chlorite zone associated with the Avoca VHMS deposit is characterised by low-grade ore mineralisation consisting of disseminations and veinlets, where stockwork veins represent feeder channels to a massive ore (Downes and Platt, 1978). T_H of quartz vein hosted FIs at Avoca range from 155°C to 198°C (Williams *et al.*, 1986) similar to the temperatures observed in FIs from Trawnamoe and Stradbally Cove vein mineralisation (Figure 5.14). However, salinities are much lower in Avoca (~2.5 eq. wt.% NaCl) as a result of dominantly magmatic fluid involved in mineralisation (Williams *et al.*, 1986). The model proposed by Downes and Platt (1978) for Avoca mineralisation suggests that the thickest sulphides precipitate along the keel of a basin due to fumarolic activity, similar to the Iberian Pyrite Belt (IPB) (Boulter, 1993), where shallow level intrusions produced highly variable topography resulting in a mineralisation ‘trap’. Magma-sediment interactions as a result of these shallow level intrusions can introduce large volumes of heated fluid into the mineralising system (Boulter, 1993). Abundant

shallow level intrusive activity and magma-sediment interaction in Waterford (Chapter Two) provided the magmatic fluid component, the heat to the system and the irregular topography required for sulphide accumulation.

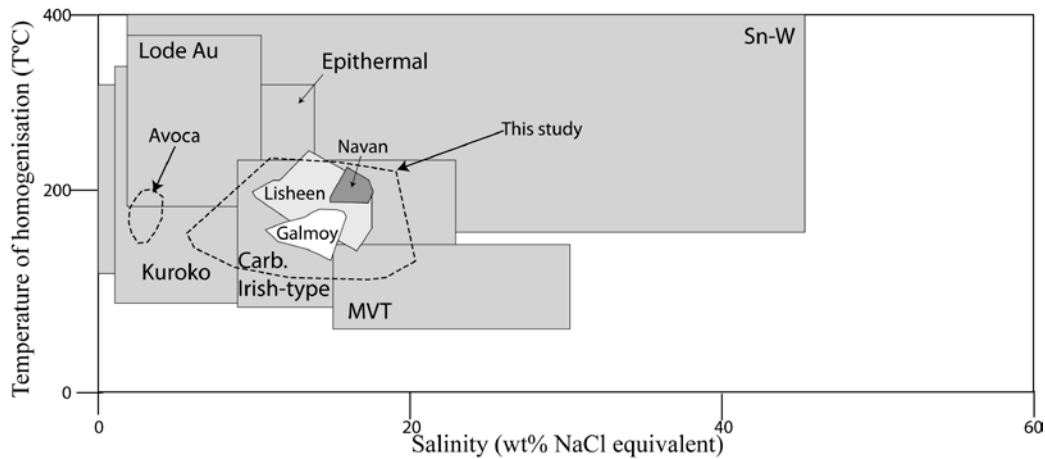


Figure 5.14: Typical ranges of salinity and T_H for inclusions from specific deposit types showing the overlap between FIs analysed in this study and Kuroko, epithermal and Carboniferous Irish-type mineralisation. (Graph modified after Wilkinson (2001) with values for the Avoca deposit from Williams *et al.* (1986)). Lode Au = vein gold formed at moderate depths at 200-300°C, Epithermal = those formed in near-surface environments and at <300°C, Kuroko = volcanic associated massive sulphide deposits, Carboniferous Irish-type = carbonate hosted Zn-Pb-Ag-Ba deposits, MVT = Mississippi Valley Type (carbonate hosted Zn-Pb-F-Ba), Sn-W = Tin-Tungsten-Copper bearing vein systems and pegmatitic deposits associated with granitoids.

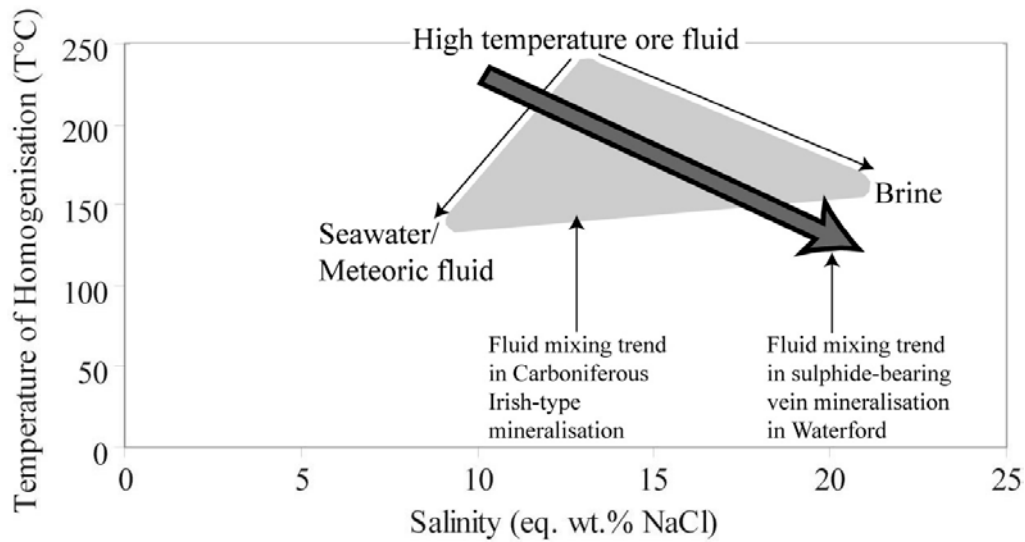


Figure 5.15: Trend of fluid mixing between a high temperature, low salinity fluid and a low temperature, high salinity fluid in the sulphide-bearing veins from Trawnamoe and Stradbally Cove compared to a similar trend of fluid mixing in Carboniferous Irish-type mineralisation between a high temperature ore fluid and low temperature seawater or low temperature brine. (Carboniferous data from Banks and Russell, 1992 and Everett *et al.*, 1999).

5.8 Conclusions

The sulphide-bearing veins and barren veins from Trawnamoe and Stradbally Cove are indistinguishable in terms of their T_H and salinity, suggesting a fluid or several fluids of similar composition were involved during the formation of both vein types. The negative correlation between T_H and salinity in FIs from sulphide-bearing veins is interpreted as a mixing event between a high temperature, low salinity fluid and a lower temperature, high salinity fluid. The mixing pattern between high and low temperature fluids was probably the primary control of sulphide precipitation, similar to Carboniferous Irish-type mineralisation. FIs in barren veins show no definite trend between T_H and salinity, and probably represent isothermal mixing of the original separate fluids (possible magmatic vs. meteoric).

The processes involved in vein mineralisation incorporate features observed in both Carboniferous Irish-type mineralisation and the formation of Avoca VHMS deposits (Figure 5.16). Shallow level intrusions produced the irregular topography and also locally heated sediment pore water and initiated hydrothermal fluid circulation. Fluid mixing occurred, some of which may have led to the precipitation of sulphides within veins, with possible sulphide deposits developed within overlying basins or topographic lows (Figure 5.16).

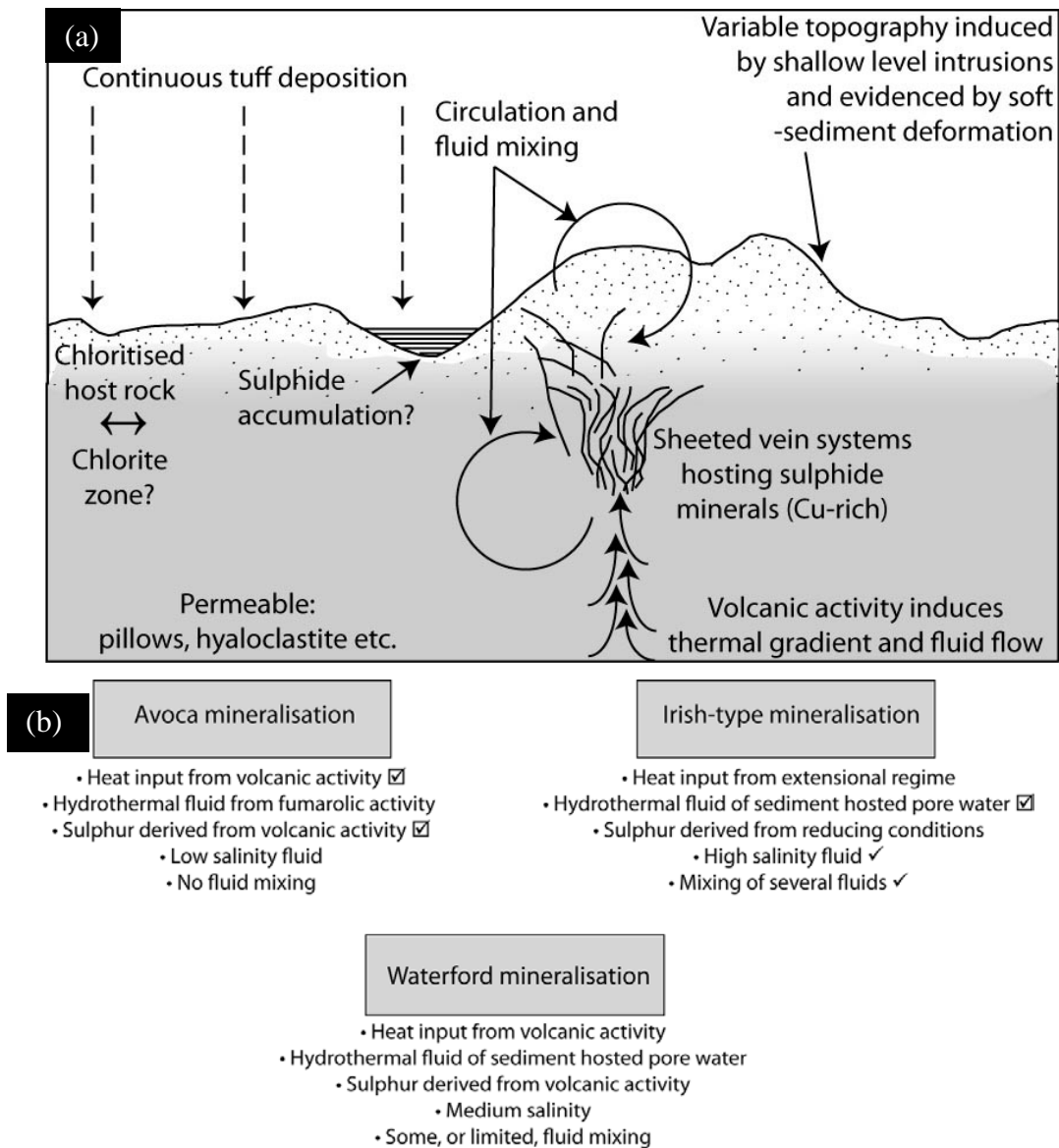


Figure 5.16: Summary of possible hydrothermal fluid flow and mineralisation leading to sheeted sulphide-bearing vein systems and the possible deposition of a massive sulphide deposit. (a) Drawn from observations at Waterford with interpretations corresponding to models for general VMS formation of Whitehead (1973), Reed (1983) and Gifkins et al. (2005) with similar features to VMS formation at Avoca (Downes and Platt, 1978; Jones, 1983) and the Iberian Pyrite Belt (Boulter, 1993), and (b) similarities between Waterford mineralisation and both Avoca and Carboniferous Irish-type mineralisation, with Waterford probably representing a mix between the two of these.

Chapter Six:

Summary and Conclusions

6.1 Introduction

The following chapter provides a brief summary of results compiled from all aspects of this study (field investigation, petrography, bulk rock and mineral geochemical analysis and fluid inclusion studies). A conceptual model of the series of events occurring at the Bunmahon Volcano and the surrounding area during active Ordovician volcanism is also presented, using data introduced and discussed in all preceding chapters.

6.2 Summary of results

Field investigations suggest that the majority of lithologies within the Bunmahon Formation are mafic-intermediate and that the earliest eruptions resulted in magma-water interaction (forming tuff, hyaloclastite and pillow lavas), while later activity resulted in magma-sediment interaction (forming peperite) (Figure 6.1a, b). Lateral variation across the volcanic pile is due to the formation of lithologies either close to the central vent (Trawnamoe) or in more distal regions such as along the flanks of the volcano (Stradbally Cove). Primary volcanic and sedimentary deposits are contemporaneous with secondary volcanoclastic deposits and these are commonly inter-bedded or inter-fingered with one another (Chapter Two).

As a result of both hydrothermal alteration and later metamorphism, the dominant mineral phases include chlorite, epidote, albite, Fe- and Ti-oxides, sericite, and occasionally pumpellyite, pyrite and calcite. The more hydrous alteration minerals such as chlorite, epidote and pumpellyite predominantly occur within the more glassy components (e.g. hyaloclastite, peperite clast margins) of all the rock types as a result of magma-water or magma-sediment interaction.

Geochemical analyses of mineral compositions indicate a circulating fluid of varying Fe/Mg ratios (dependant on the ratio between seawater and hydrothermal fluid), which produced the observed alteration mineral assemblage. The secondary mineral assemblage varies between rock types, as a result of the variation in

composition (basalt/sub-alkaline basalt to rhyolite), the variation in water/rock ratio and the variation in composition of the fluid (Chapter Four). The range of chlorite composition in rocks from the Bunmahon Formation (Figure 4.17) is predominantly attributed to the varying composition of the hydrothermal fluid, which in turn is deemed a function of temperature. Chlorite geothermometry suggests that the temperature of formation of chlorite and therefore the temperature of the hydrothermal fluid was in the region of 280-360°C. This is consistent with temperature estimates from fluid inclusion studies of vein mineralisation, which suggest that the vein forming fluid was composed of two separate fluids: a high temperature, low salinity fluid and a low temperature, high salinity fluid. However, stable isotope analysis is required to fully constrain the origin of these fluids (meteoric vs. magmatic etc.). Fluid mixing and vein formation are analogous to the fluid mixing involved in hydrothermal alteration (low temperature, Mg-rich - seawater and high temperature, Fe-rich - hydrothermal fluid). Therefore, the metasomatism or alteration of the host volcanic rocks and the formation of sulphide-bearing vein systems may have occurred as a result of the same hydrothermal event, but the timing of this event cannot be fully constrained.

6.3 The evolution of the Bunmahon Volcano and its environs

A conceptual model tracking the evolution of the Bunmahon Volcano is presented in Figure 6.1. Early volcanic activity associated with the Bunmahon Volcano was characterised by eruption of mafic-intermediate magma onto the seafloor. Violent interaction between the hot magma and cold seawater resulted in phreatomagmatic explosions and produced ash fragments that formed the numerous tuffs recorded in both Trawnamoe and Stradbally Cove. The bedded nature of both lapilli tuff and crystal tuff at Trawnamoe indicates that these were formed as a result of ash-fall and settling through a water column (primary), whereas the more massive nature of tuffs at Stradbally Cove indicates an ash-flow origin (secondary) (Figure 6.1a). In less violent eruptions cooling-contraction granulation was the dominant fragmentation process that occurred due to magma-water interaction. Large volumes of erupting magma produced abundant sheet flows throughout the Bunmahon Volcano (e.g. Trawnamoe, Kilmurrin Cove, Ballydowane Bay) as well as minor pillow lava in Trawnamoe, all of which comprise a crust of hyaloclastite that proves the occurrence of magma-water

Summary and Conclusions

interaction. Fine-grained, laminated, iron-rich sedimentary rocks such as mudstone and siltstone are more commonly deposited along the flanks of the Bunmahon Volcano (e.g. Stradbally Cove, Dunabrattin Head) and grade into sequences of ash tuff (e.g. mudstone and pyrite-rich tuff, Stradbally Cove). Petrographic and geochemical investigations of these sedimentary rocks indicate a mafic volcanic origin, from rocks probably formed in an island arc setting. Therefore, the sedimentary rocks were probably sourced from the weathered detritus of the first volcanic products in the initial phase of volcanism. Tuffs that are graded and interspersed with these sedimentary sequences are tholeiitic and genetically related to the intermediate composition lava flows and shallow intrusive rocks.

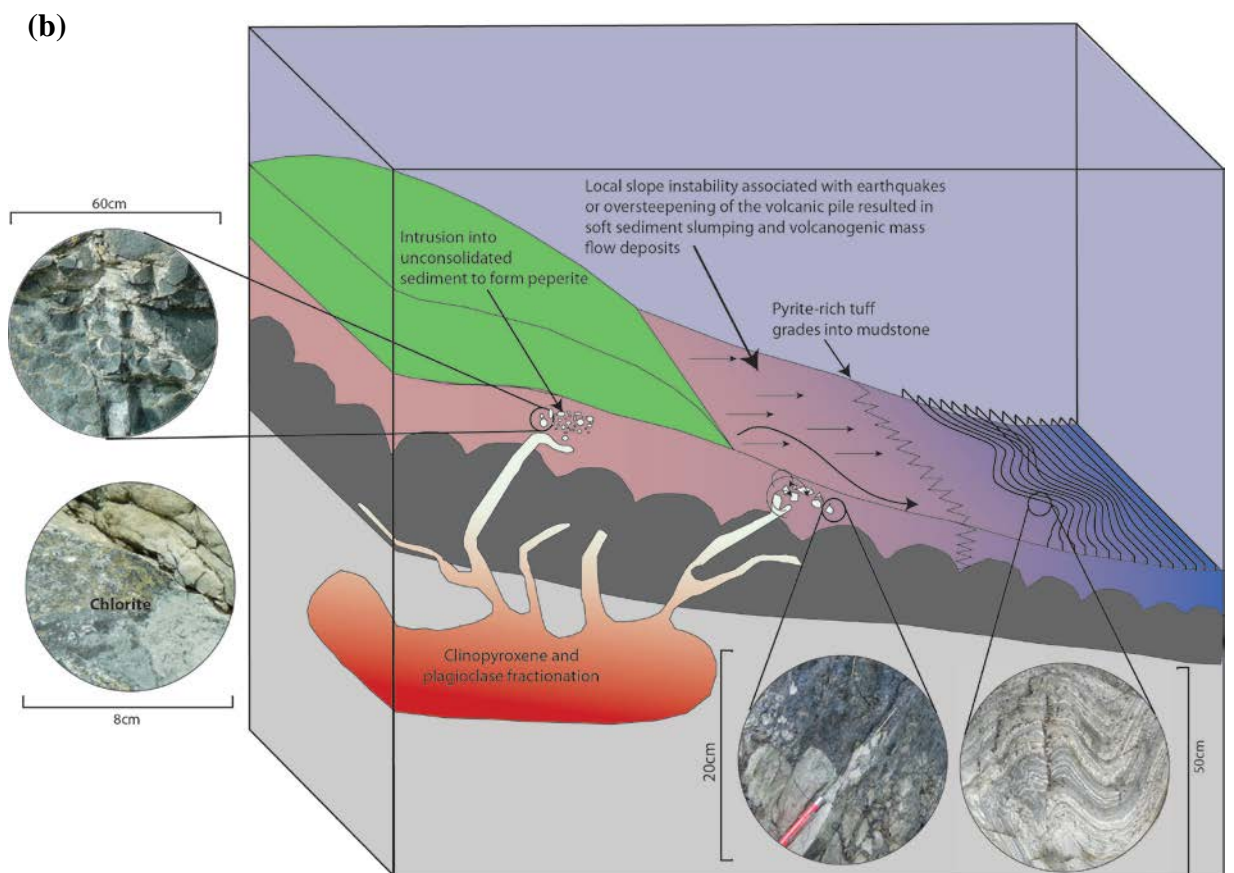
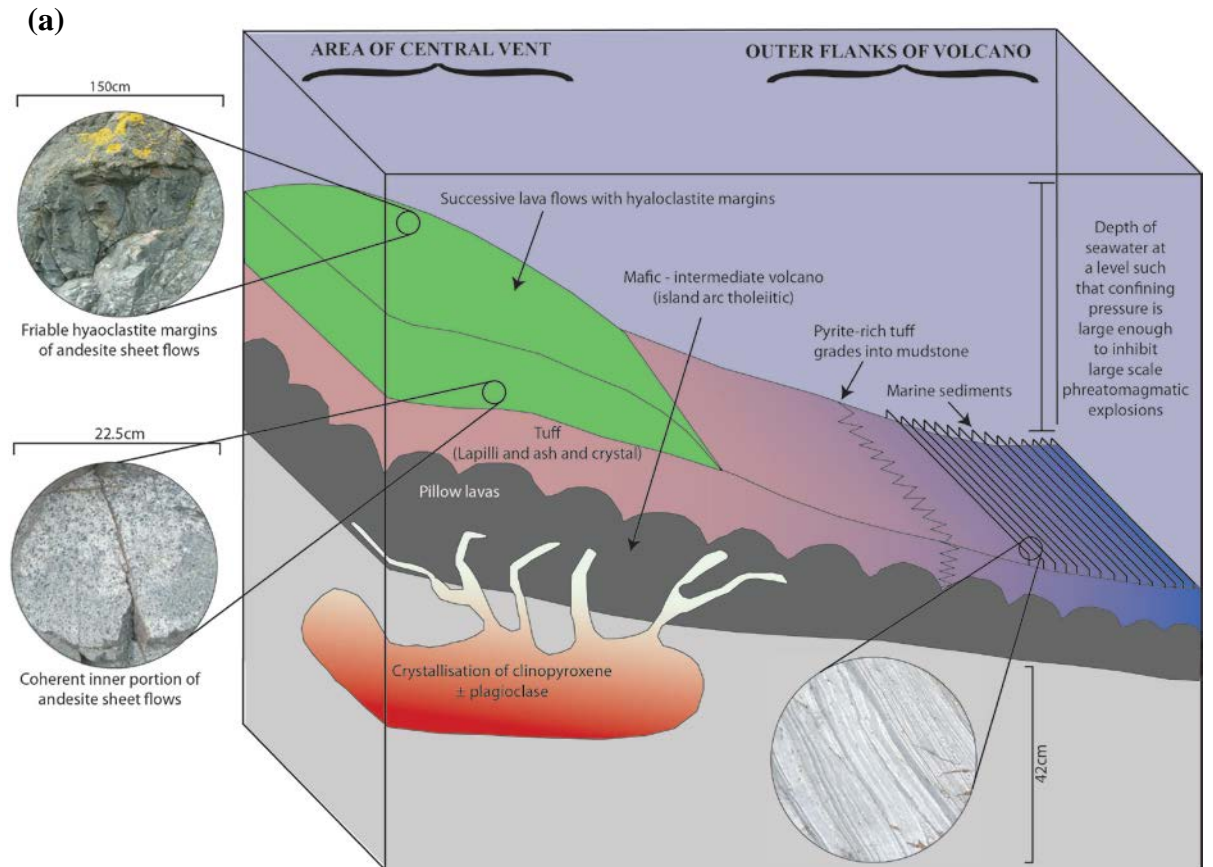
Subsequent to the deposition of large volumes of tuff covering extensive areas (recorded in all localities visited), some of the mafic-intermediate magma was unable to breach the sediment surface due to the increase in confining pressure. Consequently, these sub-volcanic intrusions spread out along weakened areas of unconsolidated sediment. Interaction between hot magma and cold, wet sediment resulted in the formation of a range of peperite morphologies. Fluidal peperite in Trawnamoe was formed as a result of intrusion of basaltic andesite into unconsolidated ash and crystal tuff. The detachment, cooling and solidifying of fluidal blobs of magma, as a result of heat transfer from magma to sediment, was accompanied by heating of the sediment pore water. Similarly, interaction between basaltic andesite and wet mud in Stradbally Cove resulted in heat transfer across the magma-sediment interface, limited sediment fluidisation and the formation of peperite with associated deposition of sulphide-bearing minerals. These shallow-level intrusions into the unconsolidated sediment pile may have contributed to irregular topography and sediment instability. Earthquakes that are typically associated with volcanic activity would have combined with the build-up and over-steepening of unconsolidated material to cause the localised slope instability that produced mass flow deposits and sediment slumping. As the sediments and tuffs continued to consolidate and became increasingly lithified, subsequent intrusions resulted in decreasing levels of interaction between the magma and the host (in particular Stradbally Cove timeline, Figure 2.29, Chapter Two). Intermediate-felsic intrusive rocks with straight and chilled margins represent the last phases of magmatism associated with the Bunmahon Volcano.

Summary and Conclusions

Later felsic intrusive rocks associated with the Campile Formation (Kilfarrasy Volcano) volcanic activity display faulted relationships with the host rocks of the Bunmahon Formation (e.g. quartz feldspar porphyry (sample CT1), Trawnamoe).

The elevated geothermal gradient in and around the area of the Bunmahon Volcano, combined with renewed volcanic activity resulted in the heating and regional circulation of a hydrothermal fluid. Sulphur contained in the volcanic rocks was remobilised and deposited as sulphide-bearing minerals (e.g. pyrite and chalcopyrite) in sheeted vein systems that dissect the rocks of the Bunmahon Formation, in nodules in tuff and replacing the more permeable sandy layers in the convoluted siltstone (Figure 6.1c). Field relations prove that the sheeted vein systems dissect the rock at an earlier less competent stage than the planar, barren veins such that there is a temporal spread (and this also indicates that there were at least two hydrothermal events). Later regional deformation associated with the Caledonian Orogeny may have subsequently remobilised some of these residing fluids along structural weaknesses (e.g. veins) and resulted in a regional scale greenschist facies mineral assemblage.

Summary and Conclusions



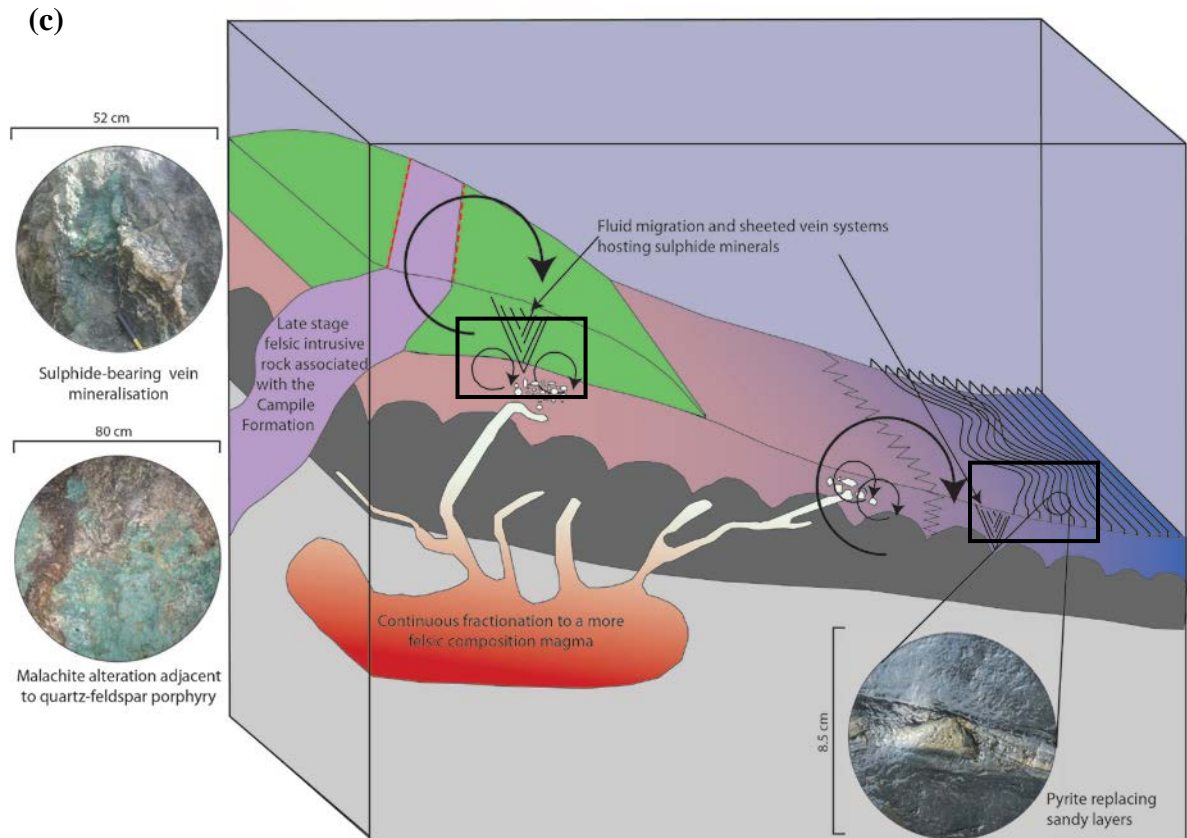


Figure 6.1: A conceptual model of the evolution of the Bunmahon Volcano, highlighting events that occurred at Trawnamoe and Stradbally Cove: (a) mafic-intermediate magma erupted onto the seafloor to form lava flows with hyaloclastite margins and tuffs that grade laterally into the surrounding sedimentary rocks, (b) sub-volcanic intrusions formed peperite while slope instability resulted in mass flow deposits and soft sediment slumping, and (c) late-stage felsic intrusive rocks cut across the Bunmahon Formation and the associated hydrothermal fluid circulation resulted in sulphide-bearing vein formation and deposition of secondary pyrite. The boxed areas in (c) corresponds to the greater resolution of fluid movement provided in Figure 6.2.

Summary and Conclusions

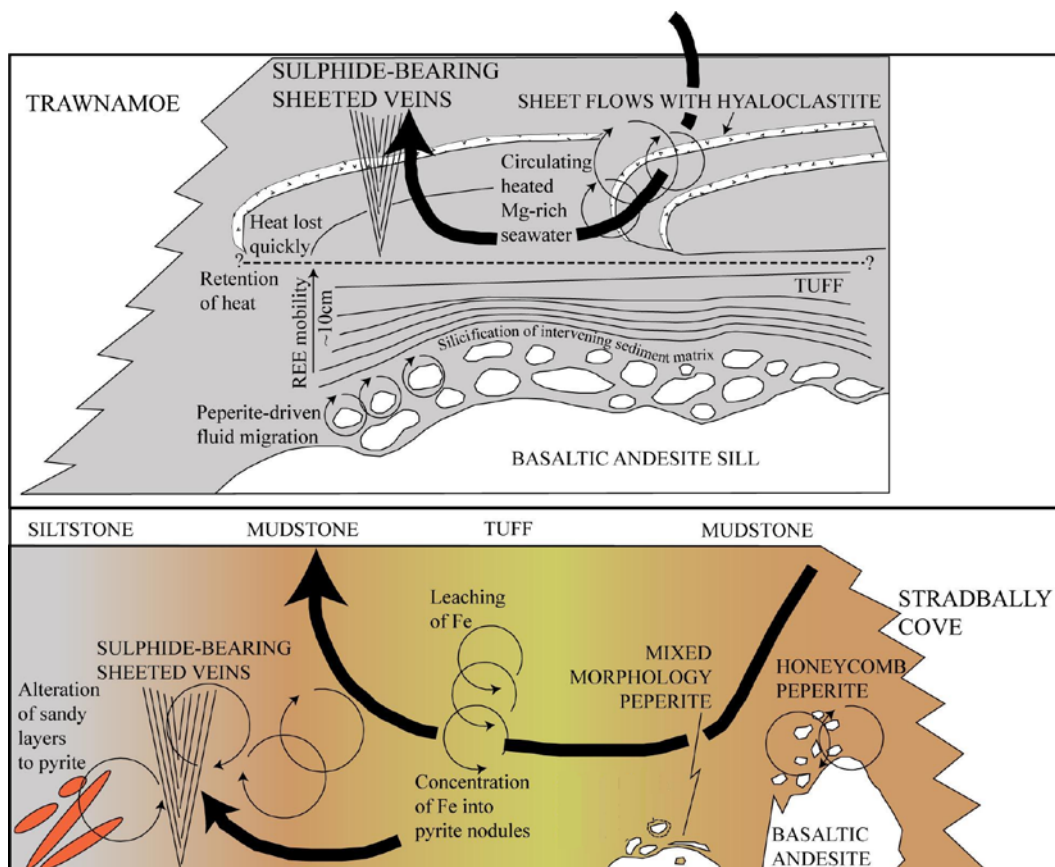


Figure 6.2: Schematic representation of hydrothermal fluid circulation in Trawnamoe and Stradbally Cove, as a result of volcanic heat generated in an area with an already elevated geothermal gradient.

Circulation of a hydrothermal fluid throughout the volcanic and sedimentary pile in south Waterford is recorded on the local (outcrop) and regional scale. Local REE mobility and Na and K depletion combined with Si enrichment is limited to the tuff matrix of peperite at Trawnamoe. The pattern of element mobility suggests that the primary cause of the redistribution of elements was peperite-driven fluid migration. Transfer of heat from the intruding body of magma to the host sediment probably induced fluid circulation that also caused sediment fluidisation within the tuff matrix of the peperite. Rapid heat transfer from magma to sediment and the subsequent fluid circulation also quenched the margins of separated magmatic clasts in peperite. Later regional scale alteration primarily targeted these glassy components in peperite (and hyaloclastite) resulting in a sub-greenschist facies mineral assemblage dominated by chlorite and epidote.

Temperatures estimated from fluid inclusions in vein samples (Chapter Five) display a similar range to the lower temperatures calculated from the chlorite

Summary and Conclusions

geothermometer (Chapter Four) of Kranidiotis and MacLean (1987), indicating that hydrothermal alteration and vein formation occurred at similar temperatures. Additional studies that give similar temperature ranges to both the volcanic rocks and vein samples from this study (determined by chlorite composition and fluid inclusion studies) include the Conodont Alteration Index (CAI) calculations of Bergström (1980) and illite crystallinity studies of Diskin (1997). Bergström (1980) stated that CAI values of 5 (corresponding to heating to $>300^{\circ}\text{C}$) implied that volcanism had a substantial, if not major, effect on the Tramore Limestone Formation (base equivalent to the top of the Bunmahon Formation). Illite crystallinity studies of the south Waterford volcanic and associated sedimentary rocks yielded Kübler Index (KI) values of 0.17-0.25 (Diskin, 1997) with a decrease in the crystallinity corresponding to an increase in temperature (Lee and Lee, 2001). The KI value of 0.25 corresponds to the boundary between the anchizone and the epizone, with an approximate temperature of 300°C (Abad, 2007) correlating well with the lower temperatures calculated from both chlorite geothermometers (Figure 6.3 and Table 6.1). The slightly lower temperature values determined from illite crystallinity compared to chlorite composition may be due to a slower reaction rate to short-lived thermal events (Lee and Lee, 2001).

Later regional scale metamorphic events (in particular related to the Caledonian Orogeny) resulted in the development of a more regional-scale greenschist facies mineral assemblage (Shannon, 1979). The Bunmahon Formation contains a higher proportion of minerals such as chlorite, epidote and pumpellyite than the Campile Formation, which contains a higher proportion of albite and sericite accompanying the dominant chlorite.

Chlorite geothermometry	Illite crystallinity	Conodont alteration index	Fluid inclusion (corrected)
279°C - 362°C	$\sim 300^{\circ}\text{C}$	300°C - 400°C	210°C - 360°C

Table 6.1: Temperature variations determined for the Waterford volcanic rocks, associated sedimentary rocks and cross-cutting vein systems.

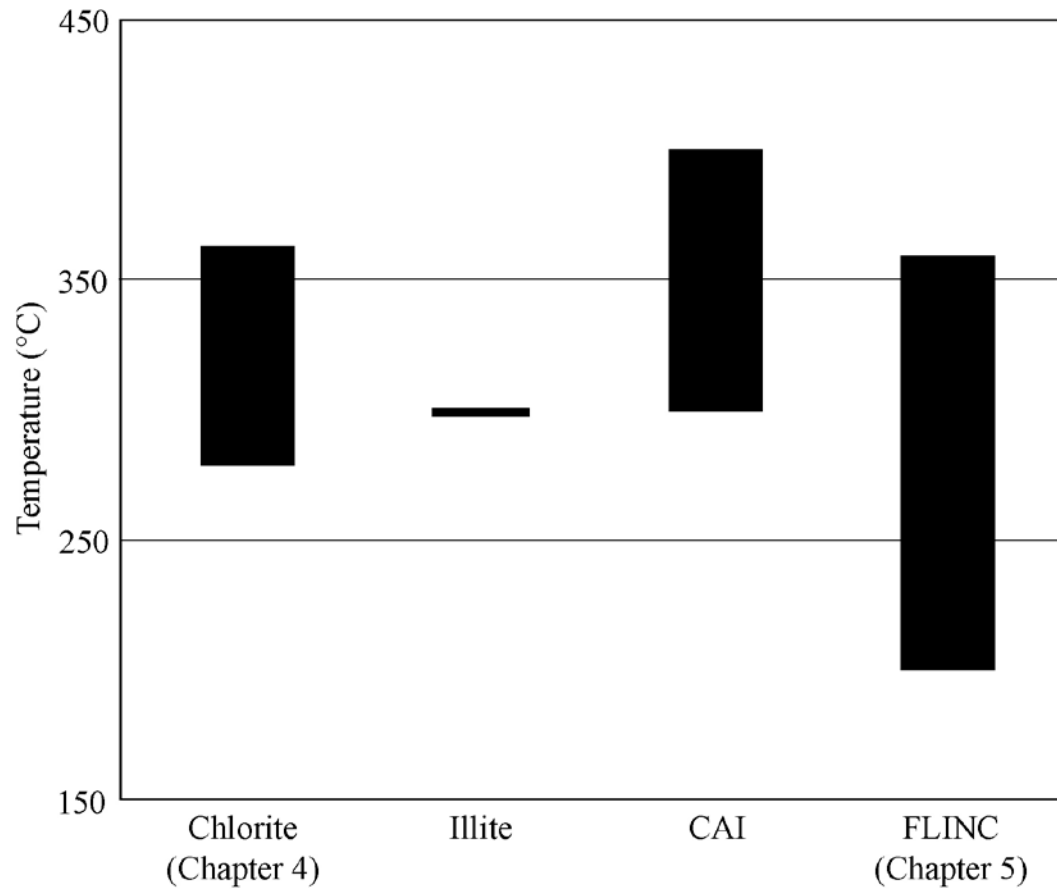


Figure 6.3: Comparisons between temperatures calculated from chlorite geothermometers, illite crystallinity, conodont alteration index and fluid inclusions. Illite crystallinity data from Diskin (1997) and CAI values from Bergström (1980).

Summary and Conclusions


	Peperite-driven fluid migration	Chlorite alteration	Sulphide-bearing vein hosted primary fluid inclusions
Temperature	>350°C	280°C - 400°C	210°C - 360°C
	 Decreasing temperature		
Scale	Local	Regional	Regional
Host rocks	Sedimentary matrix in peperite	Ordovician volcanic rocks (permeable rocks more susceptible)	Ordovician volcano-sedimentary rocks
Fluid composition	Combination of F ⁻ , Cl ⁻ , OH ⁻ , CO ₃ ²⁻ , SO ₄ ²⁻ and/or PO ₄ ³⁻	Mg, Fe, S	H ₂ O-NaCl, H ₂ O-NaCl-NaSO ₄ , H ₂ O-NaCl-KCl H ₂ O-MgCl ₂
Fluid source	Sediment pore fluid with minor magmatic fluid	Hydrothermal fluid (pore fluids) and circulating seawater	Mix of magmatic and meteoric (seawater + sediment pore water) fluid

Table 6.2: Comparisons between local and regional scale fluid temperatures, compositions and occurrences.

6.4 Conclusions

The main conclusions of this study are summarised below:

1. During the initial phases of volcanic activity at the Bunmahon Volcano, mafic-intermediate lava erupted onto the seafloor. The resulting magma-water interaction formed common hyaloclastite flow margins and tuff deposits. Accumulation of this material on the volcano resulted in an increase in confining pressure, which was sufficient to inhibit the eruption of subsequent magma. Upwelling magma consequently became entrained in the unconsolidated volcanoclastic sediment pile resulting in magma-sediment interaction and the formation of peperite. Increasing compaction and consolidation of the sediments caused a gradual decrease in the level of interaction between the magma and host sediments. Thus, the observed evolution of intrusive morphologies from peperite to straight intrusive contacts was developed, in particular at Stradbally Cove.
2. Heat transfer across the magma-sediment interface in peperite initiated sediment fluidisation and migration of heated sediment pore fluid. Element mobility (REE, Si, Na, K) recorded in peperite is probably due to the movement of this super-heated pore water.
3. Rocks which contained a significant glass component were particularly susceptible to later alteration and metamorphism and therefore contain a relatively high percentage of secondary minerals, the most common of which are chlorite, epidote and albite.
4. The majority of rocks from the Bunmahon Formation are extensively altered but still retain their primary trace element, and occasionally major element, volcanic signature. The geochemical composition of these rocks suggests they were formed in a volcanic arc setting.
5. An elevated geothermal gradient throughout the Bunmahon Volcano and its environs, combined with renewed volcanic activity at the Kilfarrasy Volcano, resulted in the generation and regional circulation of a hydrothermal fluid. Chlorite geothermometry indicates the temperature of the hydrothermal fluid was between 280°C and 360°C. This range concurs with the temperatures at which sulphide-bearing vein formation was determined to have occurred (210°-360°C). This temperature correlation may be interpreted as indicating

Summary and Conclusions

that the sulphide-bearing veins and local hydrous alteration assemblage were products of the same hydrothermal fluid system.

6. Later regional deformation caused (1) faulting of the more competent volcanic lithologies, (2) folding of intercalated sedimentary rocks and (3) the generation of a sub-greenschist facies metamorphic grade.

6.5 Suggestions for future work

Results presented in this thesis suggest a significant relationship between the volcanic and the hydrothermal systems at the Bunmahon Volcano and in the surrounding area. In order to fully constrain this relationship, and possibly aid the exploration of base metal mineralisation targets in the area, the following additional studies are recommended:

1. Stable isotope analyses (e.g. sulphur isotopes) should be carried out on pyrite and chalcopyrite hosted within the sheeted vein systems in order to determine the primary origin of the hydrothermal fluid that formed these veins. This should complement the results from fluid inclusion studies already carried out in this thesis, which suggest that the hydrothermal fluid comprised a mixed fluid originating from two sources (e.g. magmatic vs. meteoric).
2. Accurate age dating using zircon crystals (a limited number were found in this study in tuffs and sedimentary rocks) would be useful to verify the sequences of events interpreted, in this study, as a result of field relationships. This would also provide evidence of the duration of volcanic activity during both phases (Bunmahon and Kilfarrasy) and the duration of quiescence between these two phases.
3. A more regional scale investigation of the relationship between the sulphide-bearing vein mineralisation and the hydrothermal alteration of the host volcanic rocks would contribute significantly to the overall understanding of events at regional scale. However, the limited inland exposure may pose a problem for the completion of a full model of the region.

References

- Aalto, K.R., 1986. Depositional Sequence of Argillite, Diamictite, Hyaloclastite, and Lava Flows within the Franciscan Complex, Northern California *The Journal of Geology*, **94**, 744-752.
- Abad, I., 2007. Physical meaning and applications of the illite Kübler index: measuring reaction progress in low-grade metamorphism, XXVII Meeting of the Spanish Mineralogical Society.
- Archer, D.G., 1992. Thermodynamic properties of NaCl + H₂O system: II. Thermodynamic properties of NaCl(aq), NaCl2H₂O(cr) and phase equilibria *Journal of Physical and Chemical Reference Data*, **28**, 1-17.
- Armstrong-Altrin, J.S. and Verma, S.P., 2005. Critical evaluation of six tectonic setting discrimination diagrams using geochemical data of Neogene sediments from known tectonic settings *Sedimentary Geology*, **177**, 115-129.
- Baier, J., Audetat, A. and Keppler, H., 2008. The origin of the negative niobium tantalum anomaly in subduction zone magmas *Earth and Planetary Science Letters*, **267**, 290-300.
- Bakker, R.J., 2003. Package FLUIDS 1. Computer programs for analysis of fluid inclusion data and for modelling bulk fluid properties *Chemical Geology*, **194**, 3-23.
- Banks, D.A., Boyce, A.J. and Samson, I.M., 2002. Constraints on the origin of fluid forming Irish Zn-Pb-Ba deposits: evidence from the composition of fluid inclusions *Economic Geology*, **97**, 471-480.
- Banks, D.A. and Russell, M.J., 1992. Fluid mixing during ore deposition at the Tynagh base-metal deposit, Ireland *European Journal of Mineralogy*, **4**, 921-931.
- Bardintzeff, J.M. and McBirney, A.R., 2000. *Volcanology*. Jones and Barlett Publishers.
- Bareschino, P., Gravina, T., Lirer, L., Marzocchella, A., Petrosini, P., and Salatino, P., 2007. Fluidization and de-aeration of pyroclastic mixtures: the influence of fines content, polydispersity and shear flow *Journal of Volcanology and Geothermal Research*, **164**, 284-292.
- Bear, A.N. and Cas, R.A.F., 2007. The complex facies architecture and emplacement sequence of a Miocene submarine mega-pillow lava flow system, Muriwai, North Island, New Zealand *Journal of Volcanology and Geothermal Research*, **160**, 1-22.
- Befus, K.S., Hanson, R.E., Miggins, D.P., Breyer, J. A., Busbey, A. B., 2009. Nonexplosive and explosive magma/wet-sediment interaction during emplacement of Eocene intrusions into Cretaceous to Eocene strata, Trans-

Pecos igneous province, West Texas *Journal of Volcanology and Geothermal Research*, **181**, 155-172.

Bergström, S.M., 1980. Conodonts as paleotemperature tools in Ordovician rocks of the Caledonides and adjacent areas in Scandinavia and the British Isles *Geologiska Föreningen i Stockholm. Föreläsningar*, **102**, 377 - 392.

Bergström, S.M., Chen, X., Gutiérrez-Marco, J.C. and Dronov, A., 2009. The new chronostratigraphic classification of the Ordovician System and its relations to major regional series and stages and to $\delta^{13}\text{C}$ chemostratigraphy *Lethaia*, **42**, 97-107.

Best, M.G., 2006. *Igneous and Metamorphic petrology*. Blackwell publishing.

Bhatia, M.R., 1983. Plate tectonics and geochemical composition of sandstones *The Journal of Geology*, **91**, 611-627.

Boland, M., 1982. Summary of exploration work at Fennor P.L.s 2751 and 504 Co. Waterford(R.W.A. Crowe, ed. Geological Survey of Ireland, Dublin; Aquataine Mining (Ireland) Ltd, Dublin.

Boland, M.A., 1983. The Geology of the Ballyvoyle-Kilmacthomas-Kilfarassy area, County Waterford, with an account of the Lower Palaeozoic Geology of County Waterford. Unpublished Ph.D. thesis, University of Dublin, Trinity College.

Borisenko, A.S., 1977. Study of the salt composition of solutions in gas-liquid inclusions in minerals by the cryometric method *Soviet Geology and Geophysics*, **18**, 11-19.

Boulter, C.A., 1993. High-level peperitic sills at Rio Tinto, Spain: Implications for stratigraphy and mineralization *Transactions of the Institute of Mining and Metallurgy (Section B: Applied Earth Sciences)*, **102**, 30-38.

Boulter, C.A., Sariano, C. and Zimman, P., 2001. The Iberian Pyrite Belt: a mineralized system dismembered by voluminous high level sills *Terra Nova*, **13**, 99-103.

Boulter, C.A., Wilton, V.M., Cox, D.J. and Marshall, I.S., 1999. Magma-wet-sediment interaction: The most widespread yet least recognized alteration system in the Iberian Pyrite Belt. In: *Mineral deposits: Processes to processing* (C.J. Stanley, and Vaughan, D. J., ed. Balkema, Rotterdam.

Branney, M.J. and Soper, N.J., 1988. Ordovician volcano-tectonics in the English Lake District *Journal of the Geological Society of London*, **145**, 367-376.

Branney, M.J. and Suthren, R.J., 1988. High-level peperitic sills in the English Lake District: distinctions from block lavas, and implications for Borrowdale Volcanic Group stratigraphy *Geological Journal*, **23**, 171-187.

Brown, D.J. and Bell, B.R., 2007. How do you grade peperites? *Journal of Volcanology and Geothermal Research*, **159**, 409-420.

- Bruck, P.M., Colthurst, J.R.J., Feely, M., Gardiner, P. R. R., Penney, S. R., Reeves, T. J., Shannon, P. M., Smith, D. G., and Vanguetaine, M., 1979. South-east Ireland: Lower Palaeozoic stratigraphy and depositional history. In: *The Caledonides of the British Isles - reviewed* (A.L. Harris, Holland, C. H., and Leake, B. E., ed. Scottish Academic Press, The Geological Society of London.
- Buchanan, D.J. and Dullforce, T.A., 1973. Mechanism for Vapour Explosions *Nature*, **245**, 32-34.
- Bucher, K. and Frey, M., 2002. *Petrogenesis of metamorphic rocks*. Springer, New York.
- Büchl, A. and Gier, S., 2003. Petrogenesis and alteration of tuffs associated with continental flood basalts from Putorana, northern Siberia *Geological Magazine*, **140**, 649-659.
- Busby-Spera, C.J. and White, J.D.L., 1987. Variation in peperite textures associated with differing host-sediment properties *Bulletin of Volcanology*, **49**, 765-776.
- Cagnoli, B. and Romano, G.P., 2010. Effect of grain size on mobility of dry granular flows of angular rock fragments: An experimental determination *Journal of Volcanology and Geothermal Research*, **193**, 18-24.
- Campbell, I.H., Leshner, C.M., Coad, P., Franklin, J. M., Gorton, M. P., and Thurston, P. C., 1984. Rare-earth element mobility in alteration pipes below massive Cu---Zn-sulfide deposits *Chemical Geology*, **45**, 181-202.
- Cann, J.R., 1969. Spillites from the Carlsberg Ridge, Indian Ocean *Journal of Petrology*, **10**, 1-19.
- Carlisle, H., 1979. Ordovician stratigraphy of the Tramore area, County Waterford with a revised Ordovician correlation for southeast Ireland. In: *The Caledonides of the British Isles* (A.L. Harris, Holland, C. H., and Leake, B. E., ed. Geological Society of London Special Publication.
- Carr, P.F. and Jones, B.G., 2001. The influence of palaeoenvironment and lava flux on the emplacement of submarine, near-shore Late Permian basalt lavas, Sydney Basin (Australia) *Journal of Volcanology and Geothermal Research*, **112**, 247-266.
- Cathelineau, M., 1988. Cation site occupancy in chlorites and illites as a function of temperature *Clay Minerals*, **23**, 471-785.
- Cathelineau, M. and Nieva, D., 1985. A chlorite solid solution geothermometer: The Los Azufres (Mexico) geothermal system *Contributions to Mineralogy and Petrology*, **91**, 235-244.
- Cathles, L.M., 1977. An analysis of the cooling of intrusives by ground-water convection which includes boiling *Economic Geology*, **72**, 804-826.

- Chiba, H., 1995. Chemical modeling of seewater-rock interaction: Effect of rock-type on the fluid chemistry and mineral assemblage. In: *Biogeochemical processes and Ocean fluxes in the Western Pacific* (H. Sakai and Y. Nozaki, eds). Terra Scientific Publishin Company, Tokyo.
- Coats, R.R., 1940. Propylitization and related types of alteration on the Comstock Lode [Nevada] *Economic Geology*, **35**, 1-16.
- Coira, B. and Pérez, B., 2002. Peperitic textures of Ordovician dacitic synsedimentary intrusions in Argentina's Puna Highland: clues to emplacement conditions *Journal of Volcanology and Geothermal Research*, **114**, 165-180.
- Corsaro, R.A. and Mazzoleni, P., 2002. Textural evidence of peperites inside pillow lavas at Acicastello Castle Rock (Mt Etna, Sicily) *Journal of Volcanology and Geothermal Research*, **114**, 219-229.
- Cowman, D., 2005. A History of Tankardstown Mine, 1850-c.1875 *Journal of the Mining Heritage Trust of Ireland*, **5**, 3-10.
- Crawford, M.L., 1981. Phase equilibria in aqueous fluid inclusions. In: *Short course in fluid inclusions: Applications to petrology* (L.S. Hollister and M.L. Crawford, eds). Mineralogical Association Canada, Toronto.
- Critchley, M. and Morris, J., 2005. Conservation Works at Tankardstown Mine, Bunmahon, Co. Waterford *Journal of the Mining Herotage Trust of Ireland*, **5**, 75-79.
- Cullers, R.L., Barrett, T., Carlson, R. and Robinson, B., 1987. Rare-earth element and mineralogic changes in Holocene soil and stream sediment: A case study in the Wet Mountains, Colorado, U.S.A *Chemical Geology*, **63**, 275-297.
- Dadd, K.A. and Van Wagoner, N.A., 2002. Magma composition and viscosity as controls on peperite texture: an example from Passamaquoddy Bay, sotheastern Canada *Journal of Volcanology and Geothermal Research*, **114**, 63-80.
- de Hoer de Herve, A., 2000. Peperites from the Limagne Trench (Auvergne, French Massif Central): a distinctive facies of phreatomagmatic pyroclastics. History of a semantic drift. In: *Volcaniclastic rocks, from magmas to sediments* (H. Leyrit and C. Montenat, eds). Gordon and Breach Science Publishers, Amsterdam.
- Deer, W.A.R.A., Howie, R.A. and Zussman, J., 1992. *Rock Forming Minerals. Sheet Silicates*. John Wiley Book Company, New York.
- Diskin, S.M.V., 1997. Low Grade Metamorphism of the Upper Ordovician Rocks of Southeast Waterford from Tramore to Stradbally. Unpublished M.Sc. thesis, University of Dublin, Trinity College.

- Dominy, S.C., Camm, G.S., Bussell, M.A., et al., 1995. A review of tin stockwork mineralization in the south-west England orefield. In: *Proceedings of the Ussher Society*.
- Donaire, T., Saez, R. and Pascual, E., 2002. Rhyolitic globular peperites from the Aznacollar mining district (Iberian Pyrite Belt, Spain): physical and chemical controls *Journal of Volcanology and Geothermal Reserach*, **114**, 119-128.
- Downes, K., 1975. The Geology of the Ordovician Volcanics of Conty Waterford and southwest County Wexford, Ireland. Unpublished Ph.D. thesis, University of Dublin, Trinity College.
- Downes, K.M.J. and Platt, J.W., 1978. The Avoca: Ballard Mineralized Belt, County Wicklow *Journal of Earth Sciences*, **1**, 121-133.
- Doyle, M.G., 2000. Clast shape and textural associations in peperite as a guide to hydromagmatic interactions: Upper Permian basaltic and basaltic andesite examples from Kiama, Australia *Australian Journal of Earth Sciences*, **47**, 167-177.
- Dullforce, T.A., Buchanan, D.J. and Peckover, D.J., 1976. Self-triggering of small-scale fuel coolant interactions: I. Experiments *Journal of Physics D: Applied Physics*, **9**, 1295-1302.
- Erkül, F., Helvacı, C. and Sözbilir, H., 2006. Olivine basalt and trachyandesite peperites formed at the subsurface/surface interface of a semi-arid lake: An example from the Early Miocene Bigadiç basin, western Turkey *Journal of Volcanology and Geothermal Research*, **149**, 240-262.
- Esteban, J.J., Cuevas, J., Tubía, J.M., Liati, A., Seward, D., and Gebauer, D. 2007. Timing and origin of zircon-bearing chlorite schists in the Ronda peridotites (Betic Cordilleras, Southern Spain) *Lithos*, **99**, 121-135.
- Everett, C.E., Wilkinson, J.J. and Rye, D.M., 1999. Fracture-controlled fluid flow in the Lower Palaeozoic basement rocks of Ireland: implications for the genesis of Irish-type Zn-Pb deposits. In: *Fractures, fluid flow and mineralization* (K.J.W. McCaffrey, L. Lonergan and J.J. Wilkinson, eds). Geological Society of London Special Publication.
- Fisher, R.V., 1984. Submarine volcanoclastic rocks. In: *Marginal basin geology: volcanic and associated sedimentary and tectonic processes in modern and ancient marginal basins* (B. Kokelaar, P. and M.F. Howells, eds). Special Publication of the Geological Society of London, London, **16**, 5-27.
- Fitton, J.G., Thirlwall, M.F. and Hughes, D.J., 1982. Volcanism in the Caledonian orogenic belt of Britain. In: *Andesites* (R.S. Thorpe, ed. John Wiley & Sons).

- Fouquet, Y., Eissen, J.-P., Ondreas, H., et al., 1998. Extensive volcanoclastic deposits at the Mid-Atlantic Ridge axis: Results of deep-water basaltic explosive volcanic activity *Terra Nova*, **10**, 280-286.
- Franzson, H., Zierenberg, R. and Schiffman, P., 2008. Chemical transport in geothermal systems in Iceland: evidence from hydrothermal alteration *Journal of Volcanology and Geothermal Research*, **173**, 217-229.
- Fridleifsson, I.B., Furnes, H. and Atkins, F.B., 1982. Subglacial volcanics -- on the control of magma chemistry on pillow dimensions *Journal of Volcanology and Geothermal Research*, **13**, 103-117.
- Fritz, W.J. and Stillman, C.J., 1996. A subaqueous welded tuff from the Ordovician of County Waterford, Ireland *Journal of Volcanology and Geothermal Research*, **70**, 91-106.
- Furnes, H., Fridleifsson, I.B. and Atkins, F.B., 1980. Subglacial volcanics -- On the formation of acid hyaloclastites *Journal of Volcanology and Geothermal Research*, **8**, 95-110.
- Gallagher, V., O'Connor, P.J. and Aftalion, M.A., 1994. Intra-Ordovician deformation in southeast Ireland: evidence from the geological setting, geochemical affinities and U-Pb zircon age of the Croghan Kinshelagh granite *Geological Magazine*, **131**, 669-684.
- Gieré, R., 1990. Hydrothermal mobility of Ti, Zr and REE: examples from the Bergell and Adamello contact aureoles (Italy) *Terra Nova*, **2**, 60-67.
- Gieré, R., 1993. Transport and deposition of REE in H₂S-rich fluids: evidence from accessory mineral assemblages *Chemical Geology*, **110**, 251-268.
- Gifkins, C., Herrmann, W. and Large, R., 2005. *Altered volcanic rocks: A guide to description and interpretation*. Centre for Ore Deposit Research.
- Gifkins, C.C., McPhie, J. and Allen, R.L., 2002. Pumiceous rhyolitic peperite in ancient submarine volcanic settings *Journal of Volcanology and Geothermal Research*, **114**, 181-203.
- Gillis, K.M. and Robinson, P.T., 1988. Distribution of alteration zones in the upper oceanic crust *Geology*, **16**, 262-266.
- Hanson, R.E. and Hargrove, U.S., 1999. Processes of magma/wet sediment interaction in a large scale Jurassic andesitic peperite complex, northern Sierra Nevada, California *Bulletin of Volcanology*, **60**, 610-626.
- Harper, D.A.T. and Parkes, M.A., 2000. Ireland. In: *A revised correlation of Ordovician rocks in the British Isles* (F.J. Gregory, ed. Geological Society of London Special Report, London.
- Hathway, B. and Lomas, S.A., 1998. The Upper Jurassic-Lower Cretaceous Byers Group, South Shetland Islands, Antarctica: revised stratigraphy and regional correlations *Cretaceous Research*, **19**, 43-67.

- Head, J.W. and Wilson, L., 2003. Deep submarine pyroclastic eruptions: theory and predicted landforms and deposits *Journal of Volcanology and Geothermal Research*, **121**, 155-193.
- Hendry, D.A.F., 1981. Chlorites, phengites, and siderites from the Prince Lyell Ore Deposit, Tasmania, and the origin of the deposit *Economic Geology*, **76**, 285-303.
- Herron, M., 1988. Geochemical classification of terrigenous sands and shales from core or log data *Journal of Sedimentary Petrology*, **58**, 820-829.
- Hey, M.H., 1954. A new review of the chlorites *Mineralogical Magazine*, **30**, 277-292.
- Hitzmann, M.W. and Beaty, D.W., 2003. The Irish Zn-Pb-(Ba-Ag) orefield. In: *Europe's Major Base Metal Deposits* (J.G. Kelly, C.J. Andrew, J.H. Ashton, M.B. Boland, G. Earls, L. Fusciardi and G. Stanley, eds). Irish Association for Economic Geology.
- Honnorez, J. and Kirst, P., 1975. Submarine basaltic volcanism: Morphometric parameters for discriminating hyaloclastites from hyalotuffs *Bulletin of Volcanology*, **39**, 441-465.
- Hooten, J.A. and Ort, M.H., 2002. Peperite as a record of early stage phreatomagmatic fragmentation processes: an example from the Hopi Buttes volcanic field, Navajo Nation, Arizona, USA. *Journal of Volcanology and Geothermal Research*, **114**, 95-106.
- Humphries, S.E., 1976. The hydrothermal alteration of oceanic basalts by seawater. Unpublished Ph.D thesis, Massachusetts Institute of Technology.
- Hunns, S.R. and McPhie, J., 1999. Pumiceous peperite in a submarine volcanic succession at Mount Chalmers, Queensland, Australia *Journal of Volcanology and Geothermal Research*, **88**, 239-254.
- Jerram, D.A. and Stollhoffen, H., 2002. Lava-sediment interactions in desert settings; are all peperite-like textures the result of magma-water interactions *Journal of volcanology and geothermal reserach*, **114**, 231-249.
- Jones, W.B., 1983. The geological association of sulphide mineralisation at Avoca, County Wicklow - a new interpretation based on field evidence *Journal of Earth Sciences Royal Dublin Society*, **5**, 145-152.
- Jordan, B.R., Fowler, A.R., Mahmoud, B.D., El-Saiy, A. K., and Abdelghanny, O., 2008. Peperites and associated pillow lavas subjacent to the Oman Ophiolite *Journal of Volcanology and Geothermal Research*, **133**, 303-312.
- Jowett, E.C., 1991 of Conference. Fitting iron and magnesium into the hydrothermal chlorite geothermometer. *Geological Association of*

- Junqueira-Brod, T.C., Brod, J.A., Gaspar, J.C. and Jost, H., 2004. Kamafugitic diatremes: facies characterisation and genesis--examples from the Goiás Alkaline Province, Brazil *Lithos*, **76**, 261-282.
- Jutras, P., Macrae, A., Owen, J.V., Dostal, J., Preda, M., Prishonnet, G., 2006. Carbonate melting and peperite formation at the intrusive contact between large mafic dykes and clastic sediments of the Upper Palaeozoic Saint-Jules Formation, New Carlisle, Quebec *Geological Journal*, **41**, 23-48.
- Kano, K., 2002. Middle Miocene volcanoclastic dikes at Kukedo, Shimane Peninsula, SW Japan: fluidisation of volcanoclastic beds by emplacement of synvolcanic andesite dikes *Journal of volcanology and geothermal reserach*, **114**, 81-94.
- Kelemen, P.B., Shimizu, N. and Dunn, T., 1993. Relative depletion of niobium in some arc magmas and the continental crust: partitioning of K, Nb, La and Ce during melt/rock reaction in the upper mantle *Earth and Planetary Science Letters*, **120**, 111-134.
- Klingelhöfer, F., Hort, M., Kümpel, H.J. and Schmincke, H.U., 1999. Constraints on the formation of submarine lava flows from numerical model calculations *Journal of Volcanology and Geothermal Research*, **92**, 215-229.
- Kokelaar, B.P., 1982. Fluidisation of wet sediments during the emplacement and cooling of various igneous bodies *Journal of the Geological Society of London*, **139**, 21-33.
- Kokelaar, P., 1986. Magma-water interactions in subaqueous and emergent basaltic volcanism *Bulletin of Volcanology*, **48**, 275-289.
- Kokelaar, P., 1988. Tectonic controls of Ordovician arc and marginal basin volcanism in Wales *Journal of the Geological Society of London*, **145**, 759-775.
- Koyaguchi, T., 1987. Magma mixing in a squeezed conduit *Earth and Planetary Science Letters*, **84**, 339-344.
- Kranidiotis, P. and MacLean, W.H., 1987. Systematics of chlorite alteration at the Phelps Dodge Massive Sulfide Deposit, Matagami, Quebec *Economic Geology*, **82**, 1898-1911.
- Krynauw, J.R., Hunter, D.R. and Wilson, A.H., 1988. Emplacement of sills into wet sediments at Grunehogna, western Dronning Maud Land, Antarctica *Journal of the Geological Society of London*, **145**, 1019-1032.
- Kuzmichev, A.B. and Goldyrev, A.E., 2007. Permian-Triassic trap magmatism in Bel'Kov Island (New Siberian Islands) *Russian Geology and Geophysics*, **48**, 167-176.

- Large, R.R., Gemmell, J.B. and Paulick, H., 2001a. The alteration box plot: a simple approach to understanding the relationship between alteration mineralogy and lithogeochemistry associated with volcanic hosted massive sulphide deposits *Economic Geology*, **96**, 957-971.
- Large, R.R., McPhie, J., Gemmell, J.B., Herrmann, W., and Davidson, G. J., 2001b. The spectrum of ore deposit types, volcanic environments, alteration halos and related exploration vectors in submarine volcanic successions: some examples from Australia *Economic Geology*, **96**, 913-938.
- Lavine, A. and Aalto, K.R., 2002. Morphology of a crater-filling lava lake margin, the peninsula tuff cone, Tule Lake National Wildlife refuge, California: implications for formations of peperite textures *Journal of Volcanology and Geothermal Research*, **114**, 147-163.
- Le Bas, M.J., Le Maitre, R. W., Streckeisen, A., and Zanettin, B., 1989. A chemical classification of volcanic rocks on the total alkali-silica diagram *Journal of Petrology*, **27**, 745-750.
- Lécuyer, C., Grandjean, P. and Martineau, F., 1995. Seawater-sediment-basalt interactions: stable isotope (H, O) and elemental fluxes within the Ordovician volcano-sedimentary sequence of Erquy (Brittany, France) *Contributions to Mineralogy and Petrology*, **120**, 249-264.
- Lee, J.I. and Lee, Y.I., 2001. Kübler illite “crystallinity” index of the Cretaceous Gyeongsang Basin, Korea: Implications for basin evolution *Clays and Clay Minerals*, **49**, 36-43.
- Martin, U. and Nemeth, K., 2007. Blocky versus fluidal peperite textures developed in volcanic conduits, vents and crater lakes in phreatomagmatic volcanoes in Mio/Pliocene volcanic fields in Western Hungary *Journal of Volcanology and Geothermal Research*, **159**, 164-178.
- Martin, U. and White, J.D.L., 2002. Melting and mingling of phonolitic pumice deposits with intruding dykes: an example from the Otago Peninsula, New Zealand *Journal of Volcanology and Geothermal Research*, **114**, 129-146.
- McBirney, A.R., 1963. Factors governing the nature of submarine volcanism *Bulletin of Volcanology*, **26**, 455-469.
- McClintock, M.K. and White, J.D.L., 2002. Granulation of weak rock as a precursor to peperite formation: coal peperite, Coombs Hill, Antarctica *Journal of volcanology and geothermal reserach*, **114**, 205-217.
- McConnell, B., 1987. Geochemistry of Ordovician peralkaline volcanics at Avoca, Co. Wicklow and their regional association, Ph.D. thesis, University of Dublin, Dublin.

- McConnell, B., 1991. Geochemistry and mineralogy of volcanic host rocks as indicators of massive sulphide genesis at Avoca, southeast Ireland *Irish Journal of Earth Sciences*, **11**, 43-52.
- McConnell, B., 1993. A review of the Ordovician geology of southeast Co. Waterford, with an assessment of the mineral potential of P.Ls 3207 and 3208.
- McConnell, B., 2000. The Ordovician arc and marginal basin of Leinster *Irish Journal of Earth Sciences*, **18**, 41-49.
- McConnell, B.J., Stillman, C.J. and Hertogen, J., 1991. An Ordovician basalt to peralkaline rhyolite fractionation series from Avoca, Ireland *Journal of the Geological Society of London*, **148**, 711-718.
- McCulloch, M.T. and Gamble, J.A., 1991. Geochemical and geodynamical constraints on subduction zone magmatism *Earth and Planetary Science Letters*, **102**, 358-374.
- McPhie, J., 1993. The Tennant Creek porphyry revisited: a synsedimentary sill with peperite margins, Early Proterozoic, Northern Territory *Australian Journal of Earth Sciences*, **40**, 545-558.
- McPhie, J. and Orth, K., 1999 of Conference. Peperite, pumice and perlite in submarine volcanic successions: implications for VHMS mineralisation. *Proceedings of Pacrim*.
- Metcalf, R., Bevins, R.E. and Robinson, D., 1996. Fluid fluxes during low-temperature alteration: implications of multi-style alteration assemblages from the Welsh Borderland, UK *Geological Journal*, **31**, 323-347.
- Michard, A. and Albarède, F., 1986. The REE content of some hydrothermal fluids *Chemical Geology*, **55**, 51-60.
- Mills, A.A., 1984. Pillow lavas and the leidenfrost effect *Journal of the Geological Society of London*, **141**, 183-186.
- Moore, D.G., 1975. Mechanism of formation of pillow lava *American Scientist*, **63**, 269-277.
- Moore, L.N. and Mueller, W.U., 2008 of Conference. Physical volcanology of the mafic segment of the subaqueous New Senator caldera, Abitibi greenstone belt, Quebec, Canada. *IOP Conference series: Earth and Environmental Science (Collapse Calderas Workshop)*.
- Mullen, E.D., 1983. MnO/TiO₂/P₂O₅: a minor element discriminant for basaltic rocks of oceanic environments and its implications for petrogenesis *Earth and Planetary Science Letters*, **62**, 53-62.
- Németh, K. and Martin, U., 2007. Shallow sill and dyke complex in western Hungary as a possible feeding system of phreatomagmatic volcanoes in

"soft-rock" environment *Journal of Volcanology and Geothermal Research*, **159**, 138-152.

Németh, K., Pecskey, Z., Martin, U., Gmeling, K., Molnar, F., and Cronin, S. J., 2008. Hyaloclastites, peperites and soft-sediment deformation textures of a shallow subaqueous Miocene rhyolitic dome-cryptodome complex, Palhaza, Hungary *Geological Society, London, Special Publications*, **302**, 63-86.

Nichols, G., 1999. *Sedimentology and Stratigraphy*. Blackwell Science Ltd.

Orth, K. and McPhie, J., 2003. Textures formed during emplacement and cooling of a Palaeoproterozoic small volume rhyolitic sill *Journal of Volcanology and Geothermal Research*, **128**, 341-362.

Owen, A.W. and Parkes, M.A., 2000. Trilobite faunas of the Duncannon Group: Caradoc stratigraphy, environments and palaeobiogeography of the Leinster Terrane, Ireland *Palaeontology*, **43**, 219-269.

Parnell, J. and Kelly, J., 2003. Remobilization of sand from consolidated sandstones: evidence from mixed bitumen-sand intrusions. In: *Subsurface sediment mobilization* (P. Van Rensbergen, R.R. Hillis, A.J. Maltman and C.K. Morley, eds). Geological Society, London, Special Publication.

Passey, S.R. and Bell, B.R., 2007. Morphologies and emplacement mechanisms of the lava flows of the Faroe Islands Basalt Group, Faroe Islands, NE Atlantic Ocean *Bulletin of Volcanology*, **70**, 139-156.

Pearce, J.A., 1982. Trace element characteristics of lavas from destructive plate boundaries. In: *Andesites* (R.S. Thorpe, ed. John Wiley & Sons.

Pearce, J.A., 1983. Role of the sub-continental lithosphere in magma genesis at active continental margins. In: *Continental basalts and mantle xenoliths* (C.J. Hawkesworth and M.J. Norry, eds). Shiva Publications.

Pearce, J.A. and Norry, M.J., 1979. Petrogenetic implications of Ti, Zr, Y and Nb variations in volcanic rocks *Contributions to Mineralogy and Petrology*, **69**, 33-47.

Peckover, R.S., Buchanan, D.J. and Ashby, D.E.T.F., 1973. Fuel-Coolant Interactions in Submarine Vulcanism *Nature*, **245**, 307-308.

Perugini, D. and Poli, G., 2005. Viscous fingering during replenishment of felsic magma chambers by continuous inputs of mafic magmas: Field evidence and fluid-mechanics experiments *Geology*, **33**, 5-8.

Petry, K., Jerram, D.A., de Almeida, D.P.M. and Zerfass, H., 2007. Volcanic-sedimentary features in the Serra Geral Fm., Parana Basin, southern Brazil: Examples of dynamic lava-sediment interactions in an arid setting *Journal of Volcanology and Geothermal Research*, **159**, 113-125.

- Phillips, W.E.A., Stillman, C.J. and Murphy, T., 1976. A Caledonian plate tectonic model *Journal of the Geological Society of London*, **132**, 579-609.
- Platt, J.W., 1977. Volcanogenic mineralization at Avoca, Co. Wicklow, Ireland, and its regional implications *The Institute of Mining and Metallurgy and the Geological Society*, 163-170.
- Pointon, C.R., 1979. Volcanogenic sulphide mineralization at Avoca, Eire, Parys Mountain, Anglesey and in S. E. Canada - A comparative study. Unpublished Ph. D thesis., University of Aston.
- Rawlings, D.J., 1993. Mafic peperite from the Gold Creek Volcanics in the Middle Proterozoic Mc Arthur Basin, Northern Territory *Australian Journal of Earth Sciences*, **40**, 109-113.
- Reed, M.H., 1983. Seawater-basalt reaction and the origin of greenstones and related ore deposits *Economic Geology*, **78**, 466-485.
- Reed, M.H., 1997. Hydrothermal alteration and its relationship to ore fluid composition. In: *Geochemistry of hydrothermal ore deposits* (H.L. Barnes, ed.) John Wiley & Sons.
- Richards, H.G., Cann, J.R. and Jensenius, J., 1989. Mineralogical zonation and metasomatism of the alteration pipes of Cyprus sulfide deposits *Economic Geology*, **84**, 91-115.
- Roedder, E., 1984. Fluid Inclusions. In: *Reviews in Mineralogy*. Mineralogical Society of America Report.
- Roser, B.P. and Korsch, R.J., 1986. Determination of Tectonic Setting of Sandstone-Mudstone Suites Using SiO₂ Content and K₂O/Na₂O Ratio *The Journal of Geology*, **94**, 635-650.
- Roser, B.P. and Korsch, R.J., 1988. Provenance signatures of sandstone-mudstone suites determined using discriminant function analysis of major-element data *Chemical Geology*, **67**, 119-139.
- Rudnick, R.L. and Gao, S., 2003. Composition of the continental crust. In: *The crust: treatise in geochemistry* (R.L. Rudnick, ed.)
- Ryan, K.M., 2005. Geochemical fingerprinting of sedimentary basins using a revised South Mayo Lower Palaeozoic stratigraphy. Ph.D, National University of Ireland, Galway.
- Samson, I.M. and Russell, M.J., 1987. Genesis of the Silvermines zinc-lead-barite deposit, Ireland; fluid inclusion and stable isotope evidence *Economic Geology*, **82**, 371-394.
- Schaffalitzky, C., 1982. Summary of exploration work on the Lisnakill - Shinganagh area P.L.s 2755 and 736 Co. Waterford (R. Crowe, ed.)

Geological Survey of Ireland, Dublin; Aquataine Mining (Ireland) Ltd, Dublin.

- Scheiner, E.J., 1974. Syndepositional small-scale intrusions in Ordovician pyroclastics, Co. Waterford, Ireland *Journal of the Geological Society of London*, **130**, 157-161.
- Scrope, G.P., 1858. The Geology and Extinct volcanoes of Central France (J. Murray, ed.) London.
- Shannon, P.M., 1976. The Petrology and structural relations of some Lower Palaeozoic rocks in southeast Leinster. Unpublished Ph.D. thesis, National University of Ireland.
- Shannon, P.M., 1979. The petrology of the Ordovician volcanic rocks of County Wexford, Ireland *Journal of Earth Sciences Royal Dublin Society*, **2**, 41-59.
- Shepherd, T.J., Rankin, A.H. and Alderton, D.H.M., 1985. *A practical guide to fluid inclusion studies*. Chapman and Hall, New York, Glasgow and London.
- Sillitoe, R.H., Hannington, M.D. and Thompson, J.F.H., 1996. High sulfidation deposits in the volcanogenic massive sulfide environment *Economic Geology*, **91**, 204-212.
- Silvestri, S., 1963. Proposal for a genetic classification of hyaloclastites *Bulletin of Volcanology*, **25**, 315-321.
- Skilling, I.P., White, J.D.L. and McPhie, J., 2002. Peperite: a review of magma-sediment mingling. *Journal of Volcanology and Geothermal Research*, **114**, 1-17.
- Sleeman, A.G. and McConnell, B., 1995. Geology of East Cork-Waterford with accompanying Bedrock Geology 1:100,000 scale map, sheet 22. Geological Survey of Ireland.
- Smith, T.L. and Batiza, R., 1989. New field and laboratory evidence for the origin of hyaloclastite flows on seamount summits *Bulletin of Volcanology*, **51**, 96-114.
- Solomon, M., 1968. The nature and possible origin of the pillow lavas and hyaloclastite breccias of King Island, Australia *Quarterly Journal of the Geological Society*, **124**, 153-168.
- Squire, R.J. and McPhie, J., 2002. Characteristics and Origin of peperite involving coarse grained host sediment *Journal of volcanology and geothermal reserach*, **114**, 45-61.
- Stark, J.T., 1939. Discussion: Pillow lavas *The Journal of Geology*, **47**, 205-209.

- Stillman, C.J., 1971. Ordovician ash-fall tuffs from County Waterford *Scientific Proceeding of the Royal Dublin Society*, **A**, 89-101.
- Stillman, C.J., 1978. South-east County Waterford and south Tipperary Ordovician volcanic and sedimentary rocks and Silurian turbidites. In: *Geological Survey of Ireland Guide Series*.
- Stillman, C.J., 2009. Caledonian Igneous Activity. In: *The Geology of Ireland* (C.H. Holland and I. Sanders, eds). Dunedin Academic Press.
- Stillman, C.J., Downes, K. and Scheiner, E.J., 1974. Caradocian volcanic activity in East and Southeast Ireland *Scientific Proceeding of the Royal Dublin Society*, **6A**, 87-98.
- Stillman, C.J. and Francis, E.H., 1979. Caledonide volcanism in Britain and Ireland *Journal of the Geological Society of London*, 557-577.
- Stillman, C.J. and Maytham, D.K., 1973. The Ordovician Volcanic Rocks of Arklow Head, Co. Wicklow *Proceedings of the Royal Irish Academy. Section B: Biological, Geological, and Chemical Science*, **73**, 61-77.
- Stillman, C. J. and Williams, C. T., 1979. Geochemistry and tectonic setting of some Upper Ordovician volcanic rocks in East and southeast Ireland *Earth and Planetary Science Letters*, **41**, 288-310.
- Stillman, C.J. and Sevastopulo, G., 2005. *Classic Geology in Europe 6: leinster*. Terra Publishing.
- Sun, S.S. and McDonough, W.F., 1989. Chemical and isotopic systematics of oceanic basalts: implications for mantle composition and processes. In: *Magmatism in ocean basins* (A.D. Saunders, and Norry, M. J., ed. Geological Society of London Special Publication.
- Swennan, O., 1984. The geology of the Greenan - Mount Congreve - Ballyscanlon area, Co. Waterford, Ireland, University of Dublin, Trinity College.
- Teagle, D.A.H. and Alt, A.C., 2004. Hydrothermal alteration of basalts beneath the Bent Hill massive sulfide deposit, Middle Valley, Juan de Fuca Ridge *Economic Geology*, **99**, 561-584.
- Templeton, J.H. and Hanson, R.E., 2003. Jurassic sub-marine arc-apron deposits and associated magma/wet sediment interaction, northern Sierra Nevada, California *Journal of volcanology and geothermal reserach*, **128**, 299-326.
- Vezzoli, L., Matteini, M., Hauser, N., Omarini, R., Mazzuoli, R., Acocella, V., 2009. Non-explosive magma-water interaction in a continental setting: Miocene examples from the eastern Cordillera (central Andes; NW Argentina) *Bulletin of Volcanology*, **71**, 509-532.
- Vuagnat, M., 1975. Pillow lava flows: Isolated sacks or connected tubes? *Bulletin of Volcanology*, **39**, 581-589.

- Waichel, B.L., de Lima, E.F., Sommer, C.A. and Lubachesky, R., 2007. Peperite formed by lava flows over sediments: An example from the central Paraná Continental Flood Basalts, Brazil *Journal of Volcanology and Geothermal Research*, **159**, 343-354.
- Walker, G.P.L., 1992. Morphometric study of pillow-size spectrum among pillow lavas *Bulletin of Volcanology*, **54**, 459-474.
- Wells, G., Bryan, W.B. and Pearce, T.H., 1979. Comparative Morphology of Ancient and Modern Pillow Lavas *The Journal of Geology*, **87**, 427-440.
- Wheatley, C.J., 1971. Economic geology of the Avoca mineralised belt, S. E Ireland and Parys Mountain, University of London.
- White, J. D. L., McPhie, J., and Skilling, I. P., 2000. Peperite: a useful genetic term. *Bulletin of Volcanology* **62**, 65-66.
- White, J.D.L., Smellie, J.L. and Clague, D.A., 2003. Introduction: A deductive outline and topical overview of sub-aqueous explosive volcanism. In: *Explosive subaqueous volcanism* (J.D.L. White, J.L. Smellie and D.A. Clague, eds). American Geophysical Union, Geophysical Monograph Series, Washington D. C.
- Whitehead, R.E., 1973. Environment of stratiform sulphide deposition; Variation in Mn:Fe ratio in host rocks at Heath Steele Mine, New Brunswick, Canada *Mineralium Deposita*, **8**, 148-160.
- Wilkinson, J., 2003. On diagenesis, dolomitisation and mineralisation in the Irish Zn-Pb orefield *Mineralium Deposita*, **38**, 968-983.
- Wilkinson, J.J., 2001. Fluid inclusions in hydrothermal ore deposits *Lithos*, **55**, 229-272.
- Wilkinson, J.J., Boyce, A.J., Everett, C.E. and Lee, M.J., 2003. Timing and depth of mineralization in the Irish Zn-Pb orefield. In: *Europe's Major Base Metal Deposits* (J.G. Kelly, C.J. Andrew, J.H. Ashton, M.B. Boland, G. Earls, L. Fusciardi and G. Stanley, eds). Irish Association for Economic Geology, Dublin.
- Williams, F.M., Sheppard, W.A. and McArdle, P., 1986. Avoca Mine, Co. Wicklow: a review of geological and isotope studies. In: *Geology and genesis of mineral deposits in Ireland* (C.J. Andrew, R.W.A. Crowe, S. Finlay, W.M. Pennell and J.F. Pyne, eds). Irish Association for Economic Geology.
- Wilson, J.T., 1966. Did the Atlantic close and then re-open? *Nature*, **211**, 676-681.
- Wilson, M., 1989. *Igneous Petrogenesis: A global tectonic approach*. Kluwer Academic Publishers, London.

- Winchester, J.A. and Floyd, P.A., 1976. Geochemical magma type discrimination: application to altered and metamorphosed basic igneous rocks *Earth and Planetary Science Letters*, **28**, 459-469.
- Winchester, J.A. and Floyd, P.A., 1977. Geochemical discrimination of different magma series and their differentiation products using immobile elements *Chemical Geology*, **20**, 325-343.
- Wohletz, K., 2002. Water/magma interaction: some theory and experiments on peperite formation *Journal of Volcanology and Geothermal Research*, **114**, 19-35.
- Woodhead, J., Eggins, S. and Gamble, J., 1993. High field strength and transition element systematics in island arc and back-arc basin basalts: Evidence for multi-phase melt extraction and a depleted mantle wedge *Earth and Planetary Science Letters*, **114**, 491-504.
- Yongliang, X. and Yusheng, Z., 1991. The mobility of rare-earth elements during hydrothermal activity: A review *Chinese Journal of Geochemistry*, **10**, 295-306.
- Young, G.M., Shaw, C.S.J. and Fedo, C.M., 2004. New evidence favouring an endogenic origin for supposed impact breccias in Huronian (Palaeoproterozoic) sedimentary rocks *Precambrian Research*, **133**, 63-74.
- Zang, W. and Fyfe, W.S., 1995. Chloritization of the hydrothermally altered bedrocks at the Igarape Bahia gold deposit, carajas, Brazil *Mineralium Deposita*, **30**, 30-38.
- Zhang, Y., Muchez, P. and Hein, U.F., 1997. Chlorite geothermometry and the temperature conditions at the Variscan thrust front in eastern Belgium *Geologie en Mijnbouw*, **76**, 267-270.
- Zhiwei, B. and Zhenhua, Z., 2003. Rare-earth element mobility during ore-forming hydrothermal alteration: A case study of Dongping gold deposit Hebei Province, China *Chinese Journal of Geochemistry*, **22**, 45-57.
- Zhou, J. and Li, X., 2006. Geoplot: an excel VBA program for geochemical data plotting *Computers and Geosciences*, **32**, 554-560.
- Zimanowski, B. and Büttner, R., 2003. Phreatomagmatic explosions in subaqueous volcanism. In: White, J. D. L., Smellie, J. L., and Clague, D. E. Eds.), *American Geophysical Union, Geophysical Monograph Series*.

Appendix A1

Some global occurrences of peperite and details of their formation

	LOCATION	AGE	IGNEOUS COMPONENT	SEDIMENTARY COMPONENT	JUVENILE CLAST MORPHOLOGY	COMMENT/ GENESIS	REFERENCE
1	Sierra Nevada, California	Jurassic	Andesite and basalt	Wet mud and fine grained sand	B, F	Shallow level intrusion	Templeton and Hanson, 2003
2	Tule Lake National Wildlife Refuge, California	Pleistocene	Basalt lava	Wet unconsolidated tuff	F	Lava infilling crater	Lavine and Aalto, 2002
3	Tuttle Lake Formation, northern Sierra Nevada	Jurassic	Augite-phyric andesite	Unconsolidated tuff, tuff breccia and lapilli tuff	B, F, B + F		Hanson and Hargrove, 1999
4	Hopi Buttes volcanic fields, Navajo Nation, Arizona	Miocene-Pliocene	Lamprophyte dykes	Lacustrine sediment interbedded with felsic tuffs	B, F	Saturated sediments	Hooten and Ort, 2002
5	Trans-Pecos igneous Province, West Texas	Eocene	Alkaline basalt and trachyandesite	Fluvial strata	B, F	Sediments remained unconsolidated for 20-25Ma, with peperite forming after this time	Befus <i>et al</i> , 2009
6	Whitefish Falls, Ontario	Precambrian	Amphibolite and plutonic clasts	Laminated argillite with chlorite matrix	F	Now breccia, diabase represents fluidal clasts	Young <i>et al</i> , 2004

7	Passamaquoddy Bay, southeastern Canada	Silurian to perhaps early Devonian	Mafic lava flows.	Silt and sand.	B, F	More evolved composition forms blocky peperite	Dadd and Van Wagoner, 2002
			Rhyolite sills.	Silt and sand	B		
8	New Carlisle, Chaleur Bay, eastern Canada	Upper Devonian	Alkaline basalt	Coarse-grained carbonate and siliciclastics	B		Jutras <i>et al</i> , 2006
9	Lake District, NE England	Ordovician	Andesite sills	Clays, silts, sands and silt and sand grade tuff			Branney and Suthren, 1988
10	Mull Lava Field, NW Scotland	Palaeogene	Basaltic lava	Siliciclastic sediment	F	Peperite is graded	Brown and Bell, 2007
11	Suduroy, Faroe Islands	Palaeogene	Basaltic sheet lobe	Volcaniclastic silts	B		Passey and Bell, 2007
12	Aznalcollar Mining District, Iberian Pyrite Belt, Spain	Upper Devonian to Late Carboniferous	Dacite sills.	Tuffaceous sand.	B	Fluidal clasts formed in fine-grained sediment	Donaire <i>et al</i> , 2002
			Rhyolite sills.	Mud	F		
13	Limagne Trench, Auvergne, French Massif Central	Oligocene	Basalt	Marly or limy sediments	B		De Goer de Herve, 2000
14	Mt Etna, Sicily	Pleistocene	Basalt	Fine-grained bluish marly clays	F		Corsaro and Mazzoleni, 2002
15	Pannonian Basin, Western Hungary	Mio/Pliocene	Basaltic and alkali basalt dykes and lava flows	Maar forming sequence, tuff ring forming sequence, sand, silt and marly silt	B, F		Martin and Nemeth, 2007

16	Bigadiç basin, western Turkey	Early Miocene	Olivine basalt and trachy-andesite	Lacustrine, fluvial and evaporitic deposits with a high content of volcanic detritus	B, F	Sediment infiltration into fluidal clasts resulted in brecciation and formation of blocky clasts	Erkül <i>et al.</i> , 2006
16	Oman-United Emirates border region of Khattm al Shiklah	Not given	Basalt sills and pillow lavas	Water saturated carbonates	B, F	Sub-angular peperite in boundary layers	Jordan <i>et al.</i> , 2008
17	Bel’Kov Island, New Siberian Islands	Permian- Triassic	Mafic dykes	Clay sections	-	Peperite described as random shaped pieces of glass	Kuzmichev and Goldyrev, 2007
18	Kukedo, Shimane Peninsula, SW Japan	Middle Miocene	Andesite dykes	Volcaniclastic turbidites	B, F	Fluidal clasts are sparse	Kano, 2002
19	Puna Highland, Argentina, Central Andes	Early Ordovician	Crystal rich dacitic sills, laccolths and cryptodomes, and spillitic sills	Fine grained siliciclastic turbidites	B, F	Megapeperite = blocky clasts, micropeperite = fluidal clasts	Coira and Perez, 2002
20	Goiás Alkaline Province, central Brazil	Late Cretaceous	Pyroclastic material of the kamafugitic diatreme	Sand	B		Junquiera-Brod <i>et al.</i> , 2004
21	West Parana State, southern Brazil	Early cretaceous	Tholeiitic basalt	Silt with minor clay	F		Waichel <i>et al.</i> , 2007

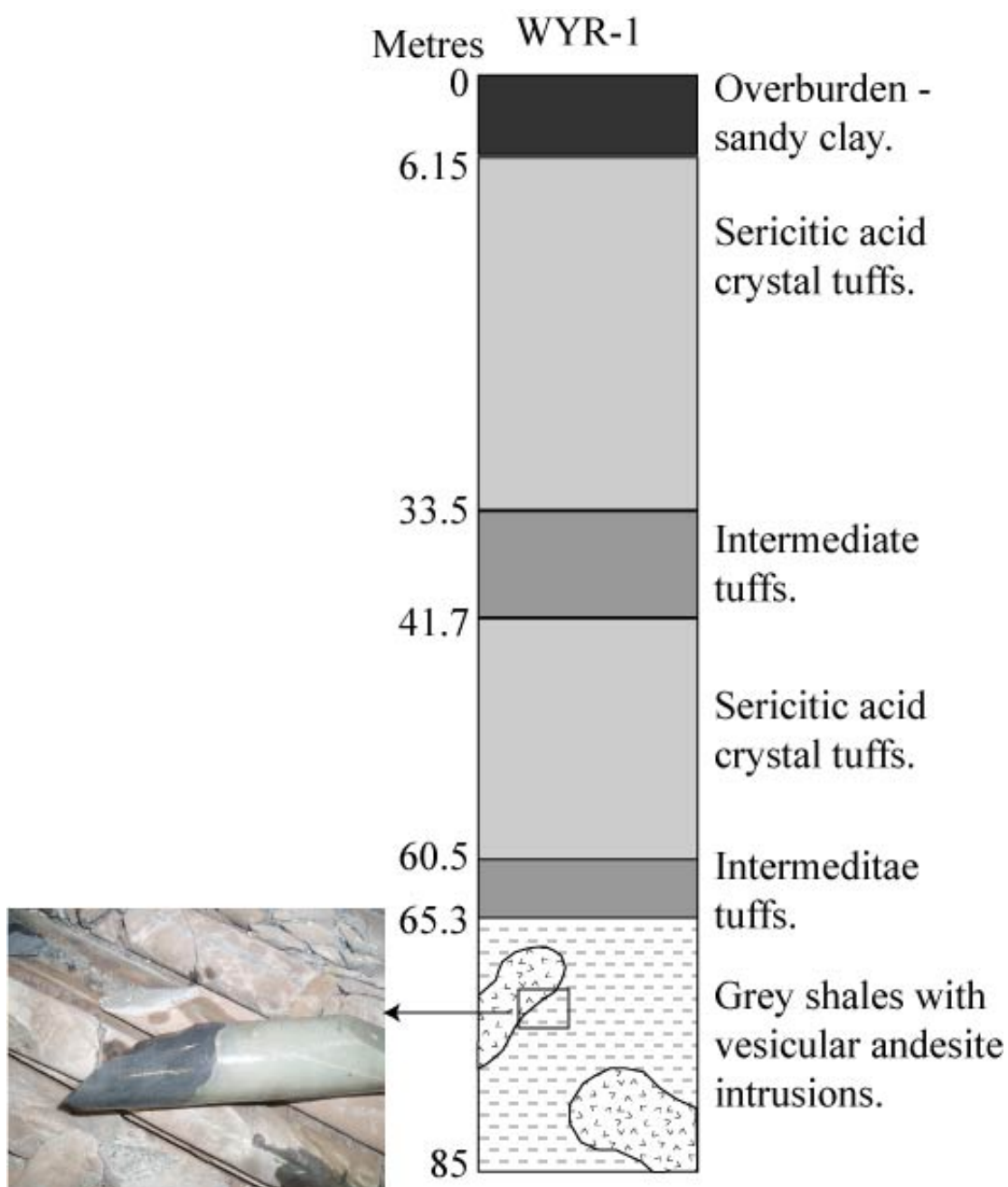
22	Parana Basin, southern Brazil	Pleistocene	Vesicular basalt	Well sorted sand with alternating fine and medium grained layers	B		Petry <i>et al</i> , 2007
23	Western South Shetland Islands, Antarctica	Late Jurassic – Early Cretaceous	Basaltic magma	Mud	-	Flames of basalt taper up into mud	Hathway and Lomas, 1998
24	Huab Basin, NW Namibia. (Etendeka Flood Basalt Province)	Early Cretaceous	Olivine-phyric basalt pahoehoe flows and basaltic andesite	Dry unconsolidated sand	B		Jerram and Stollhoffen, 2002
25	Western Dronning Maud Land, Antarctica	Mid-Proterozoic	Quartz diorite to quartz monzodiorite	Unconsolidated or partially lithified arenites and argillites			Krynauw <i>et al</i> , 1988
26	Onedin, northwestern Australia	Palaeo-proterozoic	Rholite sill	Fine sands and mud	B, F	Fluidal clasts display wispy margins and necking	Orth and McPhie, 2003
27	McArthur Basin, Northern Territory, Australia	Upper Middle Proterozoic	Variable vesicular basalt	Sandstone and mudstone	B		Rawlings, 1993
28	Tennant Creek block of the Central Northern Territory, Australia	Early Proterozoic	Medium grained quartz-feldspar porphyry	Fine grained sandstone and shale	F		McPhie, 1993

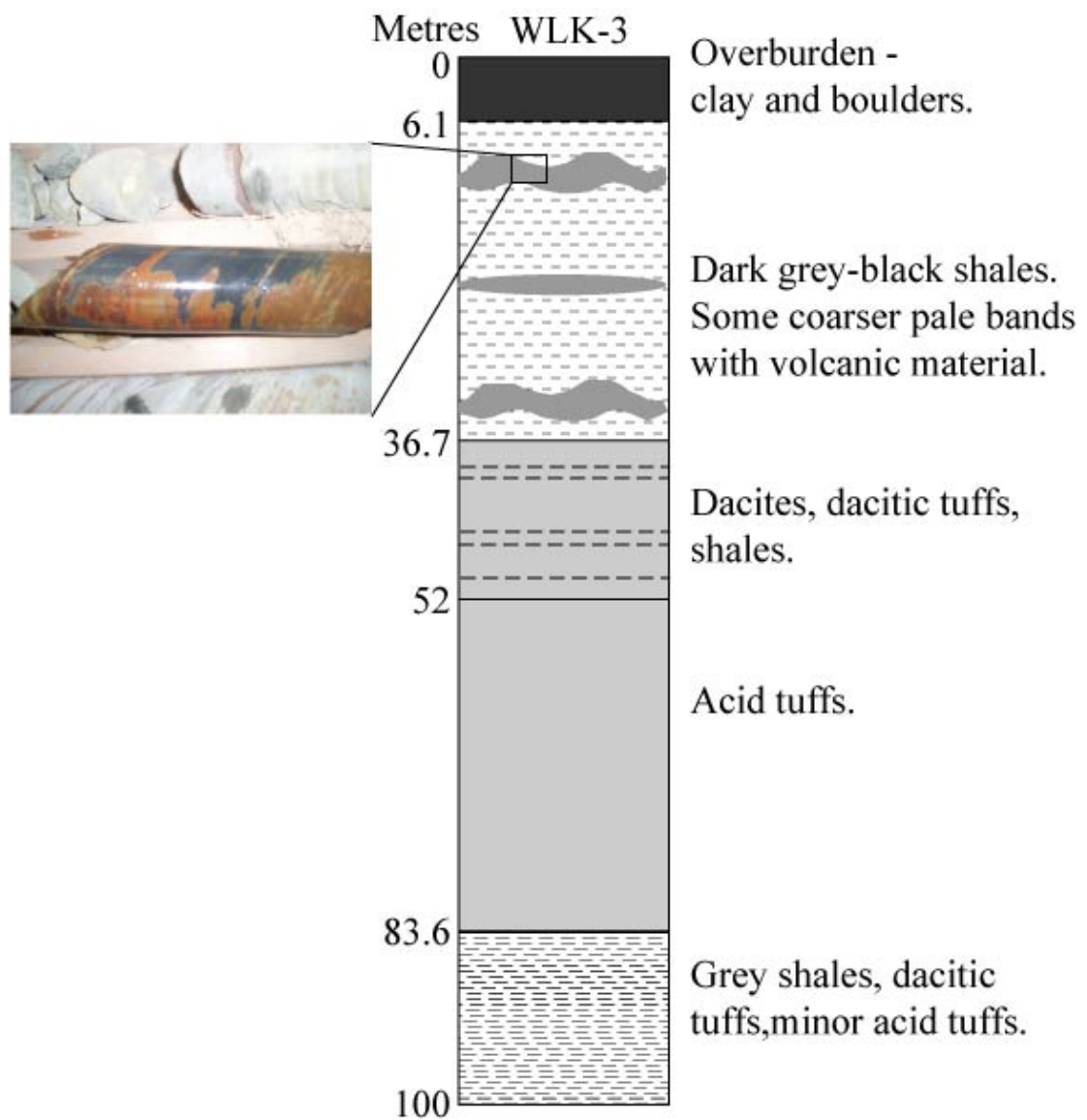
29	Mount Read Volcanics, Australia	Cambrian	Rhyolite sill	Wet, unconsolidated, stratified pumice breccia	B, F	Peperite clasts are blocky, fluidal, wispy and elongate	Gifkins <i>et al</i> , 2002
30	Kiama, New South Wales, Australia	Upper Permian	Basalt or basaltic andesite	Sandstone and siltstone	B, F	Peperite has globular, mesoblocky, blocky and platy clasts	Doyle, 2000
31	Northern Viti Levu, Fiji	Pliocene	Basaltic magma	Coarse volcanic conglomerate and breccia	B, F	Change from fluidal to blocky clasts as a result of cooling magma	Squire and McPhie, 2002
32	Maori Bay, Muriwai, North Island, New Zealand	Miocene	Basaltic andesite	Wet volcaniclastic sand and mud	B		Bear and Cas, 2007
33	Otago Peninsula, New Zealand	Miocene	Phonolite and basaltic dykes	Wet pumice	F	Peperite formed in two stages: coarse fluidal, and fine mingling	Martin and White, 2002
34	Coombs Hill, Antartica	Middle Jurassic	Basaltic magma	Coal (lignite to sub-bituminous rank)	B, F	Fluidal to blocky with distance from margins	McClintock and White, 2002

Appendix A2

Core section logs and descriptions from the Bunmahon and Campile
Formations

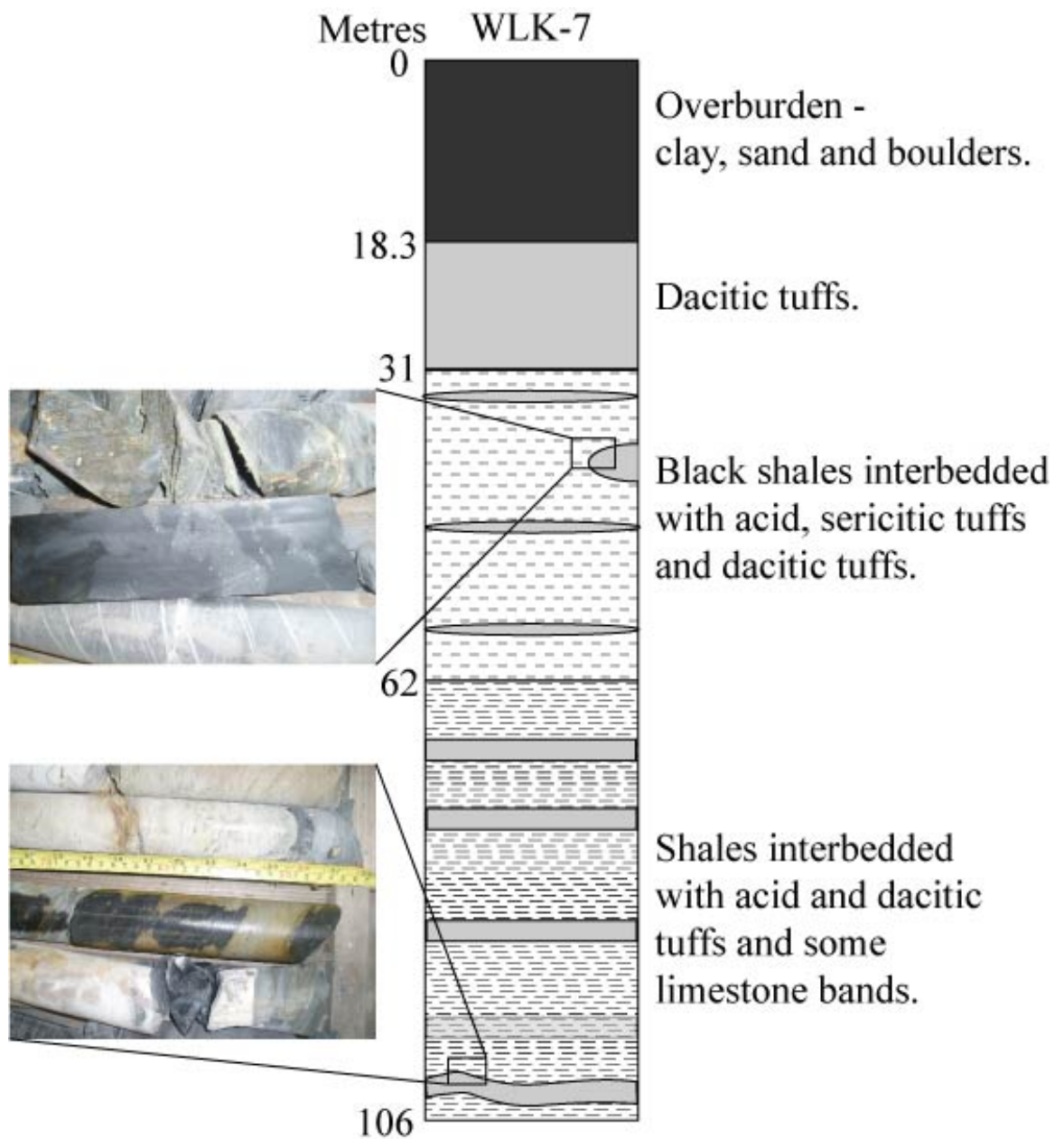
WYR-1 (Ballyristeen, X 24395 10115)





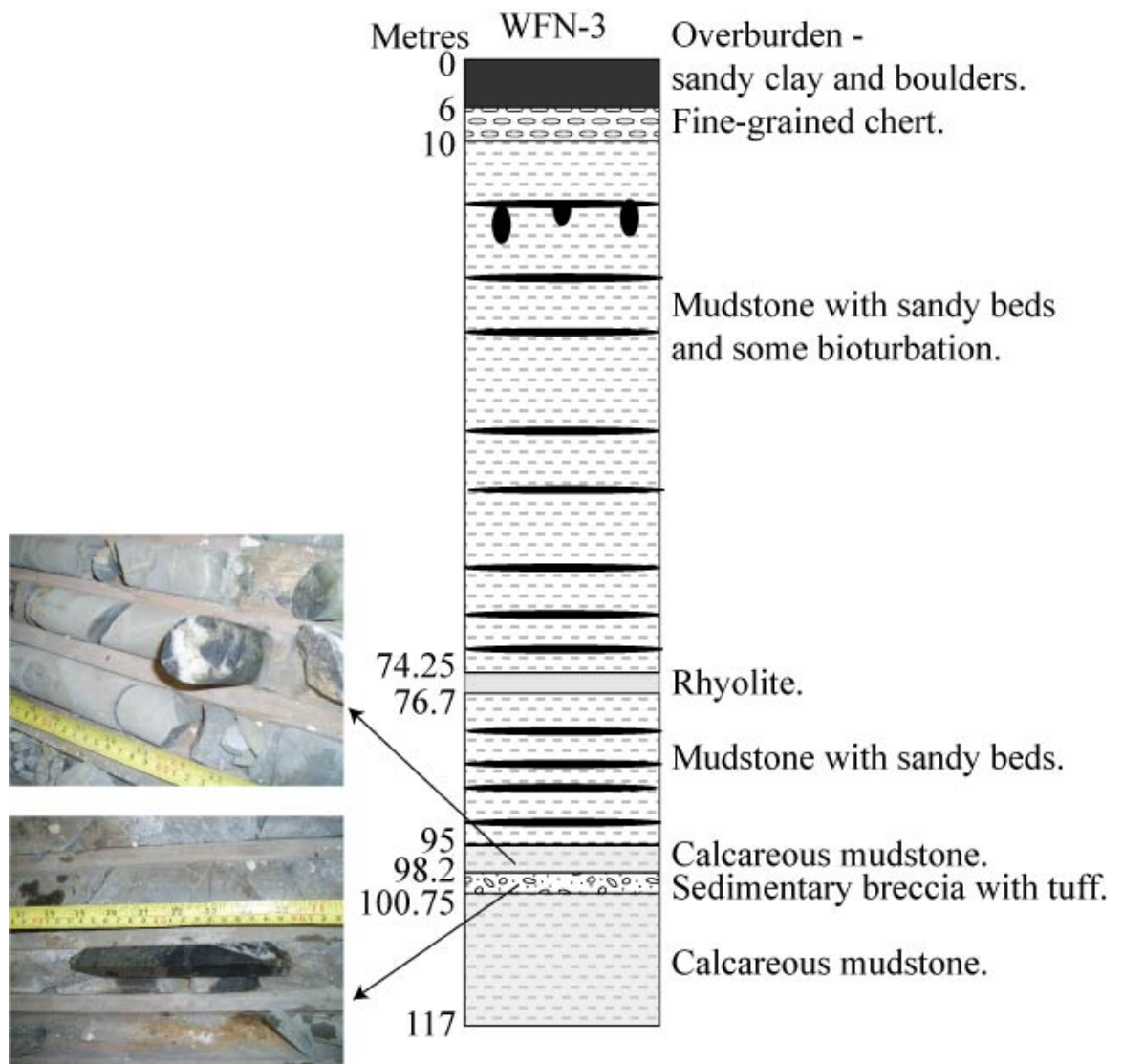
WLK-3 (Loughdeneen, X 25320 10740)

Close packed peperite clasts (one centimeter), similar in morphology to the honeycomb peperite, occur close to the top of the core section. Peperite clasts and soft sediment deformation are recorded within two metres adjacent to an intrusive basalt within the host mudstone.



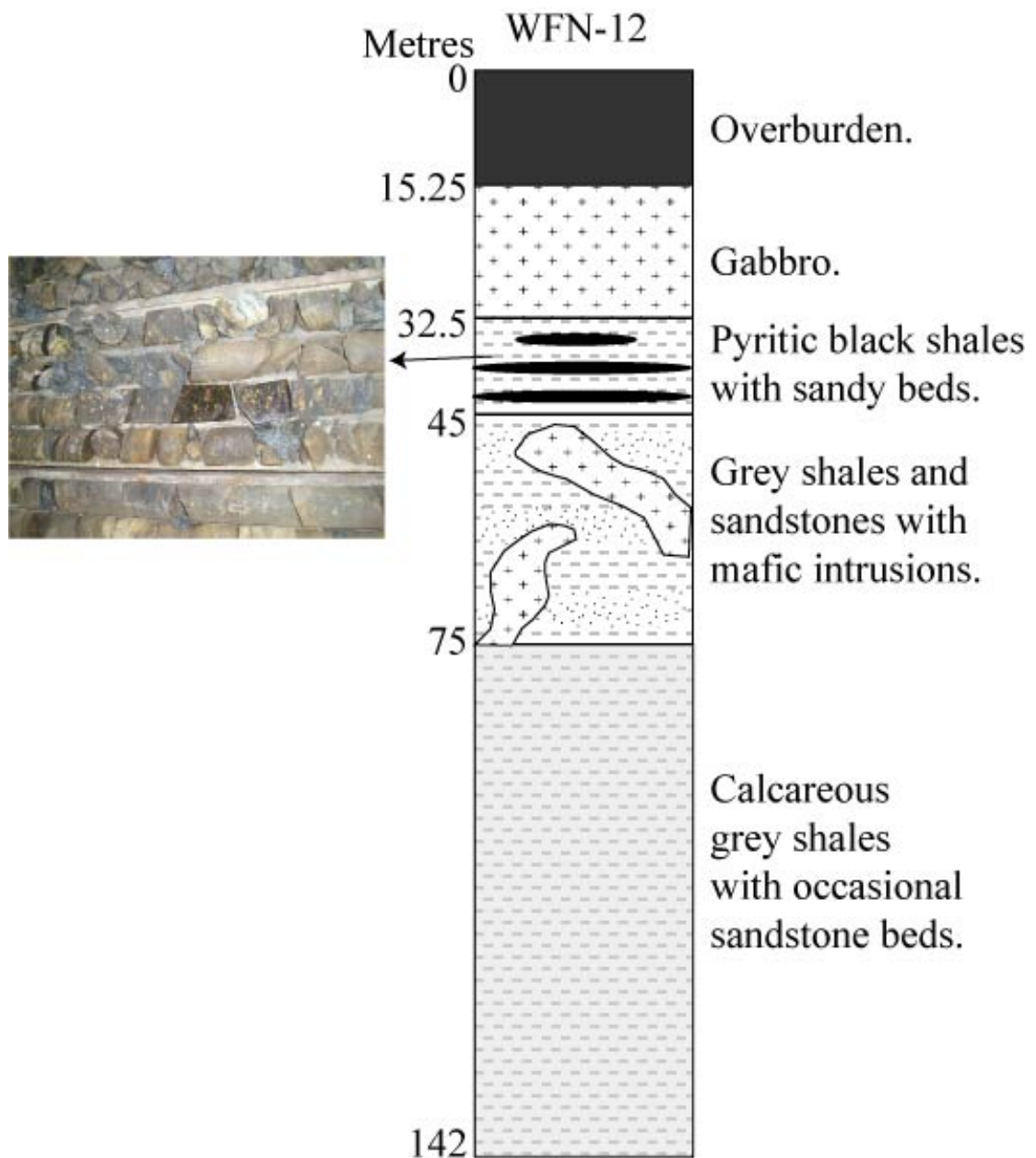
WLK-7 (Loughdeneen, X 25304 10746)

Peperite is developed in spatial association with massive quartz veins at approximately 94m depth. Abundant pyrite occurs within the quartz veins, which cross-cut the sedimentary host for ~1.5m.



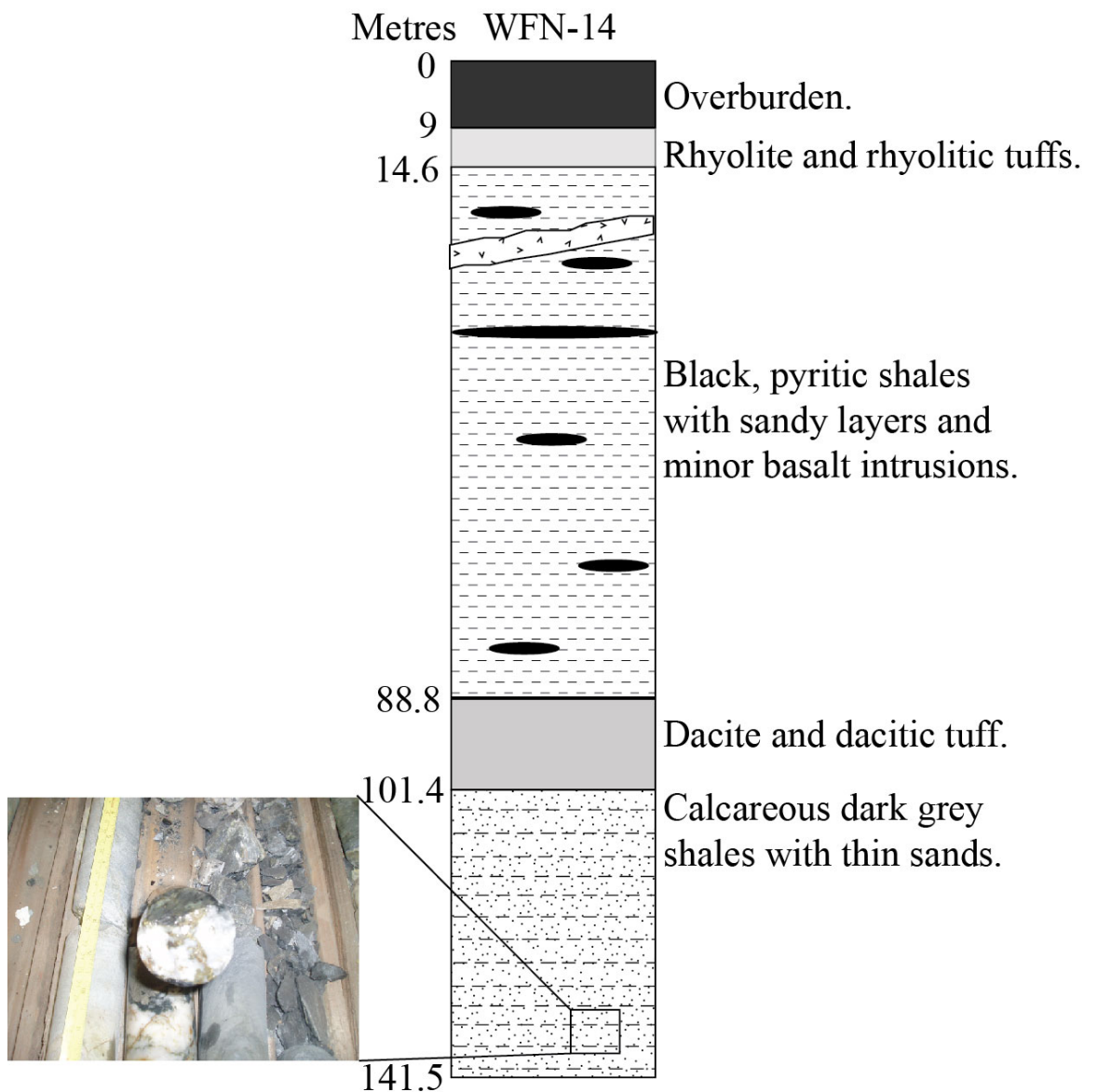
WFN-3 (Fennor, X 25290 10199)

The core section is composed predominantly of mudstone with abundant quartz veining and mineralisation. A five centimetre wide brecciated or peperitic zone is observed containing angular clasts of approximately 0.5-1cm at a depth of 91m. Quartz veining containing pyrite occurs within brecciated host rock.



WFN-12 (Fennor, X 25290 10199)

The majority of intrusive rocks within this section are fine-grained with abundant oxidised iron-rich minerals. Bedding of the sedimentary rocks becomes more coherent toward the base of the section.



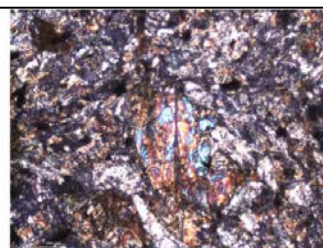
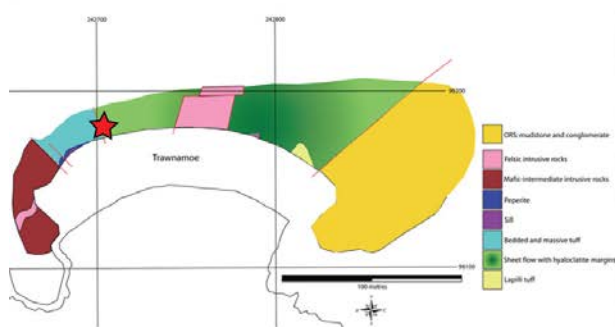
WFN-14 (Ballyscanlan, X 25320 10161)

Basalts, with a high concentration of pyrite, intrude the sedimentary sequence at a depth of approximately 25m. Soft sediment deformation occurs adjacent to a quartz vein at a depth of 139.1m.

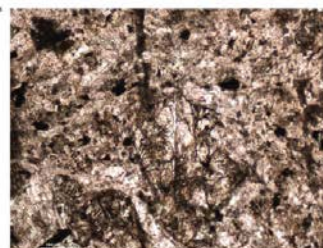
Appendix A3

Data sheets of lithological and geochemical characteristics of analysed
rocks

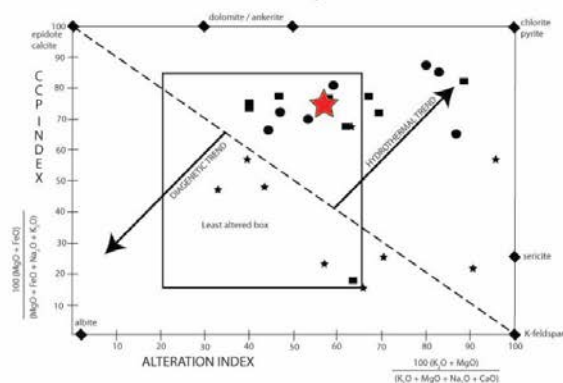
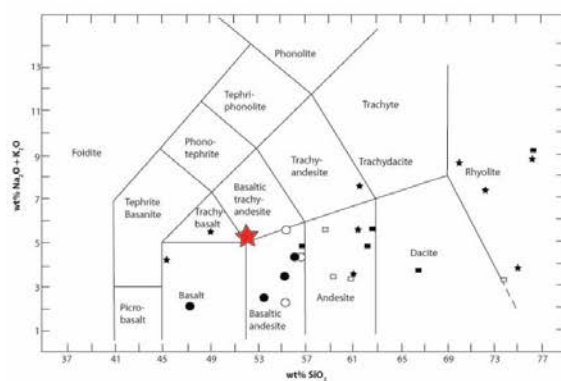
Sample number:	BT1
Location:	Trawnamoe
Formation:	Bunmahon Formation
Grid reference:	X 42703 98184
Volcanic facies:	Hyaloclastic margins of sheet flow
Composition:	Basaltic trachy-andesite
Lithofacies:	Hyaloclastite
Relict minerals:	Plagioclase
Genetic nomenclature:	Coherent facies
Alteration minerals:	Chlorite + mica
Alteration textures:	Interstitial chlorite, chlorite pseudomorphs and muscovite needles
Alteration intensity:	Moderate
Alteration style:	Hydrothermal?



Photomicrograph (XPL)



Photomicrograph (PPL)



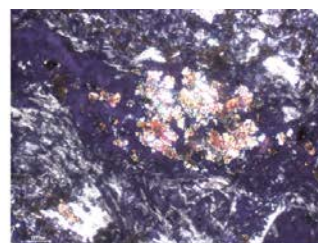
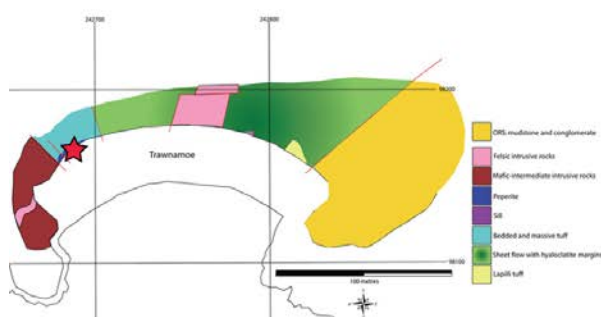
Geochemistry:

SiO ₂	51.91
TiO ₂	0.82
Al ₂ O ₃	15.37
Fe ₂ O ₃	8.62
MnO	0.15
MgO	8.22
CaO	4.49
Na ₂ O	3.24
K ₂ O	2.06
P ₂ O ₅	0.12
LOI	NA
Total	95.00

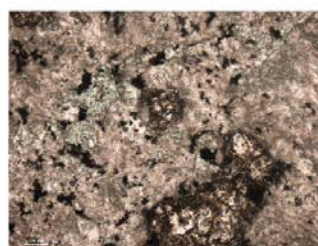
Mineral assemblage:

60% groundmass
15% chlorite
10% clinopyroxene
5% muscovite
5% feldspar
5% calcite

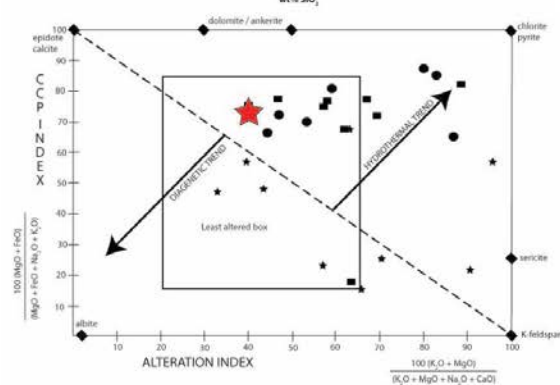
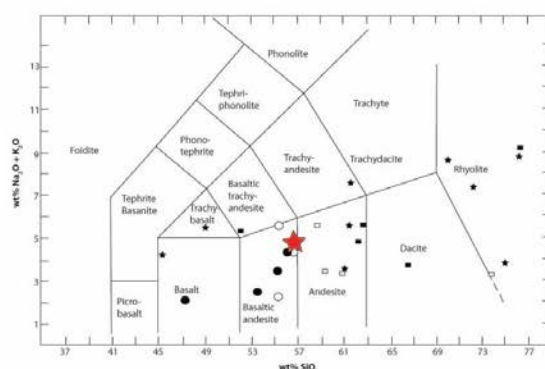
Sample number:	BT2
Location:	Trawnamoe
Formation:	Bunmahon Formation
Grid reference:	X 42687 98155
Volcanic facies:	Intrusive plagioclase and pyroxene-phyric basaltic andesite
Composition:	Basaltic andesite
Lithofacies:	Massive sill
Relict minerals:	Pyroxene
Relict textures:	Rare vesicles, glomeroporphyritic pyroxene
Genetic nomenclature:	Coherent facies
Alteration minerals:	Chlorite + epidote + pumpellyite
Alteration textures:	Interstitial chlorite, disseminated magnetite
Alteration intensity:	Moderate



Photomicrograph (XPL)



Photomicrograph (PPL)



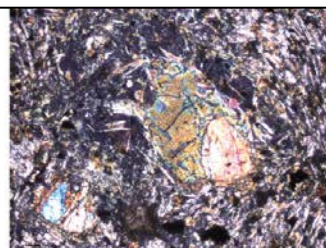
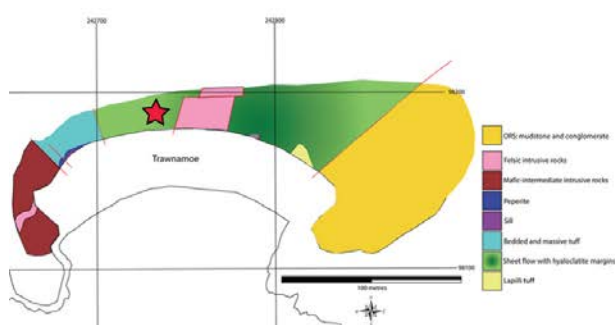
Geochemistry:

SiO ₂	56.89
TiO ₂	0.93
Al ₂ O ₃	18.22
Fe ₂ O ₃	9.71
MnO	0.16
MgO	5.40
CaO	4.70
Na ₂ O	4.28
K ₂ O	0.61
P ₂ O ₅	0.11
LOI	NA
Total	101.01

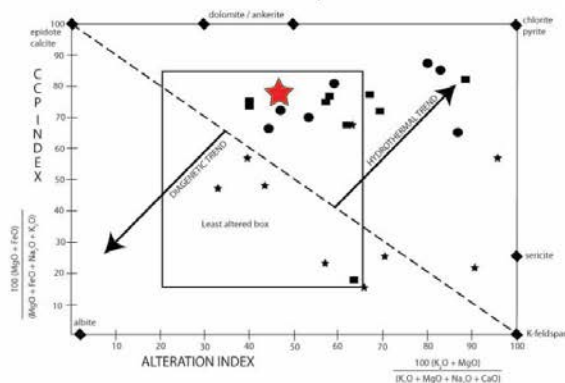
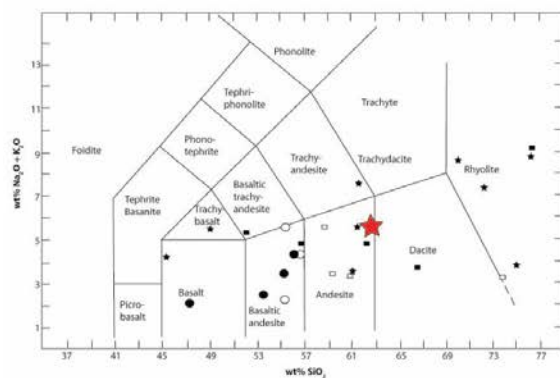
Mineral assemblage:

50% groundmass
20% pyroxene
10% muscovite
10% chlorite
8% plagioclase
2% iron oxides

Sample number:	BT3
Location:	Trawnamoe
Formation:	Bunmahon Formation
Grid reference:	X 42730 98192
Volcanic facies:	Successive porphyritic andesitic sheet flows with hyaloclastite
Composition:	Andesite
Lithofacies:	Sheet flow with hyaloclastite margins
Relict minerals:	Plagioclase
Genetic nomenclature:	Sheet flow
Alteration minerals:	Chlorite + albite
Alteration textures:	Interstitial chlorite, disseminated magnetite
Alteration intensity:	Moderate
Alteration style:	Hydrothermal



Photomicrograph (XPL)



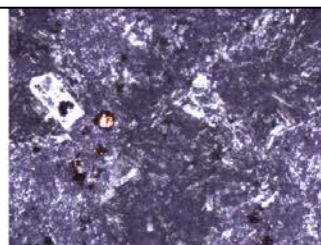
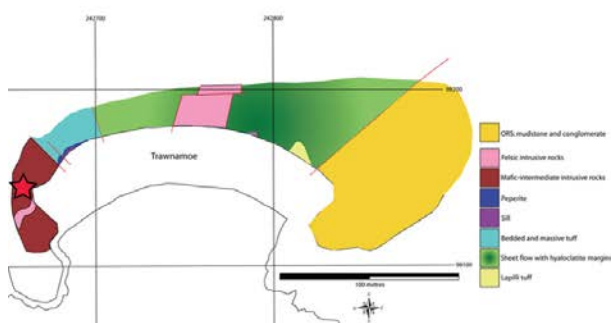
Geochemistry:

SiO ₂	55.57
TiO ₂	0.94
Al ₂ O ₃	17.04
Fe ₂ O ₃	9.04
MnO	0.15
MgO	7.12
CaO	6.33
Na ₂ O	3.11
K ₂ O	1.29
P ₂ O ₅	0.15
LOI	NA
Total	100.74

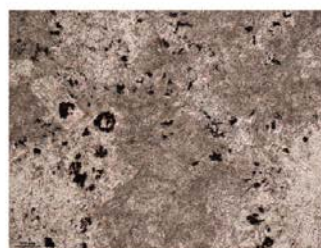
Mineral assemblage:

30% groundmass
15% iron oxides
15% feldspar
15% pyroxene
15% chlorite
10% muscovite

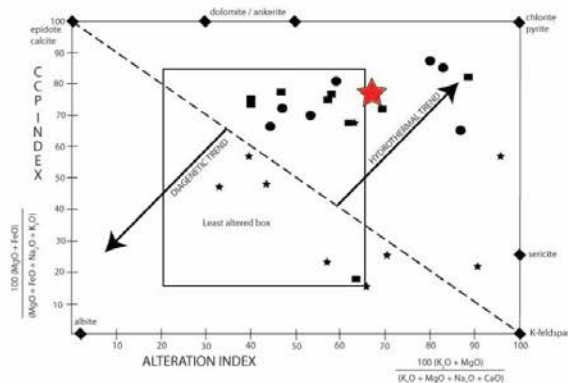
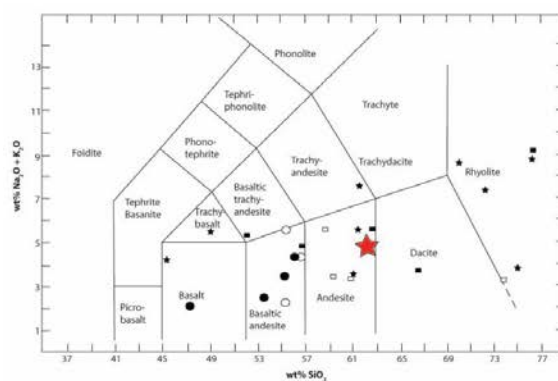
Sample number: BT4
 Location: Trawnamoe
 Formation: Bunmahon Formation
 Grid reference: X 42660 98143
 Volcanic facies: Plagioclase-phyric andesite intrusion
 Composition: Andesite
 Lithofacies: Intrusion
 Relict minerals: Plagioclase
 Genetic nomenclature: Coherent facies
 Alteration minerals: Chlorite + albite + calcite
 Alteration textures: Interstitial chlorite, disseminated magnetite
 Alteration intensity: Moderate
 Alteration style: Hydrothermal?



Photomicrograph (XPL)



Photomicrograph (PPL)



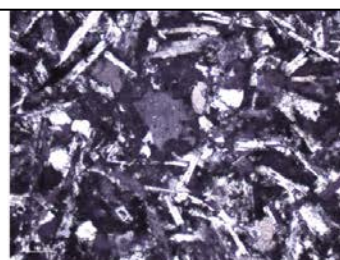
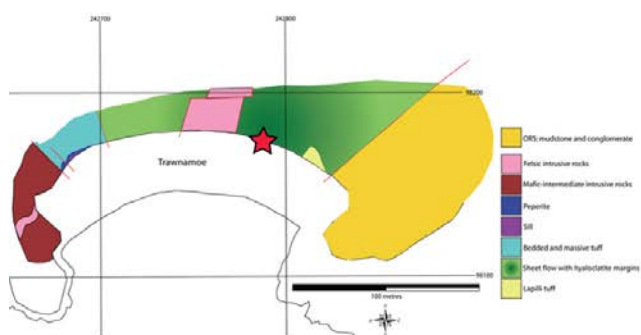
Geochemistry:

SiO ₂	53.40
TiO ₂	0.81
Al ₂ O ₃	16.62
Fe ₂ O ₃	8.07
MnO	0.12
MgO	9.66
CaO	0.32
Na ₂ O	4.60
K ₂ O	0.32
P ₂ O ₅	0.10
LOI	4.79
Total	98.81

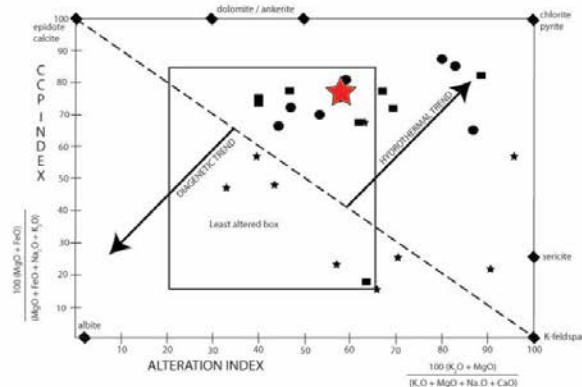
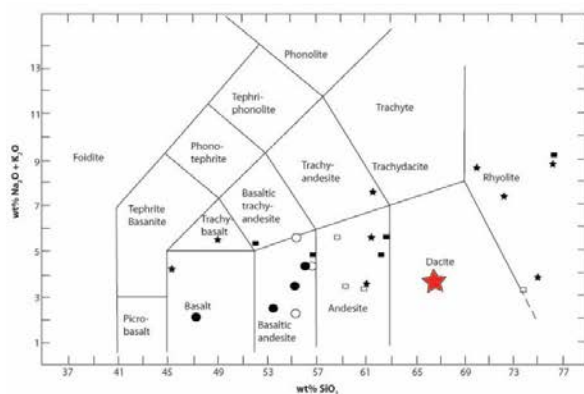
Mineral assemblage:

35% groundmass
 25% plagioclase
 15% K-feldspar
 8% iron oxides
 7% quartz
 5% pyroxene
 5% chlorite

Sample number: BT5
 Location: Trawnamoe
 Formation: Bunmahon Formation
 Grid reference: X 42778 98179
 Volcanic facies: Plagioclase- and alkali-feldspar phyric dacite intrusion
 Composition: Dacite
 Lithofacies: Massive
 Genetic nomenclature: Massive
 Alteration minerals: Chlorite + albite
 Alteration textures: Anhedral chlorite pseudomorphs (alkali feldspar?)
 Alteration intensity: Subtle-moderate
 Alteration style: Hydrothermal?



Photomicrograph (XPL)



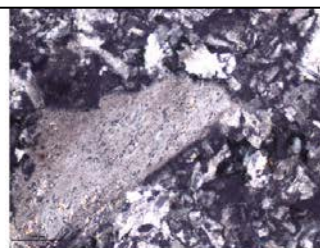
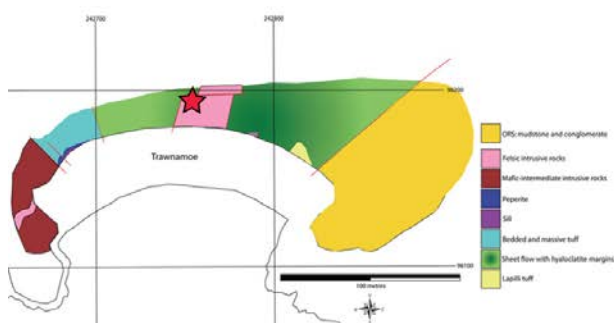
Geochemistry:

SiO ₂	66.53
TiO ₂	0.79
Al ₂ O ₃	13.29
Fe ₂ O ₃	8.48
MnO	0.11
MgO	5.30
CaO	0.51
Na ₂ O	3.55
K ₂ O	0.35
P ₂ O ₅	0.29
LOI	4.17
Total	103.37

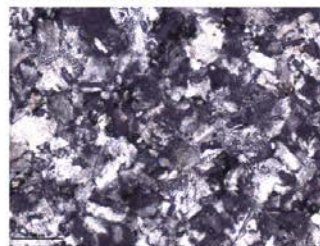
Mineral assemblage:

40% plagioclase
 30% alkali
 feldspar
 15% quartz
 10% groundmass
 5% iron oxides

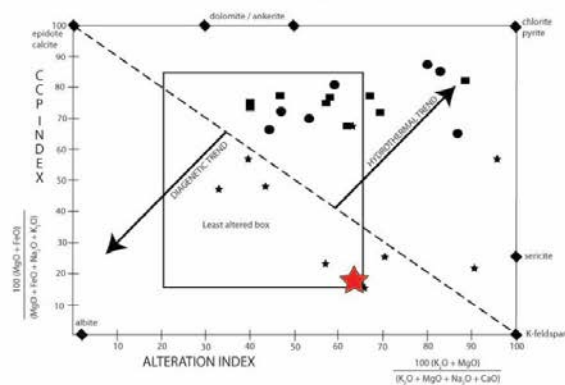
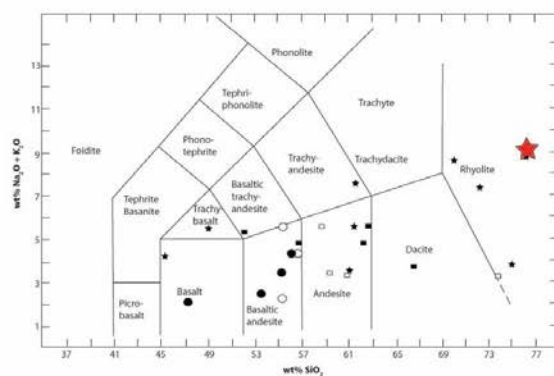
Sample number: BT6
 Location: Trawnamoe
 Formation: Bunmahon Formation
 Grid reference: X 42752 98198
 Volcanic facies: Quartz- and feldspar-phyrlic intrusion
 Composition: Rhyolite
 Lithofacies: Quartz-feldspar porphyry intrusion
 Relict textures: Granophyric intergrowths
 Genetic nomenclature: Massive
 Alteration minerals: Chlorite + mica chains
 Alteration textures: Interstitial chlorite, and quartz veins
 Alteration intensity: Subtle-moderate
 Alteration style: Diagenetic



Photomicrograph (XPL)



Photomicrograph (XPL)



Geochemistry:

SiO ₂	76.23
TiO ₂	0.14
Al ₂ O ₃	12.90
Fe ₂ O ₃	1.40
MnO	0.02
MgO	0.76
CaO	0.09
Na ₂ O	3.53
K ₂ O	5.68
P ₂ O ₅	<0.01
LOI	0.74
Total	101.49

Mineral assemblage:

45% quartz
 40% feldspar
 10% groundmass
 5% muscovite

Sample number: BT7

Location: Trawnamoe

Formation: Bunmahon Formation

Grid reference: X 42687 98155

Volcanic facies: Laminated ash and crystal tuff

Composition: Rhyolite

Lithofacies: Pyroclastic deposit

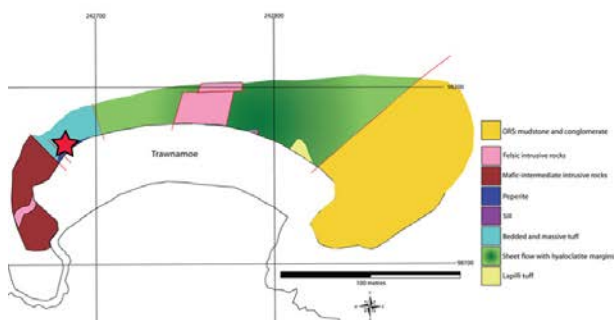
Genetic nomenclature: Normally graded tuff

Alteration minerals: Chlorite + iron oxides

Alteration textures: Interstitial chlorite, chlorite veins, and disseminated magnetite associated with pyroxene layers

Alteration intensity: Moderate

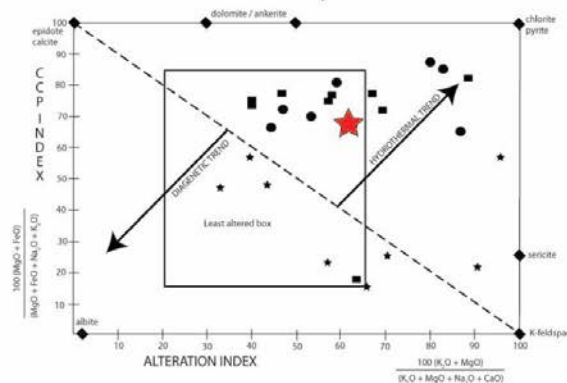
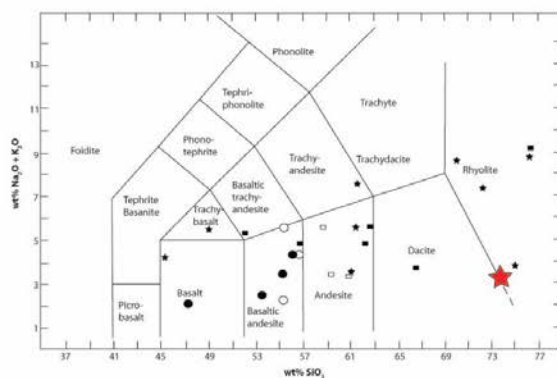
Alteration style: Hydrothermal



Photomicrograph (XPL)



Photomicrograph (PPL)



Geochemistry:

SiO ₂	73.75
TiO ₂	0.11
Al ₂ O ₃	11.44
Fe ₂ O ₃	5.08
MnO	0.08
MgO	2.92
CaO	0.78
Na ₂ O	1.91
K ₂ O	1.48
P ₂ O ₅	0.02
LOI	NA
Total	97.57

Mineral assemblage:

70% groundmass
 10% pyroxene
 10% plagioclase
 5% iron oxides
 5% chlorite

Sample number: BT8

Location: Trawnamoe

Formation: Bunmahon Formation

Grid reference: X 42810 98170

Volcanic facies: Graded lapilli tuff

Composition: Andesite

Lithofacies: Normally graded

Relict minerals: Plagioclase

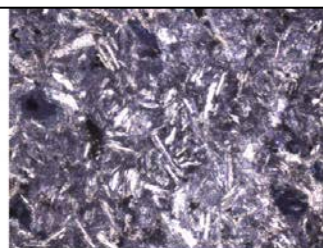
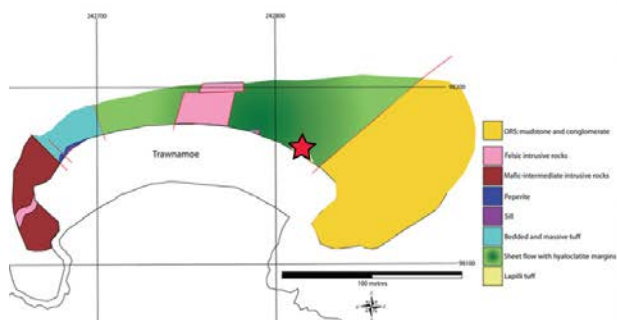
Genetic nomenclature: Coherent facies

Alteration minerals: Chlorite

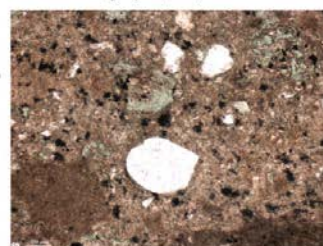
Alteration textures: Interstitial chlorite, and chlorite pseudomorphs

Alteration intensity: Moderate

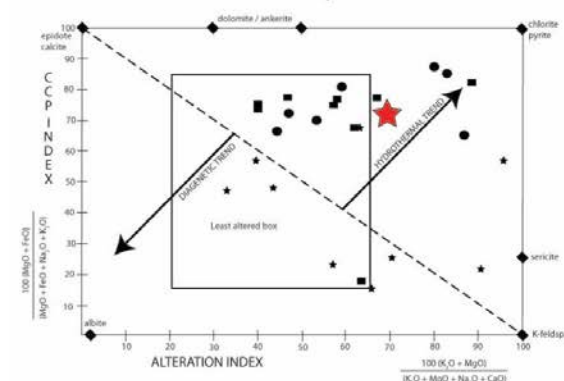
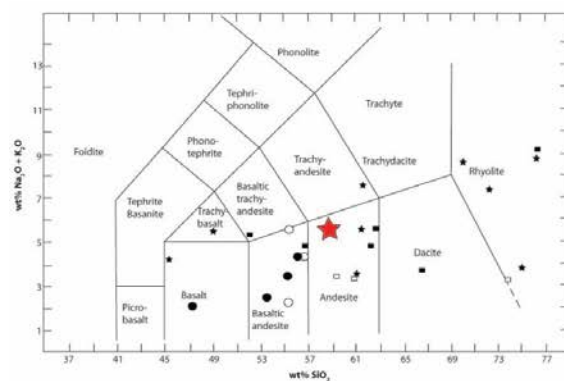
Alteration style: Hydrothermal



Photomicrograph (XPL)



Photomicrograph (PPL)



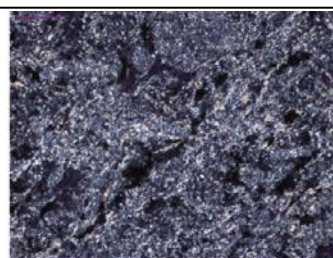
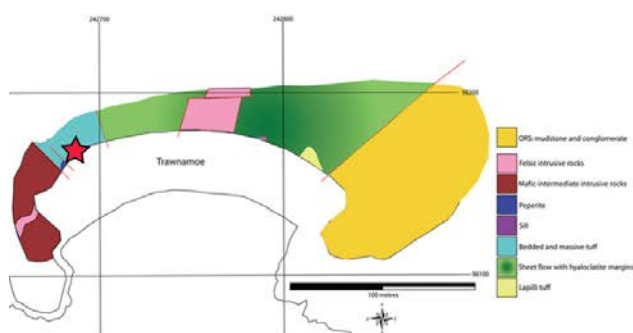
Geochemistry:

SiO ₂	58.74
TiO ₂	0.92
Al ₂ O ₃	19.10
Fe ₂ O ₃	9.77
MnO	0.12
MgO	5.52
CaO	1.29
Na ₂ O	2.48
K ₂ O	3.04
P ₂ O ₅	0.15
LOI	NA
Total	101.13

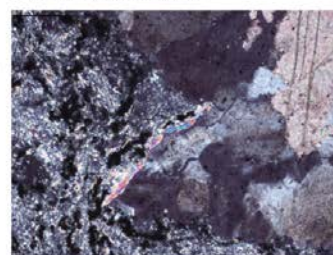
Mineral assemblage:

35% groundmass
15% lithic fragments
15% plagioclase
12% lapilli
12% quartz
6% iron oxides
5% chlorite

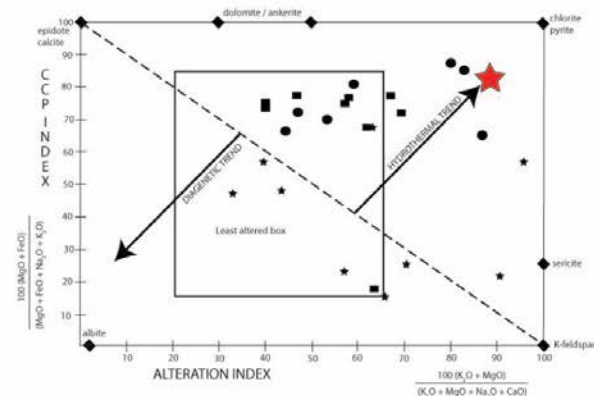
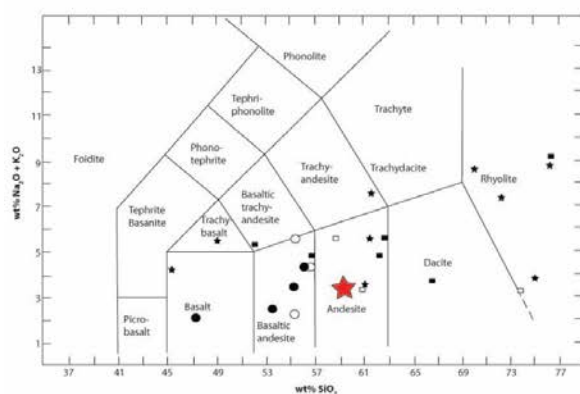
Sample number:	BT9
Location:	Trawnamoe
Formation:	Bunmahon Formation
Grid reference:	X 42687 98155 (~50 centimetres above peperite)
Volcanic facies:	Laminated ash and crystal tuff
Composition:	Andesite
Lithofacies:	Pyroclastic deposit
Genetic nomenclature:	Graded tuff
Alteration minerals:	Chlorite + iron oxides
Alteration textures:	Interstitial chlorite, chlorite veins and disseminated magnetite
Alteration intensity:	Moderate
Alteration style:	Hydrothermal



Photomicrograph (XPL)



Photomicrograph (XPL)



Geochemistry:

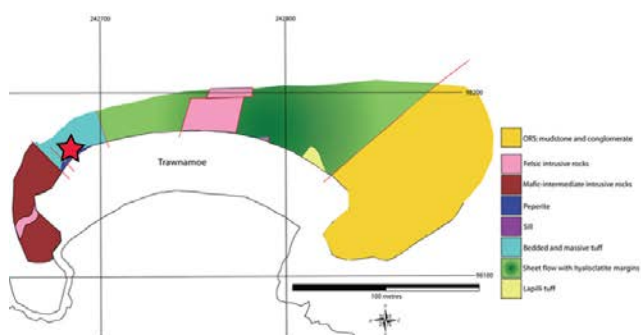
SiO ₂	59.10
TiO ₂	0.77
Al ₂ O ₃	16.26
Fe ₂ O ₃	11.63
MnO	0.18
MgO	7.12
CaO	6.04
Na ₂ O	0.36
K ₂ O	0.79
P ₂ O ₅	0.02
LOI	5.00
Total	102.86

Mineral assemblage:

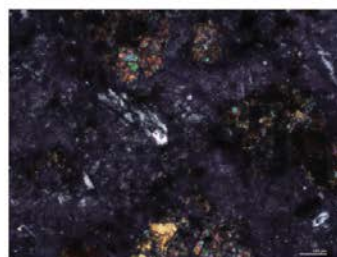
70% groundmass*
10% iron oxides
10% quartz
5% feldspar
5% calcite
5% chlorite

*groundmass of quartz and feldspar predominantly altered to chlorite

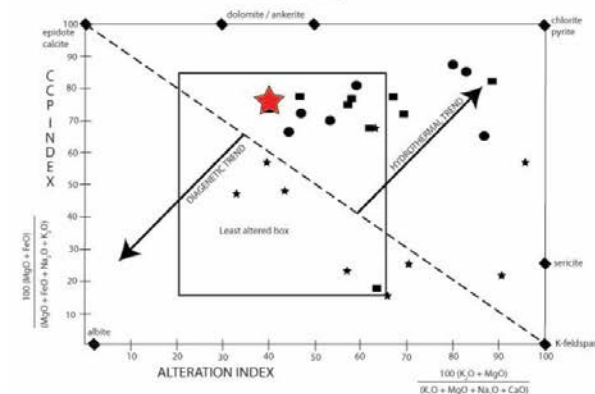
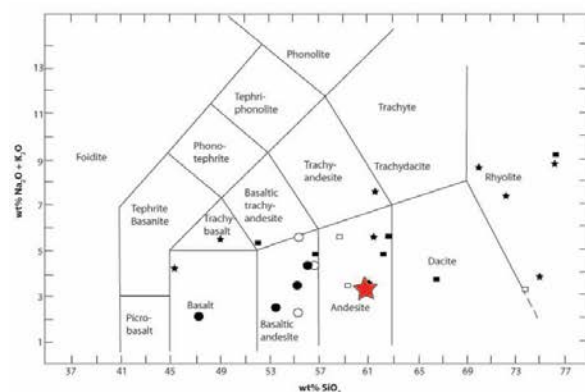
Sample number: BT10
 Location: Trawnamoe
 Formation: Bunmahon Formation
 Grid reference: X 42687 98155 (~two metres above peperite)
 Volcanic facies: Massive ash and crystal tuff
 Composition: Andesite
 Lithofacies: Pyroclastic/mass flow deposit
 Genetic nomenclature: Massive tuff
 Alteration minerals: Chlorite + iron oxides
 Alteration textures: Interstitial chlorite, and disseminated magnetite
 Alteration intensity: Moderate
 Alteration style: Hydrothermal



Photomicrograph (PPL)



Photomicrograph (XPL)



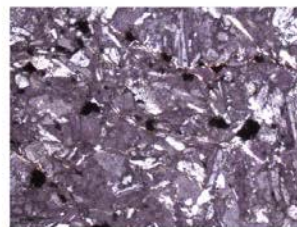
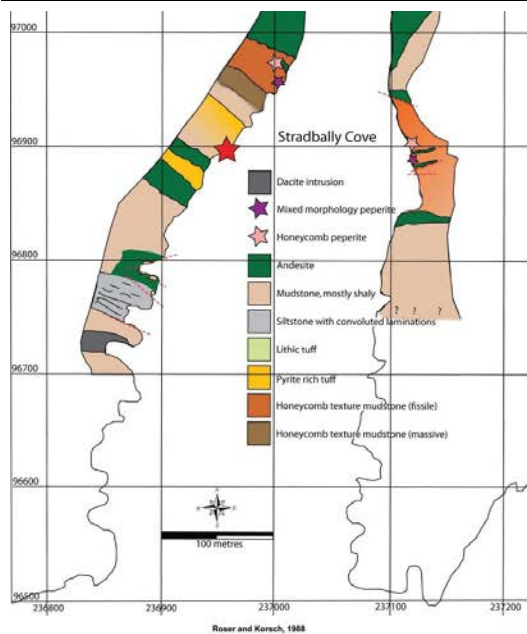
Geochemistry:

SiO ₂	55.19
TiO ₂	0.77
Al ₂ O ₃	16.91
Fe ₂ O ₃	6.94
MnO	0.095
MgO	5.35
CaO	1.88
Na ₂ O	5.36
K ₂ O	0.44
P ₂ O ₅	0.15
LOI	3.31
Total	96.395

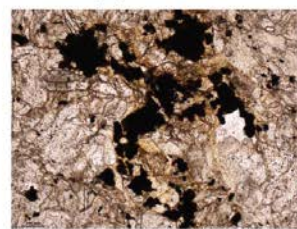
Mineral assemblage:

65% groundmass
 10% muscovite
 10% chlorite
 5% pyroxene
 5% quartz
 5% feldspar

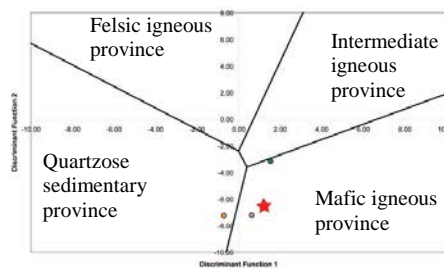
Sample number:	BS1
Location:	Stradbally Cove
Formation:	Bunmahon/Dunabrattin Formation
Grid reference:	X 36965 69896
Provenance:	Mafic igneous provenance
Composition:	Fe-sand
Lithofacies:	Coherent graded mudstone-tuff
Genetic nomenclature:	Volcanogenic sedimentary deposit
Alteration minerals:	Chlorite + iron oxides + pyrite
Alteration textures:	Interstitial chlorite, disseminated hematite, pyrite associated with quartz veining and chlorite alteration
Alteration intensity:	Intense
Alteration style:	Hydrothermal?



Photomicrograph (XPL)

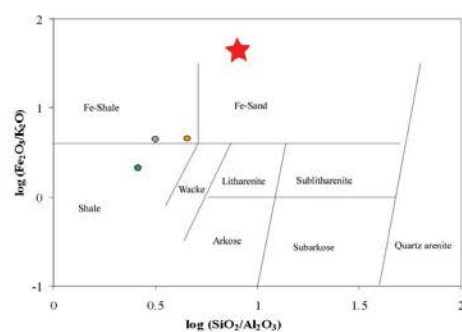


Photomicrograph (PPL)



Geochemistry:

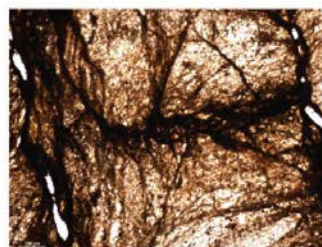
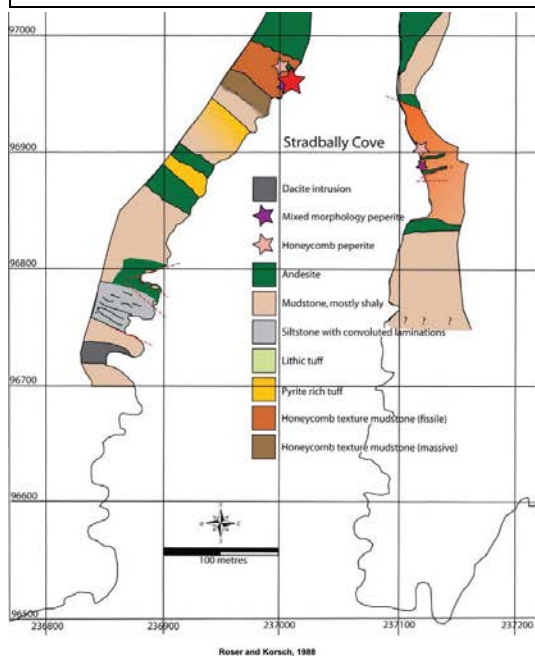
SiO ₂	78.16	CaO	0.00
TiO ₂	0.83	Na ₂ O	1.63
Al ₂ O ₃	9.82	K ₂ O	0.19
Fe ₂ O ₃	8.32	P ₂ O ₅	0.11
MnO	0.10	LOI	NA
MgO	1.19	Total	100.35



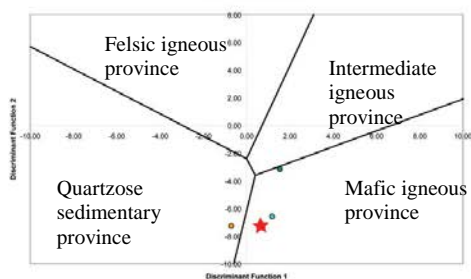
Mineral assemblage:

35% plagioclase
25% matrix
15% pyrite
10% chlorite
5% quartz
5% feldspar

Sample number:	BS2
Location:	Stradbally Cove
Formation:	Bunmahon/Dunabrattin Formation
Grid reference:	X 37020 96958
Provenance:	Mafic igneous provenance
Composition:	Fe-shale
Lithofacies:	Friable, honeycomb texture mudstone
Genetic nomenclature:	Volcanogenic sedimentary deposit
Alteration minerals:	Iron oxides
Alteration textures:	Disseminated iron oxides and iron rich veinlets
Alteration intensity:	Moderate-intense
Alteration style:	Hydrothermal?

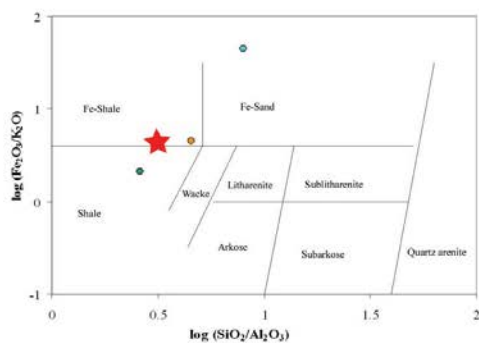


Photomicrograph (XPL)



Geochemistry:

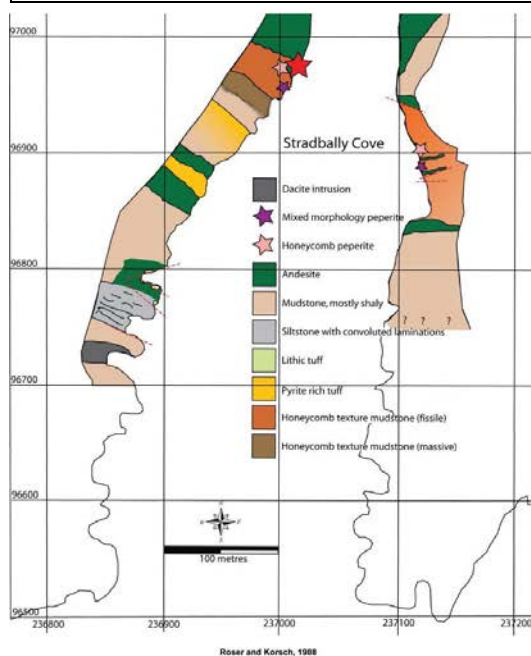
SiO ₂	57.64	CaO	0.18
TiO ₂	1.04	Na ₂ O	0.93
Al ₂ O ₃	18.13	K ₂ O	2.19
Fe ₂ O ₃	9.74	P ₂ O ₅	0.10
MnO	0.22	LOI	NA
MgO	3.70	Total	93.87



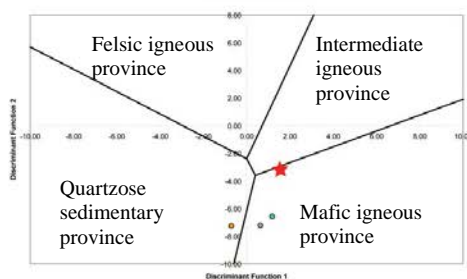
Mineral assemblage:

70% matrix
15% feldspar
10% Fe-oxides
5% quartz

Sample number:	BS3
Location:	Stradbally Cove
Formation:	Bunmahon/Dunabrattin Formation
Grid reference:	X 37019 96970
Provenance:	Mafic igneous provenance
Composition:	Shale
Lithofacies:	Baked shaly mudstone
Genetic nomenclature:	Volcanogenic sedimentary deposit
Alteration minerals:	Chlorite + iron oxides
Alteration textures:	Interstitial chlorite and disseminated magnetite
Alteration intensity:	Moderate
Alteration style:	Hydrothermal?

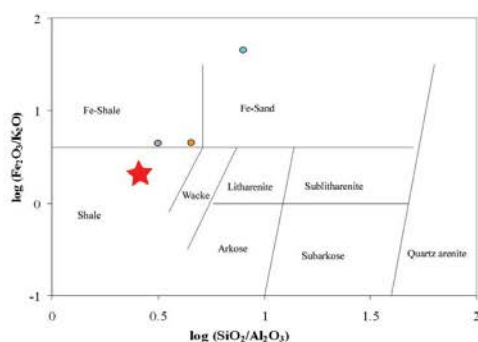


Photomicrograph (XPL)



Geochemistry:

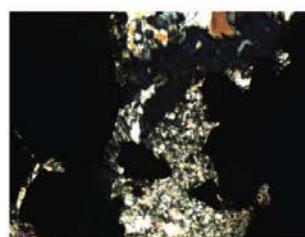
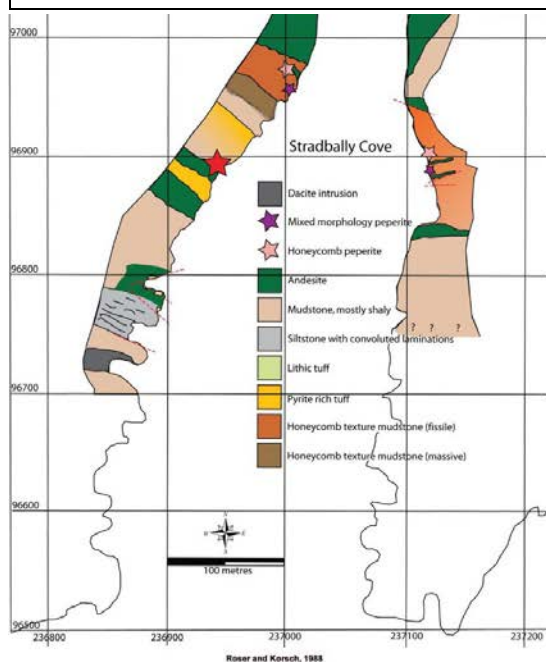
SiO ₂	59.80	CaO	0.14
TiO ₂	1.19	Na ₂ O	0.68
Al ₂ O ₃	22.93	K ₂ O	3.92
Fe ₂ O ₃	8.25	P ₂ O ₅	0.12
MnO	0.07	LOI	NA
MgO	2.66	Total	99.76



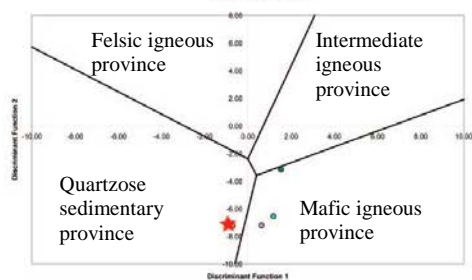
Mineral assemblage:

Extremely fine-grained:
Composed of quartz,
feldspar and Fe-oxides

Sample number:	BS4
Location:	Stradbally Cove
Formation:	Bunmahon/Dunabrattin Formation
Grid reference:	X 36931 96896
Provenance:	Quartzose sedimentary provenance
Composition:	Fe-shale
Lithofacies:	Fine-grained, pyrite rich graded mudstone-tuff
Genetic nomenclature:	Sedimentary deposit
Alteration minerals:	Chlorite + pyrite
Alteration textures:	Disseminated pyrite, interstitial chlorite and pyrite nodules
Alteration intensity:	Moderate-intense
Alteration style:	Hydrothermal?

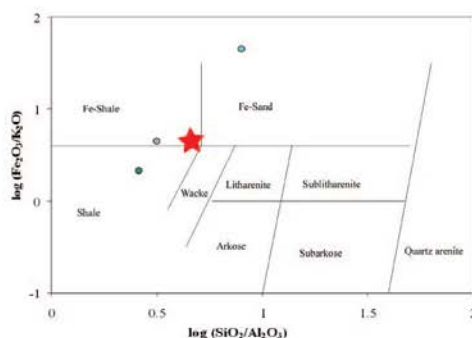


Photomicrograph (XPL)



Geochemistry:

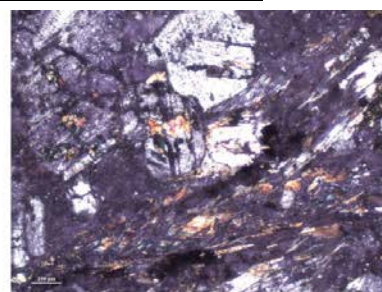
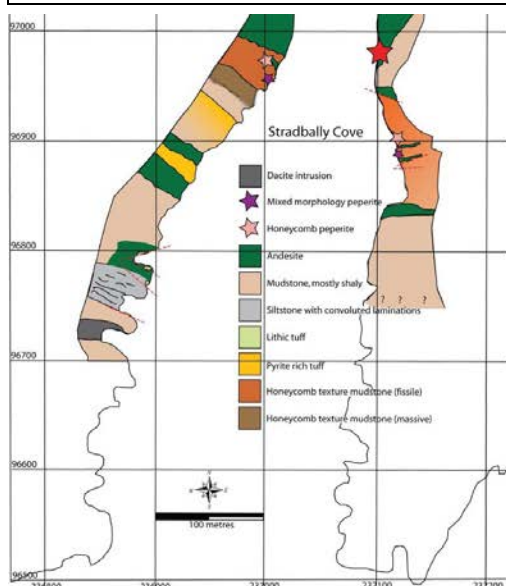
SiO ₂	65.35	CaO	0.12
TiO ₂	0.86	Na ₂ O	0.47
Al ₂ O ₃	14.39	K ₂ O	1.99
Fe ₂ O ₃	8.89	P ₂ O ₅	0.14
MnO	0.065	LOI	3.65
MgO	2.74	Total	98.67



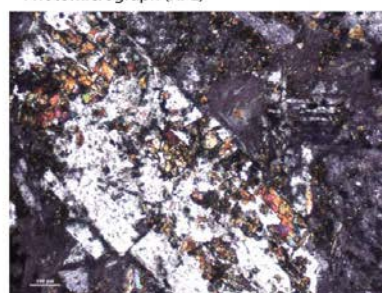
Mineral assemblage:

45% matrix
25% feldspar
15% quartz
10% pyrite
5% chlorite

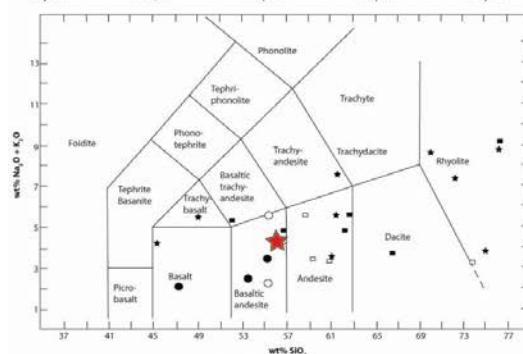
Sample number: BS5
 Location: Stradbally Cove
 Formation: Bunmahon Formation
 Grid reference: X 37100 96982
 Volcanic facies: Coherent coarse grained intrusive
 Composition: Basaltic-andesite
 Lithofacies: Massive
 Genetic nomenclature: Coherent facies
 Alteration minerals: Chlorite + albite
 Alteration textures: Interstitial chlorite
 Alteration intensity: Moderate
 Alteration style: Hydrothermal



Photomicrograph (XPL)

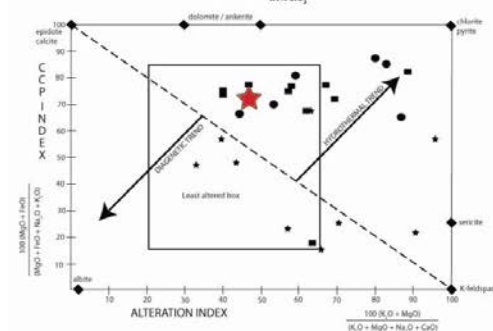


Photomicrograph (XPL)



Geochemistry:

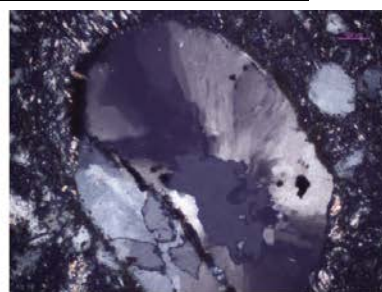
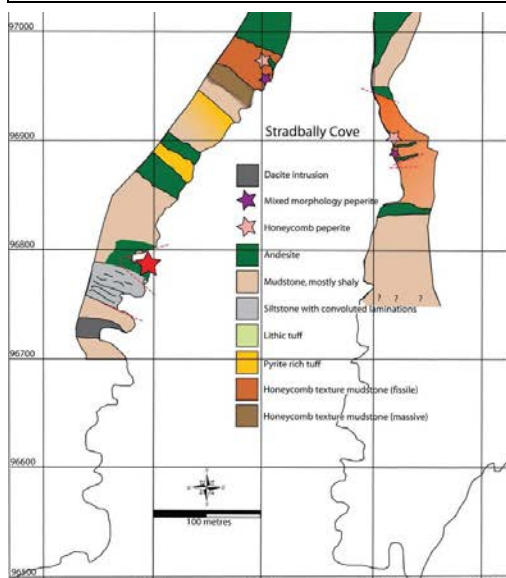
SiO ₂	54.33	CaO	3.20
TiO ₂	0.84	Na ₂ O	5.44
Al ₂ O ₃	17.84	K ₂ O	0.31
Fe ₂ O ₃	8.70	P ₂ O ₅	0.13
MnO	0.14	LOI	3.87
MgO	7.46	Total	102.26



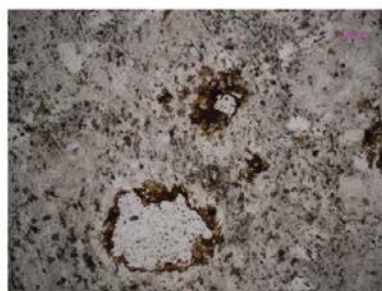
Mineral assemblage:

40% plagioclase feldspar
 15% groundmass
 15% alkali feldspar
 10% biotite
 10% muscovite
 5% chlorite
 5% oxides

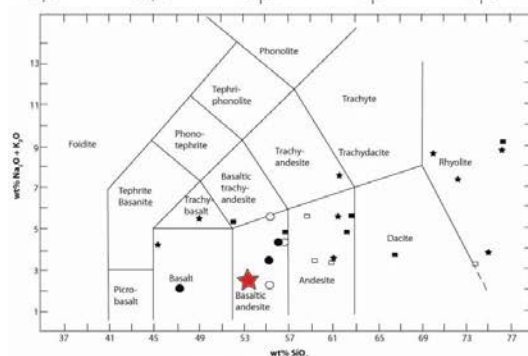
Sample number:	BS7
Location:	Stradbally Cove
Formation:	Bunmahon Formation
Grid reference:	X 36896 96779
Volcanic facies:	Medium grained intrusive
Composition:	Basaltic-andesite
Lithofacies:	Massive
Genetic nomenclature:	Coherent facies
Alteration minerals:	Chlorite + albite
Alteration textures:	Interstitial chlorite and chlorite overgrowths
Alteration intensity:	Moderate
Alteration style:	Hydrothermal



Photomicrograph (XPL)

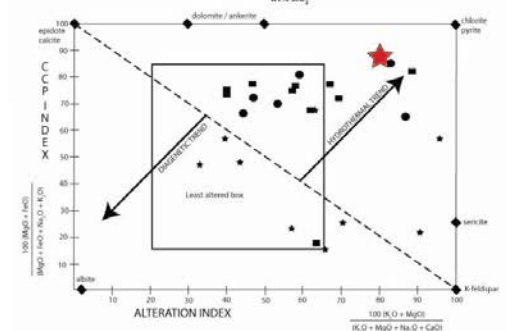


Photomicrograph (PPL)



Geochemistry:

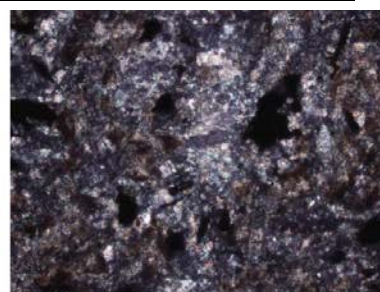
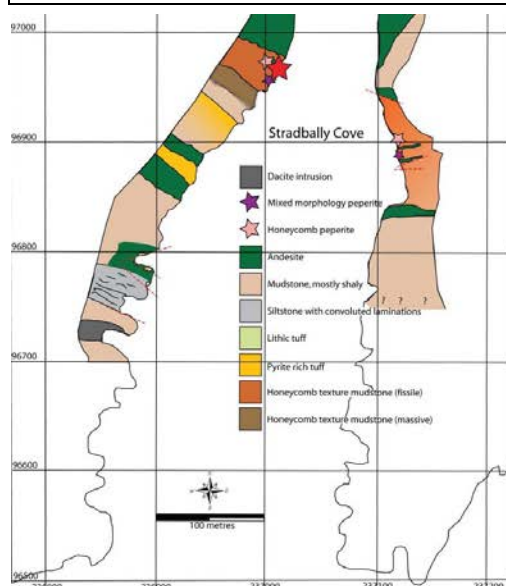
SiO ₂	53.49	CaO	0.17
TiO ₂	0.91	Na ₂ O	1.67
Al ₂ O ₃	16.53	K ₂ O	0.77
Fe ₂ O ₃	13.00	P ₂ O ₅	0.15
MnO	0.154	LOI	4.93
MgO	6.83	Total	98.604



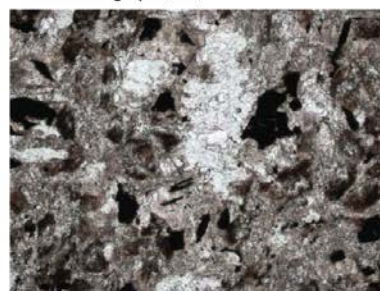
Mineral assemblage:

40% fine-grained groundmass
30% potassium feldspar
10% plagioclase feldspar
10% muscovite
10% chlorite
5% iron oxides

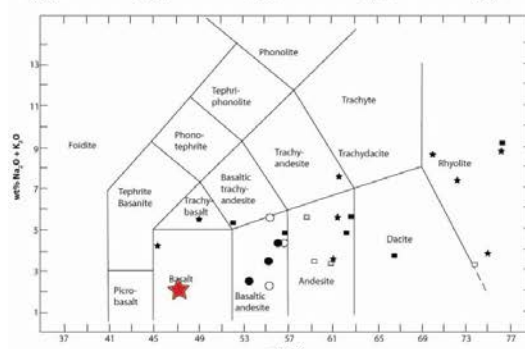
Sample number:	BS8
Location:	Stradbally Cove
Formation:	Bunmahon Formation
Grid reference:	X 37113 96967
Volcanic facies:	Coherent intrusive
Composition:	Basalt
Lithofacies:	Massive
Genetic nomenclature:	Coherent facies
Alteration minerals:	Chlorite + calcite + iron oxides
Alteration textures:	Interstitial chlorite and disseminated iron oxides
Alteration intensity:	Moderate
Alteration style:	Hydrothermal?



Photomicrograph (XPL)



Photomicrograph (PPL)

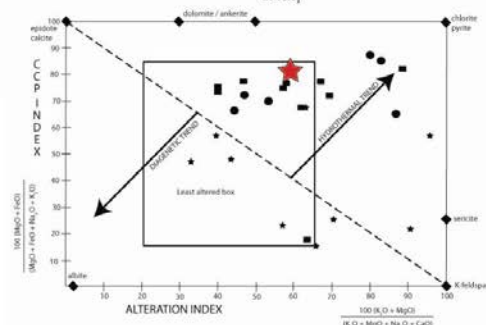


Geochemistry:

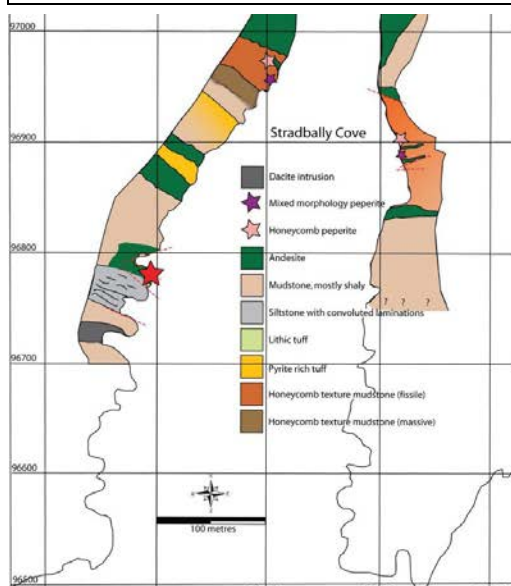
SiO ₂	47.05	CaO	1.88
TiO ₂	1.24	Na ₂ O	1.6
Al ₂ O ₃	15.46	K ₂ O	0.54
Fe ₂ O ₃	10.18	P ₂ O ₅	0.18
MnO	0.136	LOI	8.7
MgO	9.42	Total	96.386

Mineral assemblage:

55% groundmass
20% feldspars
15% iron oxides
5% chlorite
5% calcite



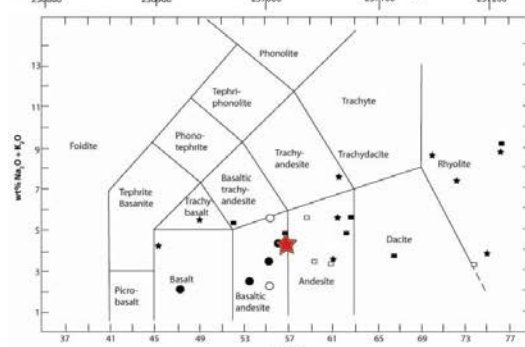
Sample number:	BS9
Location:	Stradbally Cove
Formation:	Bunmahon Formation
Grid reference:	X 36896 96779
Volcanic facies:	Lithic tuff
Composition:	Basaltic-andesite
Lithofacies:	Pyroclastic deposit containing lithic fragments
Genetic nomenclature:	Coherent facies
Alteration minerals:	Chlorite
Alteration textures:	Interstitial chlorite
Alteration intensity:	Moderate - strong
Alteration style:	Hydrothermal



Photomicrograph (XPL)

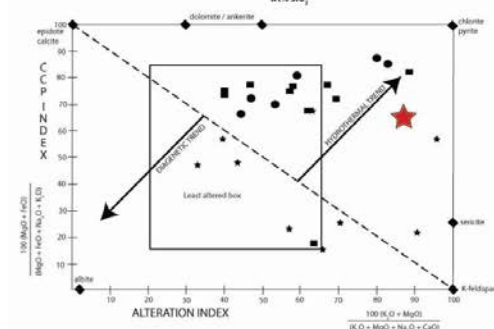


Photomicrograph (PPL)



Geochemistry:

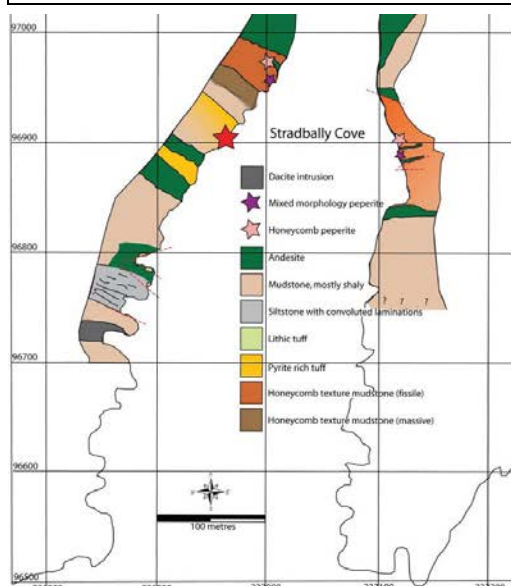
SiO ₂	55.20	CaO	0.44
TiO ₂	0.81	Na ₂ O	0.94
Al ₂ O ₃	18.38	K ₂ O	1.30
Fe ₂ O ₃	9.10	P ₂ O ₅	0.14
MnO	0.162	LOI	5.46
MgO	5.53	Total	97.462



Mineral assemblage:

- 30% potassium feldspar
- 20% matrix
- 20% quartz
- 20% lithic clasts
- 10% chlorite

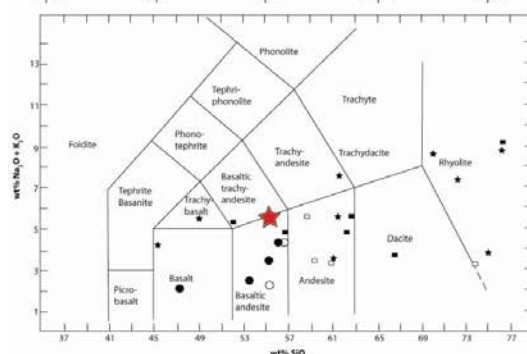
Sample number:	BS10
Location:	Stradbally Cove
Formation:	Bunmahon Formation
Grid reference:	X 36962 96904
Volcanic facies:	Pyrite rich tuff
Composition:	Basaltic-andesite
Lithofacies:	Pyroclastic deposit
Genetic nomenclature:	Coherent facies
Alteration minerals:	Chlorite + pyrite
Alteration textures:	Interstitial chlorite, disseminated pyrite and pyrite nodules
Alteration intensity:	Moderate
Alteration style:	Hydrothermal?



Photomicrograph (PPL)

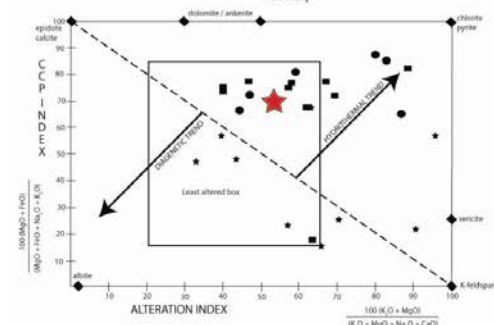


Photomicrograph (PPL)



Geochemistry:

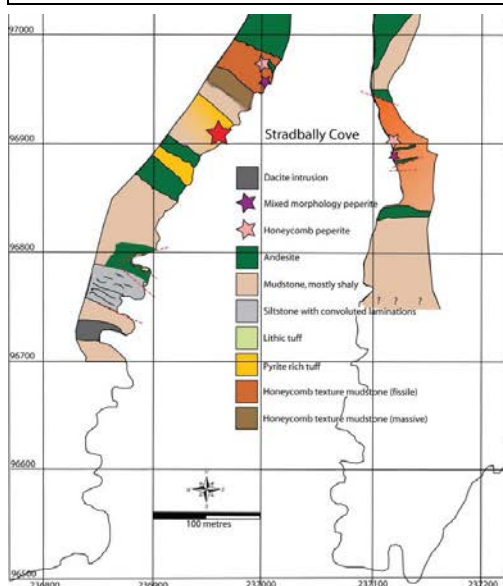
SiO ₂	55.20	CaO	0.44
TiO ₂	0.81	Na ₂ O	0.94
Al ₂ O ₃	18.38	K ₂ O	1.30
Fe ₂ O ₃	9.10	P ₂ O ₅	0.14
MnO	0.162	LOI	5.46
MgO	5.53	Total	97.53



Mineral assemblage:

45% matrix
20% feldspar
15% pyrite
10% quartz
10% chlorite

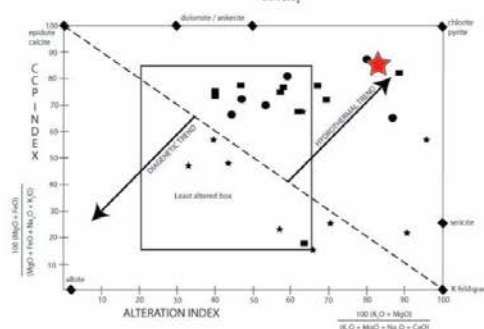
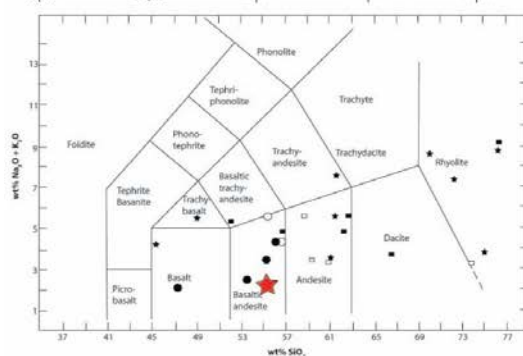
Sample number:	BS11
Location:	Stradbally Cove
Formation:	Bunmahon/Dunabrattin Formation
Grid reference:	X 36963 96907
Volcanic facies:	Fine-grained pyrite rich tuff
Composition:	Basaltic-andesite
Lithofacies:	Pyroclastic deposit
Genetic nomenclature:	Coherent facies
Alteration minerals:	Chlorite + pyrite
Alteration textures:	Interstitial chlorite, disseminated pyrite and pyrite nodules
Alteration intensity:	Moderate
Alteration style:	Hydrothermal?



Photomicrograph (XPL)

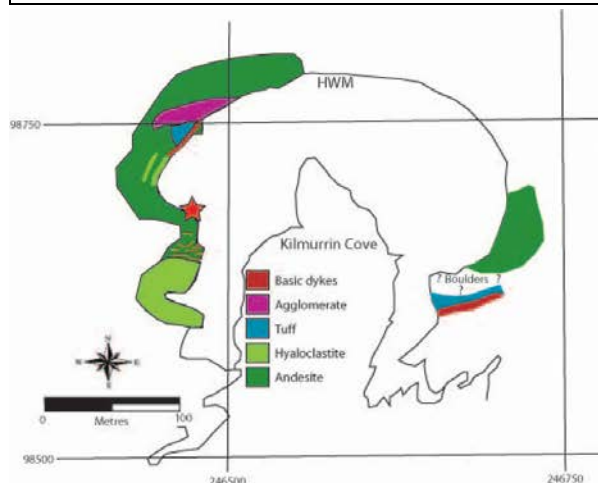
Geochemistry:

SiO ₂	55.20
TiO ₂	0.81
Al ₂ O ₃	18.38
Fe ₂ O ₃	9.10
MnO	0.162
MgO	5.53
CaO	0.44
Na ₂ O	0.94
K ₂ O	1.30
P ₂ O ₅	0.14
LOI	5.46
Total	97.53

**Mineral assemblage:**

55% matrix
20% feldspar
10% pyrite
10% quartz
5% chlorite

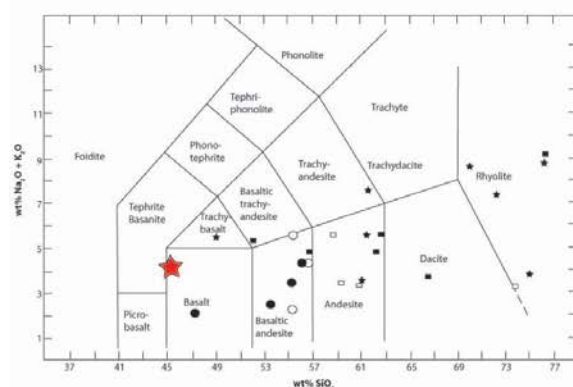
Sample number:	BK1
Location:	Kilmurrin Cove
Formation:	Bunmahon Formation
Grid reference:	X 46481 98684
Volcanic facies:	Coarse grained intrusive
Composition:	Basalt
Lithofacies:	Massive
Genetic nomenclature:	Coherent facies
Alteration minerals:	Chlorite
Alteration textures:	Interstitial chlorite and iron oxidation
Alteration intensity:	Weak-moderate
Alteration style:	Hydrothermal



Photomicrograph (XPL)

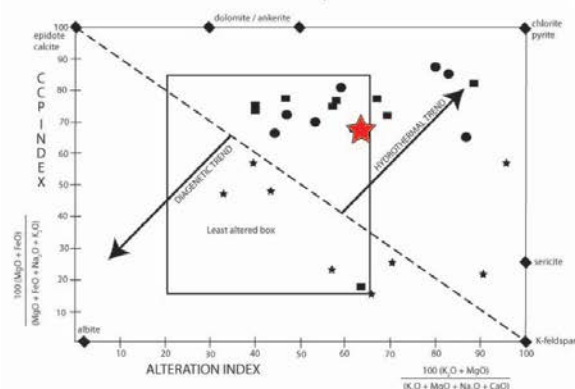


Photomicrograph (PPL)



Geochemistry:

SiO ₂	46.48
TiO ₂	1.50
Al ₂ O ₃	16.71
Fe ₂ O ₃	10.27
MnO	0.274
MgO	8.77
CaO	4.05
Na ₂ O	2.20
K ₂ O	1.96
P ₂ O ₅	0.16
LOI	8.88
Total	101.254



Mineral assemblage:

40% plagioclase feldspar
30% clinopyroxene
20% groundmass
10% chlorite

Appendix A4

Techniques and error calculations used in image analysis of rock
textures

Method

Digital images were taken using a Canon PowerShot A95 CCD with a resolution of 1600 x 1200 pixels, and uploaded to a Compaq Presario V4000. For outcrops of appropriate size with clasts large enough to be resolved, a grid of photographs was used to reproduce and analyse the entire face of the outcrop. For less extensively exposed outcrops, photographs were taken of the typical texture to represent the total section. Contrast between the magmatic and sedimentary components was initially enhanced using Adobe Photoshop CS2, to create a false colour image. Colour contrast for each image was manual and based on observation of the magmatic and sedimentary compositions on a case-by-case basis for each image.

The enhanced digitised images were converted to a greyscale image using ImageTool version 3.00 and processed to a binary image using a manually selected value between 0 and 255, in order to differentiate between magmatic and sedimentary components. The areas occupied by magmatic and sedimentary components were calculated as the number of monochromatic pixels as a percentage of the total numbers of pixels within the image. To investigate the error associated with manual selection of greyscale threshold values for each peperite type, the percentage areas of magmatic and sedimentary components were calculated for similar threshold values as chosen in ImageTool and for different computer programs. In order to determine if Imagetool was sufficiently accurate, Adobe Photoshop CS2 was also used to produce similar binary images, which were then subjected to identical analysis. Largest standard deviations are recorded within peperite samples where the contrast between clasts and host material is low and chosen threshold values within various programmes vary assignment of black and white pixels between lithologies accordingly. As a result, percentages determined using Imagetool 3.00 represent the most accurate, where conversion to greyscale, selection of threshold values and the counting of pixels are all carried out within one programme and are assigned to 'best fit' visually the original peperite samples.

Analysis of the peperite clasts was performed using the count pixels tool in Imagetool 3.00. This method, used only for binary images to count both the black and white pixels, yields a count of pixels for both tones, which is translated into

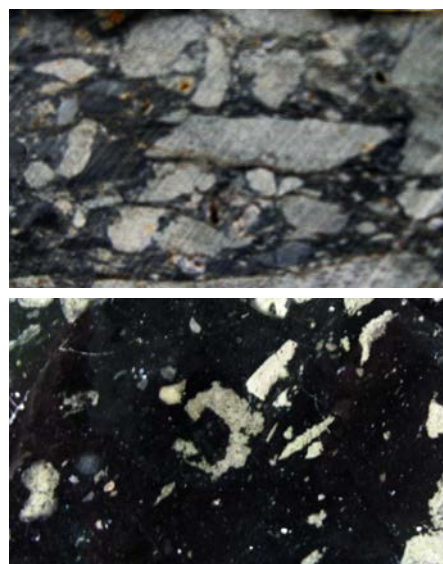
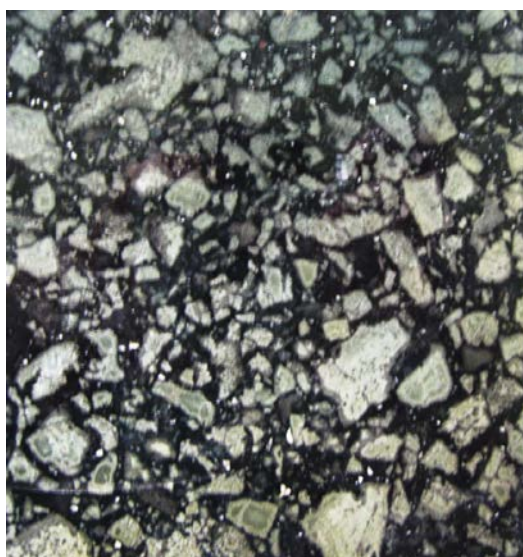
percentage values in the results window. For each sample analysed the separate black or white pixels represents a specific assigned composition. This establishes the area covered in 2D sections by both the magmatic and sedimentary components.

Sample	Black pixels			Mean	Standard deviation (between mean & (1))
	(1)	(2)	(3)		
Fluidal	67.33	75.6	70.79	71.26	3.93
Fluidal	65.06	64.7	66.78	65.53	0.47
Honeycomb	72.54	74.4	72.9	73.29	0.75
Mixed morphology	66.06	71.6	69.16	68.96	2.9

Percentages of black pixels calculated given greyscale threshold values as used in (1) Imagetool 3.00, (2) Adobe Photoshop CS2 using the same values as used in Imagetool 3.00 and (3) Adobe Photoshop CS2 using manually chosen values for clearer definition.

In order to compensate for variations in dark and light shades in images of peperite outcrops (due to surface variations) a cut slabs of the honeycomb peperite was also imaged and analysed. The cut sample is taken 5cm from the surface where the original analysed image was taken. The same technique was employed in two peperite samples from the Isle of Mull to use as a comparison exercise between images taken at the surface and images taken from a cut surface. A field of view of the cut surface of these peperite slabs are shown below. Results yield differences of up to ~3% in black pixel percentage count.

	Honeycomb	Mull 1	Mull 2
Cut sample	70	62.4	86
Outcrop	72.5	60	88.5
Mean	71.25	61.2	87.25
St. Dev	1.7	1.7	1.7



Appendix A5

Methods, standards and error calculations used for geochemical whole
rock analysis and table of bulk rock geochemical results

Method:

Samples were collected in a manner so as to get the most variety of all rock types studied in the region but also more importantly to determine the bulk rock chemistry of the magmas and sediments involved in peperite formation. Heavy mineralisation, veining and hydrothermal alteration is recorded in the sampling region and these outcrops or rock types were avoided if at all possible when determining original composition using bulk rock analysis. Rock samples taken were in the range of 2Kg up to as large as 7Kg, and these were collected using a standard geological hammer or where required a 5lb geological hammer and in some cases using a con saw. The samples were split using hammers, and a specialised rock splitter. Crushing was then carried out using a Jaw Crusher, which uses a toughened tungsten carbide 'jaw' until a size of approximately 5mm, or less, was obtained. These smaller pieces were then sifted through to ensure no weathered or contaminated sections, and the remaining rubble was powdered using an agate swing mill.

The use of a jaw crusher could cause serious contamination of the sample due to both dust harbouring and the wearing of the steel plates. In order to overcome this problem, after each sample was crushed all movable parts of the jaw crusher were taken out and these, along with the main body of the machine, were washed in acetone. Although agate mills are described as fragile, slow and expensive they are also found to be the least likely to contaminate samples, particularly those destined for low-level trace element discrimination (Gifkins *et al.*, 2005).

The digestion procedure used to prepare samples for major and trace element analysis by ICP MS uses a multi-acid technique using HF, HNO₃, HClO₄ and HCl, with a dilution factor ranging from 1:200 to 1:250.

0.25g of each of the well mixed, powdered samples were transferred to separate 15ml Teflon bottles and then each was moistened with 0.5ml of suprapure water. Each of these samples were then prepared with an acid mix comprising 5ml of hydrofluoric acid (HF), 3ml of nitric acid (HNO₃) and 1ml of perchloric acid (HClO₄). Each of these acids were added in this order so the perchloric acid does not react with any organic material present within the samples. The samples were then tightly covered and heated in an oven for approximately three hours (or until complete dissolution occurs) at 105°C. The resulting solution was evaporated to dryness on a hotplate in a fume cupboard. After evaporation was complete, 5ml of 1M HCL was then added to each

sample, the covers replaced and the bottles heated again at 105°C in the oven overnight. This solution is then allowed to cool after being removed from the oven, before they were made up to 50ml with suprapure water. This was done by first placing the final sample jars on the mass balance, setting to zero and then adding the sample solution and rinsing the Teflon bottle with the suprapure water, until 50ml had been reached, to reduce the chance of sample loss. The sample was then labelled appropriately and sent for analysis.

Sample decomposition for silica analysis

The technique used for determination of silica is similar to that used previously, using several acids to break down the sample. With this sample decomposition, however, a closed digestion method was used, not allowing evaporation to take place. Unlike the previous preparation method, the measured 0.2g of each sample was added to supra pure water to make a total of 100g, resulting in a dilution factor of 1:500.

The first stage involved measuring 0.2g of each well mixed powdered sample into separate Teflon beakers. The acids were then added, 5ml HF, and 3ml HNO₃. The lids were placed on the beakers and labelled accordingly. These beakers were then placed in an oven at 105°C for approximately 7-8 hours. After the allowed time had lapsed the samples were allowed to cool. 2.8g of boric acid powder was then weighed out into 250ml plastic containers. The water was then added to the Teflon beakers and the resultant solution was added to the bottles with the boric acid. This was repeated several times in order to reduce the amount of loss of the sample. The bottles were then placed on a weighing scale and the solution was made up to 100ml with distilled water, before being sealed and labelled.

Loss on ignition values have also been determined due to the possibility of errors introduced through the oxidation of ferrous iron and a resultant weight gain due to the addition of oxygen (Lechler and Desilets, 1987). All iron has been determined as Fe₂O₃ but for each lithology the most likely weight percent of both Fe₂O₃ and FeO are also calculated using the ratios of Middlemost (1989).

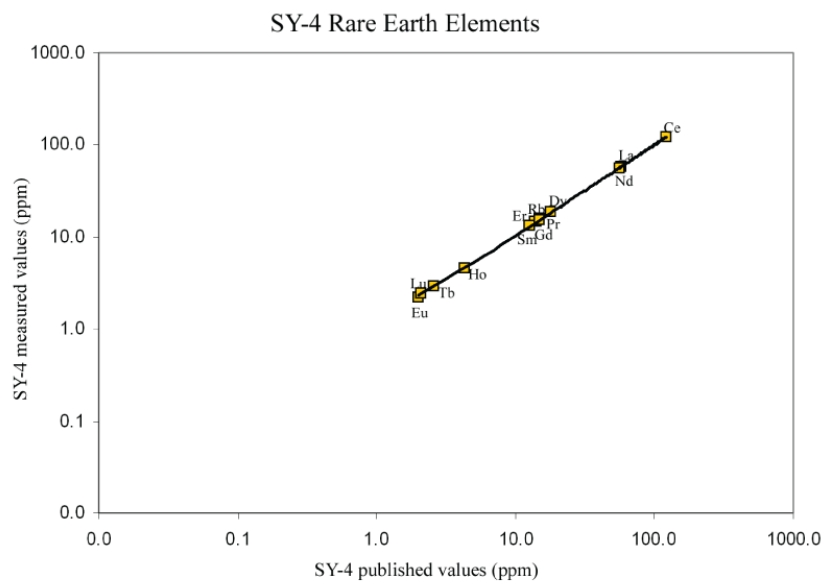
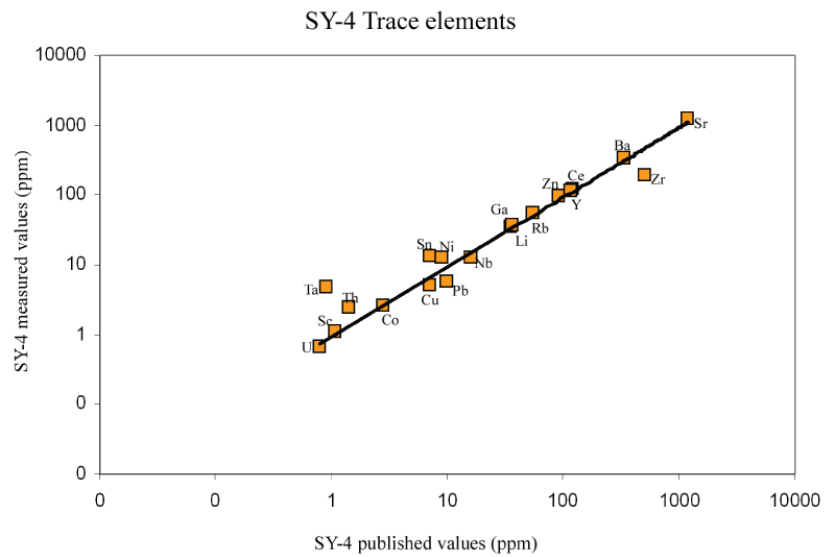
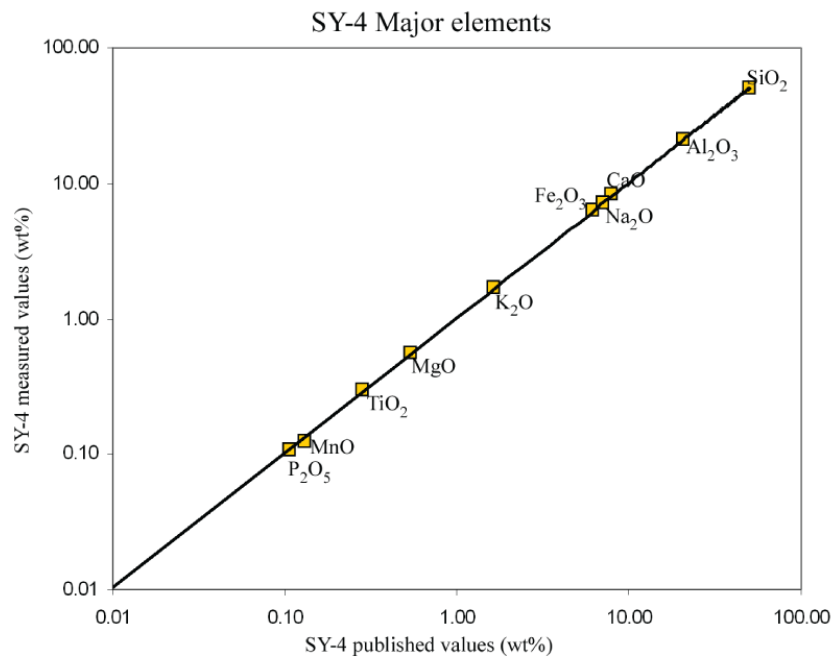
Although thirty samples in total were selected for analysis, further samples were prepared and analysed. Reference materials were specifically selected to match as close as possible to those samples chosen from the Bunmahon and Campile Formations and were chosen to ensure the techniques used were sufficiently accurate and to determine any areas in which there was a change in results. Errors were calculated from published values of the reference materials and values obtained from this analysis. The R^2 test was used to test for accuracy of the results. The Pearson product moment correlation coefficient, r , is a dimensionless coefficient that ranges from -1.0 to 1.0 inclusive and reflects the extent of a linear relationship between the two data sets. Coefficients of -1 indicate an exact negative relationship, 0 indicates no relationship and +1 indicates an exact positive relationship. As several batches of samples were analysed using different reference materials, the R^2 value for each of these is given in the table below, along with samples analysed in each set.

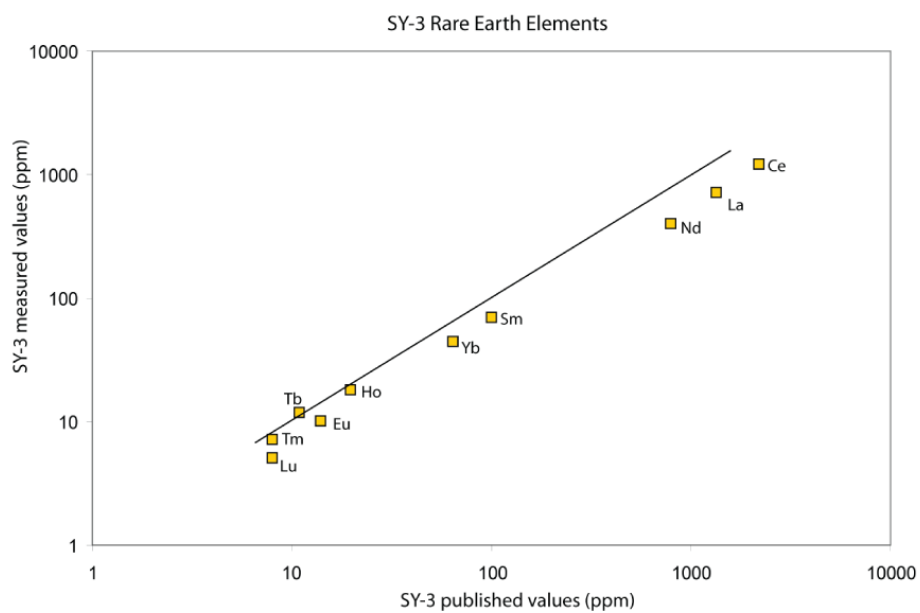
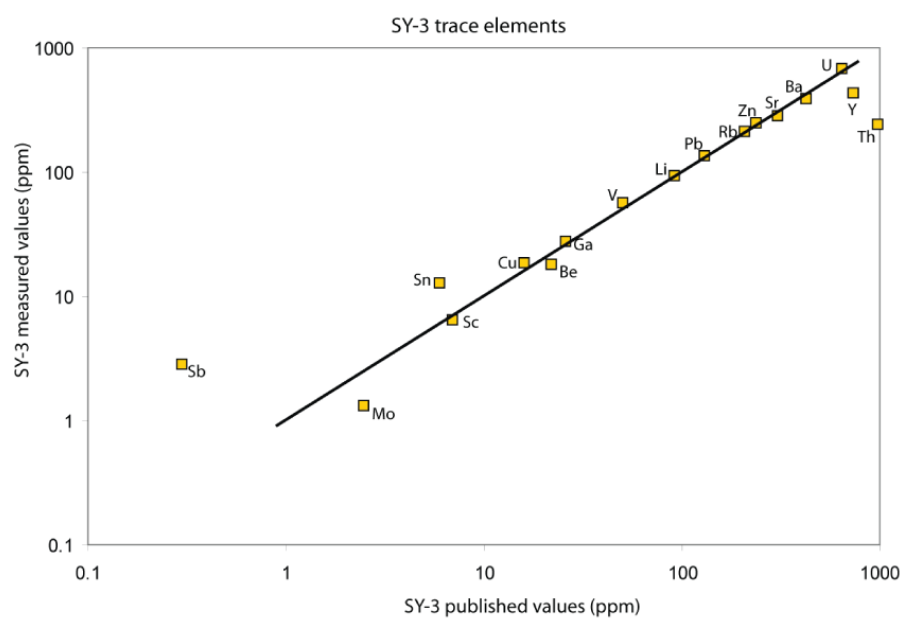
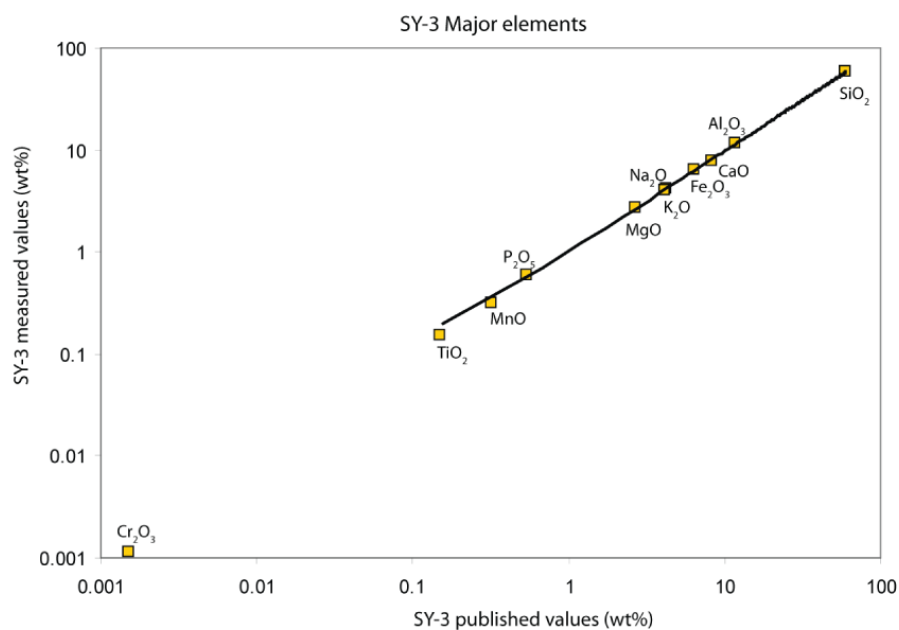
Detection limits for the range of elements analysed using the X Series ICP-MS at OMAC laboratories, Loughrea.

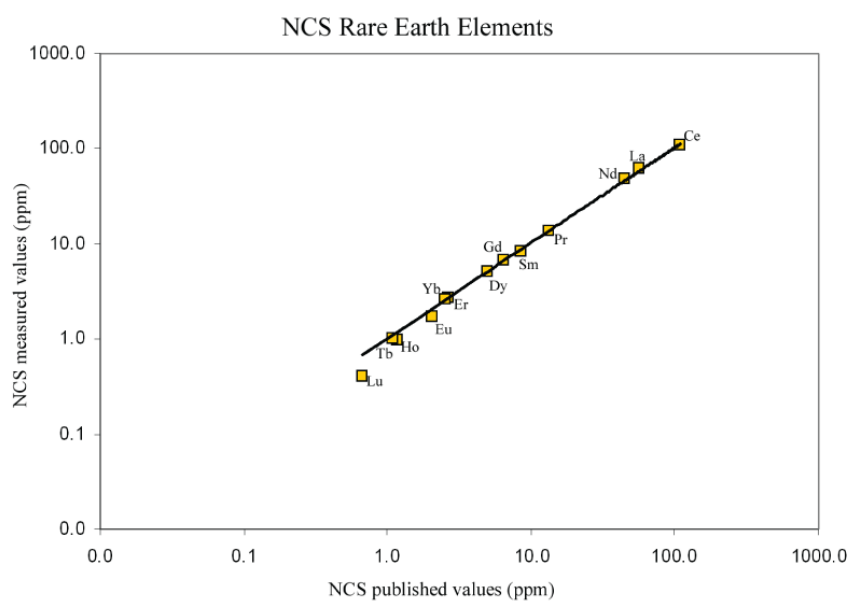
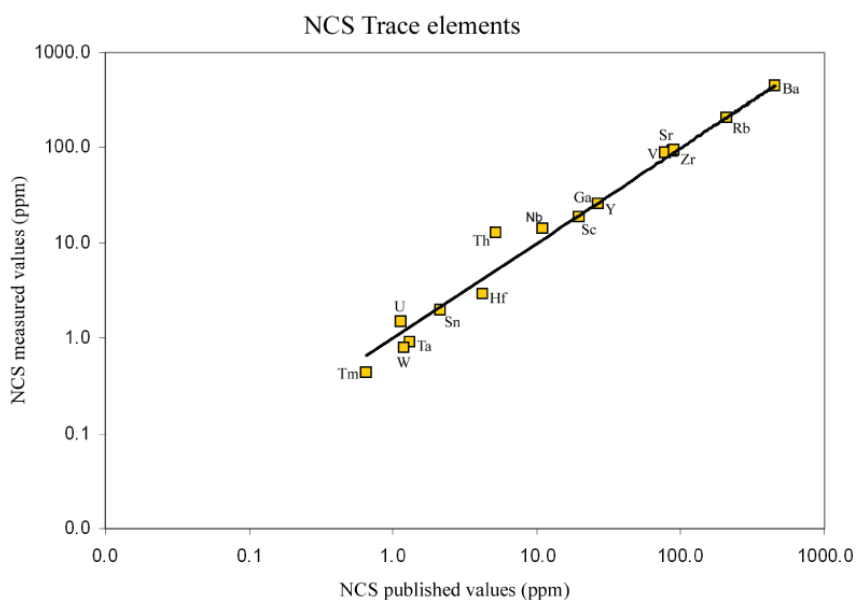
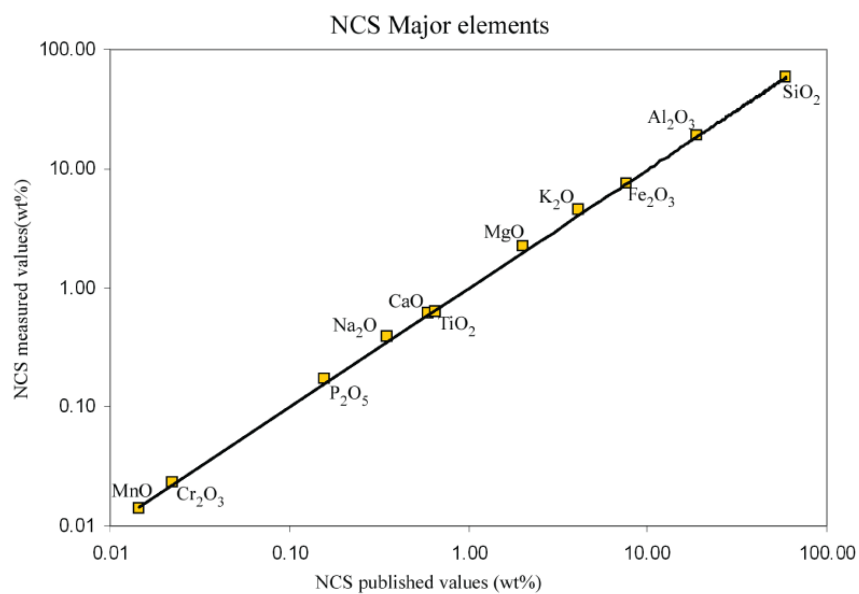
SAMPLE	SY4 (1)	SY3	SY4 (2)	NCS	TILL 4	SY4 (3)
1	▪	▪				
2	▪	▪				
3	▪	▪				
4					▪	
5			▪	▪		
6					▪	
7					▪	
8						▪
9					▪	
10					▪	
11					▪	
12	▪	▪				
13	▪	▪				
14	▪	▪				
15			▪	▪		
16	▪	▪				
17			▪	▪		
18	▪	▪				
19	▪	▪				
20			▪	▪		
21			▪	▪		
22			▪	▪		
23			▪	▪		
24						▪
25						▪
26						▪
27						▪
28						▪
29						▪
30						▪

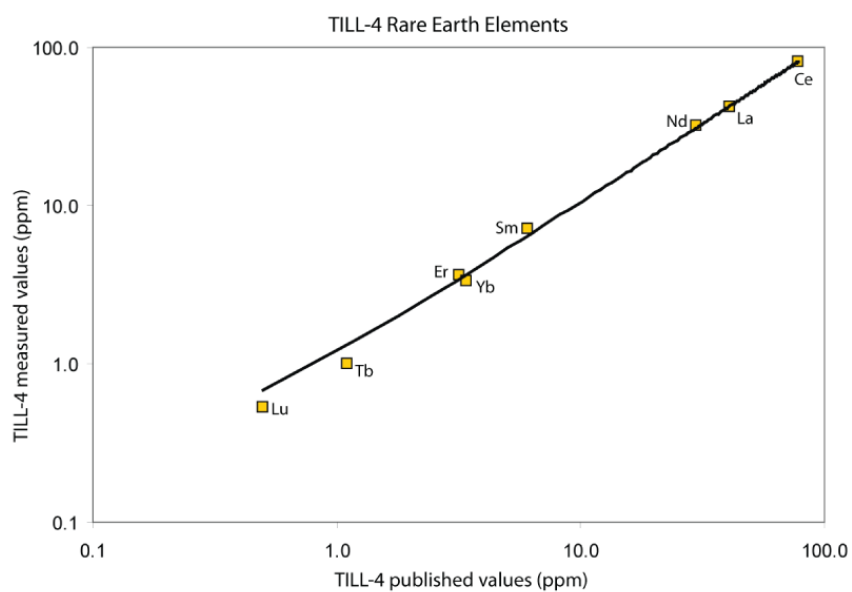
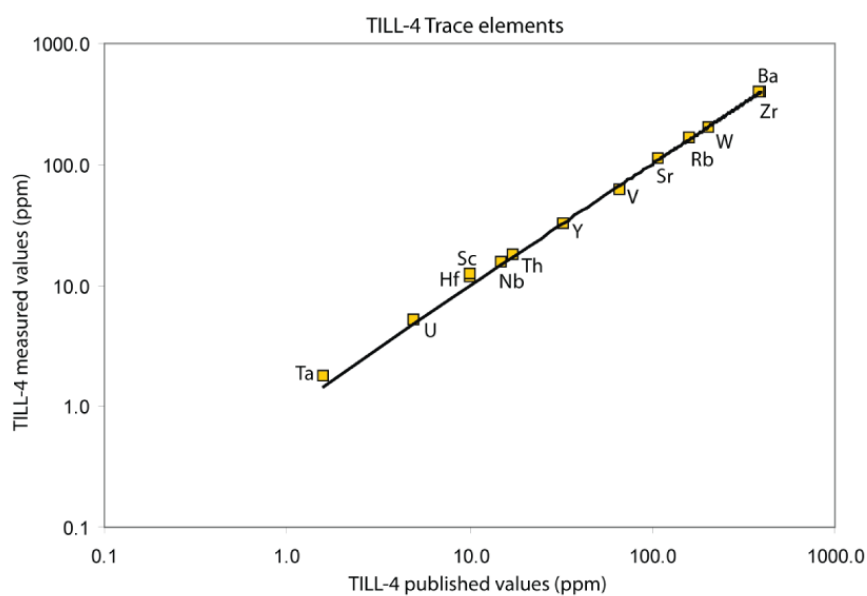
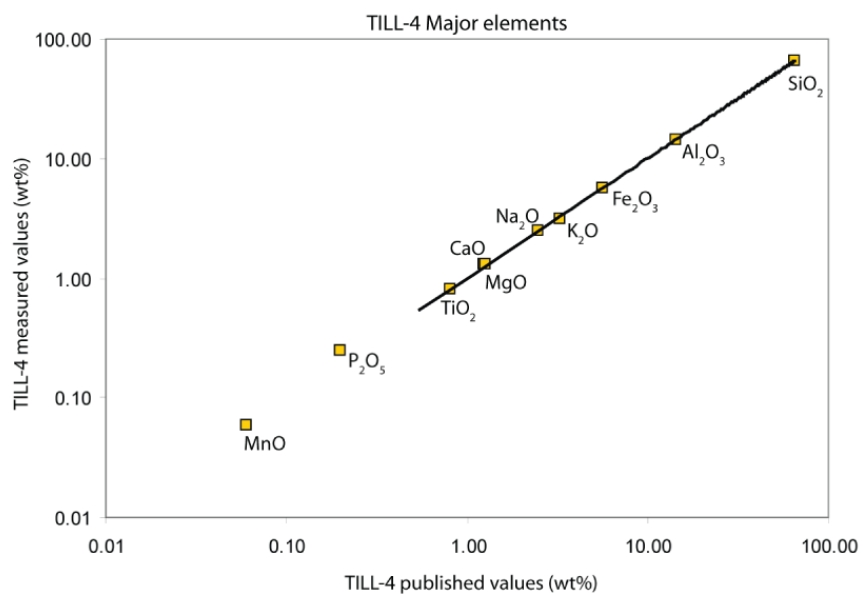
	SY4 (1)	SY3	SY4 (2)	NCS	TILL4	SY4 (3)
R ² (oxides)	0.999952	0.999977	0.999984	0.999958	0.99999	0.99999
R ² (trace)	0.964305	0.928572	0.99983	0.9995	0.99982	0.99998
R ² (REE)	0.998986	0.999354	1	0.99896	0.99989	0.99998

Table of certified reference materials (CRM) used for each sample during analysis and the R² value obtained for each of the CRM.









Whole rock compositions of volcanic and sedimentary rocks from south Waterford. Prefix B = Bunmahon Formation, C = Campile Formation. Second prefix corresponds to localities, where T = Trawnamoe, S = Stradbally Cove, BW = Ballydowane Bay, B = Bunmahon, KC = Kilmurrin Cove, KS = Kilfarrasy Strand, BN = Ballynaneen, K = Kill and C = Carrighalia. n.a. = not analysed, b.d. = below detection limit.

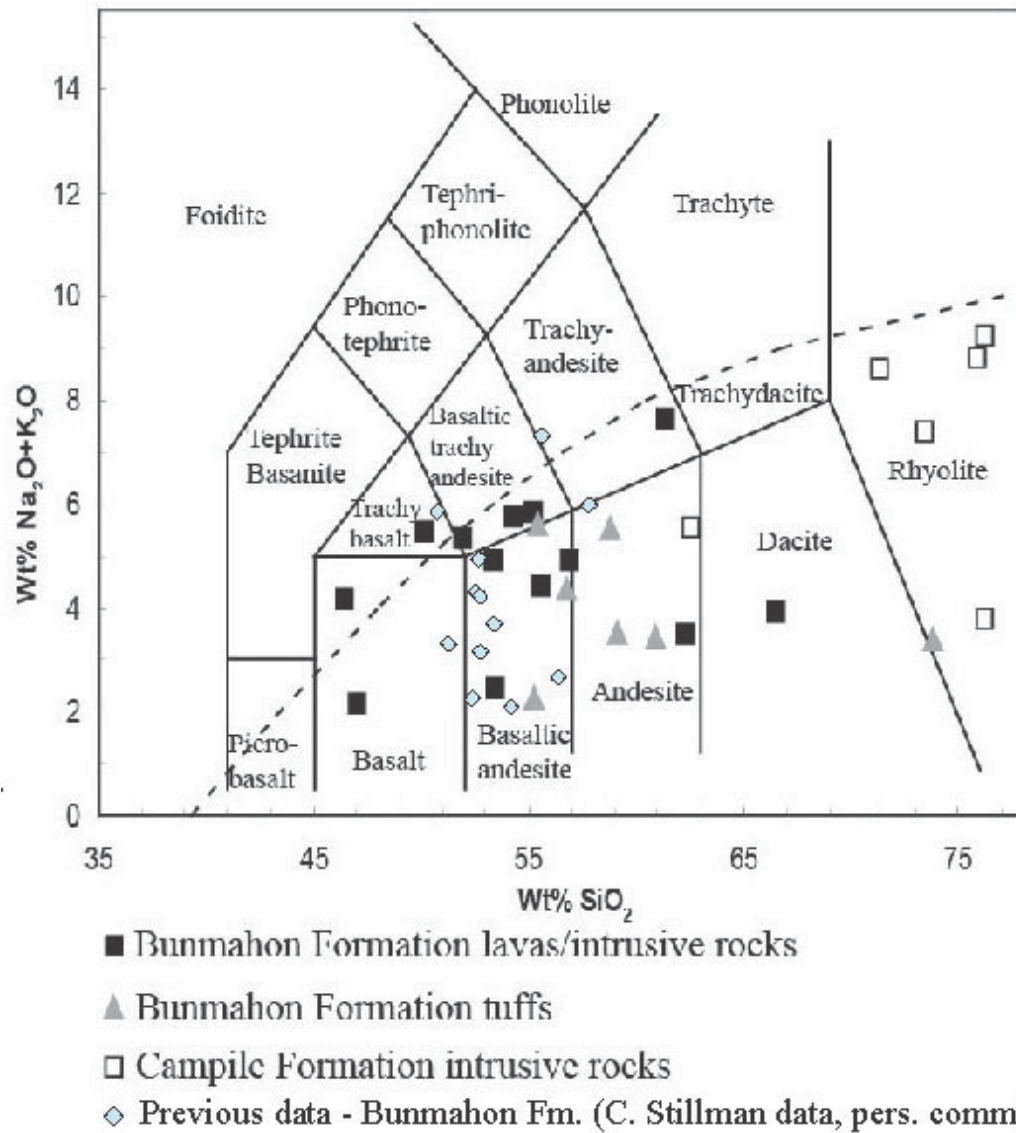
Sample	BT1	BT2	BT3	BT4	BT5	CT1
SiO₂	51.91	56.89	55.57	53.40	66.53	76.23
TiO₂	0.82	0.93	0.94	0.81	0.79	0.14
Al₂O₃	15.37	18.22	17.04	16.62	13.29	12.90
Fe₂O₃	8.62	9.71	9.04	8.07	8.48	1.40
MnO	0.15	0.16	0.15	0.12	0.11	0.02
MgO	8.22	5.40	7.12	9.66	5.30	0.76
CaO	4.49	4.70	6.33	0.32	0.51	0.09
Na₂O	3.24	4.28	3.11	4.60	3.55	3.53
K₂O	2.06	0.61	1.29	0.32	0.35	5.68
P₂O₅	0.12	0.11	0.15	0.10	0.29	b.d.
LOI	-	-	-	4.79	4.17	0.74
TOTAL	95.03	101.04	100.78	98.84	103.37	101.48
ppm						
Sr	255.19	191.3	245.28	25.3	51.9	40.0
Rb	47.57	17.65	36.56	9.3	11.0	101.7
Ba	439.64	92.15	230.37	20.5	52.3	894.4
Th	3.05	4.23	3.43	b.d.	5.0	6.0
Ta	2.34	4.72	4.32	0.5	1.7	1.8
Nb	5.2	6.63	10.2	2.0	12.4	11.1
Ce	18.17	16.36	22.16	11.5	93.7	101.3
Zr	79.29	80.75	91.99	67	303	346
Hf	n.a	n.a	n.a	2.0	7.0	8.0
Sm	3.03	2.81	3.27	2.1	10.9	11.5
Y	20.88	21.25	25.29	15.8	58.8	61.7
W	2.22	12.02	8.74	5.5	14.3	7.7
U	0.38	0.34	0.44	0.3	2.3	4.0
La	8.34	8.04	10.20	5.1	42.2	48.3
Pr	2.39	2.15	2.75	1.9	11.9	13.1
Nd	11.12	1030	12.97	7.3	46.7	49.7
Eu	0.95	0.89	1.17	0.9	2.6	1.7
Gd	3.36	3.36	4.03	2.5	10.6	11.3
Tb	0.6	0.55	0.65	0.6	2.0	2.0
Dy	3.76	3.94	4.38	2.7	10.6	10.9
Ho	0.76	0.74	0.9	0.8	2.3	2.4
Er	2.35	2.27	2.80	2.0	6.7	6.9
Tm	0.33	0.33	0.35	0.6	1.2	1.4
Yb	2.35	2.27	2.49	2.1	6.2	7.5
Lu	0.35	0.31	0.38	0.6	1.2	1.3

Sample	BT7	BT8	BT9	BT10	BS1	BS2
SiO₂	73.75	58.74	59.10	60.91	78.16	57.64
TiO₂	0.11	0.92	0.77	0.63	0.83	1.04
Al₂O₃	11.44	19.10	16.26	14.38	9.82	18.13
Fe₂O₃	5.08	9.77	11.63	7.20	8.32	9.74
MnO	0.08	0.12	0.18	0.15	0.10	0.22
MgO	2.92	5.52	6.04	4.85	1.19	3.70
CaO	0.78	1.29	0.36	6.06	0.00	0.18
Na₂O	1.91	2.48	0.79	2.48	1.63	0.93
K₂O	1.48	3.04	2.71	0.95	0.19	2.19
P₂O₅	0.02	0.15	0.02	0.06	0.11	0.10
LOI	-	-	5.00	4.28	-	-
TOTAL	97.57	101.16	102.89	102	100.39	93.91
ppm						
Sr	43.86	75.25	30.5	103.7	7.12	45.83
Rb	55.26	130.57	100.5	35.8	3.87	70.68
Ba	189.17	262.37	258.6	68.6	20.90	149.97
Th	4.46	5.95	3.0	2.0	79.96	5.65
Ta	4.6	5.38	0.8	0.7	69.2	4.8
Nb	9.98	9.44	5.8	22.6	61.09	13.04
Ce	61.34	25.88	34.4	26.3	6.41	38.25
Zr	70.64	110.16	103	68	173.52	130.28
Hf	n.a	n.a	3.0	3.0	n.a	n.a
Sm	6.34	3.65	3.5	3.6	0.42	1.99
Y	8.53	28.92	13.4	18.8	3.04	23.05
W	21.09	5.63	5.3	3.4	22.81	3.17
U	2.48	0.94	1.3	2.1	0.64	2.17
La	26.83	11.82	17.5	12.3	b.d.	16.6
Pr	6.82	2.99	4.4	3.6	0.18	2.08
Nd	27.62	13.66	15.5	13.9	1.02	9.54
Eu	1.25	1.11	0.8	1.4	0.11	0.53
Gd	4.29	4.01	3.0	3.3	0.55	2.59
Tb	0.39	0.69	0.7	0.7	0.12	0.39
Dy	1.57	4.97	2.8	3.6	0.76	2.86
Ho	0.24	0.96	0.80	1.0	0.14	0.53
Er	0.58	3.13	1.7	2.4	0.45	1.79
Tm	b.d.	0.44	0.5	0.6	b.d.	0.26
Yb	0.51	2.86	2.2	2.3	0.56	1.91
Lu	b.d.	0.42	0.6	0.6	b.d.	0.25

Sample	BS3	BS4	BS5	BS6	BS7	BS8
SiO₂	59.80	65.35	54.33	55.19	53.49	47.05
TiO₂	1.19	0.86	0.84	0.77	0.91	1.24
Al₂O₃	22.93	14.39	17.84	16.91	16.53	15.46
Fe₂O₃	8.25	8.89	8.70	6.94	13.00	10.18
MnO	0.07	0.065	0.14	0.095	0.154	0.136
MgO	2.66	2.74	7.46	5.35	6.83	9.42
CaO	0.14	0.12	3.20	1.88	0.17	5.26
Na₂O	0.68	0.47	5.44	5.36	1.67	1.60
K₂O	3.92	1.99	0.31	0.44	0.77	0.54
P₂O₅	0.12	0.14	0.13	0.15	0.15	0.18
LOI	-	3.65	3.87	3.31	4.93	8.70
TOTAL	99.78	98.67	102.3	96.43	98.61	99.79
ppm						
Sr	64.46	37.5	17.2	277.5	24.7	67.1
Rb	169.52	84.8	b.d.	8.5	33.0	17.8
Ba	535.92	229.7	94.5	115.4	80.2	94.7
Th	8.11	11.0	b.d.	1.0	2.0	2.8
Ta	3.04	1.2	0.3	0.2	0.3	0.3
Nb	15.6	15.1	b.d.	3.8	5.2	5.2
Ce	95.84	59.8	b.d.	16.9	22.6	92.1
Zr	161.43	154	79	85	87	84
Hf	n.a	5.0	b.d.	3.0	3.0	3.0
Sm	8.98	6.5	0.2	3.0	3.2	4.6
Y	37.69	29.1	b.d.	19.8	20.9	23.8
W	5.21	4.8	2.6	2.0	1.3	<0.5
U	4.59	3.7	b.d.	0.5	0.8	0.9
La	51.06	33.5	b.d.	7.7	11.1	59.1
Pr	11.24	8.1	0.3	2.6	3.1	9.0
Nd	44.90	27.6	b.d.	10.6	11.9	30.3
Eu	1.71	1.4	0.3	1.1	0.8	1.3
Gd	7.67	5.9	0.20	3.2	3.7	4.7
Tb	1.14	0.9	0.3	0.6	0.6	0.7
Dy	7.08	6.0	0.2	3.9	4.1	4.2
Ho	1.42	1.2	0.3	0.8	0.9	0.9
Er	4.20	3.4	0.2	2.2	2.4	2.6
Tm	0.58	0.5	0.3	0.3	0.4	0.4
Yb	4.01	3.2	0.2	2.2	2.2	2.3
Lu	0.57	0.5	0.3	0.3	0.4	0.4

Sample	BS9	BS10	BS11	BBW1	BB1	BB2
SiO₂	56.78	55.37	55.20	61.43	50.21	62.34
TiO₂	1.05	0.75	0.81	1.02	0.86	1.52
Al₂O₃	21.76	16.92	18.38	16.83	17.01	14.44
Fe₂O₃	6.14	8.24	9.10	5.36	8.69	10.05
MnO	0.056	0.100	0.162	0.07	0.143	0.088
MgO	3.04	6.03	5.53	5.29	4.87	4.66
CaO	0.08	0.24	0.44	1.08	7.00	0.17
Na₂O	0.94	5.36	0.94	7.40	4.62	0.16
K₂O	3.42	0.26	1.30	0.22	0.85	3.33
P₂O₅	0.10	0.12	0.14	0.66	0.14	0.07
LOI	4.86	4.44	5.46	3.00	6.50	4.18
TOTAL	98.26	97.88	97.53	102.36	100.91	101.08
ppm						
Sr	80.9	101.3	143.9	138.0	346.8	18.2
Rb	151.5	7.2	60.4	3.8	33.9	129.3
Ba	432.2	45.8	176.2	47.5	22.0	285.9
Th	16.0	2.0	2.0	5.0	3.2	3.0
Ta	1.6	0.2	0.3	2.4	0.4	0.6
Nb	21.7	3.8	4.8	22.6	5.8	10.4
Ce	103.7	17.1	23.6	136.3	51.0	36.2
Zr	180	76	80	362	88	101
Hf	6.0	6.0	2.0	7.0	3.0	3.0
Sm	10.1	2.7	4.4	7.9	3.6	3.3
Y	34.6	16.6	27.0	14.2	18.2	18.9
W	3.4	4.8	1.2	2.4	0.7	2.4
U	3.7	0.5	0.5	1.6	0.5	1.4
La	50.3	8.3	11.5	70.6	29.8	19.5
Pr	13.1	2.6	3.7	15.1	5.4	4.4
Nd	45.6	9.8	14.9	16.1	19.2	16.8
Eu	2.1	0.7	1.2	2.2	1.1	1.1
Gd	8.4	2.7	4.6	5.7	3.4	3.3
Tb	1.2	0.4	0.8	0.9	0.5	0.5
Dy	7.7	2.9	5.2	3.4	3.2	3.3
Ho	1.5	0.7	1.1	0.8	0.7	0.7
Er	4.3	1.9	3.1	1.6	1.9	2.1
Tm	0.5	0.3	0.4	0.5	0.3	0.3
Yb	3.8	1.9	2.7	1.2	1.7	2.1
Lu	0.6	0.3	0.4	0.4	0.3	0.3

Sample	BKC1	CKS1	CBN1	CBN2	CK1	CC1
SiO₂	46.48	76.22	75.87	71.36	73.42	62.56
TiO₂	1.50	0.14	0.22	0.32	0.13	0.58
Al₂O₃	16.71	10.90	12.69	13.54	11.30	16.09
Fe₂O₃	10.27	1.81	1.86	2.05	1.79	6.18
MnO	0.274	0.05	0.06	0.062	0.057	0.092
MgO	8.77	1.10	1.33	1.49	1.99	5.12
CaO	4.05	1.74	0.12	0.13	0.06	2.00
Na₂O	2.20	1.09	2.89	3.37	0.80	5.16
K₂O	1.96	2.67	5.91	5.24	6.55	0.36
P₂O₅	0.16	0.03	0.03	0.05	0.05	0.13
LOI	8.88	3.80	0.94	1.04	1.57	3.33
TOTAL	101.28	99.55	101.91	101.61	97.72	101.61
ppm						
Sr	51.4	40.8	73.6	105.4	42.2	198.3
Rb	73.0	87.7	148.2	147.7	165.7	12.8
Ba	223.5	126.1	892.3	784.4	559.9	99.6
Th	1.3	12.7	6.0	16.2	15.3	2.4
Ta	0.3	1.1	1.5	1.0	1.4	0.4
Nb	5.8	13.9	6.6	7.6	17.3	5.0
Ce	21.7	117.0	45.9	49.0	72.6	35.2
Zr	92	270	86	92	166	91
Hf	3.0	8.0	3.0	3.0	6	3
Sm	3.1	11.5	3.7	3.3	6.0	2.7
Y	23.5	62.9	18.4	20.5	33.4	18.1
W	2.2	0.7	7.7	2.9	1.9	b.d.
U	0.3	3.3	3.5	4.2	2.8	0.6
La	10.7	57.1	25.1	26.9	33.6	20.8
Pr	2.9	14.1	5.1	5.2	8.4	3.9
Nd	12.2	53.5	16.1	17.5	29.9	14.0
Eu	0.9	1.3	0.7	0.5	0.7	0.8
Gd	3.6	11.0	3.0	3.3	5.4	3.0
Tb	0.7	1.8	0.8	0.6	0.9	0.5
Dy	4.3	10.6	3.4	3.3	6.0	2.9
Ho	0.9	2.3	0.9	0.7	1.2	0.6
Er	2.6	6.7	2.2	2.2	3.8	1.9
Tm	0.4	1.0	0.6	0.3	0.6	0.3
Yb	2.4	6.4	2.4	2.1	3.7	1.8
Lu	0.4	0.9	0.6	0.3	0.6	0.3



Total alkalis vs. silica diagram (discussion in Chapter Four), showing the comparison between the authors own samples and analysed data and previously published results of the Bunmahon Formation. Compositions from the Bunmahon Formation are predominantly basaltic andesite.

Europium anomaly (Eu/Eu*) calculated for volcanic rocks where $Eu^* = \sqrt{Sm/Gd}$.

Sample	S5	S6	S7	S8	S9	S10	S11	T1	T2	T3	T4	T5	T6
Eu/Eu*	3.28	1.09	0.66	0.85	0.70	0.73	0.81	0.91	0.88	0.99	1.17	0.74	0.45

Sample	T7	T8	T9	T10	OL1	OL2	OL3	OL4	OL5	OL6	OL7	OL8	OL9
Eu/Eu*	0.74	0.89	0.80	1.26	0.99	0.69	0.86	0.36	0.94	1.04	0.86	0.38	0.47

Measure of LREE to HREE calculated as the normalised Lanthanum/Ytterbium (La_N/Yb_N) ratio.

Sample	S5	S6	S7	S8	S9	S10	S11	T1	T2	T3	T4	T5	T6
La_N/Yb_N		2.5	3.6	18.7	9.4	3.1	3.0	2.5	2.5	2.9	1.7	4.8	4.6
	NA	2	4	5	8	8	2	5	4	4	8	9	1

Sample	T7	T8	T9	T10	OL1	OL2	OL3	OL4	OL5	OL6	OL7	OL8	OL9
La_N/Yb_N	37.70	2.96	5.70	3.81	41.90	7.63	8.10	6.44	12.70	6.61	3.21	6.45	9.29

Appendix A6

Microthermometric results

T16

	Sample	Area total μm^2	Area vap μm^2	Area liq μm^2	Degree of Fill (F)	Length μm	T _{FM} °C	T _{LM} °C	T _H °C	Salinity eq %wt NaCl
1	T16-01	100.63	8	92.63	0.92	14.2	-29.1	-8.7	135	12.51
2	T16-02	22.25	4.44	17.81	0.80	9			167	
3	T16-03.1	288	22	266	0.92	15.2			117	
4	T16-03.2	558	44	514	0.92	17	-29.5	-10.4	142	14.36
5	T16-04	29.97	4.2	25.77	0.86	10.2			138	
6	T16-05	35.52	4.45	31.07	0.87	8.9		-8		11.7

T17

	Sample	Area total μm^2	Area vap μm^2	Area liq μm^2	Degree of Fill (F)	Length μm	T _{FM} °C	T _{LM} °C	T _H °C	Salinity eq %wt NaCl
7	T17-01.1	46.01	4.44	41.57	0.90	9.61			145	
8	T17-01.2	54.76	5.97	48.79	0.89	9.1		-7.8	147.6	11.46
9	T17-02.1	34.29	6.28	28.01	0.82	8.2			159	
10	T17-02.2	17.22	2.69	14.53	0.84	5.3		-9.7	119.3	13.62
11	T17-02.3	76.62	8.83	67.79	0.88	12.9	-24.6		157	
12	T17-02.4	25.3	2.47	22.83	0.90	6			148	
13	T17-03.1	28.31	4.31	24	0.85	7.5	-26.8		148	
14	T17-03.2	29.63	3.72	25.91	0.87	6.5		-11.2	157.6	15.17
15	T17-04.2	54.65	4.34	50.31	0.92	12.6			139	
16	T17-04.3	13.89	1.05	12.84	0.92	3.8			140	
17	T17-04.4	16.06	1.12	14.94	0.93	6.4	-28.3		123	
18	T17-04.5	39.79	3.94	35.85	0.90	11.3	-25	-11.5	140	15.47
19	T17-05.1	70.33	5.27	65.06	0.93	12.6	-32.7		135.3	
20	T17-05.2	29.43	3.52	25.91	0.88	7.87	-24	-10.3	151	14.25
21	T17-05.3	38.1	2.41	35.69	0.94	10.91	-26.9		107.4	
22	T17-06	17.16	2.18	14.98	0.87	6.5	-28.2	-10.6	157	14.57
23	T17-07.1	16.01	1.32	14.69	0.92	9.2			146.3	
24	T17-07.2	27.44	2.98	24.46	0.89	6.66	-25.2	-7.2	148.2	10.73
25	T17-08.1	40.1	6	34.1	0.85	10.8			168.6	
26	T17-08.2	23.56	2.83	20.73	0.88	7.57			161	
27	T17-08.3	14.91	2.01	12.9	0.87	7.1	-28.6		127.7	
28	T17-09.1	5.29	0.5	4.79	0.91	4.42			129.9	
29	T17-09.2	3.37	0.5	2.87	0.85	4.4			136.4	
30	T17-09.3	22.12	5.9	16.22	0.73	6.9	-27.8		170.1	
31	T17-10.1	22.27	3.17	19.1	0.86	5.8	-32.9		129	
32	T17-10.2	20.7	2.82	17.88	0.86	7.7			150.1	
33	T17-10.3	18.12	3	15.12	0.83	5.6	-30		135.8	
34	T17-10.4	23.14	3.44	19.7	0.85	7.2			134.2	
35	T17-10.5	16.7	2.9	13.8	0.83	5.3			142.6	
36	T17-11	24.61	3	21.61	0.88	7.4	-33.2		166.2	
37	T17-12.1	25.35	3.34	22.01	0.87	11.1			115	
38	T17-12.2	11.79	1.39	10.4	0.88	7.3	-28			
39	T17-12.3	34.4	2.3	32.1	0.93	11.1			152.9	
40	T17-13.1	10.97	1.99	8.98	0.82	5.8			182.2	
41	T17-13.2	14.63	2.61	12.02	0.82	5.6			172.3	
42	T17-13.3	13.2	1.42	11.78	0.89	7.5			169.5	
43	T17-14	14.72	2.08	12.64	0.86	6.8			157.5	
44	T17-15.1	57.4	4.25	53.15	0.93	8.9			174.5	
45	T17-15.2	17.86	4	13.86	0.78	5.6	-29.7		170	
46	T17-15.3	88.34	10.2	78.14	0.88	13	-33			
47	T17-16.1	20.55	2.98	17.57	0.85	8.3			173	
48	T17-16.2	12.41	2	10.41	0.84	4.8			183	
49	T17-16.3	14.6	1.5	13.1	0.90	6			177	

T20

	Sample	Area total μm ²	Area vap μm ²	Area liq μm ²	Degree of Fill (F)	Length μm	T _{FM} °C	T _{LM} °C	T _H °C	Salinity eq %wt NaCl
50	T20-01.1	4.19	0.43	3.76	0.90	3.6			143	
51	T20-01.2	8.47	0.74	7.73	0.91	3.2	-28		177	
52	T20-02.1	42.12	3.44	38.68	0.92	8.7	-26.9		148	
53	T20-02.2	22.05	2.93	19.12	0.87	6		-9	155	12.85
54	T20-02.3	43.75	3.98	39.77	0.91	8.3	-26.1	-8.6	152	12.39
55	T20-02.4	14.48	2	12.48	0.86	4.8	-26			
56	T20-03	28.13	2.65	25.48	0.91	7.5		-9.4	174	13.29
57	T20-04.1	21.24	2.73	18.51	0.87	5.6			176.2	
58	T20-04.2	14.93	2.05	12.88	0.86	5.9			237.8	
59	T20-04.3	29.37	3.59	25.78	0.88	9.9	-26.8			
60	T20-05.1	94.75	6.87	87.88	0.93	18.7	-29.5	-10.5	162	14.46
61	T20-05.2	36.12	4.19	31.93	0.88	11.1		-10		13.94
62	T20-05.3	141.4	10.59	130.81	0.93	19.9			196	
63	T20-05.4	61.09	7.12	53.97	0.88	12		-9		12.85
64	T20-05.5	57.62	6.96	50.66	0.88	9.8	-27.8	-10.3	208	14.25
65	T20-06.1	25.37	2.12	23.25	0.92	6.7		-11.8	139	15.76
66	T20-06.2	49.6	4.5	45.1	0.91	13.5			173.5	
67	T20-06.3	43.68	2.85	40.83	0.93	9.7	-28.5	-10		13.94
68	T20-06.4	23.03	2	21.03	0.91	9.4			151	
69	T20-06.5	33.2	2.8	30.4	0.92	11.2			158	
70	T20-07.1	63.79	4.88	58.91	0.92	11.1	-25	-10.3	183	14.25
71	T20-07.2	26.99	3.18	23.81	0.88	7.17			213	
72	T20-07.3	38.91	2.19	36.72	0.94	8.6			127	
73	T20-07.4	37.79	2.89	34.9	0.92	9.8			153	
74	T20-08.1	78.52	8.91	69.61	0.89	12.13	-27	-10.4	141	14.36
75	T20-08.2	34.99	4.81	30.18	0.86	11.1	-29.3	-11	167	14.97
76	T20-08.3	9.32	1.43	7.89	0.85	7		-10	146.7	13.94
77	T20-08.4	21.11	2.18	18.93	0.90	7.13			132	
78	T20-09	20.78	3.85	16.93	0.81	6.5	-29.1		220	
79	T20-10.1	36.34	3.38	32.96	0.91	7.7			242.1	
80	T20-10.2	57.05	4.42	52.63	0.92	14		-10.2	181	14.15
81	T20-10.3	48.29	5.87	42.42	0.88	10.2		-9.1		12.96
82	T20-11.1	40.21	2.94	37.27	0.93	10.1			173	
83	T2011.2	36.99	3.25	33.74	0.91	9.4		-8	165	11.7
84	T20-11.3	45.83	2.97	42.86	0.94	11.8	-27.8	-6.2	193.4	9.452
85	T20-11.4	18.09	3.47	14.62	0.81	6.8			183.5	
86	T20-12.1	30.06	4.19	25.87	0.86	8.4		-8.3	195.1	12.05
87	T20-12.2	31.45	3.42	28.03	0.89	7			184	
88	T20-12.3	18.52	2.18	16.34	0.88	5.8		-9.8	145	13.72
89	T20-12.4	12.83	0.95	11.88	0.93	6.3		-5.4	138	8.375
90	T20-12.5	57.32	6.07	51.25	0.89	6.6			241.9	
91	T20-13.1	19.54	2.52	17.02	0.87	7.7		-8.5	222.6	12.28
92	T20-13.3	15.58	1.97	13.61	0.87	7.2			148	
93	T20-13.4	17.35	3.29	14.06	0.81	6.7	-28.2	-9.5	169.8	13.4
94	T20-14.1	40.05	4.75	35.3	0.88	6.8	-25.6	-9.1	151	12.96
95	T20-14.2	53.54	4.98	48.56	0.91	13.4			186	
96	T20-14.3	68.83	5.7	63.13	0.92	11.3	-32	-11.2	191.6	15.17
97	T20-15.2	19	1.6	17.4	0.92	4.6			167	
98	T20-15.3	21.89	3.33	18.56	0.85	4.6			168.1	
99	T20-15.4	9.23	1.13	8.1	0.88	3.2			179.4	
100	T20-17.1	26.05	4.44	21.61	0.83	9.9			234	
101	T20-19	41.81	4.55	37.26	0.89	11			154.3	
102	T20-20.1	20.87	3.75	17.12	0.82	6.9	-25.3		150	
103	T20-20.2	10.9	0.5	10.4	0.95	7.32			152.3	
104	T20-20.3	18.43	1.71	16.72	0.91	7.5			136	
105	T20-21	17.48	3.82	13.66	0.78	7	-24.8	-11.8	162.8	15.76
106	T20-22.1	51.99	3.21	48.78	0.94	13.5		-13.6	111.4	17.43
107	T20-22.2	38.72	3.34	35.38	0.91	10.45			149.7	
108	T20-22.3	16.61	2.02	14.59	0.88	8			155	
109	T20-22.4	7.86	1.2	6.66	0.85	4.4			158	

110	T20-23.1	13.13	1.52	11.61	0.88	6.3			148.6	
111	T20-23.2	25.75	8.3	17.45	0.68	10.2			157.1	
112	T20-23.3	17.43	3.11	14.32	0.82	10.3			157.5	

T22

	Sample	Area total μm^2	Area vap μm^2	Area liq μm^2	Degree of Fill (F)	Length μm	T _{FM} °C	T _{LM} °C	T _H °C	Salinity eq %wt NaCl
113	T22-01.1	48.99	3.1	45.89	0.94	12.9			127	
114	T22-01.2	23.75	1	22.75	0.96	8.6			130	
115	T22-2.1	38.42	1.5	36.92	0.96	12			108	
116	T22-02.2	16.56	0.75	15.81	0.95	5.6			132	
117	T22-04.1	18.66	2	16.66	0.89	4.5			152	
118	T22-04.2	22.34	2.8	19.54	0.87	8.7			138.9	
119	T22-04.3	21.41	1.3	20.11	0.94	5.5			126	
120	T22-05.1	26.98	1.5	25.48	0.94	9.5			109	
121	T22-05.2	10.66	1.87	8.79	0.82	10.5			115	
122	T22-05.3	14.6	1	13.6	0.93	5			144.9	
123	T22-06.1	20.91	2	18.91	0.90	6.3			161.9	
124	T22-06.2	22.92	1.3	21.62	0.94	7.7			141.5	
125	T22-06.3	70.75	5.6	65.15	0.92	13.4	-28.8			
126	T22-06.4	29.46	2.7	26.76	0.91	6	-26.7	-9	133	12.85
127	T22-07	26.39	4.32	22.07	0.84	8.19		-8	129.3	11.7
128	T22-08.1	27	2.7	24.3	0.90	6.7	-31		141.6	
129	T22-08.2	15.18	1.3	13.88	0.91	8.8	-30		141.4	
130	T22-08.3	88.83	5.5	83.33	0.94	14			159.4	
131	T22-09.1	17.5	2.8	14.7	0.84	7.1	-26	-7.7	182.2	11.34
132	T22-09.2	8.12	0.2	7.92	0.98	3.2		-11.1	153.4	15.07
133	T22-09.3	9.44	1.38	8.06	0.85	4.8			147.4	
134	T22-09.4	15.35	2	13.35	0.87	6			166.8	
135	T22-09.5	20.85	2.5	18.35	0.88	8			184.7	
136	T22-10.1	47.42	6.23	41.19	0.87	14			163.2	
137	T22-10.2	8.84	0.6	8.24	0.93	3.2			184.7	
138	T22-10.3	12.55	1.3	11.25	0.90	5.5			153	
139	T22-10.4	17.52	2.7	14.82	0.85	7.7			154.2	
140	T22-10.5	19.5	1.98	17.52	0.90	9.9			126	
141	T22-10.6	48.11	3.21	44.9	0.93	9.5			121	
142	T22-10.7	11.92	0.6	11.32	0.95	5.4		-12.5		16.43
143	T22-10.8	36.96	2.5	34.46	0.93	10.7			130	
144	T22-11.1	6.72	0.2	6.52	0.97	3.5			160.7	
145	T22-11.2	30.55	2.6	27.95	0.91	10.25	-28.9		134	
146	T22-11.3	34.09	4.4	29.69	0.87	9.2			137	
147	T22-11.4	25.93	3	22.93	0.88	7.6	-26.4		151.3	
148	T22-11.5	26	2.9	23.1	0.89	8.3			145.8	
149	T22-11.6	12.36	1.3	11.06	0.89	6			136.2	
150	T22-11.7	13.77	2.7	9.66	0.78	8.7			130	
151	T22-11.8	30.62	1.97	11.8	0.86	5.6			215.9	
152	T22-11.9	24.82	2.5	28.12	0.92	9.7			138	
153	T22-12.1	46.22	3.27	21.55	0.87	8.8			155.4	
154	T22-12.2	16.73	5.5	40.72	0.88	9.3			155.3	
155	T22-12.3	10.77	1.4	15.33	0.92	7.5			117	
156	T22-12.4	52.67	2.3	8.47	0.79	5.8			112.9	
157	T22-13.1	31.22	7.15	45.52	0.86	11.9			118	
158	T22-13.2	12.27	4.4	26.82	0.86	9.3			155.6	
159	T22-14	15.08	1.6	10.67	0.87	5.1			160.5	
160	T22-15	13.5	2.25	12.83	0.85	7.3			165	
161	T22-16.1	21.47	2.41	11.09	0.82	10.55			168.4	
162	T22-16.2	12.5	3.59	17.88	0.83	8.4			138.6	
163	T22-16.3	20.84	2	10.5	0.84	4.6			183	
164	T22-16.4	34.25	3.3	17.54	0.84	8.2			183.2	
165	T22-16.5	16.34	4.47	29.78	0.87	9.25			157.1	
166	T22-17.1	12.53	3.5	12.84	0.79	5.3			139.9	
167	T22-17.2	11.38	1.6	10.93	0.87	5.9			111.1	

168	T22-17.3	11.38	2.8	8.58	0.75	4.6			153.1	
169	T22-17.4	32.7	3.13	29.57	0.90	9.2			106.8	
170	T22-18.1	48.15	4.74	43.41	0.90	8.6	-28		133	
171	T22-18.2	44.92	3.35	41.57	0.93	11.5			134	
172	T22-18.3	42.66	4.17	38.49	0.90	12.7		-11.6		15.57
173	T22-18.4	93.34	8.48	84.86	0.91	10.9	-26		132.6	
174	T22-18.5	20.83	1.8	19.03	0.91	9.5		-8.7		12.51
175	T22-18.6	32.09	2.78	29.31	0.91	7.8	-23.6		114.6	
176	T22-19.1	64.78	4.6	60.18	0.93	11.3			133.9	
177	T22-19.2	6.76	0.5	6.26	0.93	3.9			154.8	
178	T22-20.1	34.72	2.8	31.92	0.92	9.7	-29.5	-11.5	138.1	15.47
179	T22-20.2	29.95	4.7	25.25	0.84	6.9	-30.2	-10.3	166.5	14.25
180	T22-20.3	18.79	2.4	16.39	0.87	7.8			140	
181	T22-20.4	40.91	4.3	36.61	0.89	15		-8.5	148.1	12.28
182	T22-20.5	19.19	1.8	17.39	0.91	7.3			104.4	
183	T22-20.6	11.09	1.08	10.01	0.90	5.7			165	
184	T22-21.1	110.42	8.7	101.72	0.92	16.2	-29		151.7	
185	T22-21.2	53.28	6.44	46.84	0.88	15	-31	-9.7	136.8	13.62
186	T22-21.3	31.93	4.03	27.9	0.87	9.6			152	
187	T22-21.4	36.56	3.25	33.31	0.91	10.1			160.1	
188	T22-21.5	9.6	1.3	8.3	0.86	4.9			170.3	
189	T22-22.2	34.29	5.4	28.89	0.84	14.4			164	
190	T22-22.2	19.15	1	18.15	0.95	6.1			159	
191	T22-22.3	28.14	3.23	24.91	0.89	11			122	
192	T22-22.4	15.08	1.5	13.58	0.90	6.8			153.4	
193	T22-22.5	20.93	2.26	18.67	0.89	9.9			156.7	

T24

	Sample	Area total μm^2	Area vap μm^2	Area liq μm^2	Degree of Fill (F)	Length μm	T _{FM} °C	T _{LM} °C	T _H °C	Salinity eq %wt NaCl
194	T24-02.2	4.7	0.2	4.5	0.96	2.9			154.8	
195	T24-02.2	3.58	0.1	3.48	0.97	3.4			129.5	
196	T24-03.1	12.27	2.2	10.07	0.82	8			171.5	
197	T24-03.2	6.07	0.5	5.57	0.92	4.8			161.8	
198	T24-03.3	5.3	0.5	4.8	0.91	5.1			169.2	
199	T24-03.4	9.7	0.5	9.2	0.95	4.1			176	
200	T24-04	16.15	2.4	13.75	0.85	5.8			154.1	
201	T24-05	19.54	0.6	18.94	0.97	7			154	
202	T24-06					4.2			164.6	
203	T24-07.1					6.5			183.6	
204	T24-07.2					4.6			210	
205	T24-07.3					3.6			181.4	
206	T24-07.4					5.2			177.1	
207	T24-09					4.9			219.4	

T26

	Sample	Area total μm^2	Area vap μm^2	Area liq μm^2	Degree of Fill (F)	Length μm	T _{FM} °C	T _{LM} °C	T _H °C	Salinity eq %wt NaCl
208	T26-01.1	86.67	8.45	78.22	0.90	25.4	-32		173.1	
209	T26-01.2	12.26	2.1	10.16	0.83	6.8			155.7	
210	T26-02.1	23.08	4	19.08	0.83	8.7			169	
211	T26-02.2	12.72	1.84	10.88	0.86	4.4		-13.2	134	17.08
212	T26-02.3	29.04	2.46	26.58	0.92	8.9	-34.6		170.2	
213	T26-02.4	6.78	0.5	6.28	0.93	4.8			152.5	
214	T26-03.1	38.48	5.68	32.8	0.85	10.1	-33			
215	T26-04.1	29.39	3.61	25.78	0.88	8.1			143.6	
216	T26-05.1	33.48	3.53	29.95	0.89	8.9			138.1	
217	T26-05.2	32.24	2.3	29.94	0.93	8.9			130.3	
218	T26-06.1	47.01	6	41.01	0.87	9.5			141.9	

219	T26-06.2	153.16	10.29	142.87	0.93	21.5			130	
220	T26-06.3	29.44	3	26.44	0.90	8.65			149.3	
221	T26-07.1	132.01	7.63	124.38	0.94	22.04	-30	-15.5	126	19.05
222	T26-07.2	65.12	5.77	59.35	0.91	10.6	-32.3	-12.3	130.4	16.24
223	T26-08.1	87.96	7.8	80.16	0.91	13.3	-34	-16.9	129.3	20.15
224	T26-08.2	42.76	6.63	36.13	0.84	8.7	-35		148.9	
225	T26-11	23.35	1.3	22.05	0.94	7			128.6	

S17

	Sample	Area total μm ²	Area vap μm ²	Area liq μm ²	Degree of Fill (F)	Length μm	T _{FM} °C	T _{LM} °C	T _H °C	Salinity eq %wt NaCl
226	S17-01.1	71.14	12.01	59.13	0.83	8.44	-26	-15	191.9	18.63
227	S17-01.2	22.32	3.7	18.62	0.83	6.26	-26	-7.4	188.3	10.978
228	S17-05	22.43	3.6	18.83	0.84	5.14	-21.6	-8.5	181.9	12.28
229	S17-08	59.45	12.06	47.39	0.80	9.9	-25.8	-12.5	197.8	16.43
230	S17-09	60.09	8.83	51.26	0.85	12.87	-30.9	-11.1	199.5	15.07
231	S17-11.1	20.81	4.27	16.54	0.79				206.4	
232	S17-12.2	55.69	8.3	47.39	0.85				148	
233	S17-13.1	74.32	5.02	69.3	0.93		-32.9	-8	198	11.7
234	S17-13.2	120.32	10.49	109.83	0.91				194	
235	S17-13.3	27.55	4.69	22.86	0.83				198	
236	S17-15.1	43.63	5.07	38.56	0.88			-9.7	176.2	13.62
237	S17-15.2	22.58	2.84	19.74	0.87		-29.1	-10.2	195.1	14.15
238	S17-16.1	30.96	4.42	26.54	0.86			-9.8		13.72
239	S17-16.2	40.95	3.56	37.39	0.91		-28.3	-7.8	199.8	11.46
240	S17-18	74.3	13.3	61	0.82				184	
241	S17-19.1	65.65	6.09	59.56	0.91	12.2			185	
242	S17-19.2	19.02	2	17.02	0.89			-9.4	209.8	13.29
243	S17-19.3	43.64	3.67	39.97	0.92		-25.8	-4.9	183.3	7.677
244	S17-22.3	82.08	6.24	75.84	0.92	15.6			240	
245	S17-23.1	78.11	7.45	70.66	0.90	13.1	-33.8			
246	S17-23.2	69.5	7.94	61.56	0.89	12.4	-26		195.8	
247	S17-24.1	154.4	11.81	142.59	0.92	17.92	-29.5		205	
248	S17-24.2	59.07	5.87	53.2	0.90	15	-33.4		236.5	
249	S17-25.1	59.27	6.16	53.11	0.90	14.2	-31.2			
250	S17-26.1	108.77	14.71	94.06	0.86	13.9	-37.4		199	
251	S17-26.2	55.38	6.55	48.83	0.88	10.25	-33.7	-8.3	211.6	12.05
252	S17-27.1	91.46	9.12	82.34	0.90	12.5		-7		10.481
253	S17-27.2	23.31	2.7	20.61	0.88	11.69	-29.5		226	
254	S17-29.1	45.97	5.1	40.87	0.89	10.8			204	
255	S17-30.1	30.36	3.75	26.61	0.88				229	
256	S17-30.2	23.89	3.75	20.14	0.84	6.7	-29.8	-9.7	193	13.62
257	S17-31.1	90.35	10.44	79.91	0.88	13.5	-28.5		180	
258	S17-31.2	104.81	11.65	93.16	0.89	15.7	-24.3	-15.4	219	18.96
259	S17-31.3	103.05	16.95	86.1	0.84		-28.1		164.7	
260	S17-33.1	24.11	4.9	19.21	0.80	8.3			170	
261	S17-33.2	120.88	10.17	110.71	0.92	15.3	-39.2	-8.4	200.7	12.16
262	S17-34.1	49.77	2.33	47.44	0.95	13	-37.1		197	
263	S17-34.2	57.72	8.26	49.46	0.86	13.5	-34.4	-11.5	230	15.47
264	S17-35.1	119.79	8.21	111.58	0.93	20.9	-36.6	-12.4	221	16.34
265	S17-35.2	75.86	10.99	64.87	0.86		-33.1	-9.4	180	13.29
266	S17-35.3	71.3	8.74	62.56	0.88	9.9			164	
267	S17-36.2	73.26	5.95	67.31	0.92	13.2			164	
268	S17-37	84.84	9.63	75.21	0.89	18.5	-30.1	-11.9	202	15.86
269	S17-38.1	75.26	10.22	65.04	0.86	15.2	-27.9		194	
270	S17-38.2	42.52	6.19	36.33	0.85	15.5	-30.6		198.6	
271	S17-38.3	29.02	3.75	25.27	0.87	7	-27.8	-8	186	11.7
272	S17-39.1	107.93	5.8	102.13	0.95	13.1	-30.6	-8.9	195	12.73
273	S17-39.2	129.36	7.91	121.45	0.94	17.1			199.6	

S27

	Sample	Area total μm ²	Area vap μm ²	Area liq μm ²	Degree of Fill (F)	Length μm	T _{FM} °C	T _{LM} °C	T _H °C	Salinity eq %wt NaCl
--	--------	-------------------------------	-----------------------------	-----------------------------	-----------------------	--------------	-----------------------	-----------------------	----------------------	----------------------------

274	S27-01.1	50.48	4.13	46.35	0.92	16.95			169.3	
275	S27-01.2	50.3	4.16	46.14	0.92	9.2			170	
276	S27-03	21.56	1.3	20.26	0.94	8.1			165	
277	S27-06	78.63	5.08	73.55	0.94	13.2	-26.6	-7.2	188.7	10.73
278	S27-07.1	48.26	7.86	40.4	0.84	13.94			185	
279	S27-07.2	26.58	4.1	22.48	0.85	8	-28.7	-6	159.1	5.86
280	S27-07.4	25.21	3.53	21.68	0.86	6.8			165.5	
281	S27-07.5	8.74	0.94	7.8	0.89	5.5			158	
282	S27-07.6	15.73	1.7	14.03	0.89	6.7			151.2	
283	S27-07.7	37.88	3.16	34.72	0.92	7		-6.5	157.6	9.86
284	S27-08.1	65.97	4.8	61.17	0.93	12.5		-5.9	120.8	9.08
285	S27-08.2	15.59	3.1	12.49	0.80	6		-8.4	187.8	12.16
286	S27-08.3	9.3	0.37	8.93	0.96	3.32			154.2	
287	S27-09.1	284.83	38.96	245.87	0.86	24.3	-23		229.5	
288	S27-09.2	92	9.54	82.46	0.90	15.5	-25		178.4	
289	S27-09.3	28.41	3.15	25.26	0.89	8.9			156	
290	S27-09.4	48.69	6.46	42.23	0.87	9.9		-9.8	169.6	13.72
291	S27-09.5	37.04	4.06	32.98	0.89	11.3			175	
292	S27-10.1	25.1	3.07	22.03	0.88	7.01			170	
293	S27-10.2	47.56	3.77	43.79	0.92	9.9			190.7	
294	S27-10.3	93.65	15.74	77.91	0.83	16.4	-26	-7	194.5	10.49
295	S27-10.4	36.98	5.34	31.64	0.86	8.2			155.2	
296	S27-11.1	19.34	4	15.34	0.79	6.8			192.8	
297	S27-11.2	48.72	4.52	44.2	0.91	12.7		-6.4	183.7	9.73
298	S27-11.3	30.37	4.15	26.22	0.86	8.7			176.2	
299	S27-12.1	40.33	2	38.33	0.95	8.4		-6.9	203	10.36
300	S27-12.2	67.92	6.22	61.7	0.91	13.89			189.2	
301	S27-13.1	117.15	20.07	97.08	0.83	24.1			242.5	
302	S27-13.2	5.1	0.6	4.5	0.88	2.46			132.2	
303	S27-14.1	29.68	3.53	26.15	0.88	9			164.3	
304	S27-14.2	82.47	12.46	70.01	0.85	14	-28.8	-8.5	196.4	12.28
305	S27-15	48.45	9.89	38.56	0.80	14.3	-28.4		241	
306	S27-17.1	31.16	3.78	27.38	0.88	7.6			178.5	
307	S27-17.2	20.29	3.33	16.96	0.84	5.6			193.8	
308	S27-17.3	37.76	2.69	35.07	0.93	9.17			132.1	
309	S27-17.4	18.24	3.08	15.16	0.83	7.4		-7.4	178	10.98
310	S27-17.5	36.06	4.74	31.32	0.87	10.12		-6.9	155.8	10.36
311	S27-19	33.92	3.11	30.81	0.91	9			144	
312	S27-20	150.52	13.31	137.21	0.91	26.5	-26.1	-7	150.8	10.49
313	S27-21.1	67.92	12.32	55.6	0.82	12.25			160	
314	S27-21.2	98.91	5.71	93.2	0.94	19.24		-6.2	130.7	9.47
315	S27-21.3	86.48	8.36	78.12	0.90	10.86	-31	-6.5		9.86
316	S27-21.4	56.02	5.45	50.57	0.90	12.66			146	
317	S27-21.5	33.96	3.76	30.2	0.89	7.41			161	
318	S27-22.1	88.92	6.19	82.73	0.93	27.05	-28.5	-9.2	176.7	13.07
319	S27-22.2	40.57	5.1	35.47	0.87	9.93	-25	-7.7	162.4	11.34
320	S27-23.1	154.77	26	128.77	0.83	20.5	-23.1	-9.1	173.6	12.96
321	S27-23.2	25.65	2.6	23.05	0.90	6.34			161.3	
322	S27-23.3	29.78	5.8	23.98	0.81	9.25		-9.1	153.6	12.96
323	S27-23.4	85.21	6.4	78.81	0.92	25.61			171.1	
324	S27-24.1	21.85	4.3	17.55	0.80	7.08	-24.7	-6.6	175	9.98
325	S27-24.2	30.47	2.8	27.67	0.91	10.47			162.1	
326	S27-25.1	27.14	3.2	23.94	0.88	6.81		-7.5	170.5	11.1
327	S27-25.2	39.83	5.34	34.49	0.87	9.96		-6.1	180	9.34
328	S27-25.3	45.75	3.7	42.05	0.92	8.68			178	
329	S27-26.1	85.11	14.28	70.83	0.83	18.91	-28.8	-9.1		12.96
330	S27-26.2	33.48	5.13	28.35	0.85	10.08	-22.5		170.4	
331	S27-26.3	38.61	6.4	32.21	0.83	10.6			157.6	
332	S27-27.1	155.46	13.7	141.76	0.91	20.02		-6.5	160.4	9.86
333	S27-28.2	46.65	8.2	38.45	0.82	8.17			185.2	
334	S27-28.3	22.9	1.9	21	0.92	6.9		-7	191.6	10.49
335	S27-28.4								180.1	
336	S27-29.2	70.67	6.88	63.79	0.90	12.5		-7	162.5	10.49
337	S27-29.3	40.31	4.65	35.66	0.88	8.43		-6.4	171	9.73
338	S27-30.1	31.95	3.6	28.35	0.89	9.19			243.9	
339	S27-30.2	28.4	4.23	24.17	0.85	7.81	-22.5	-8.4	224.4	12.16

340	S27-30.3	109.12	18.67	90.45	0.83	15.22		-7.3	231.3	10.86
-----	----------	--------	-------	-------	------	-------	--	------	-------	-------

S30

	Sample	Area total μm^2	Area vap μm^2	Area liq μm^2	Degree of Fill (F)	Length μm	T _{FM} °C	T _{LM} °C	T _H °C	Salinity eq %wt NaCl
341	S30-01.1	33.72	4.8	28.92	0.86				183	
342	S30-01.2	33.75	2.82	30.93	0.92		25.8	12.5	125	16.43
343	S30-01.3	8.3	1.36	6.94	0.84				190	
344	S30-02.1	33.08	4.24	28.84	0.87		27.3	9.9	189	13.83
345	S30-03.1	34.38	4.64	29.74	0.87		24	8.7	214	12.51
346	S30-03.2	27.82	1.29	26.53	0.95			7	161	10.481
347	S30-03.3	24.01	2.84	21.17	0.88		27	7.2		10.731
348	S30-04.1	32	4.5	27.5	0.86	9		10.5		14.46
349	S30-04.2	42.4	4.9	37.5	0.88	10.5		9.8	192.3	13.72
350	S30-05	12.9	2.2	10.7	0.83	8.3			184	
351	S30-06.1	38.4	3.7	34.7	0.90	11.6	24.8	10.7	160	14.67
352	S30-06.2	27.1	3.2	23.9	0.88	8.4	29.3	12.1	178.5	16.05
353	S30-07.1	28.5	2	26.5	0.93	9.4	30.5	12.2		16.15
354	S30-08.1	9.65	0.4	9.25	0.96	4.2	28.8	10.7	127	14.67
355	S30-08.2	3.61	0.5	3.11	0.86	2.6			189	
356	S30-09.1	25.73	0.9	24.83	0.97	7.2	28.7			
357	S30-09.2	7.58	0.83	6.75	0.89	3.2	33	10.6	126	14.57
358	S30-10.1	10.7	0.7	10	0.93	4.5	29.5		130	
359	S30-10.2	6.62	0.96	5.66	0.85	4.7	25.7	9.7	190	13.62
360	S30-10.3	7.8	0.6	7.2	0.92	3.5	22.7	12.5	164	16.43
361	S30-11	6.5	0.5	6	0.92	4.2	21	9.8	125	13.72
362	S30-12.1	6.46	0.53	5.93	0.92	4.57			148	
363	S30-12.2	5.69	0.58	5.11	0.90	4.9			197.3	
364	S30-13	8.04	0.61	7.43	0.92	4.8	28.5	8.5	117	12.28
365	S30-14.1	6.46	0.66	5.8	0.90	4			167	
366	S30-14.2	4.92	0.75	4.17	0.85	3			149	
367	S30-14.3	3.33	0.23	3.1	0.93	2.7		3.9	143	6.225
368	S30-15	5.26	0.56	4.7	0.89	2.7	21.3	10	140	13.94
369	S30-17.1	56.44	7.23	49.21	0.87	12.3	22.2	14.5	114.2	18.22
370	S30-17.2	14.01	3.43	10.58	0.76	7.1			150.9	
371	S30-18.1	21.94	4.05	17.89	0.82	8.6			139.3	
372	S30-18.2	10.77	2.3	8.47	0.79	6.2		5.6	123.4	8.649
373	S30-19.1	44.52	4.05	40.47	0.91	14.7		10.3	158.6	14.25
374	S30-20.1	8.95	1.4	7.55	0.84	5.9			145.3	
375	S30-20.2	14.78	2.11	12.67	0.86	6.2			142.7	
376	S30-22.1	13.89	1.28	12.61	0.91	7			143.4	
378	S30-22.2	8.81	1.21	7.6	0.86	4.6			149.8	
379	S30-22.3	27.95	1.61	26.34	0.94	8.67			124.4	
380	S30-22.4	20.15	2.76	17.39	0.86	6.5	26.7	8.6	160.9	12.39
381	S30-23.1	14.41	1.26	13.15	0.91	5.2			175	
382	S30-23.2	15.96	1.07	14.89	0.93	4.88			110.1	
383	S30-23.3	14.04	0.63	13.41	0.96	4.55			113.4	
384	S30-23.4	14.45	2.34	12.11	0.84	6.6		6.5	154	9.86
385	S30-23.5	10.02	0.7	9.32	0.93	4.05			154.4	
386	S30-23.6	27.75	1.7	26.05	0.94	6.7			175	
387	S30-24.1	26.62	2.46	24.16	0.91	8.8		8.4	168.8	12.16
388	S30-24.2	7.72	1.06	6.66	0.86	4.6			122.3	
389	S30-24.3	12.89	1.59	11.3	0.88	5.7			114.2	
390	S30-24.4	8.81	1	7.81	0.89	5.1			136.6	
391	S30-24.5	16.79	1.1	15.69	0.93	6.7		9	129.4	12.85
392	S30-25.1	13.08	1	12.08	0.92	5.17			123.9	
393	S30-25.2	21.6	2.33	19.27	0.89	8.11			190.6	
394	S30-25.3	18.35	3.59	14.76	0.80	7.8			157.1	
395	S30-26.1	35.46	4.24	31.22	0.88	9.6		7.1	129.6	10.61
396	S30-26.2	23.19	1.2	21.99	0.95	7.29			107.9	

Appendix A7

Dissemination of results

In order to demonstrate the geological importance of the part of the Copper Coast investigated in this study, research findings were presented at several stages, aimed at the scientific community, amateur geologists and the general public. Geological guides were also devised that may be made available to the wider community (included in the pocket in the back cover of this thesis), that can be combined with the pre-existing bank of self-directed guides made available through the Copper Coast Geopark. Similar field excursion guides were published in the ES2K magazine. The main geological objective of the self-guided field excursions that have been designed is to demonstrate, in a simple manner, the various volcanological features preserved in the geology today and interpretations drawn from these features. Moreover, the nature of the contacts between igneous and sedimentary lithologies (from peperite, to bulbous intrusions to sharp contact intrusions) is used to convey a sense of repeated intrusions over time into sediment that is becoming increasingly lithified. Dissemination of the basic field-guides through amateur national Earth Science awareness magazines were aimed towards amateur geologists while drafts of the field-guides are being finalised to be possibly distributed from the Geopark Office and local Tourist Information Centres. Data sheets of selected lithologies from the studied area have also been produced (Appendix A2) that may be made available to the Copper Coast Geopark to provide additional information that may be published in field guides.

The purpose of the Copper Coast Geopark, designated as a European Geopark in 1999 and as a Global Geopark in 2001 by the United Nations Educational, Scientific and Cultural Organisation (UNESCO), is to provide a means of communication to the general public regarding the geological, economic and social importance of this site. The Geopark has been involved in conservation of mining heritage, including archaeological excavations, conservation and reconstruction. Conservation work was carried out on the Tankardstown mine between 2004 and 2005 with the main work being carried out on the pumping engine house and the winding engine house (Critchley and Morris, 2005). Other features provided by the Geopark include a geological garden in Bunmahon village and information related to the history of mining and the area and the subsequent archaeological and conservation work carried out on engine houses in the area. More importantly for communication of scientific results, is that the Geopark maintains geological information boards and an office as a venue for

public contact. A scientific poster entitled “Submarine magmatism and alteration at the Bunmahon Volcano, County Waterford”, presented as part of ongoing research within this project, has also been donated to the Geopark Office.



Sites of interest in the Copper Coast Geopark include (a) Trawnamoe and (b) Stradbally Cove, with the self-guided field trip pamphlets produced as a result of this study providing field localities and descriptions, (c) the Monksland Centre within an old church housing the Geopark office, (d) information noticeboards produced by the Geopark erected at various localities including the Bunmahon Geological Garden, (e) the old engine house and (f) accompanying shaft in Tankardstown.

[Photograph (c) from www.coppercoastgeopark.com]

A number of publications and presentations have been disseminated to both the public and scientific community during the course of this research.

Publications

Breheny, C., and Moore, K. R., 2008: Ocean floor lavas in County Waterford: *Earth Science Ireland*, 3, 8-11.

Pamphlets (see back pocket)

The Copper Coast Geopark, County Waterford, Ireland. Geological guide – Trawnamoe: Volcanism on a 460 million year old seafloor.

The Copper Coast Geopark, County Waterford, Ireland. Geological guide – Stradbally Cove: Volcanism on a 460 million year old seafloor (2).

Presentations

Breheny, C., Moore, K. R., Costanzo, A., and Feely M., 2010: Magma-sediment-water interaction: a precursor to base metal mineralisation?: *The 20th general meeting of the International Mineralogical Association*: Budapest, Hungary. **Oral presentation.**

Breheny, C., Costanzo, A., Feely, M., and Moore, K. R., 2010: The role of magma-sediment-water interaction for base metal mineralisation on the Ordovician ocean floor: Microbeam and fluid inclusion investigations of the Bunmahon Formation, County Waterford: *53rd Irish Geological Research Meeting*: Ulster Museum, Belfast. **Oral presentation.**

Breheny, C., and Moore, K. R., 2009: Submarine magmatism and alteration at the Bunmahon Volcano, County Waterford: *Volcanic and Magmatic Studies Group Winter Meeting*: Bournemouth University. **Poster presentation.**

Breheny, C., and Moore, K. R., 2008: Self-guided field excursions to Ordovician ocean floor processes in the Copper Coast Geopark of County Waterford, Ireland: *The 33rd International Geological Congress*, Oslo. **Poster presentation.**

Breheeny, C., and Moore, K. R., 2008: Shallow magmatic processes in the Ordovician ocean floor: juvenile clast morphology and compositional variation in peperite from the Bunmahon Formation, County Waterford, Ireland: *The 33rd International Geological Congress*, Oslo, Norway. **Oral presentation.**

Breheeny, C., and Moore, K. R., 2008: Investigating the processes involved in peperite formation: *Volcanic and Magmatic Studies Group Winter Meeting*, Trinity College, Dublin. **Oral presentation.**

Breheeny, C., and Moore K. R., 2007: Image analysis of the Bunmahon peperite, County Waterford, and application to the behaviour of magma in sediment: *Frontiers in Mineral Sciences*, Fitzwilliam College, University of Cambridge. **Poster presentation.**

Breheeny, C., and Moore, K. R., 2007: Passive versus explosive emplacement of Bunmahon peperite: *Volcanic and Magmatic Studies Group Winter Meeting*, St. Annes College, Oxford. **Poster presentation.**